Molecular Microscopy on Graphene

by

Zachary Peter Lewin Laker

Thesis

Submitted to the University of Warwick

for the degree of

Doctor of Philosophy

Physics

March 2018

Contents

List of Figures

List of Tables

Acknowledgments

I would like to begin by acknowledging several people for their overwhelming support throughout this work.

Firstly, I thank Dr Neil Wilson for providing me the opportunity to pursue a PhD, and for his tireless help and guidance throughout the PhD process. His unrivaled enthusiasm for science has helped keep me motivated during challenging periods, and continues to remind me as to why I set out on this journey in the first place - the pleasure of finding things out.

I am also greatly indebted to Laurence Hampton for igniting my scientific curiosity to begin with. His wonderful enthusiasm for physics and inspirational teaching led me to pursue a course in physics at university, for which I am eternally grateful.

Throughout this work I have received countless help from many academics: Dr Giovanni Costantini and Dr Jon Rourke have both helped improve my limited understanding of chemistry, as well as demonstrate how to successfully debate with Dr Neil Wilson; Dr Ana Sanchez has taught me much about TEM and continues to spoil the group with numerous cakes. Dr Richard Beanland and Dr Jeremey Sloan also have helped to make the group a very enjoyable place to work.

I have been fortunate enough to make many great friends over these last four years. In particular, I thank Maria Chiara Roffin for her wonderful friendship and the countless hours spent enjoying well-needed coffee together. She has always been willing to listen to any and every problem I have had, and I can only hope that I have been able to return her the favour. I also owe a great deal of thanks to Alex Marsden, for his unwavering support during the beginning of my PhD and for

acting as an excellent role model. He also taught me a great many lessons in supervisor management. Jonathan JP Peters has also provided a great deal of support throughout the PhD process, including countless TEM advice, and introductions to TV programmes and alcoholic beverages that have helped shaped my life. There are countless others both inside and outside the microscopy group that I would like to acknowledge, and I know that if I were to express my true gratitude for each of them in writing then this thesis would double in length at least.

I also greatly appreciate the tireless effort of the wonderful technicians that the department is so lucky to have been afforded. Steve York and Steve Hindmarsh have always been friendly and approachable at the worst of times, no matter what microscope I have managed to break.

Finally, I would like to express significant thanks to my family. Throughout my struggles as an undergraduate and graduate student, you have all helped to keep me motivated and supported me in ways I cannot thank you enough for. My wonderful parents have both provided me with unrivaled encouragement and support throughout all of my life, and have always been willing to offer me assistance without hesitation. This thesis would never have been completed without your help, and I am forever indebted to you both.

Declarations

I declare that this thesis contains an account of my research work carried out at the Department of Physics, University of Warwick, between October 2014 and March 2018 under the supervision of Dr N. R. Wilson. The research reported here has not been previously submitted, wholly or in part, at this or any other academic institution for admission to a higher degree. Parts of this thesis have been published by the author and his collaborators between October 2014 and March 2018:

- The material on multislice image simulation applied to large molecular crystal systems in section 2.3.1 was included within the publication titled 'Growth of Large Crystalline Grains of Vanadyl Phthalocyanine without Epitaxy on Graphene' [1].

- The material on graphene TEM grid functionalisation using non-covalent and covalent means in section 3.3.5 was published under the titles 'Non-covalent functionalization of graphene with a hydrophilic self-limiting monolayer for macro molecule immobilization' [2] and 'Thermochemical functionalisation of graphenes with minimal framework damage' [3].

- The crystal structures of polylactide-based block copolymer nanostructures were determined using the low-dose molecular diffraction methods described in section 4.3.1, and published under the titles '1D vs. 2D shape selectivity in the crystallization-driven self-assembly of polylactide block copolymers' [4] and 'Precision Epitaxy for Aqueous 1D and 2D Poly(ϵ-caprolactone) Assemblies' [5].

- Chapter 5 was published under the title 'Monolayer-to-thin-film transition in supramolecular assemblies: the role of topological protection' [6].
- The material on Au_9 nanoclusters studied using real-time HRTEM in section 7.3.1 was published under the title 'Covalently Binding Atomically Designed Au_9 Clusters to Chemically Modified Graphene' [7].

Other parts of the thesis are to be published shortly:

- The material on holey-formvar graphene TEM grid fabrication in section 3.3.4 is to be submitted under the title 'Holey-formvar graphene TEM grids'.
- The material in chapter 6 is to be submitted under the title 'Remote molecular epitaxy across graphene'.
- The material in section 7.3.2 is to be submitted under the title 'Atomically-resolved molecular dynamics on graphene'.

All the work presented here was completed by myself, except for the following:

- The pyrene samples used in section 3.3.5 were prepared by Dr Concha Bosch-Navarro and Dr Jon Rourke, University of Warwick.
- The thermochemical functionalisation methods used in section 3.3.5 were performed by Dr Hu Cheng and Professor Milo Shaffer, Imperial College London.
- The polylactide-based block copolymer nanostructure samples used in section 4.3.1 were provided by Dr Maria Inam and Professor Rachel O'Reilly, University of Warwick.
- The graphene dose-dependent data obtained for Gatan OneView and Medipix3 cameras, shown in figures 4.8 and 4.9, was obtained under the supervision of Dr Christopher Allen, Diamond Light Source.
- The scanning tunneling microscopy images shown in figure 5.1 were obtained by Dr Luis Alves, University of Warwick.

- The transmission electron microscopy images and some of the diffraction patterns shown in figure 5.2 were obtained by Dr Alexander Marsden, University of Warwick.
- The scanning tunneling microscopy images shown in figure 5.4 were obtained by Dr Luis Alves, University of Warwick.
- The transmission electron microscopy images shown in figure 5.5 were obtained by Dr Alexander Marsden, University of Warwick.
- The transmission electron microscopy images and diffraction patterns shown in figure 5.8 were obtained by Dr Alexander Marsden, University of Warwick.
- The transmission electron microscopy images shown in figure 5.10 were obtained by Dr Alexander Marsden, University of Warwick.
- The transmission electron microscopy images shown in figure 7.4 were obtained by Dr Alexander Marsden, University of Warwick.

Abstract

The autonomous ordering and assembly of atoms and molecules on atomically well-defined surfaces combines ease of fabrication with exquisite control over the shape, composition and mesoscale organization of the surface structures formed. Once the mechanisms controlling the self-ordering phenomena are fully understood, the self-assembly and growth processes can be steered to create a wide range of nanostructures with exotic and desirable properties, synthesised from the *bottom-up*, on an industrial scale from metallic, semiconducting and molecular materials. The work of this thesis aims to address questions concerning molecular self-assembly on graphene.

Firstly, techniques for fabricating graphene membranes for electron microscopy (EM) are outlined. The complete fabrication process is described, beginning with the growth of CVD graphene, followed by the transfer of graphene from chemical vapour deposition (CVD) foils to a transmission electron microscope (TEM) support, and finishing with the cleaning steps involved to produce pristene regions of graphene. Strategies to chemically functionalise graphene through covalent and non-covalent means are detailed, as well as methods to fabricate more specialised graphene TEM membranes consisting of stacked and sandwiched graphene layers.

With the methods used to fabricate and modify graphene EM membranes described, attention is next focused on specific microscopy techniques developed in order to study organic materials that readily damage when exposed to the electron beam in an electron microscope. Strategies to mitigate the damage arising due to beam exposure are investigated for a range of different organic molecules, and the effects of using a range of detection devices are also studied.

Next, the growth of two very similar overlayer systems on graphene are studied. Trimesic acid (TMA) and terephthalic acid (TPA) thin films are grown on both freestanding and CVD graphene substrates for a range of thicknesses, and the resulting structures are probed using a range of microscopy techniques. For TMA, van der Waals epitaxy results in two preferred orientations of the assembly structure that grows in a layer-by-layer Frank-van der Merwe fashion, up to a height of ≈ 20 nm. In stark contrast, TPA assembles into a 2D monolayer before rapidly transitioning to its bulk-like structure as further layers are deposited, following a layer-plus-island, or Stranski-Krastanov, growth mode.

Continuing the investigations into the structure of self-assembling molecular films on graphene, a pair of porphyrin-based molecules of the octaethyl porphyrin (OEP) class are studied. A monolayer film of OEP molecules is deposited either side of a freestanding graphene membrane, and the resulting assembly structure is driven by a remote interaction across the graphene between the two OEP films. The remote interaction is shown to diminish on the length scale of two graphene layers.

Finally, the structure and motion of individual metal nanoclusters (M-NCs) deposited on freestanding graphene is studied using high-resolution TEM. Computational routines involving cross-correlation techniques are developed in order to better study the dynamic behaviour of M-NCs in atomically-resolved time-series image sequences. The strategies developed provide a means for accurately studying more complex systems, structural changes, and chemical reactions at atomic-resolution and in real-time.

Abbreviations

1D	One-Dimensional
2D	Two-Dimensional
3D	Three-Dimensional
AFM	Atomic Force Microscope (Microscopy)
AP-G	As-produced Graphene
ARM	Atomic Resolution Microscope
Au_9	$[Au_9(PPh_3)_9]^+$ Nanocluster
CB	Carbon Black
CMG	Chemically Modified Graphene
CMOS	Complementary Metal-Oxide-Semiconductor
CNT	Carbon Nanotube
CPD	Critical Point Dryer (Drying)
CVD	Chemical Vapour Deposition
DDD	Direct Detection Device
DFT	Density Functional Theory
DI	De-Ionised
DQE	Detector Quantum Efficiency
ED	Electron Diffraction
EM	Electron Microscope (Microscopy)
FEG	Field Emission Gun
FFT	Fast Fourier Transform
FM	Frank van der Merwe
GNP	Graphene Nanoparticle
GO	Graphene Oxide
GPU	Graphical Processing Unit
hBN	Hexagonal Boron-Nitride
HOPG	Highly Oriented Pyrolytic Graphite
HRTEM	High Resolution Transmission Electron Microscope (Microscopy)
LDOS	Local Density of States
LD	Low Dose
LED	Light Emitting diode

MD	Molecular Dynamics
MFC	Mass Flow Controller (Control)
ML	Monolayer
M-NC	Metal-Nanocluster
MTF	Modulation Transfer Function
MWCNT	Multi-Walled Carbon Nanotube
NiOEP	Nickel(II) Octaethyl Porphyrin
NP	Nanoparticle
NPS	Noise Power Spectrum
ODE	Ordinary Differential Equation
OEP	Octaethyl Porphyrin
OMBD	Organic Molecular Beam Deposition
PCTF	Phase Contrast Transfer Function
PLLA	Poly-l-Lactic Acid
POM	Phosphotungstic acid $[W_{12}O_{40}P]^{3-}$ Polyoxometalate
pyr$^-$	Sodium (2-oxo-2-pyren-1-yl-ethyl)-sulfonate
pyr$^+$	Trimethyl-(2-oxo-2-pyren-1-yl-ethyl)-ammonium bromide
QCM	Quartz Crystal Microbalance
RE	Rate Equation
SAED	Selected Area Electron Diffraction
sccm	Standard Cubic Centimetres per Minute
SK	Stranski-Krastanov
SNR	Signal-to-Noise Ratio
STM	Scanning Tunneling Microscope (Microscopy)
SWCNT	Single-Walled Carbon Nanotube
TCNQ	Tetracyanoquinodimethane
TEM	Transmission Electron Microscope (Microscopy)
TFI-G	1,1,1−trifluoro−2−iodoethane Graphene
TMA	Trimesic Acid
TPA	Terephthalic Acid
TTC-G	Thermally-Treated Control Graphene
TTF	Tetrathiafulvalene
VOPc	Vanadyl-Oxide Phthalocyanine
VW	Volmer-Weber
WPO	Weak Phase Object

Chapter 1

Introduction

> "But I am not afraid to consider the final question as to whether, ultimately - in the great future - we can arrange the atoms the way we want; the very *atoms*, all the way down! What would happen if we could arrange the atoms one by one the way we want them? ... What would we do with layered structures with just the right layers? What would the properties of materials be if we could really arrange the atoms the way we want them? They would be very interesting to investigate theoretically. I can't see exactly what would happen, but I can hardly doubt that when we have some *control* of the arrangement of things on a small scale we will get an enormously greater range of possible properties that substances can have, and of different things that we can do."
>
> - Richard P. Feynman, *"There's plenty of room at the bottom"*, 1959

1.1 Background

In 1959, Richard Feynman presented a lecture to the American Physical Society in which he described some of the challenges and potential applications of probing and manipulating materials at the nanoscale; if you have not read it already, you should interrupt this introduction to read it now. "There's plenty of room at the bottom" commonly forms the basis of people's first impression of Nanoscience, due to the amazing technological developments Feynman described, although Nanoscience extends far beyond technological applications. The world of the atom is dominated by quantum mechanics, and nanosystems typically contain tens to tens of thousands of atoms. Nanosystems lead to the convergence of atomic physics with the statistical behaviour of complex physical and chemical systems, from which many new and interesting phenomena emerge. These phenomena arise for a range of system sizes, from the smallest nanoscale objects through to biological processes. What makes these systems even more attractive for study is the relatively small number of total atoms contained - within the realms of modern computational simulation techniques. In addition, nanoscale phenomena transcend the specific scientific field in which they are studied, be it physics, materials science, chemistry, or biology. This provides a remarkably diverse and wide-ranging field of research, with ample opportunity for collaboration and fresh scientific developments.

During Feynamn's legendary talk, he predicted several technological innovations, along with descriptions of how they could be achieved. Many of these predictions have already been realised to great success, including: electron beam lithography, focused ion beam etching, nanostructure stamping, biological motors, miniaturising computer components to build supercomputers, using quantum phenomena in electronic devices, making atomic scale structure by evaporating layers of atoms, and performing analysis of complex chemical and biological molecules by direct imaging. These final two predictions, *fabricating atomic materials through evaporation* and *directly imaging complex molecular structures*, are central to the work presented in this thesis.

In 2004 and 2005, two revolutionary papers were published by Novoselov et al. [8, 9] that led to the awarding of the Nobel prize for physics in 2010 to Sir Professor Andrei Geim and Sir Professor Kostya Novoselov, from the Manchester University, for their '*ground-breaking experiments regarding the two-dimensional material graphene*'. Through their work, Novoselov and Geim successfully managed to isolate, manipulate, and measure the properties of a single sheet of graphite only one atom thick - called *graphene*. These investigations ignited the field of graphene research, which has grown and evolved significantly, and has led to the discovery of many other types of exotic two-dimensional (2D) materials [10–12].

The great interest in 2D material research stems from the exotic phenomena they exhibit, arising due to quantum effects, and subsequently their vast and significant technological potential [11, 12]. Not only are the fundamental properties and behaviour of such materials interesting, but also their integration to form complex heterostructures along with molecules and other materials. Following on from the words of Feynman, it is now possible to produce with great precision and repeatability complex material structures consisting of individual layers of atoms in different arrangements. As well as forming heterostructures using layers of atomic materials, the integration of molecular materials adds even further depth to the material properties that can be engineered with atomic precision [13–16].

The autonomous ordering and assembly of atoms and molecules on atomically well-defined surfaces combines the ease of fabrication with exquisite control over the shape, composition and mesoscale organization of the surface structures formed. Once the mechanisms controlling the self-ordering phenomena are fully understood, the self-assembly and growth processes can be steered to create a wide range of nanostructures, synthesised from the *bottom-up*, on an industrial scale from metallic, semiconducting and molecular materials.

The work of this thesis aims to address some of the questions on the mechanisms controlling self-ordering phenomena involving graphene. Specifically, it explores how graphene interacts with a range of atoms and molecules. The influence of graphene on self-ordering behaviour, and the mechanisms involved in such processes, are studied in detail. Understanding these phenomena allows the engineering of useful and exotic nanostructures with great control, and enables further complex physical, chemical, and biological processes to be studied.

1.1.1 Graphene

Graphene is a structural form (allotrope) of carbon consisting of a single layer of carbon atoms arranged in a honeycomb arrangement [17], as shown in figure 1.1. Graphene forms the basic structural component of several other carbon allotropes, including graphite, carbon nanotubes, fullerenes, and charcoal. The structure of graphene can be described using a real-space lattice with vectors:

$$\mathbf{a} = \left(\frac{\sqrt{3}a}{2}, \frac{a}{2}\right) \quad \text{and} \quad \mathbf{b} = \left(\frac{\sqrt{3}a}{2}, -\frac{a}{2}\right) \tag{1.1}$$

where $a = \sqrt{3}a_0$ ($a_0 = 0.142$ nm, the carbon-carbon bond distance) and the lattice angle separating $\mathbf{a}$ and $\mathbf{b}$ is $\gamma = 60°$. The graphene lattice has an associated basis consisting of two carbon atoms separated by $a_0 = 0.142$ nm.

Each carbon atom possesses four bonds, due to its valency of +4. These are divided between its three neighbours in the form of σ bonds, leaving a single $\pi-$bond, as shown in figure 1.1. The σ bonds arise due to the hybridisation of the $2s$, $2p_x$, and $2p_y$ orbitals to form three sp^2 hybridised orbitals (σ bonds). The remaining $2p_z$ orbital overlaps between carbon atoms and delocalises, forming a continuous π orbital above and below the entire graphene sheet. This free movement of delocalised electrons across the entire graphene layer is what drives the high conductivity of graphene.

As well as a real-space lattice, graphene possesses a corresponding reciprocal-space lattice:

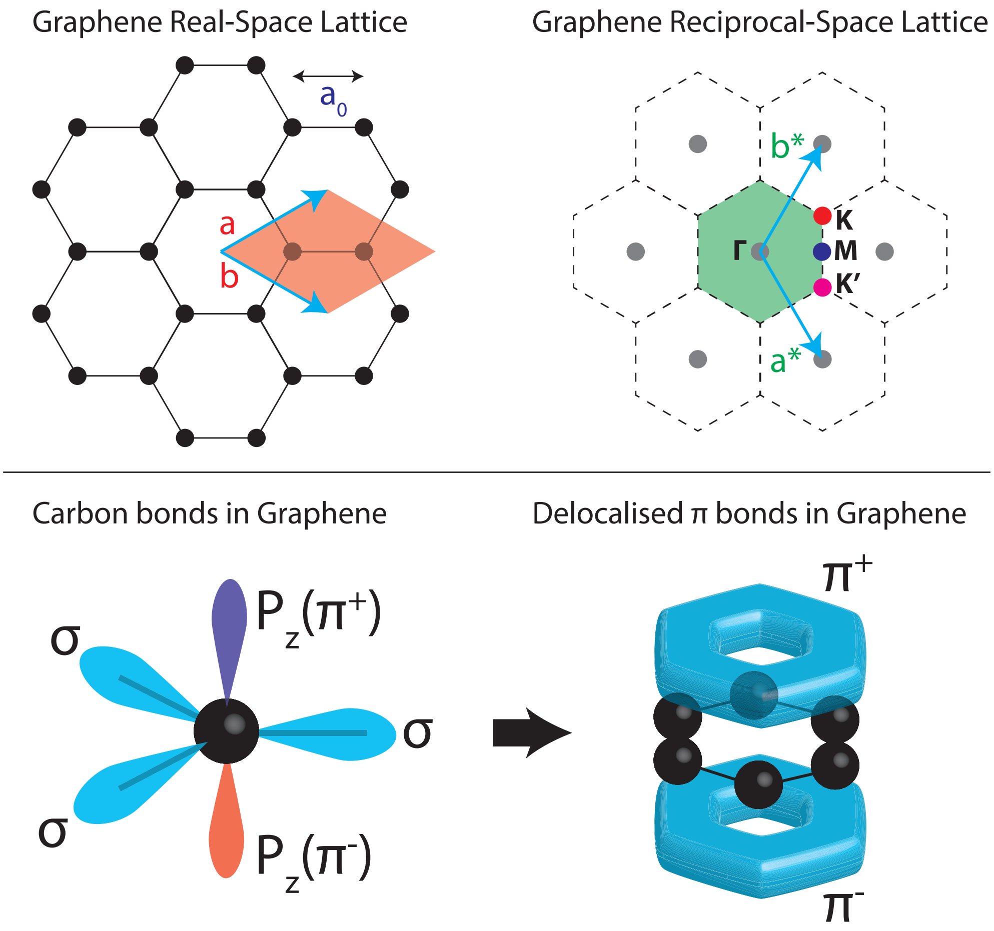

Figure 1.1: Graphene real-space and reciprocal-space lattices (Top) and orbitals and bond formation of carbon atoms within the graphene lattice (Bottom).

$$\mathbf{a}^* = \left(\frac{1}{\sqrt{3}a}, \frac{1}{a}\right) \quad \text{and} \quad \mathbf{b}^* = \left(\frac{1}{\sqrt{3}a}, -\frac{1}{a}\right) \tag{1.2}$$

$$\Gamma = (0,0), \quad K = \left(\frac{1}{\sqrt{3}a}, \frac{1}{3a}\right), \quad K' = \left(\frac{1}{\sqrt{3}a}, -\frac{1}{3a}\right), \quad M = \left(\frac{1}{\sqrt{3}a}, 0\right) \tag{1.3}$$

The high-symmetry points (Γ, K, K', M) of the reciprocal lattice are illustrated in figure 1.1. The relation between real-space and reciprocal-space lattices is described in detail in chapter 2. The first Brillouin zone is a uniquely defined primitive cell in reciprocal space, and is highlighted in green in figure 1.1.

By Bloch's theorem, the wavenumber of electrons in a crystalline solid are defined within the first Brillouin zone; the relation between their energies and momenta describes the electronic structure of a material. In this context, the two reciprocal-space points K and K', also referred to as the *Dirac points*, are of significant importance [18]. At the Dirac points, the conduction and valence bands touch (figure 1.2), categorising graphene as a semi-metal (zero bandgap material). In addition, the dispersion relation at the Dirac points exhibits linear behaviour [9], as shown in figure 1.2. The dispersion relation for graphene may be described by:

$$E_{\pm}(\mathbf{k}) = \pm t\sqrt{3 + f(\mathbf{k})} - t' f(\mathbf{k}) \tag{1.4}$$

$$f(\mathbf{k}) = 2\cos\left(\sqrt{3}k_y a_0\right) + 4\cos\left(\frac{\sqrt{3}}{2}k_y a_0\right)\cos\left(\frac{3}{2}k_x a_0\right) \tag{1.5}$$

where $\mathbf{k}$ is the electron wavevector, t ($\approx$ 2.8 eV) is the nearest−neighbour hopping energy (hopping between different sublattices), and t' is the nearest−neighbour hopping energy (hopping in the same sublattice) [18]. The band structure described by Equation 1.4 is plotted in figure 1.2.

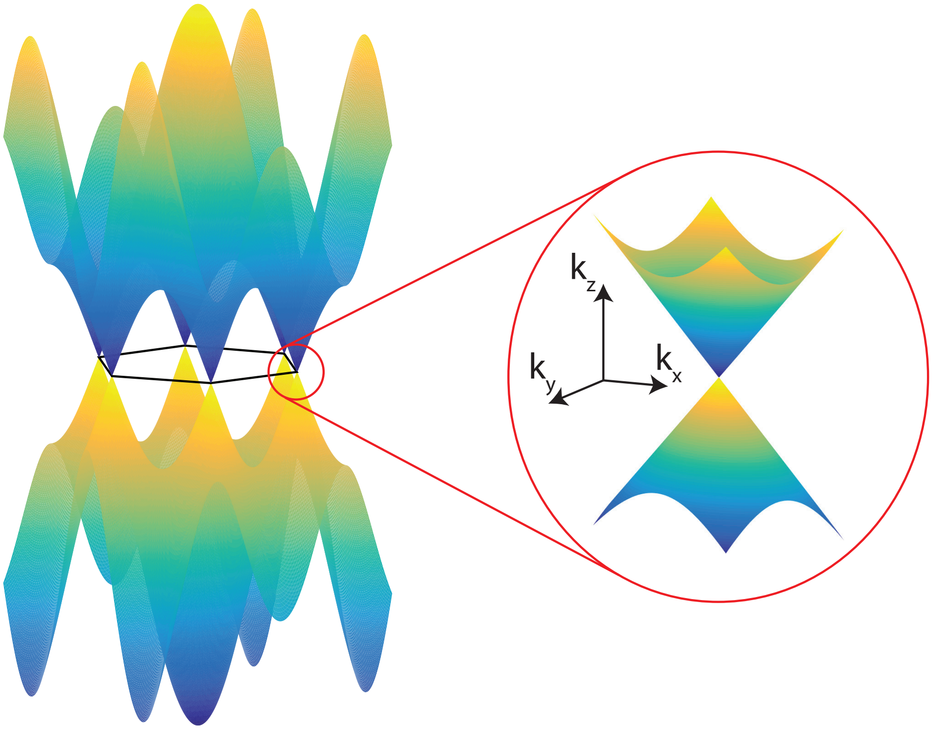

Figure 1.2: Graphene band structure, illustrating the linear dispersion existing around the Dirac point.

The zero-band gap and linear dispersion about the Dirac points gives rise to the unique electronic properties of graphene. The charge carriers behave like Dirac fermions, quantum mechanically described by the relativistic Dirac equation [9], which produces an extremely high intrinsic carrier mobility. As a result, graphene provides an ideal candidate for application in molecular electronics [17].

As well as high electrical conductivity and atomic thinness, graphene possesses several other remarkable properties. The extremely high thermal conductivity of graphene has been measured in the range $\approx (4.84 \pm 0.44)\ \times 10^3$ to (5.30 ± 0.48) $\times 10^3$ W mK^{-1}, suggesting that graphene can outperform carbon nanotubes in heat conduction [19]. Graphene also possesses an unrivaled intrinsic strength of (42 ± 4) Nm^{-1} and an effective Youngs modulus of (1.0 ± 0.1) TPa, which makes graphene the strongest material ever measured [20]. In addition, graphene sheets are very flexible. They can be suspended over trenches micrometres across, indented with a sharp cantilever tip to great extension, and still return to their original shape [20]. Sheets suspended in this manner could be used as resonators with a very low noise floor, suitable for extremely low mass and force detection [21].

Another key property of graphene is its optical transparency. It has an opacity of (2.3 ± 0.1) % that is almost independent of the wavelength, and a reflectance of $< 0.1\%$ [22]. Additional layers of graphene add 2.3 % to the total opacity, making graphene ideal as an electrode for opto-electronic devices such as photodetectors or photovoltaics. The close-knit honeycomb network of carbon atoms also makes graphene completely impermeable to almost everything bar hydrogen and protons; not even Helium can pass through a single layer of graphene [23, 24].

Combined, each of these exquisite properties show promise for many applications, and this potential is enhanced with graphene's 2D nature. With the ultimate surface area of 2630 m^{2}g^{-1} [25], graphene is ideally suited for use as a contact sensor in chemical detection [26, 27], with its low noise levels ideal for single-molecule sensitivity [28]. The large surface area of graphene is also conducive to energy storage [25], and as already mentioned, its high carrier mobility enables high-frequency electronics applications such as 100 GHz transistors [29, 30]. Finally, the optical transparency of graphene makes it suitable as a replacement for transparent conducting electrodes used in photonics, providing a route to flexible light-emitting diodes (LEDs) and other photovoltaic devices [31]. These examples only scratch the surface of the full potential of graphene, and there are numerous other current technological applications that graphene is at the centre of [12].

There are several methods available for the fabrication of graphene, including mechanical exfoliation, chemical exfoliation, bottom-up synthesis from molecular precursors, and chemical vapour deposition (CVD) using a variety of different substrates [12, 17]. Each strategy has its own benefits and limitations with respect to quality, affinity for scaling, and ease of graphene isolation. The growth of graphene on metal substrates via CVD is one of the most popular synthesis routes, if not the most popular. CVD graphene has significant potential for scaling up to industrial fabrication sizes, with 100 m long 0.21 m wide roll−to−roll growth already demonstrated [32, 33].

The basic premise of CVD graphene growth involves passing a carbon feedstock over the surface of a catalyst substrate (typically a transition metal) at elevated temperatures. The catalyst then catalytically decomposes the feedstock to provide a supply of carbon, which may then assemble on the substrate to form graphene. Although the basic experimental procedure is simple, our understanding of the dynamics of carbon deposition and domain growth remain somewhat limited. The CVD parameters that most affect the graphene outcome are cooling rate, carbon exposure time and concentration, flow rate and carbon feedstock (source). In addition, the geometry of the reactor can affect the flow and deposition characteristics. Moreover, the role of impurities can also play a negative role in the final growth of the desired graphene [17].

1.1.2 Epitaxial Thin film growth

The basic reaction kinetics driving the growth of graphene during the CVD process can be better understood using the basic theory of epitaxial thin film growth. The term epitaxy stems from the Greek words epi ($\grave{\epsilon}\pi\iota$), meaning 'above', and taxis ($\tau\grave{\alpha}\xi\iota\sigma$), meaning an 'ordered manner', and can be translated as 'arranging upon'. In a scientific context, epitaxy refers to the deposition of a crystalline overlayer on a crystalline substrate.

For many technological applications, particularly in the semiconductor industry, it is desirable to deposit a crystalline overlayer with a well−defined orientation with respect to the crystalline substrate, referred to as single−domain epitaxy [34]. Films may be grown on substrates of the same composition (*homoepitaxy*) and of a different composition (*heteroepitaxy*). In addition, the overlayer does not necessarily have to deposit with a well−defined orientation with respect to the substrate. An overlayer growing with a random orientation is referred to as *non-epitaxial growth.*

The different modes of growth result in a rich variety of overlayer−substrate relationships, and can produce overlayer films with varying degrees of strain, dislocations, and exotic lattice structures based on the crystal structure and composition of substrate and depositing material [35]. As shown in figure 1.3, the presence of dangling bonds between a lattice mismatched overlayer and substrate can induce strains within both the overlayer and substrate, as well as structural defects [36]. The lattice mismatch can be characterised by [37]:

$$f = \frac{a_s - a}{a} \tag{1.6}$$

where a_s is the lattice parameter of the substrate and a is the lattice parameter of the overlayer. For even small lattice mismatches, the strain induced on the films can significantly degrade the interface's properties [38]. Lattice mismatches greater than 5% will typically induce dislocations and stacking faults, which again degrade the interface's performance significantly [39].

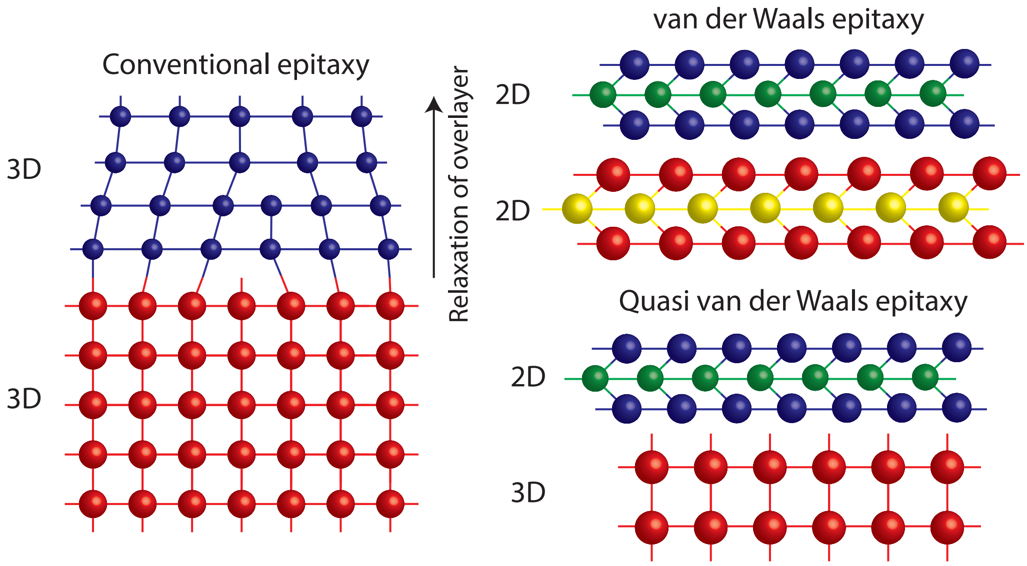

Figure 1.3: Interfaces connected by dangling bonds (left), van der Waals gap (upper right) and quasi van der Waals gap (bottom right).

van der Waals Epitaxy

In addition to standard epitaxy involving covalent bonding between the overlayer and substrate, epitaxial films can be grown with weaker non-covalent van der Waals interactions between overlayer and substrate [40]. As shown in figure 1.3, this can occur at the interface between a 2D material and another 2D material (van der Waals epitaxy), or at the interface between a 2D material and a 3D material (quasi van der Waals epitaxy). Van der Waals interface growth again can involve epitaxial and non−epitaxial growth modes, and is typified by the following conditions: **1**)

The lattice planes at the interface are incoherent (no lattice matching of interface lattice vectors at any point) and incommensurate (irrational relationship between interface lattice vectors). **2**) The interface shows no excessive strain induced by the epitaxy even for large lattice mismatches ($f > 50\%$). **3**) The epitaxy persists even for large lattice mismatches and different symmetries.

Films deposited with only weak van der Waals interactions with the substrate typically exhibit a consistent orientation relationship with the substrate, although this is not always the case [1]. Relaxing the requirement of matching lattices and symmetries between overlayer and substrate allows a much greater freedom in choice of depositing and substrate materials, including molecular self−assemblies and other organic films [6, 40, 41].

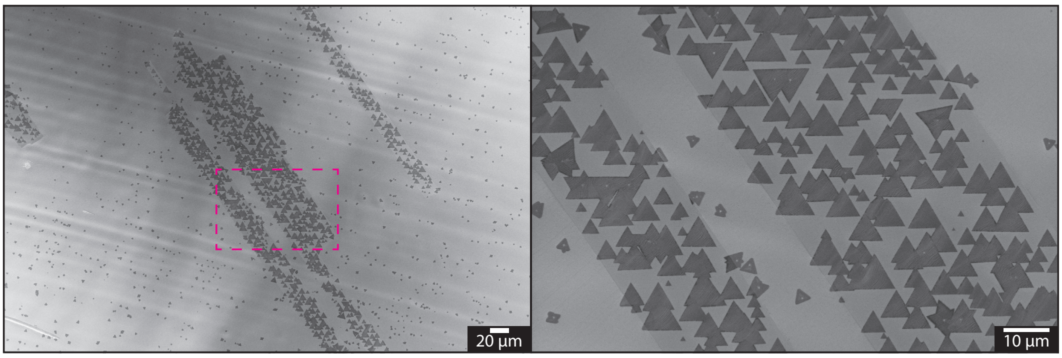

Figure 1.4: hBN preferential growth on Cu(111) crystal surface. hBN islands, visible as dark triangles, grow preferentially on the Cu(111) surface, as visible in both images. The difference in contrast of the Cu(111) microstripe is also visible. In addition, the hBN islands have a much stronger van der Waals interaction with the Cu(111) surface, producing epitaxial islands with a stricter orientation with respect to the Cu(111) surface [42].

The relaxation of matching lattice requirements can also result in a difference in growth rates of the overlayer in different regions of substrate, depending on the substrate crystallography [42–44]. This is illustrated in figure 1.4, which shows SEM images from a CVD−prepared sample of hexagonal boron−nitride (hBN), a 2D analogue of graphene comprised of alternating boron and nitrogen atoms, which grows preferentially on the Cu(111) surface. For the case of graphene grown on Cu substrates, there is an apparent structural feedback between the graphene and copper surface, whereby the graphene induces and stabilises restructuring of the Cu surface to form (n10) facets, and in turn these facets play an important role in the nucleation and growth of the graphene [44].

With the key concepts of epitaxial growth now introduced, the atomic pro-

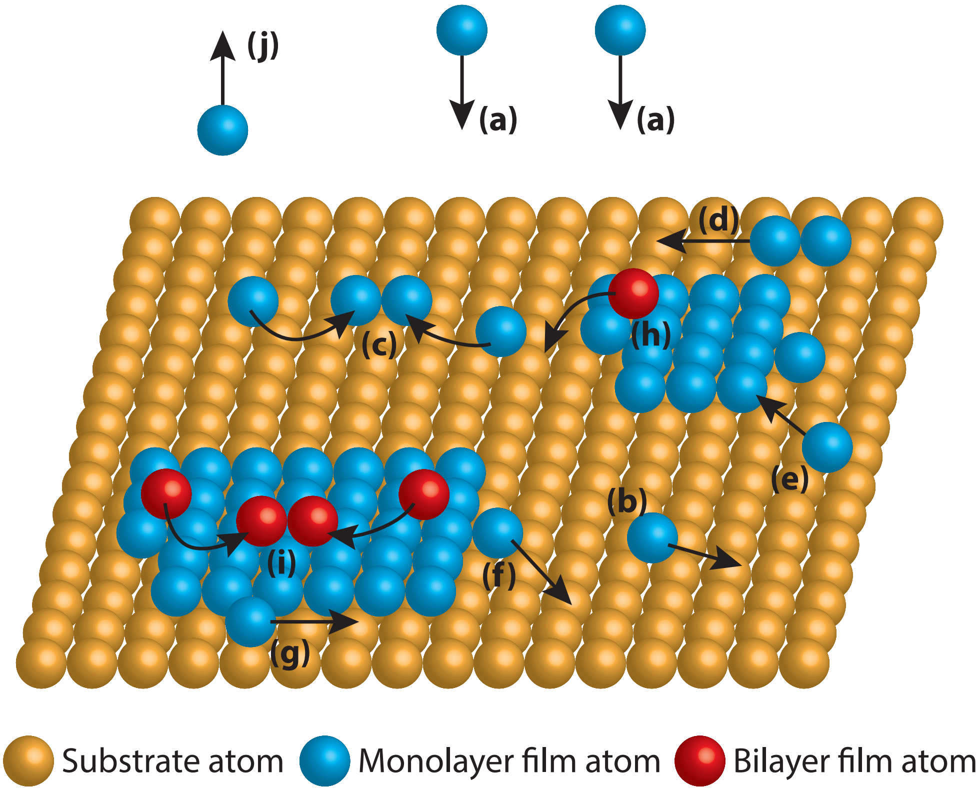

Figure 1.5: Typical atomistic processes occurring during epitaxial growth.

cesses that occur during growth can now be described. The typical processes that occur during growth of a crystal on the surface of a substrate are as follows [35]: **a**) adatoms (surface-adsorbed atoms) can adsorb onto a surface. **b**) adatoms can diffuse across the surface with a diffusion constant D. **c**) adatoms can meet other adatoms to form a dimer. **d**) dimer adatoms can detach. **e**) adatoms can attach to existing islands. **f**) adatoms can detach from island edges. **g**) adatoms can diffuse along island edges. **h**) adatoms can deposit on top of islands, and can diffuse onto the surface. **i**) adatoms can meet other atoms on top of islands, forming a dimer. Subsequent secondary layer processes can then occur. **j**) adatoms can desorp at high temperatures.

These processes are illustrated in figure 1.5. The time-evolution of mean-field quantities, such as the density of islands n_s of size s, can be described by a set of coupled ordinary differential equations (ODEs) known as rate equations (REs). Atoms arrive with a flux F or rate R and adsorb onto a surface to become adatoms. Adatoms (islands of size $s = 1$ with density n_1) can get captured by islands of size s with a capture efficiency σ_s. Adatoms can also meet another adatom with a capture efficiency σ_1 to form a dimer (an island of size $s = 2$). At high substrate temperature, these adatoms can re-evaporate. If the adsorption energy E_a is low, then the evaporation time τ_a is short, and this evaporative quasi-equilibrium is quickly established at low adatom density, with $n_1 = F\tau_a$. These processes are illustrated in figure 1.6. Within the literature, there are two main types of RE model. These emphasize either the role of the critical nucleus of size i, or the attachment and detachment rates for islands of all size [45].

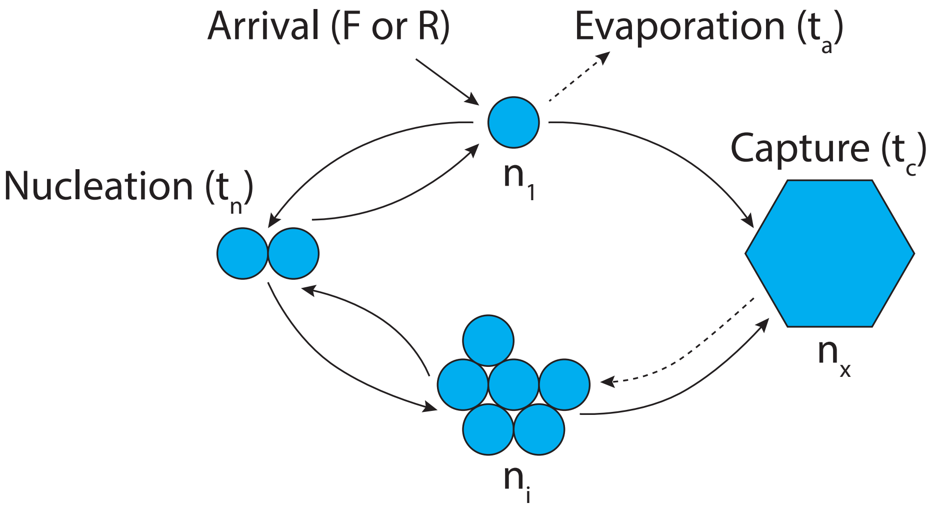

Figure 1.6: Critical size in nucleation and growth models.

Classification of growth modes

The difference between bulk crystal growth and epitaxial growth is of purely thermodynamic nature [45]. The overlayer possesses a different chemical potential to its isolated counterpart due to the interactions across the overlayer/substrate interface, and also to mismatch in the lattice parameters induced by the substrate epitaxy. These differences produce a chemical potential for the first layer of atoms in the overlayer that may be higher or lower compared to the isolated crystal. In addition, the overlayer may relax if it is strained as its thickness increases, which may lead to a chemical potential that varies with overlayer thickness. The alteration of chemical potential due to the presence of a growth substrate leads to several different modes of growth, as shown in figure 1.7.

For an overlayer A deposited on a substrate B, the overlayer will grow according to:

$$\gamma_A \begin{cases} < \gamma_B - \gamma^* & \text{Frank-van der Merwe (FM)} \\ > \gamma_B - \gamma^* & \text{Volmer-Weber (VW)} \end{cases}$$

where $\gamma_{A,B}$ is the surface energy for growth on A (overlayer) and B (substrate) respectively and γ^* is the interface energy between A and B. The energetics favour growth on A when adatom-adatom interactions are stronger than those of the adatom with the surface, leading to the formation of three−dimensional adatom clusters or islands [46]. This is referred to as Volmer-Weber (VW) growth. Conversely, if the adatoms attach preferentially to surface sites than to other adatoms, then this results in layer−by−layer growth, whereby complete 2D films form prior to the growth of subsequent layer [34, 46]. This is referred to as Frank−van der Merwe (FM) growth. There is a third and final class of growth that bridges between VW and FM growth, referred to as Stranski−Krastanov (SK) growth. Characterised by both 2D layer and 3D island growth, SK growth involves a transition from layer−by−layer growth to island−based growth beyond a critical thickness, which is highly dependent on the physical and chemical properties of the overlayer and substrate [34, 35, 46]. For small thickness t, the surface energy growth condition is $\gamma_A < \gamma_B - \gamma^*$ (FM growth). For large thickness (beyond the critical thickness), the surface energy growth condition is $\gamma_A > \gamma_B - \gamma^*$ (VW growth)

Organic film growth

As well as describing the epitaxial growth of inorganic crystals on a substrate, the same processes outlined above can be applied directly to the growth of organic thin films [40, 41, 47]. Organic molecular beam deposition (OMBD) is the process by which molecular precursors are heated in vacuum, producing a beam of molecules that can be directed towards a target surface on which the molecules can assemble. Through a variety of intermolecular bonding mechanisms, and interactions with the surface, many different molecular lattice structures can form. Again, organic thin films can be grown both with [6, 48, 49] and without an epitaxial relationship with the underlying substrate [1]. The growth of organic molecular films often leads to non−equilibrium structures due to the growth kinetics, as can be seen from significant post−growth re−organisation [50–52]. This is due to irreversible atomic scale processes occurring during OMBD [45, 53, 54].

OMBD growth differs from standard inorganic film growth due to the extended nature of molecules, and their associated internal degrees of freedom. The

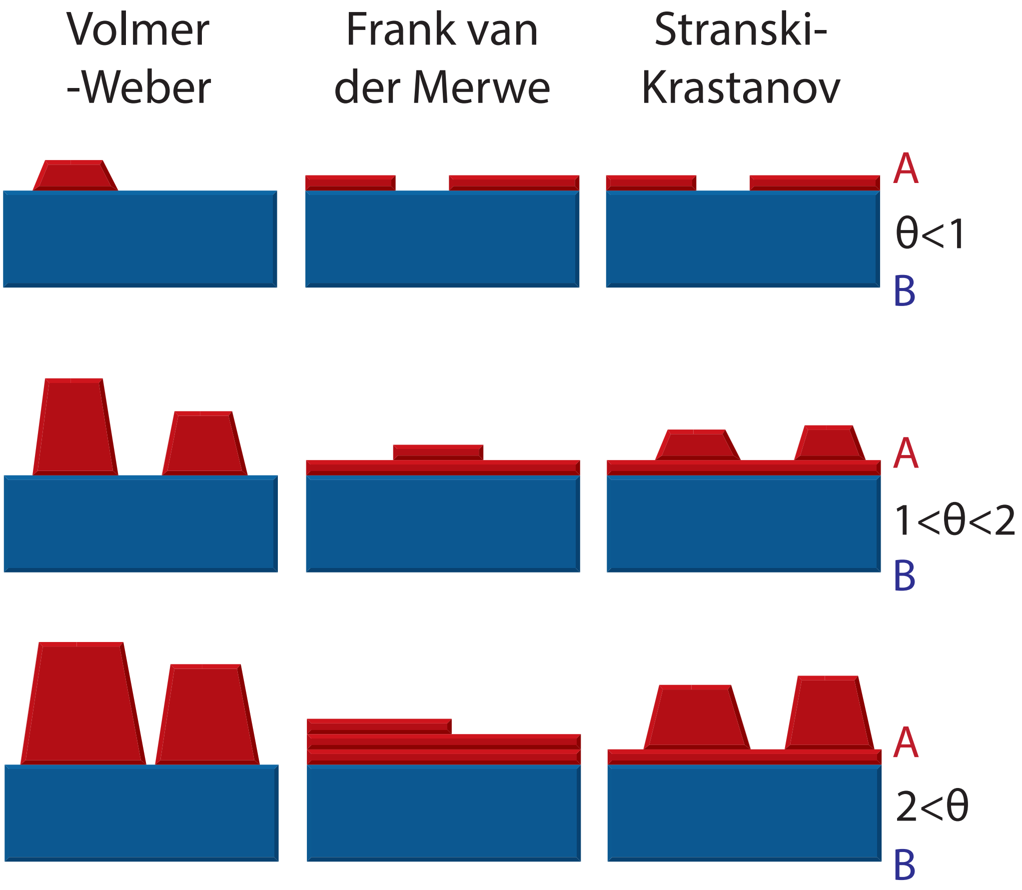

Figure 1.7: Schematic representation of the three growth modes for different levels of coverage θ, in units of monolayer coverage. Blue represents substrate material, and red represents overlayer material.

internal vibrational energy can impact the interaction with the substrate and also the molecule's thermalisation upon adsorption, particularly as the translational energy of a molecule can be converted to vibrational energy. Additionally, conformational degrees of freedom within the molecule mean that the molecular unit can change within the film, in order to compensate for lattice strain. The conformation of the organic semiconductor rubrene has been found to change during growth [55], which may influence the film morphology [56]. Another key difference not accommodated for in conventional growth models is the orientational degrees of freedom a molecule possesses, which can give rise to tilted domains and thereby an additional source of disorder, or may even give rise to 'standing-up' and 'lying-down' structures [56, 57].

For the case of molecular film growth, weak van der Waals forces typically play a much bigger role in directing growth. When integrated across all constituent atoms within a molecule, the weak interaction energies sum to a substantial molecular binding energy in the eV range, and can have significant influence on the resulting molecular lattice structure [58, 59].

The inherent size of molecules, and consequently the size of the molecular unit cell, is typically much larger than that of inorganic crystals. The interaction potential is therefore spread over a much greater area, weakening any effective substrate corrugation experienced by individual molecules. This is because the small length scale of the substrate corrugation is averaged to some extent over the size of the molecule, which generally has constituent bond lengths different from the substrate. Finally, the differences in unit cell size between molecular layer and substrate, and the relatively weak intermolecular bonds involved, can produce many more orientational and translational domains than would be expected for two inorganic layers with differences in unit cell sizes [40]. This introduces additional disorder, and a plethora of interaction phenomena that are ideal for investigating. In the timeless words of Carl Sagan: “The beauty of a living thing is not the atoms that go into it, but the way those atoms are put together”. The same can be said for organic materials and thin films, and there is still much to be learnt about how their constituent atoms and molecules are put together.

1.2 Scope of this thesis

In this thesis, molecular materials are studied in combination with graphene, heavily utilising graphene’s role as a low−contrast support for electron microscopy. The use of microscopy techniques and associated simulations allows a better understanding to be gained of the physical, chemical, and electronic structures of molecular materials, and the interactions that drive their structural arrangements. The wide variety of intermolecular and interatomic forces involved result in a rich tapestry of growth phenomena and resultant film structures.

Firstly, in chapter 3, techniques for fabricating graphene membranes for electron microscopy (EM) are outlined. The complete fabrication process is described, beginning with the growth of CVD graphene, followed by the transfer of graphene from CVD foils to a TEM support, and finishing with the cleaning steps involved to produce pristene regions of graphene. Strategies to functionalise graphene through covalent and non−covalent means are detailed, as well as methods to fabricate more specialised graphene TEM membranes consisting of stacked and sandwiched graphene layers.

With the methods used to fabricate and modify graphene EM membranes described, attention is next focused on specific microscopy techniques developed in order to study organic materials that readily damage when exposed to the electron beam in an electron microscope. Strategies to mitigate the damage arising due to beam exposure are investigated for a range of different organic molecules, and the effects of using a range of detection devices are also studied.

Having outlined methods for fabricating graphene membranes, and the best strategies for gathering information on beam−sensitive organic specimens using EM, the growth of two very similar overlayer systems on graphene are studied. Trimesic acid (TMA) and terephthalic acid (TPA) thin films are grown on both freestanding and CVD graphene substrates for a range of thicknesses, and the resulting assembly structures are probed using a range of microscopy techniques. For TMA, van der Waals epitaxy results in two preferred orientations of the assembly structure that grows in a layer−by−layer Frank−van der Merwe fashion, to a height of $\approx$ 20 nm. In stark contrast, TPA assembles into a 2D monolayer before rapidly transitioning to its bulk−like structure as further layers are deposited, following a layer−plus−island, or Stranski−Krastanov, growth mode.

The structure of self−assembling molecules on graphene is further investigated using a pair of porphyrin−based molecules of the octaethyl porphyrin (OEP) class. A monolayer film of OEP molecules is deposited either side of a freestanding graphene membrane, and the resulting assembly structure is driven by a remote interaction across the graphene between the two OEP films. The remote interaction is shown to diminish on the length scale of two graphene layers.

Finally, the atomically-resolved structure and motion of individual metal nanoclusters (M−NCs) deposited on freestanding graphene is studied using high−resolution TEM. Computational routines involving cross−correlation techniques are developed in order to better study the behaviour of dynamic M−NCs in time−series image sequences. The strategies developed provide a means for accurately studying more complex systems, structural changes, and chemical reactions at atomic−resolution and in real−time.

Chapter 2

Methods

2.1 Film Growth

Chemical Vapour Deposition

For the work presented in this thesis, graphene samples were prepared by chemical-vapour deposition (CVD) using a methane precursor gas and a copper foil substrate. The first demonstrations of CVD-grown graphene were presented by Li *et al.* [60], and there have been many developments in the methodology since [17, 43]. The procedure described here is the culmination of those evolutions in methodology.

The CVD system used for this work comprises of an outer quartz tube and movable inner quartz tube, used for loading copper foils into (figure 2.1). Once loaded, the system is evacuated using a combined turbo/backing pump, achieving a base pressure of $\approx 10^{-3}$ mbar. The outer quartz tube is housed within a furnace, and connected upstream to a series of mass-flow controllers (MFCs). The MFCs are linked to separate methane and hydrogen gas bottles, and the flows are controlled via an integrated LabVIEW programme. The temperature of the furnace is also linked to the LabVIEW programme, allowing complete automation of the growth process, providing optimal controllability and reproducibility of samples.

The standard growth method for complete sample coverage, $\approx 90\%$ monolayer, involves flowing hydrogen at 5 standard cubic centimetres per minute (sccm) whilst the furnace is heated to 1000°C at a rate of 15°C min^{-1}, raising the pressure to $\approx 2\times10^{-2}$ mbar. Once at 1000°C, the copper foil is annealed for 10 minutes. Methane is then introduced at 3 sccm, and the hydrogen flow rate adjusted to 10 sccm, for a growth period of 30 minutes. The furnace is then cooled, with the flow rates adjusted to 2 sccm methane and 5 sccm hydrogen until 600°C is reached, after which the methane flow is stopped. The hydrogen flow is continued until 150°C, at

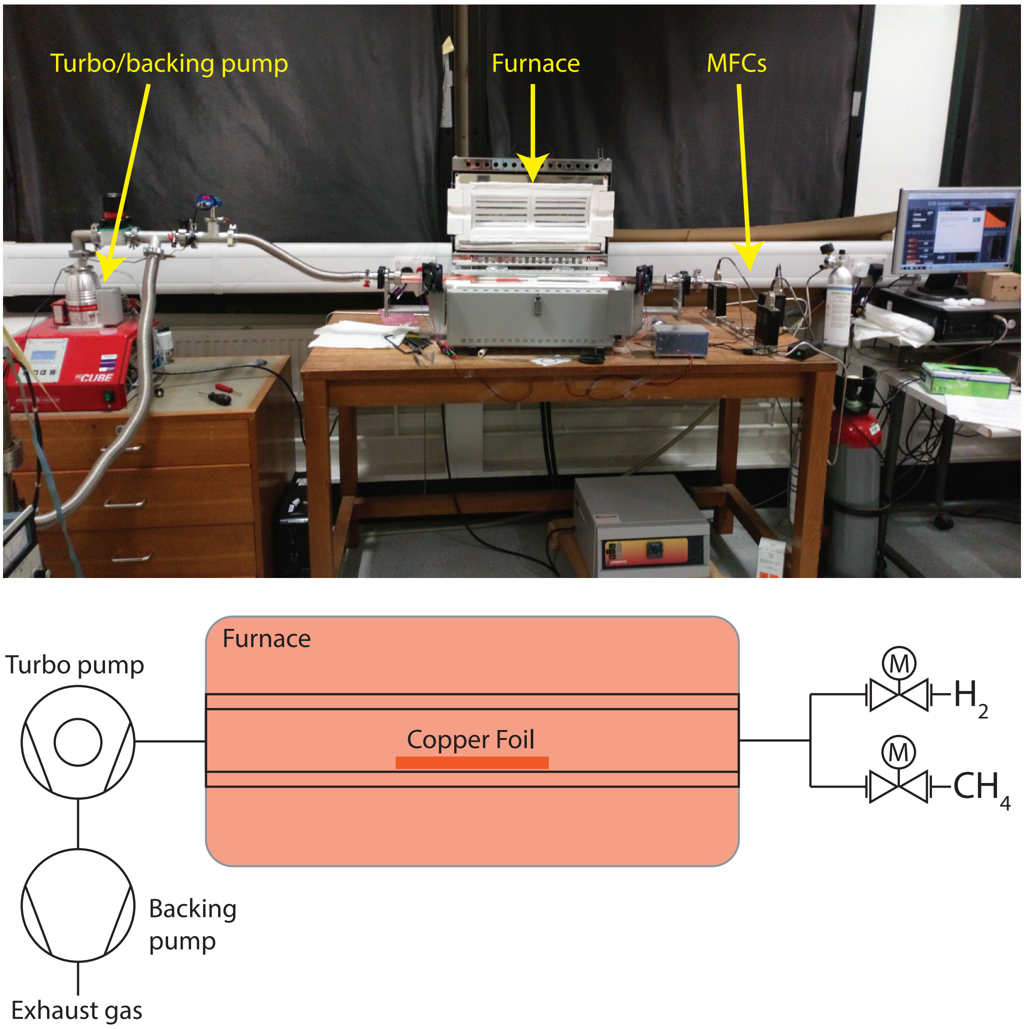

Figure 2.1: Photograph of graphene CVD setup and corresponding schematic.

which point the system is vented and the copper foil is removed. Scanning electron microscope images, figure 2.2, reveal the presence of graphene on the foil through observation of wrinkles in the film and multilayer islands [61]. In addition, the lack of surface contamination reveals the high levels of cleanliness.

In order to achieve clean CVD samples, the copper foils must first be prepared using electropolishing [62]. The copper foils (Alfa Aesar, product no. 13382, purity 99.5%) arrive from the manufacturer with an anti-corrosion protective coating that must be removed, along with any surface contaminants present [43]. To do this, the copper foil is immersed in an electrolytic solution (50 mL orthophosphoric acid, 1 g urea, 50 mL ethanol, 50 mL isopropanol, and 10 mL deionised water) and attached

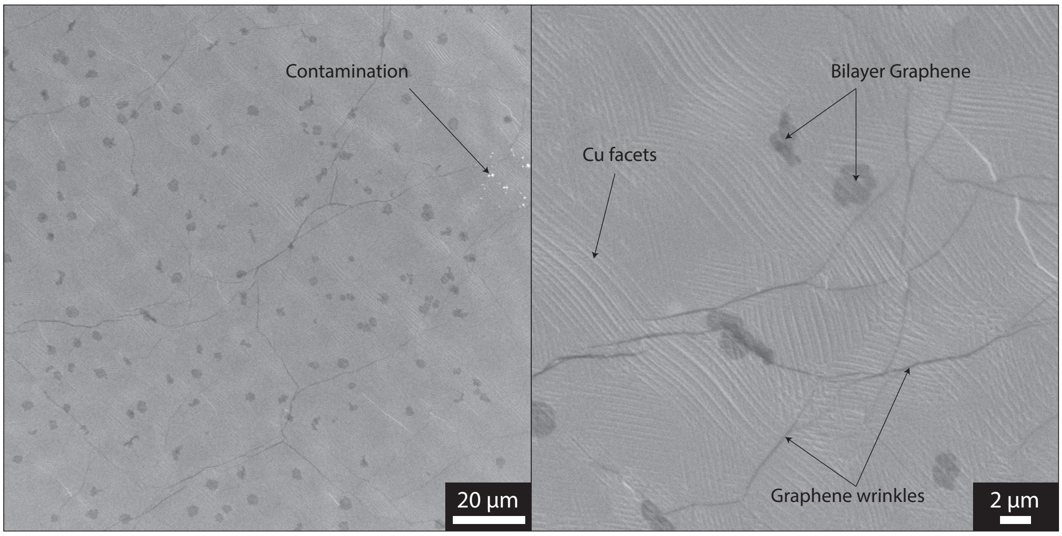

Figure 2.2: CVD graphene SEM images. The CVD-prepared foils are clean, with only small areas of multilayer graphene (darker contrast patches). The presence of monolayer graphene is evident from dark wrinkles in the film as well as the visible copper faceting [61].

to the anode of a power supply (figure 2.3). Another piece of copper foil is attached to the cathode of the power supply, and also immersed in the solution. Applying a current of ≈ 2 A and potential difference of ≈ 5 V for 10 seconds causes the surface atoms of the anode foil to migrate towards the cathode foil through the solution. This removes several hundred nm from the anode foil surface, along with the anti-corrosion coating and any other contaminants. Once electropolished, the anode foil is rinsed using deionised water and isopropanol, before sonicating in acetone for 5 minutes. The foil is once again rinsed in isopropanol before drying using a nitrogen gun.

Organic Molecular Beam Deposition

Much of the work featured within this thesis involved the growth of molecular films on graphene-based substrates using OMBD. This is the process by which a crucible containing solid organic material is heated under high vacuum. The process of heating causes the organic material to sublime, producing a beam of molecules that is directed towards the choice substrate, resulting in molecular film growth [40, 41, 47]. In order to monitor the film growth, the system used included a quartz-crystal microbalance (QCM), which monitors the mass variation of the substrate to high precision. Through precise measurement of the deposition rate, molecular films of a

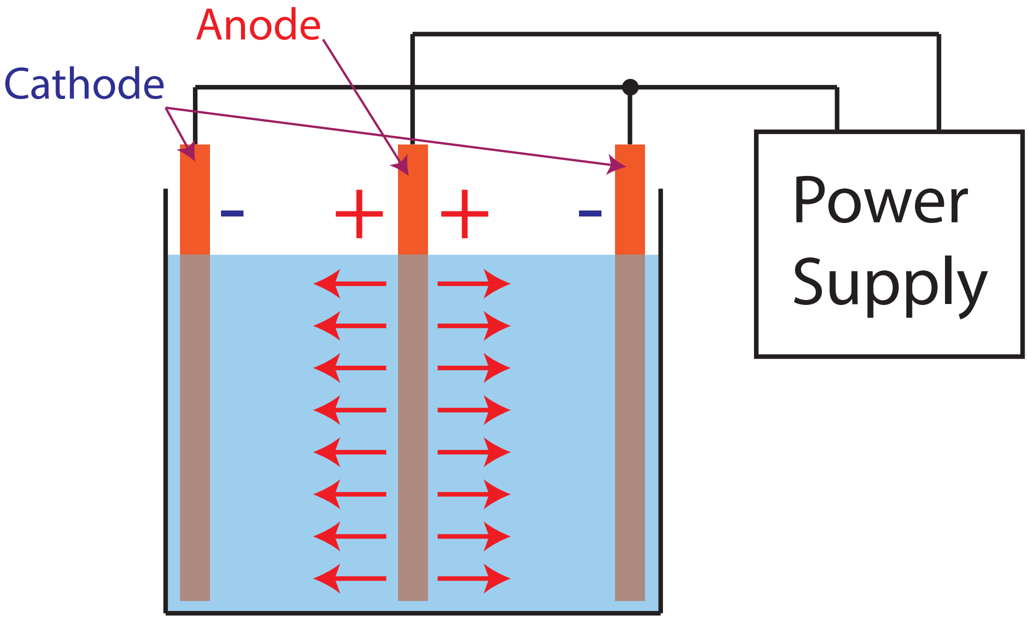

Figure 2.3: Electropolishing copper foils for CVD growth. The current and applied potential difference cause surface ions to migrate from the anode foil (centre) to the cathode foils through the electrolytic solution (blue), as indicated by the red arrows. This causes the removal of several hundred nm of surface, along with any contaminants, producing a clean foil ideal for CVD growth.

specific thickness can be grown with good reproducibility. The apparatus used for OMBD growth in this thesis is illustrated in Figure 2.4.

In addition to OMBD film growth, several studies were conducted as part of this work using liquid-phase deposition. For these, a specific molecular species was dissolved in an organic solvent and the substrate of choice was then immersed briefly. Molecules in solution adsorb onto the substrate surface, and upon removal and rinsing with additional solvent, monolayer molecular films can be formed with high uniformity and controllability [63], as shown in Figure 2.4

2.2 Molecular Crystallography and Diffraction

2.2.1 Atomic and Molecular lattices

When studying the properties of a material, one immediately recognises that a macroscopic material contains very many atoms (10^{23}). Thus, describing the material properties directly using every constituent atom proves impossible. However, many materials possess intrinsic periodicities in their atomic structure arrangements,

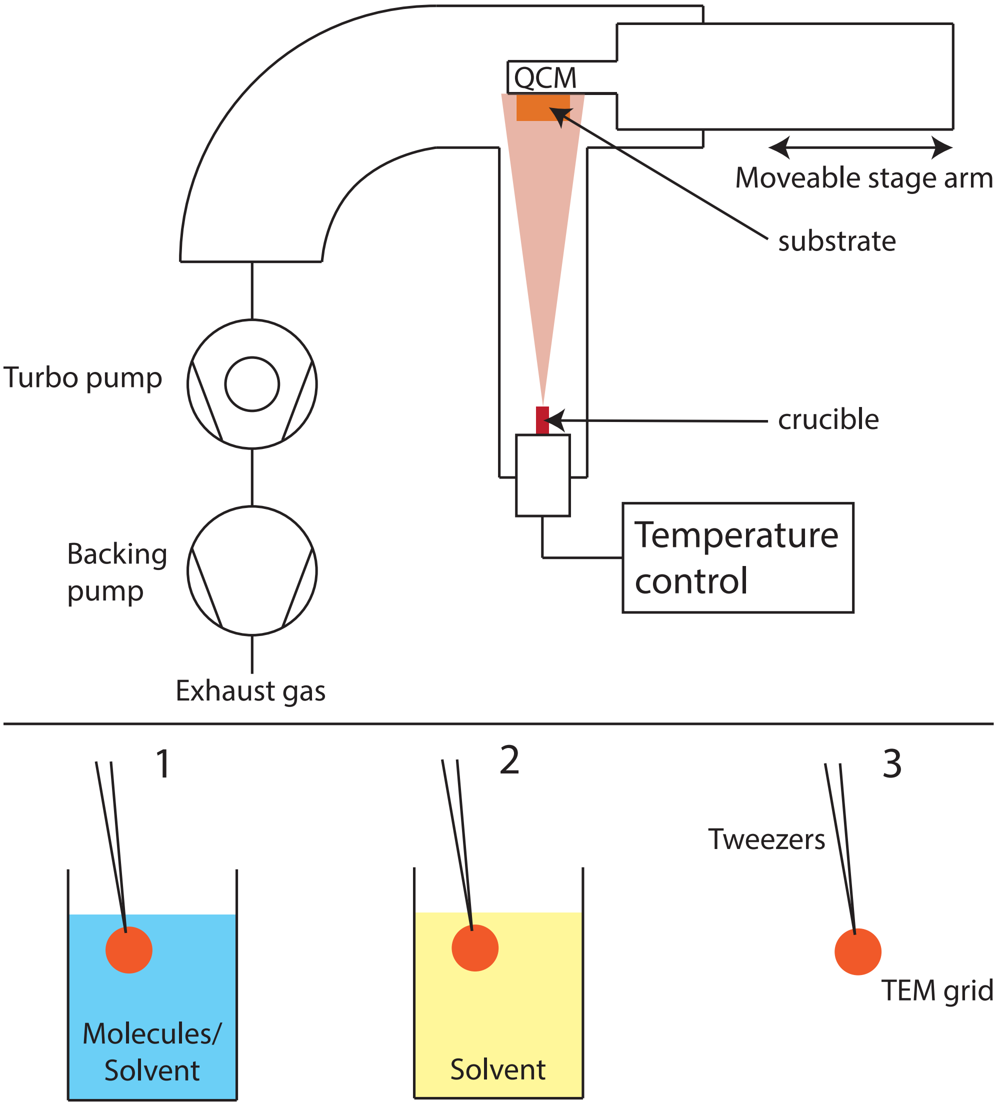

Figure 2.4: OMBD system schematic.

allowing a quantitative description of the material using the crystal symmetries present. The same holds true for a vast array of molecular materials, which possess innate symmetries in the arrangement of constituent molecules, even if the constituent molecules are non-symmetric.

In order to describe the periodic atomic and/or molecular structure of a material, the *Bravais lattice* is introduced, as shown in Figure 2.5. The Bravais lattice describes the tiling of the smallest possible periodic unit within the atomic structure, and the volume of material encompassed by a single periodic unit is referred to as the *primitive unit cell*. For a full description of the crystal, the *basis* is introduced, which describes the relative positions of atoms or molecules within the unit cell.

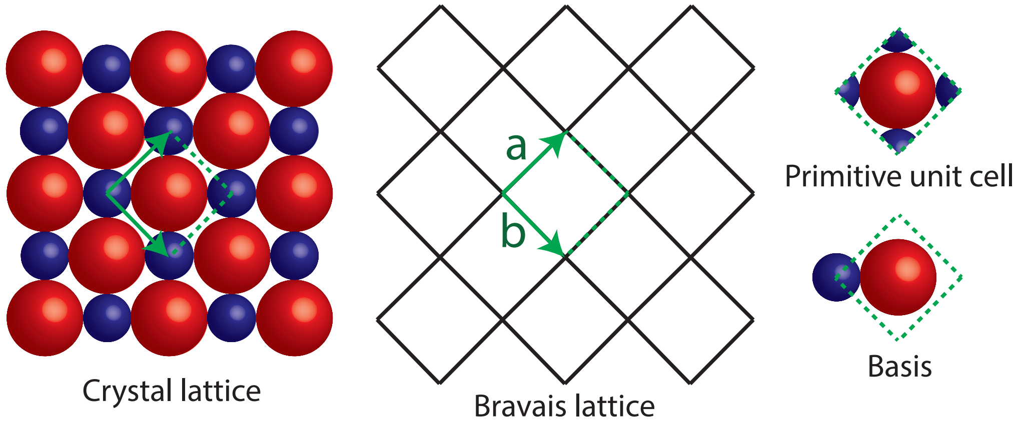

Figure 2.5: Description of a crystal lattice using a Bravais lattice and corresponding basis. The volume occupied by a single unit of Bravais lattice vectors is the primitive unit cell.

Formally, the Bravais lattice is described by a set of position vectors [64]:

$$\mathbf{R} = u\mathbf{a} + v\mathbf{b} + w\mathbf{c} \tag{2.1}$$

where (u, v, w) are integers; $\mathbf{R}$ can be expressed as a matrix in Euclidean space:

$$\mathbf{R} = (u\mathbf{a}, v\mathbf{b}, w\mathbf{c})(\hat{\mathbf{e}}_x, \hat{\mathbf{e}}_y, \hat{\mathbf{e}}_z)^T = \begin{bmatrix} ua_x & ua_y & ua_z \\ vb_x & vb_y & vb_z \\ wc_x & wc_y & wc_z \end{bmatrix} \tag{2.2}$$

where the vector unit $\hat{\mathbf{r}} = (\hat{\mathbf{e}}_x, \hat{\mathbf{e}}_y, \hat{\mathbf{e}}_z)$ in Euclidean space allows the matrix expression of $\mathbf{R}$ in its Euclidean components. For 2D crystal systems, as studied for the majority of the work presented in this thesis, the Bravais lattice and unit cell may be restricted to two dimensions, as shown in Figure 2.5.

As well as defining the atomic/molecular lattice with an atomistic description, it is possible to define the related electron density function ρ using an identical Bravais lattice:

$$\rho(\mathbf{r}) = \rho(\mathbf{r} + \mathbf{R}) \tag{2.3}$$

where $\mathbf{r} = (u'\mathbf{a}, v'\mathbf{b}, w'\mathbf{c})$ is an arbitrary vector expressed in the basis of $\mathbf{R}$ and the electron density ρ is invariant under translation between unit cells. As a continuous function, it is convenient to express the electron density function ρ by means of a Fourier series. Fourier series expansion is particularly useful as a means of approximating periodic functions using a finite series, with the level of approximation improving as the number of terms in the Fourier series is increased. Using Eulers formula, the Fourier series expansion of a function $f(x)$ may be expressed as:

$$f(x) = \sum_n C_n e^{-i2\pi nx} \tag{2.4}$$

where n is an integer and C_n is the nth expansion coefficient. Applying this to the electron density function ρ then gives:

$$\rho(x,y,z) = \sum_h \sum_k \sum_l F(hkl) \exp\left[-i2\pi(hx + ky + lz)\right] \tag{2.5}$$

where the expansion is performed over a triple series, corresponding to the three spatial dimensions of the crystal. Here, $F(hkl)$ is defined as the *structure factor* of the crystal:

$$F(hkl) = \sum_{j=1}^{N} f_j(hkl) \exp\left[i2\pi(hx_j + ky_j + lz_j)\right] \tag{2.6}$$

where $f(hkl)_j$ is the atomic scattering factor of the jth atom within the unit cell, described in more detail in section 2.3.1. The crystal structure factor $F(hkl)$ is a complex function comprising of amplitude and phase terms, and is dependent on the species of atoms contained within the unit cell and their relative positions. In order to evaluate the expansion coefficients $F(hkl)$, the following integration may be performed:

$$\int_0^1 \int_0^1 \int_0^1 \rho(x,y,z) \exp\left[2\pi i(hx + ky + lz)\right] dx\, dy\, dz = F(hkl) \tag{2.7}$$

where a scaling factor V has been ignored which represents the unit cell volume. Equation 2.7 may readily be interpreted as the Fourier transform of the electron density function, $\mathcal{F}\{\rho(x,y,z)\}$. Therefore, one may readily calculate either the electron density function through Equation 2.5 with knowledge of $F(hkl)$, or conversely, may calculate $F(hkl)$ through Equation 2.7 with knowledge of $\rho(x,y,z)$.

2.2.2 Diffraction and reciprocal space lattices

A wave of radiation (this mathematical formalism holds true for both photons and electrons) may be described with an amplitude A, wavelength λ, wavevector $\mathbf{k}$ with magnitude $k = 1/\lambda$, velocity v, and angular frequency $\omega = 2\pi v/\lambda$. The wave may be expressed as [64, 65]:

$$\mathbf{E}(\mathbf{r}, t) = A \exp\left[i(2\pi \mathbf{k} \cdot \mathbf{r} - \omega t)\right] \tag{2.8}$$

Assuming elastic scattering (described in greater detail in section 2.3.1) from a discrete periodic lattice, the emergent wave will propagate with an altered wavevector $\mathbf{k}'$, whilst maintaining its wavelength λ. Measuring at an observation point $\mathbf{r}'$, the wavevector scattered from an atom at location $\mathbf{r}$ is:

$$\mathbf{E}'(\mathbf{r}', t) = A' \exp\left[i(2\pi \mathbf{k}' \cdot \mathbf{r}' - \omega t)\right] \exp\left[i2\pi(\mathbf{k} - \mathbf{k}') \cdot \mathbf{r}\right] \tag{2.9}$$

which accommodates the phase shift induced by the atomic scattering event. Assuming the point of observation $\mathbf{r}'$ is sufficiently far from the discrete lattice in order that all scattered $\mathbf{k}'$ from all atoms in the lattice are in the same direction (Fraunhofer diffraction [65]), then the total scattered wavevector may be calculated by summing over all lattice points $\mathbf{r}$:

$$\mathbf{E}_{total}(\mathbf{r}', t) = A' \exp\left[i(2\pi \mathbf{k}' \cdot \mathbf{r}' - \omega t)\right] \sum_{all\ atoms} \exp\left[i2\pi(\mathbf{k} - \mathbf{k}') \cdot \mathbf{r}\right] \tag{2.10}$$

This may be expressed in the form of a volume integral over the entire lattice:

$$\mathbf{E}_{total}(\mathbf{r}', t) = A' \exp\left[i(2\pi \mathbf{k}' \cdot \mathbf{r}' - \omega t)\right] \int_{all\ space} \rho(\mathbf{r}) \exp\left[i2\pi(\mathbf{k} - \mathbf{k}') \cdot \mathbf{r}\right] d\mathbf{r} \tag{2.11}$$

Here, $\rho(\mathbf{r})$ represents the electron density function already encountered. This function is non-zero anywhere in the lattice that has some electron density, and zero elsewhere. The expression in Equation 2.7 relates the Fourier transform of the electron density function to $F(hkl)$, allowing the interpretation of $\mathbf{E}_{total}(\mathbf{r}', t)$ as $F(hkl)$ less some scaling factor.

In order for $\mathbf{E}_{total}$ to be maximised in Equation 2.11, $\exp\left[i2\pi(\mathbf{k} - \mathbf{k}') \cdot \mathbf{r}\right] = 1$, which occurs when $(\mathbf{k} - \mathbf{k}') \cdot \mathbf{r} = n$, where n is an integer. The spatial vector $\mathbf{r}$ may be re-expressed as the Bravais lattice $\mathbf{R}$, and the wavevector difference $(\mathbf{k} - \mathbf{k}')$ may be re-expressed as some vector $\mathbf{G}$:

$$\mathbf{G} \cdot \mathbf{R} = n \tag{2.12}$$

Thus, for a crystal described by the Bravais lattice $\mathbf{R}$, the scattered wave of radiation will be most intense when the wavevector difference is equivalent to positions in the lattice $\mathbf{G}$. This is equivalent to the condition of Bragg diffraction:

$$n\lambda = d \sin(\theta) \tag{2.13}$$

where d_{hkl} is the crystal lattice spacing and θ_{hkl} is the scattering angle. The conditions of Bragg diffraction are depicted in Figure 2.6.

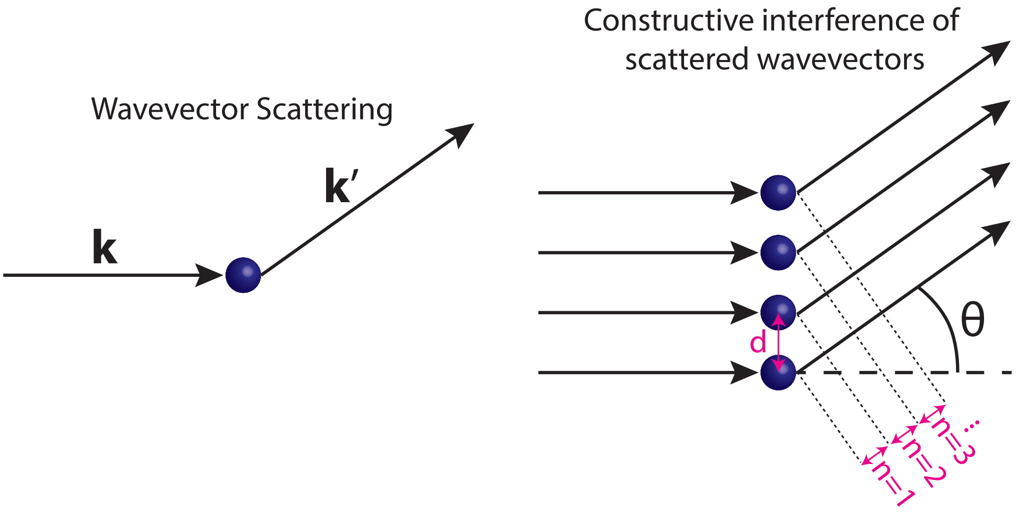

Figure 2.6: Elastic scattering of wavevectors by crystal lattices.

The lattice $\mathbf{G}$ may be expressed as:

$$\mathbf{G} = h\mathbf{a}^* + k\mathbf{b}^* + l\mathbf{c}^* \tag{2.14}$$

where (h, k, l) are integers and $\mathbf{G}$ can be expressed as a matrix in Euclidean space:

$$\mathbf{G} = (\mathbf{a}^*, \mathbf{b}^*, \mathbf{c}^*)(\hat{\mathbf{e}}_x, \hat{\mathbf{e}}_y, \hat{\mathbf{e}}_z)^T = \begin{bmatrix} a_x^* & a_y^* & a_z^* \\ b_x^* & b_y^* & b_z^* \\ c_x^* & c_y^* & c_z^* \end{bmatrix} \tag{2.15}$$

In order to satisfy Equation 2.12, the constituent vectors $\mathbf{i}$ and $\mathbf{j}^*$ of the lattices $\mathbf{R}$ and $\mathbf{G}$, where $\mathbf{i}, \mathbf{j} = \mathbf{a}, \mathbf{b}, \mathbf{c}$ must satisfy the relation:

$$\mathbf{i} \cdot \mathbf{j}^* = \delta_{i,j} \begin{cases} 0, & \text{if } i \neq j \\ 2\pi, & \text{if } i = j \end{cases} \tag{2.16}$$

which is equivalent to the matrix equation:

$$\mathbf{RG} = (\mathbf{a}, \mathbf{b}, \mathbf{c})(\mathbf{a}^*, \mathbf{b}^*, \mathbf{c}^*)^T = \begin{bmatrix} \mathbf{a} \cdot \mathbf{a}^* & \mathbf{a} \cdot \mathbf{b}^* & \mathbf{a} \cdot \mathbf{c}^* \\ \mathbf{b} \cdot \mathbf{a}^* & \mathbf{b} \cdot \mathbf{b}^* & \mathbf{b} \cdot \mathbf{c}^* \\ \mathbf{c} \cdot \mathbf{a}^* & \mathbf{c} \cdot \mathbf{b}^* & \mathbf{c} \cdot \mathbf{c}^* \end{bmatrix} = \begin{bmatrix} 1 & 0 & 0 \\ 0 & 1 & 0 \\ 0 & 0 & 1 \end{bmatrix} = \mathbf{I} \tag{2.17}$$

In summary, the matrix forms of **R** and **G** satisfy the following relations:

$$\mathbf{RG} = \mathbf{I}, \quad \mathbf{R} = \mathbf{IG}^{-1}, \quad \mathbf{G} = \mathbf{R}^{-1}\mathbf{I} \tag{2.18}$$

Due to the inverse nature of the lattice **G** with respect to the Bravais lattice **R**, **G** is referred to as the *reciprocal lattice*. The constituent vectors of the reciprocal lattice **G** can be defined explicitly using the constituent vectors of the Bravais lattice **R**:

$$\mathbf{a}^* = \frac{\mathbf{b} \times \mathbf{c}}{\mathbf{a} \cdot (\mathbf{b} \times \mathbf{c})} \quad \mathbf{b}^* = \frac{\mathbf{c} \times \mathbf{a}}{\mathbf{b} \cdot (\mathbf{c} \times \mathbf{a})} \quad \mathbf{c}^* = \frac{\mathbf{a} \times \mathbf{b}}{\mathbf{c} \cdot (\mathbf{a} \times \mathbf{b})} \tag{2.19}$$

In addition, the angles between reciprocal lattice vectors $(\alpha^*, \beta^*, \gamma^*)$ can be defined directly with respect to the Bravais lattice vector angles (α, β, γ):

$$\alpha^* = \pi - \alpha, \quad \beta^* = \pi - \beta, \quad \gamma^* = \pi - \gamma \tag{2.20}$$

The relations between real and reciprocal lattices, including lattice angles, are depicted in Figure 2.7.

2.3 Microscopy

In order to investigate the structure and properties of materials, it is necessary to use a variety of microscopy tools in order to establish a clear and extensive description of the material. Here, the key microscopy tools utilised for the work presented in this thesis are introduced.

2.3.1 Transmission Electron Microscopy

The transmission electron microscope (TEM) is a powerful tool for the study of inorganic, organic, and biological specimens. Similar in principle to the typical optical microscope, an electron illumination source is focused onto a specimen using

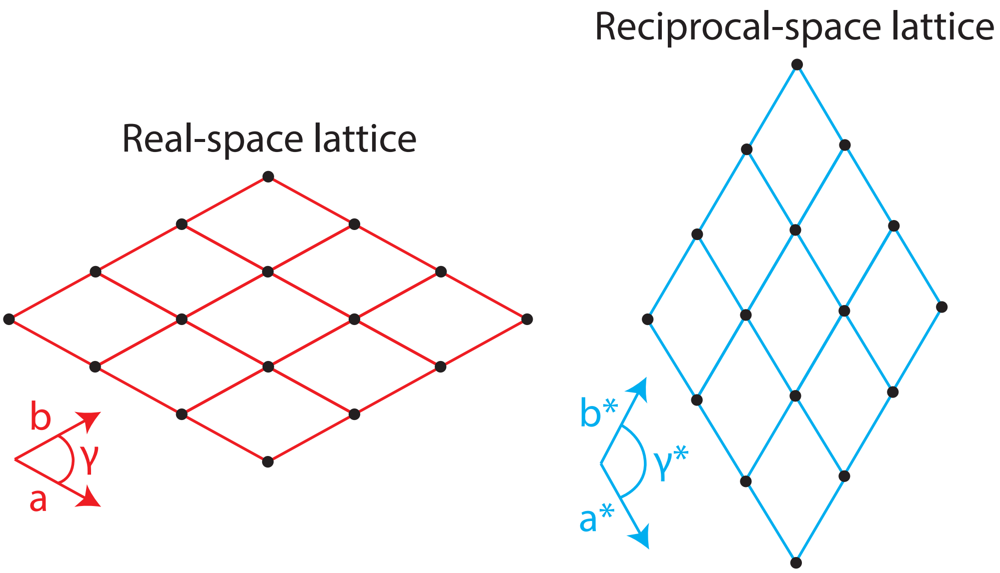

Figure 2.7: Real-space and reciprocal-space lattices.

a series of lenses. The incident beam interacts with the specimen, and the emerging wave is focused using another set of lenses onto an electron detector, producing an image (Figure 2.8).

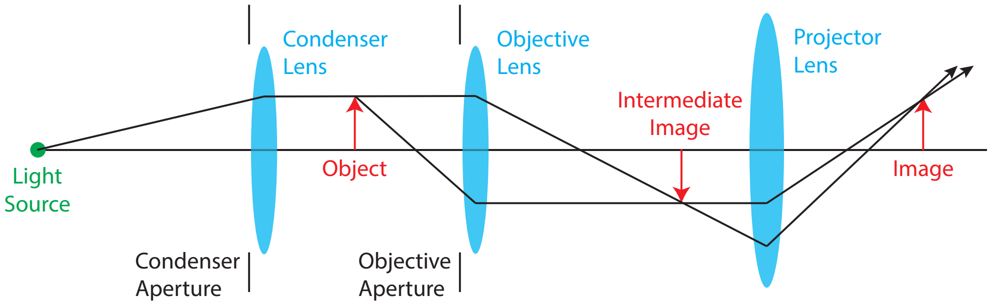

Figure 2.8: Ray diagram for basic microscope setup.

Fundamentals of Electrons

There are several significant differences between TEMs and optical microscopes. In accordance with the Rayleigh resolution criterion, the minimum resolvable distance for a wave with wavelength λ, passing through a medium with refractive index μ, with semi-angle between source and lens α is:

$$r = \frac{d}{2} = \frac{0.61\lambda}{\mu \sin \alpha} \tag{2.21}$$

Clearly, the resolution of an imaging system is limited significantly by the wavelength of radiation used. For electrons accelerated through a potential difference V, the relativistic wavelength is:

$$\lambda = \frac{h}{\sqrt{2em_eV\left(1 + \frac{eV}{2m_ec^2}\right)}} \tag{2.22}$$

where h is Planck's constant, e is the electron charge, m_e is the electron mass, and c is the speed of light in vacuum. Electrons are typically accelerated to between 60 - 300 keV within the microscope, reducing their wavelength in accordance with Equation 2.22. At such accelerating voltages, the wavelengths are below 5 pm (Figure 2.9), allowing length scales on the atomic level to be probed. The first 2D EM lattice images with useful information on crystal chemistry and defects were obtained from a thin crystal of $Ti_2Nb_{10}O_{29}$ by Iijima (1971) [66], with a resolution of 0.4 nm.

As well as having much smaller wavelengths in comparison to visible light and X-rays, electrons differ as a source of illumination due to their much stronger interactions with matter and their mass m_e. Electrons are negatively charged, and so interact with the electrons and nuclei of atoms via Coulomb forces, compared to X-rays that only interact weakly with the electrons of atoms [64]. The scattering amplitude for X-rays [67] can be expressed as:

$$\begin{aligned} A_X(\mathbf{k}) = \frac{e^2}{4\pi\epsilon_0 m_e c^2} \int \rho(\mathbf{r}) \exp(2\pi i \mathbf{k} \cdot \mathbf{r}) d\mathbf{r} = \\ \frac{e^2}{4\pi\epsilon_0 m_e c^2} f_X(\mathbf{k}) = 2.82 \times 10^{-15} f_X(\mathbf{k}) \end{aligned} \tag{2.23}$$

whilst the scattering amplitude for electrons [68] can be expressed as:

$$A_e(\mathbf{k}) = \frac{2m_e e^2}{4\pi h^2 \epsilon_0 k^2}\Big(Z - f_X(\mathbf{k})\Big) \approx 3.8 \times 10^{-11}\Big(Z - f_X(\mathbf{k})\Big) \tag{2.24}$$

where k is the length of the scattering vector $\mathbf{k}$. Taking an example of $d = 0.2$ nm $= 2\times10^{-10}$ m then $k = 1/d = 5\times10^{-9}$ m^{-1}, then the ratio of scattering amplitudes for electrons and X-rays is $A_e(\mathbf{k})/A_X(\mathbf{k}) \approx 10^4$ [64]. As will be shown, the intensity of an image is proportional to the square of the scattering amplitude ($I \propto A^2$), and so electrons can be used to gather information on much thinner samples compared to X-rays due to the much stronger interactions between electrons and matter.

However, this also produces complications when dealing with thick samples.

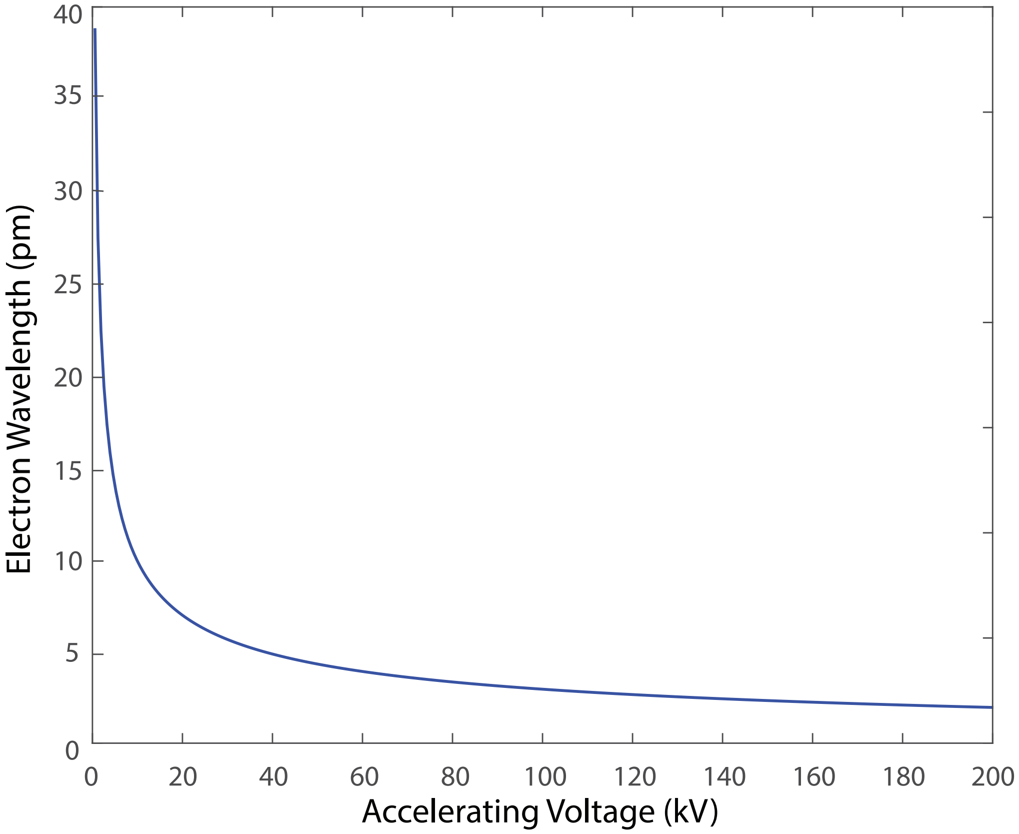

Figure 2.9: Relativistic wavelength of electrons accelerated through a set potential difference.

Firstly, due to the strong interactions between electrons and matter, electrons can undergo multiple scattering whilst traversing a sample, complicating image interpretation. In addition, for samples of thickness $>\approx$ 200 nm containing predominantly light atoms, all electrons will be scattered to such an extent that there is no detectable signal arriving at the detector. Fortunately, the samples investigated throughout this thesis are particularly thin, and so multiple scattering effects do not need to be considered.

When interacting with an atom, if the kinetic energy of the incident electron is conserved then the scattering process is considered to be *elastic*. Here we describe elastic scattering in detail as it is responsible for the formation of conventional and diffraction images. Processes that result in *inelastic* scattering are discussed in chapter 4 due to their role in specimen damage.

The Mott-Bethe formula for atomic scattering factors for electrons describes the probabilities that an electron will be scattered through a specific direction when passing near an isolated atom [64]:

$$f_e(\theta) = \frac{2m_e e^2}{4\pi h^2 \epsilon_0}\Big(\frac{\lambda}{2\sin\theta}\Big)^2\Big(Z - f_X(\theta)\Big) = 0.023934\Big(\frac{\lambda}{\sin\theta}\Big)^2\Big(Z - f_X(\theta)\Big) \tag{2.25}$$

where Z is the atomic number, θ is the scattering angle relative to the optical axis, λ is the wavelength of the incident electron, and $f_X(\theta)$ is the scattering factor for X-rays. The electron scattering factor $f_e(\theta)$ is plotted for a number of different atoms in figure 2.10. As can be seen, the scattering factor is largest for $\theta = 0$ and falls off rapidly with scattering angle. Also, for a set scattering angle, the scattering factor falls rapidly with decreasing wavelength, due to the reduction in cross-section σ. In addition, the scattering factor grows rapidly with atomic number Z, driving the significant contrast variations seen in TEM images of different atomic materials.

For the work presented in this thesis, TEM is applied to the characterisation of molecular materials. Constituent atoms of molecules interact with the fast electrons of the electron beam via their valence electrons or the atomic nuclei. The energy transferred to valence electrons can result in a number of secondary effects such as ionisation, heating, and direct electron attachment [69], and may be expressed as:

$$E_T(b) = \frac{e^4}{(4\pi\epsilon_0)^2 E b^2} \tag{2.26}$$

where e is the electron charge, b is the distance between incident and valence electrons, ϵ_0 is the permittivity of free space, and E is is the energy of the electron beam.

Interactions between the electron beam and atomic nuclei can result in the displacement of atoms from molecules, and the energy transferred to the atom due to momentum transfer can be expressed as:

$$E_T(\theta) = \frac{2m_a E(E + 2m_e c^2)}{(m_a + m_e)^2 c^2 + 2m_a E}\sin^2\Big(\frac{\theta}{2}\Big) \tag{2.27}$$

where m_a is the mass of the atom and θ is the electron scattering angle. For thin specimens, such as single molecules suspended on a graphene monolayer, the dominant source of energy transfer is expected to be due to atomic displacement from momentum transfer [69].

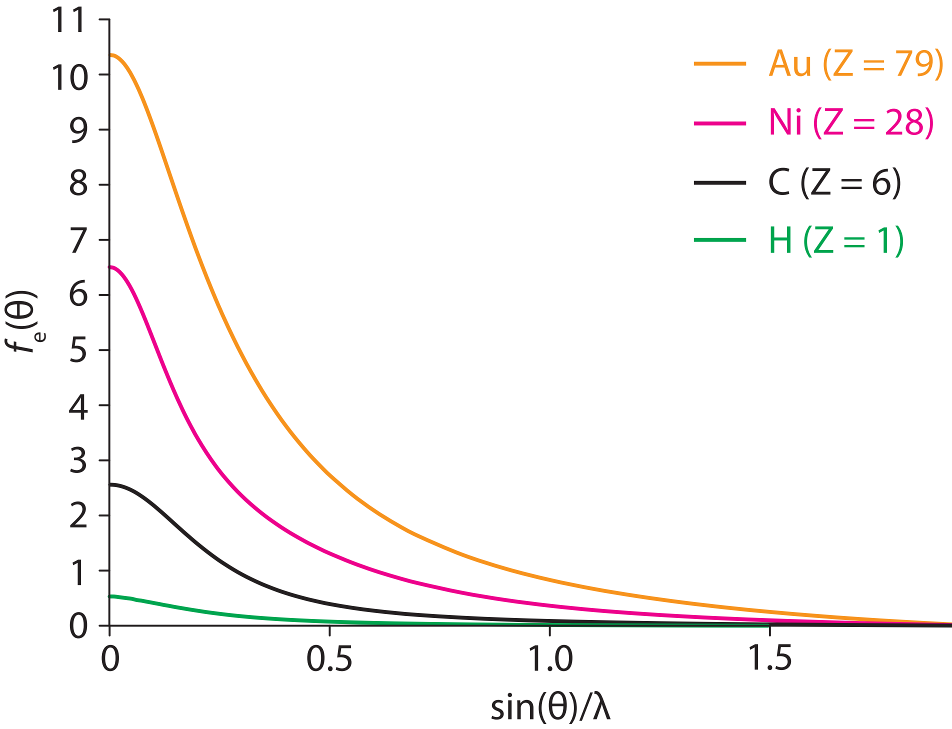

Figure 2.10: Electron scattering factor $f_e(\theta)$ data obtained from the International Tables for Crystallography, Volume C [68].

Electron Sources

The illumination source in a TEM provides a stream of electrons that are accelerated to the operating voltage of the microscope before entering the main column. Typical electron sources consist of two parts: an emission system and an accelerating system. Different sources can provide electron beams of varying quality, and contribute significantly to the ultimate performance of the microscope. The key parameters dictating the quality of an electron source are the brightness, source size, and energy spread. An ideal source will have high brightness (large current density per solid angle), small source size (high spatial coherence), and low energy spread (high temporal coherence) [65].

There are several types of illumination sources that can provide an electron beam for the TEM. These can be divided into two main groups: thermal emission and field emission sources. The most common thermal emission sources include tungsten (W) hair pin filaments and LaB_6 single crystal filaments. Both sources operate via resistive heating, producing an emission of thermal electrons that can then be accelerated to operating voltages. Field emission sources emit electrons via quantum tunneling, whereby a high-density electric field is applied to a sharp metal tip, allowing electrons to tunnel out of the tip material and be accelerated into the main column. The standard properties for all three sources are summarised in Table 2.1, and are illustrated in figure 2.11.

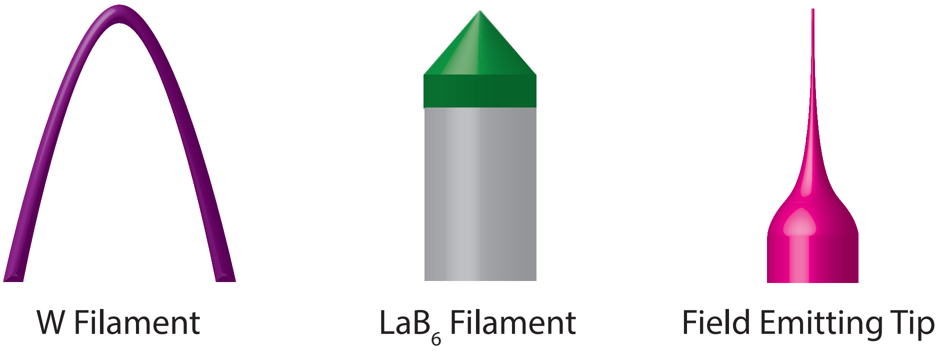

Figure 2.11: Illustrations of typical electron sources used in TEM. W hairpin filament and LaB_6 crystal are both resistively heated to produce thermal electrons, whilst the field emission gun (FEG) relies on dense electric fields to allow quantum tunneling of electrons out of the sharp metal tip.

Table 2.1: Typical values for the three main types of electron sources used in TEM. Values obtained from [64].

Source -	Temperature (K)	Brightness (A/cm^2 sr^{-1})	Source size (μm)	Energy spread (eV)
W	2800	$4x10^4$	50	3.0
LaB_6	1900-2000	$4x10^6$	1	1.5
Schottky FEG	1800	$4x10^5$	0.015	0.7
Cold FEG	293	$4x10^8$	0.005	0.4

The sharp tip and strong electric field in a field emission gun (FEG) provides a source with very high brightness and low spatial/temporal coherence, making them ideally suited for high-resolution work. For the work described in this thesis, three main TEMs were used, each armed with a different electron source. High-resolution imaging was carried out on a JEOL ARM200F (Schottky FEG source), electron diffraction imaging was carried out on a JEOL 2100LaB_6 (LaB_6 thermal source), and low-magnification imaging was carried out on a JEOL 2000FX (W thermal source).

Magnetic lenses and aberrations

Due to the strong interactions between electrons and matter outlined in section 2.3.1, it is not possible to fabricate a material lens in order to focus electron waves akin to the glass lenses used in optical microscopy. Instead, the charged nature of electrons is exploited through use of the Lorentz force:

$$\mathbf{F} = q\mathbf{E} + q\mathbf{v} \times \mathbf{B} \tag{2.28}$$

where $\mathbf{F}$ is the force on the charged particle, q is the particle charge, $\mathbf{E}$ is the electric field present, $\mathbf{v}$ is the particle velocity, and $\mathbf{B}$ is the magnetic field present. A force may therefore be applied to a charged particle using both an electric field and a magnetic field. For electron microscopes, magnetic lenses are used due to the greater practicality and stability of magnetic fields for influencing the trajectories of electrons [65].

Magnetic lenses consist of a series of windings (typically copper) contained within a magnetic material (typically an iron alloy) as shown in figure 2.12. The windings are subject to a large DC current flow, which produces a magnetic field in accordance with the Biot−Savart law at an arbitrary position $\mathbf{R} = (x, y, z)$:

$$B(\mathbf{R}) = \frac{\mu_0 I}{4\pi} \oint \frac{d\mathbf{L} \times \mathbf{R}}{\mathbf{R}^3} \tag{2.29}$$

where μ_0 is the permeability of free space, I is the steady-state current within the current loop, and $d\mathbf{L}$ is a length element along the current loop path. The magnetic material is designed with a gap, allowing the magnetic field to extend out towards the electron beam near the optical axis (figure 2.12). The size, shape, and strength of the magnetic lens may be engineered in order to provide optimum focusing conditions of the electron beam in a fashion similar to the glass lenses used in optical microscopy.

A simple circular current loop model can be evaluated using the Biot−Savart law in order to visualise the magnetic field produced by a magnetic lens (figure 2.13). From equation 2.29, the vector components of B can be calculated by dividing a circular current loop into N equal length approximately-straight sectors, with direction tangential to the current-loop sector. Neglecting the constant terms and choosing a unit current for simplicity, the magnetic field $B(\mathbf{R})$ can be split into radial $\mathbf{B}_r$ and azimuthal $\mathbf{B}_z$ components, which vary in magnitude in relation to the distance along the optical axis from the lens centre (figure 2.13). The magnetic field $B(\mathbf{R})$ at an arbitrary position $\mathbf{r}$ can be calculated through a summation:

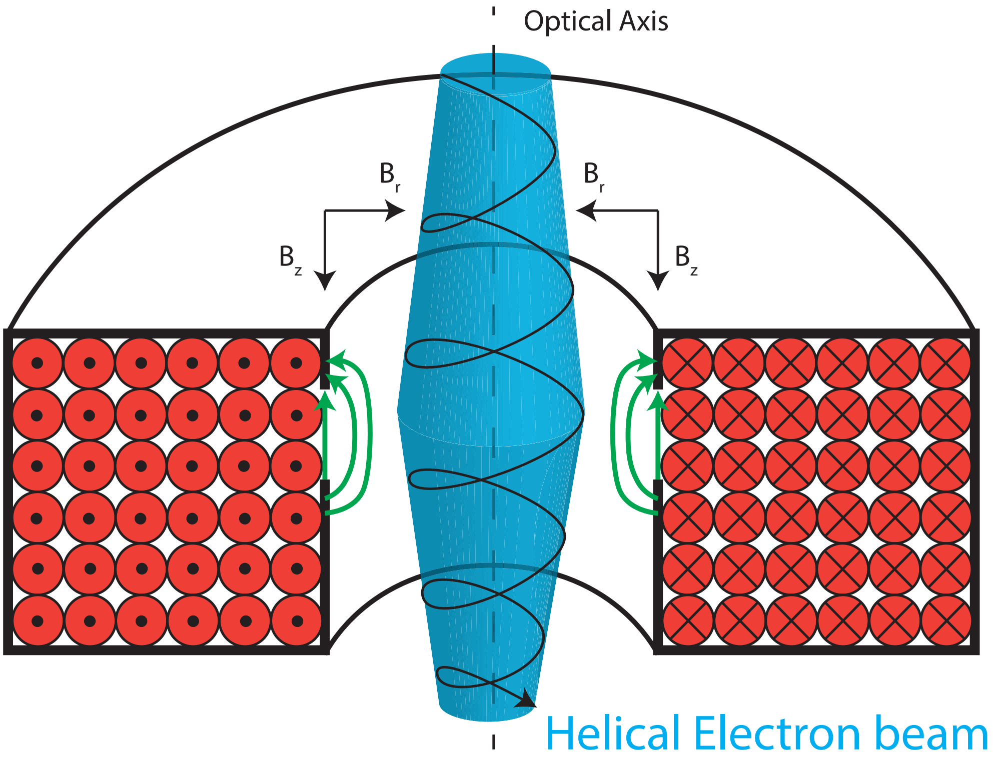

Figure 2.12: Circular magnetic lens schematic. Windings (red) containing a steady current I are embedded in a magnetic material containing a pole piece gap. This produces a strong localised magnetic field (green field lines) that acts to focus the electron beam.

$$B(\mathbf{R}) = \sum_{i=1}^{N} \frac{(\hat{\mathbf{e}}_x \cos\left(\frac{2\pi}{N}\right) - \hat{\mathbf{e}}_y \sin\left(\frac{2\pi}{N}\right)) \times \mathbf{R}}{\mathbf{R}^3} \tag{2.30}$$

where the current loop is located in the (x, y) plane. From the summation in equation 2.30, it is possible to separately evaluate the radial and azimuthal magnetic field componentsAs shown in figure 2.13, the strength of the radial field component increases with both distance along the optical axis, and radial distance from the centre of the optical axis; optical glass lenses follow similar principles of greater focusing strength with distance from the lens centre [70].

Image formation in Transmission Electron Microscopy

With the key components of a TEM introduced, as featured in figure 2.14, the process by which the electron beam forms an image of a specimen can be described mathematically. The electron wave $\psi(\mathbf{R})$ acting as a source illumination obeys the

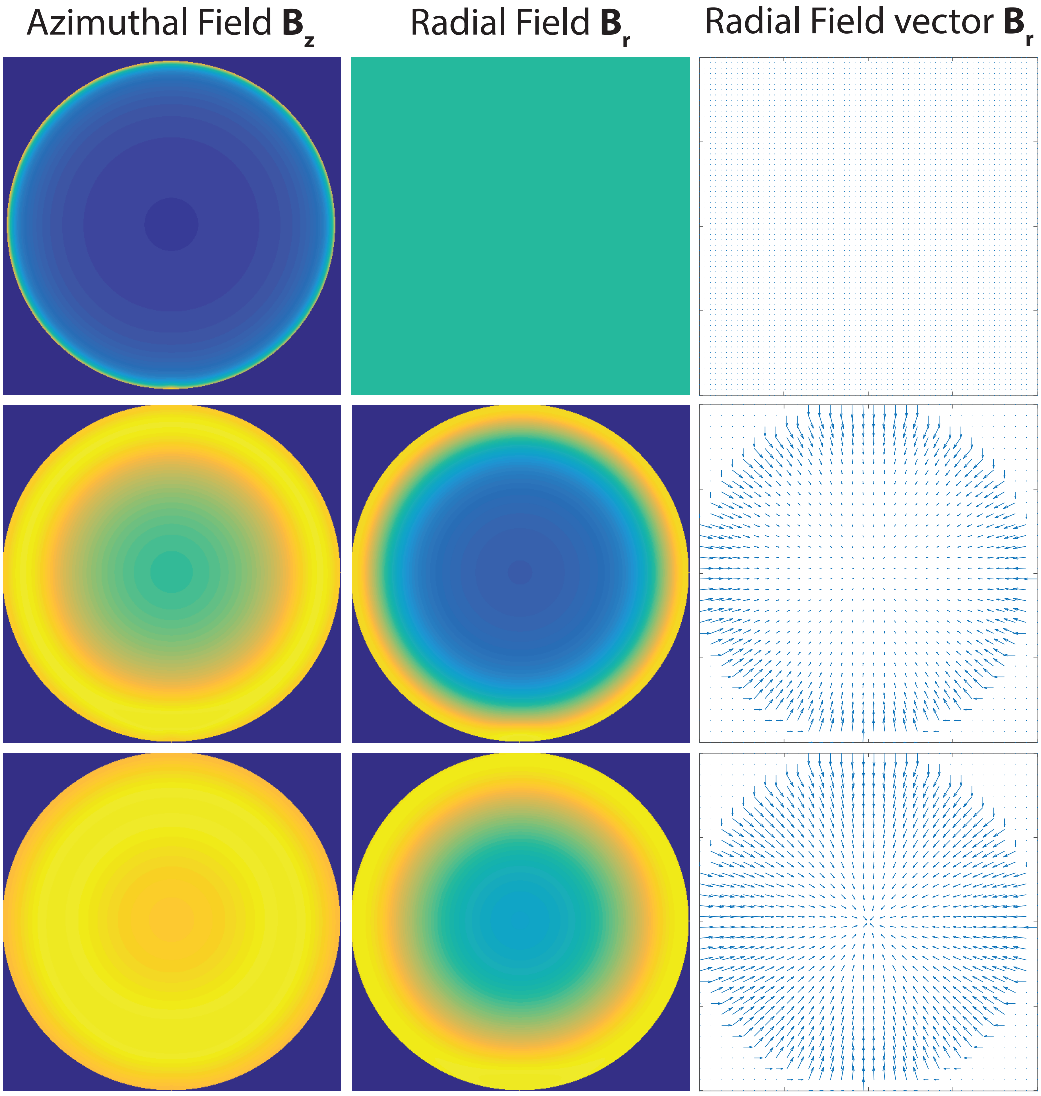

Figure 2.13: Circular magnetic lens field diagrams. (Left column) Azimuthal field component $\mathbf{B}_z$ at different positions along the optical axis (z=0, 1, 2 a.u.). (Centre column) Radial field component $\mathbf{B}_r$ at different positions along the optical axis (z=0, 1, 2 a.u.). (Right column) vector plots of the radial field component $\mathbf{B}_r$ at different positions along the optical axis (z=0, 1, 2 a.u.).

same Fourier optics theory that can be used to describe optical microscopes. The electron wave propagated to a new position **R'** $= (x', y', z')$ can be calculated:

$$\psi'(\mathbf{R}') = A\psi(\mathbf{R}') \otimes \mathcal{P}_{\delta z}(\mathbf{R}') = A\int_{-\infty}^{+\infty} \psi(\mathbf{R})\mathcal{P}_{\delta z}(\mathbf{R}' - \mathbf{R})d\mathbf{R} \tag{2.31}$$

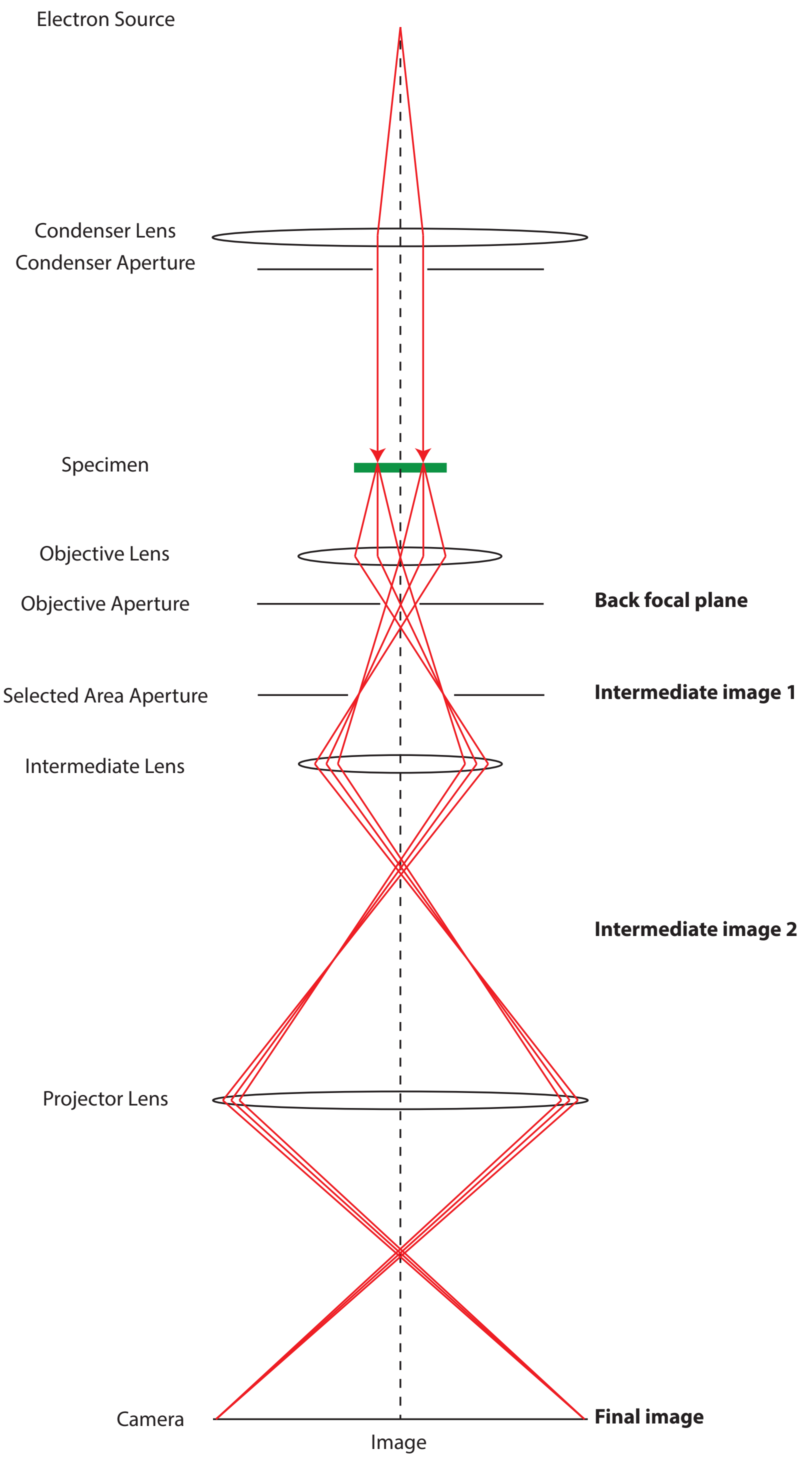

Figure 2.14: TEM ray diagram for conventional-imaging mode.

where A is a complex constant, the wave propagates along the z axis (optical axis) to a new position $z' = z + \delta z$, and

$$\mathcal{P}_{\delta z}(\mathbf{R}) = \exp\left(-\frac{i\pi(x^2+y^2)}{\lambda\delta z}\right) \tag{2.32}$$

is the Fresnel free-space propagator. As well as being able to apply free-space propagation operations to electron waves, the effect of a specimen interaction can be calculated using a transmission function $\phi(\mathbf{R})$:

$$\psi_{exit}(\mathbf{R}) = \phi(\mathbf{R})\psi(\mathbf{R}) \tag{2.33}$$

where $\psi_{exit}(\mathbf{R})$ is the electron wave exiting the specimen (referred to as the exit-wavefunction), $\psi(\mathbf{R})$ is the electron wave incident on the specimen, and $\phi(\mathbf{R})$ is an approximation of the complex specimen transmission function neglecting focus variation (Fresnel diffraction) within the sample [71]:

$$\phi(\mathbf{R}) = \exp(-i\sigma V(\mathbf{R})) \tag{2.34}$$

where σ is the scattering cross section of the specimen material:

$$\sigma = \frac{2\pi m e\lambda}{h^2} \tag{2.35}$$

and m is the relativistic electron mass. For the case of thin, weakly-scattering specimens, as dealt with in this thesis, the phase changes induced in Equation 2.34 are small ($\phi(\mathbf{R}) \ll 1$), and can be approximated using the weak phase object (WPO) approximation [65, 71]:

$$\phi(\mathbf{R}) = \exp(-i\sigma V(\mathbf{R})) \approx 1 - i\sigma V(\mathbf{R}) \tag{2.36}$$

The TEM satisfies the conditions of Fraunhofer diffraction [65], meaning that the electron wavefunction in the back focal plane (diffraction plane) can be obtained by taking the Fourier transform of the exit-wavefunction:

$$\widetilde{\psi}_{exit}(\mathbf{K}) = \mathcal{F}(\psi(\mathbf{R})\phi(\mathbf{R})) \tag{2.37}$$

where $\mathcal{F}$ denotes a Fourier transform. This is illustrated in the ray diagrams illustrating the TEM in an imaging setup in figure 2.14. The wavefunction in the image plane $\psi(\mathbf{R})_{image}$ can be obtained by applying an inverse Fourier transform to the diffraction-plane wavefunction $\widetilde{\psi}_{exit}(\mathbf{K})$:

$$\psi_{image}(\mathbf{R}) = \mathcal{F}^{-1}(\widetilde{\psi}_{exit}(\mathbf{K})) = \mathcal{F}^{-1}(\mathcal{F}(\psi(\mathbf{R})\phi(\mathbf{R}))) = \psi(\mathbf{R})\phi(\mathbf{R}) \tag{2.38}$$

where $\mathcal{F}^{-1}$ denotes an inverse Fourier transform. The final image $I_{image}(\mathbf{R})$ that is recorded is then obtained through the square modulus of the image-plane wavefunction:

$$I_{image}(\mathbf{R}) = |\psi_{image}(\mathbf{R})|^2 = |\psi(\mathbf{R})|^2 \tag{2.39}$$

Aberration Correction and High-Resolution Imaging

The mathematical formalism outlined in Equations 2.37, 2.38, and 2.39 lacked a vital component: the presence of microscope aberrations. Although the presence of aberrations can hinder image resolution as will be shown, the case of perfect imaging free from aberrations results in zero contrast being imparted on the electron wave by the specimen, in accordance with Equation 2.39.

Aberrations are commonplace in electron microscopes, arising due to imperfections in the magnetic lenses, the finite size of objective lens apertures, and the partial coherence of the electron source. These aberrations can be described using an aperture function [71]:

$$A(\mathbf{K}) = H(\mathbf{K})\exp[-i\chi(\mathbf{K})] \tag{2.40}$$

where $H(\mathbf{K})$ described the effects of the objective lens apertures and the partial coherence of the electron beam, and $\chi(\mathbf{K})$ is the wave aberration function describing the objective lens aberrations. The addition of an aperture function modifies the final image-plane wavefunction accordingly:

$$\psi_{image}(\mathbf{R}) = \mathcal{F}^{-1}\{\widetilde{\psi}_{exit}(\mathbf{K})A(\mathbf{K})\} = \psi(1 - i\sigma V(\mathbf{R})) \otimes \widetilde{A}(\mathbf{R}) \tag{2.41}$$

giving a final image intensity:

$$I(\mathbf{R}) = \psi_{image}(\mathbf{R})\psi^*_{image}(\mathbf{R}) = 1 + 2\sigma V(\mathbf{R}) \otimes \mathcal{F}^{-1}\{H(\mathbf{K})\sin(\chi(\mathbf{K}))\} \tag{2.42}$$

where terms of the order σ^2V^2 have been neglected. It is clear from Equation 2.42 that only the imaginary contributions of the aperture function $A(\mathbf{K})$ affect the final image intensity, and so this is referred to as the phase contrast transfer function

(PCTF):

$$PCTF(\mathbf{K}) = H(\mathbf{K})\sin(\chi(\mathbf{K})) \tag{2.43}$$

As already described, the wave-aberration function $\chi(\mathbf{K})$ represents the perturbations introduced to the wavefront due to imperfections in the objective lenses. This produces a phase change $\exp[-i\chi(\mathbf{K})]$ in the exit-wavefunction $\psi_{exit}(\mathbf{R})$, as illustrated in figure 2.15.

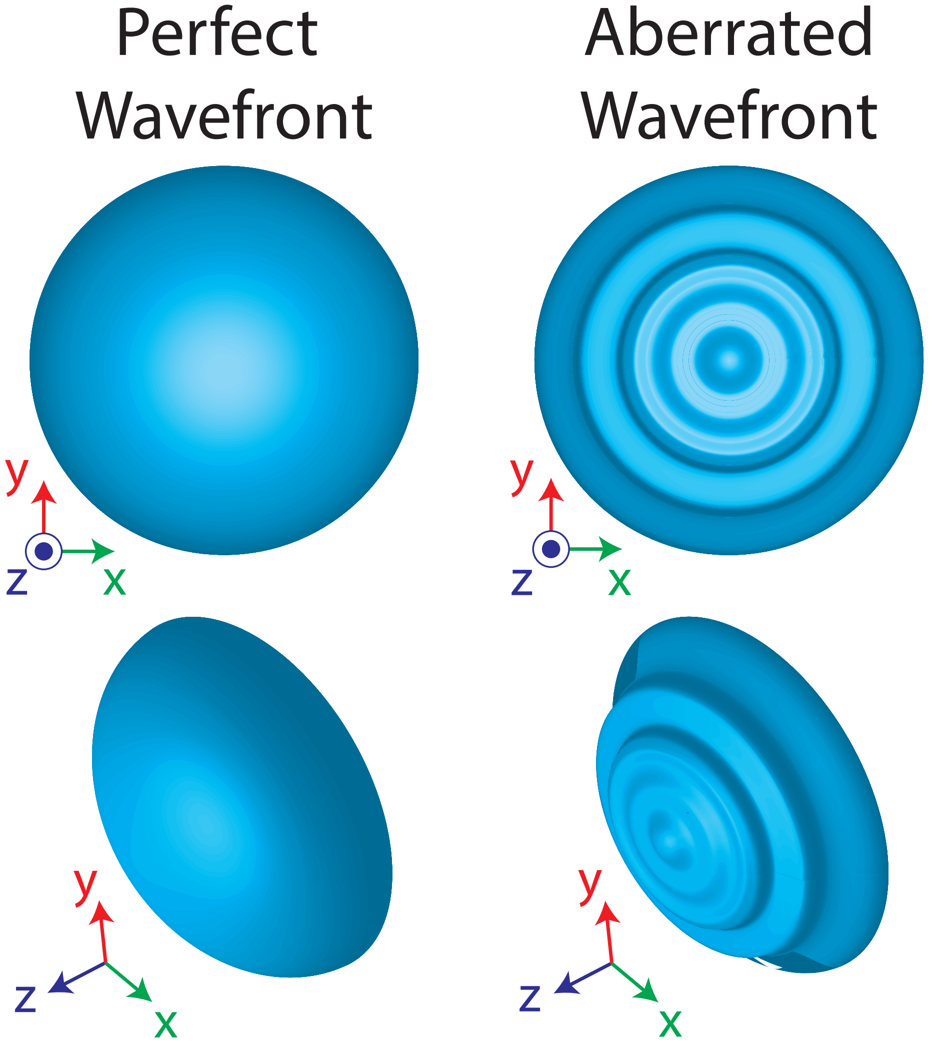

Figure 2.15: Perfect vs aberrated wavefront cartoon depictions. Top row: azimuthal projections. Bottom row: perspective views.

The wave-aberration function may be expressed as a Taylor-series expansion as a function of the spatial frequency vector $\mathbf{K}$:

$$\begin{aligned}\chi(\mathbf{K}) = \Re\Bigg(\frac{2\pi}{\lambda}\Bigg(&C_{0,1}\lambda\mathbf{K}^{*} + \frac{1}{2}C_{1,2}\lambda^{2}\mathbf{K}^{*}\mathbf{K} + \frac{1}{2}C_{1,2}\lambda^{2}\mathbf{K}^{*2}\\ &+ \frac{1}{3}C_{2,1}\lambda^{3}\mathbf{K}^{*2}\mathbf{K} + \frac{1}{3}C_{2,3}\lambda^{3}\mathbf{K}^{*3}\\ &+ \frac{1}{4}C_{3,0}\lambda^{4}\mathbf{K}^{*2}\mathbf{K}^{2} + \frac{1}{4}C_{3,2}\lambda^{4}\mathbf{K}^{*3}\mathbf{K} + \frac{1}{4}C_{3,4}\lambda^{4}\mathbf{K}^{*4}\\ &+ \frac{1}{5}C_{4,1}\lambda^{5}\mathbf{K}^{*3}\mathbf{K}^{2} + \frac{1}{5}C_{4,3}\lambda^{5}\mathbf{K}^{*4}\mathbf{K} + \frac{1}{5}C_{4,5}\lambda^{5}\mathbf{K}^{*5}\\ &+ \frac{1}{6}C_{5,0}\lambda^{6}\mathbf{K}^{*6} + \frac{1}{6}C_{5,2}\lambda^{6}\mathbf{K}^{*4}\mathbf{K}^{2}\Bigg)\Bigg)\end{aligned} \tag{2.44}$$

where the coefficients $C_{i,j}$ denote the aberration contribution with radial symmetry i and azimuthal symmetry j, as listed in Table 2.2.

Table 2.2: The name, radial symmetry i, and azimuthal symmetry j for the aberration coefficients $C_{i,j}$.

Aberration Coefficient	Krivanek notation	Uhlemann and Haider Notation	Radial and Azimuthal symmetry (i,j)
Image shift	$C_{0,1}$	C_0	$i = 0$, $j = 1$
Defocus	$C_{1,0}$	C_1	$i = 1$, $j = 0$
Two-fold astigmatism	$C_{1,2}$	A_1	$i = 1$, $j = 2$
Axial comma	$C_{2,1}$	$B_2 = C^{*}_{2,1}/3$	$i = 2$, $j = 1$
Three-fold astigmatism	$C_{2,3}$	A_2	$i = 2$, $j = 3$
Spherical aberration	$C_{3,0}$	$C_s = C_3$	$i = 3$, $j = 0$
Axial star aberration	$C_{3,2}$	$S_3 = C^{*}_{3,2}/4$	$i = 3$, $j = 2$
Four-fold astigmatism	$C_{3,4}$	A_3	$i = 3$, $j = 4$
Fourth-order axial comma	$C_{4,1}$	$B_4 = C^{*}_{4,1}/5$	$i = 4$, $j = 1$
Three-lobe aberration	$C_{4,3}$	$D_4 = C^{*}_{4,3}/5$	$i = 4$, $j = 3$
Five-fold astigmatism	$C_{4,5}$	A_4	$i = 4$, $j = 5$
Fifth-order spherical aberration	$C_{5,0}$	C_5	$i = 5$, $j = 0$
Fifth-order axial star aberration	$C_{5,2}$	$S_5 = C^{*}_{5,2}/6$	$i = 5$, $j = 2$
Fifth-order rosette aberration	$C_{5,4}$	A_5	$i = 5$, $j = 4$
Six-fold astigmatism	$C_{5,6}$	$R_5 = C^{*}_{5,4}/6$	$i = 5$, $j = 6$

The individual phase profiles of the aberrations listed in Table 2.2 can be calculated and plotted, as shown in figure 2.16. Both the perspective and azimuthal projections are shown, indicating the shape and symmetry of each aberration.

For uncorrected instruments, the dominant sources of aberration are defocus $C_{1,0}$, two-fold astigmatism $C_{1,2}$, and spherical aberration $C_{3,0}$. For instruments with aberration correctors installed, higher order aberrations become dominant. In order

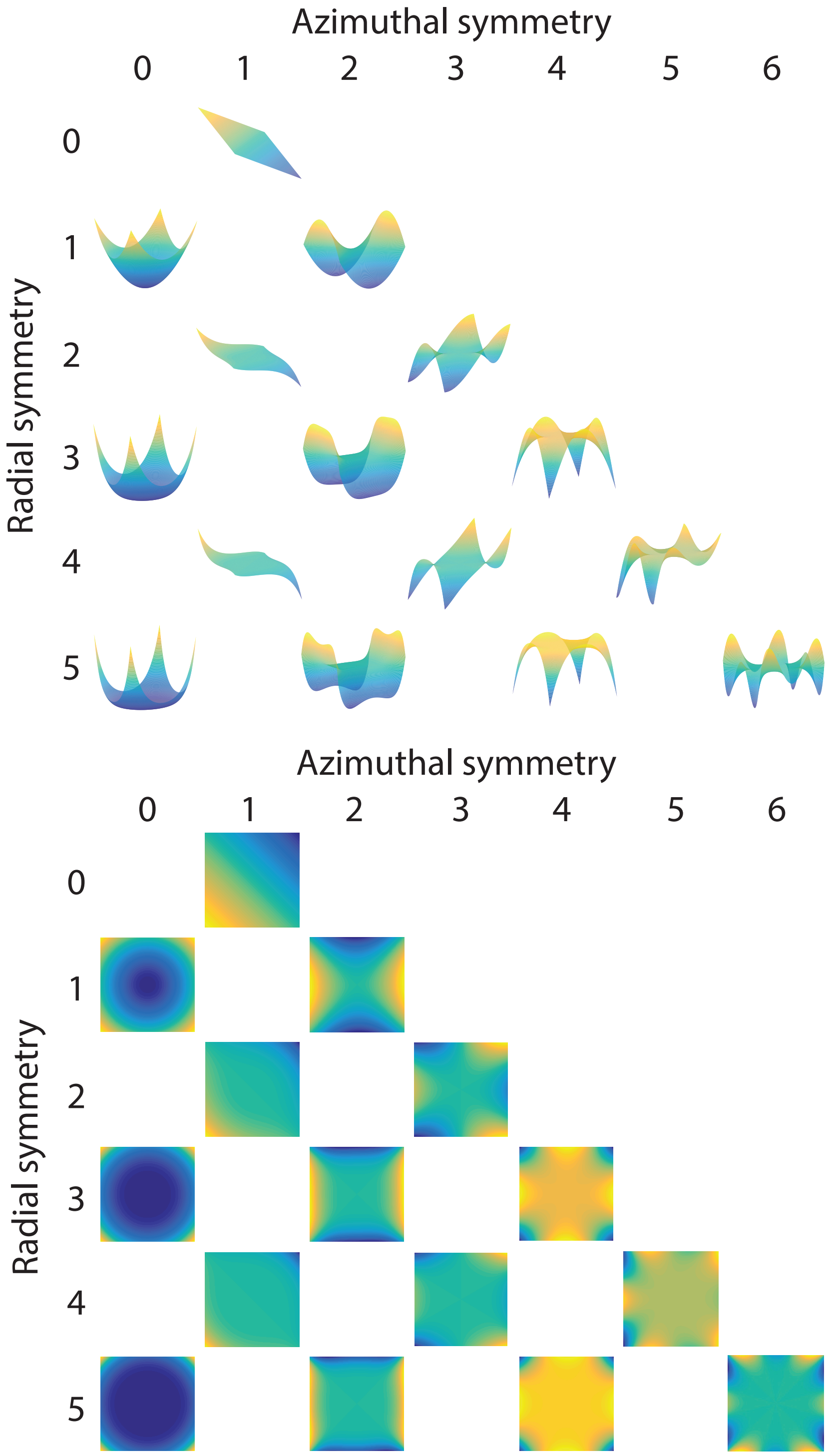

Figure 2.16: Perspective (top) and azimuthal projection (bottom) of the sources wave aberration presented in Table 2.2.

to correct for any wave-aberrations present, the wave-aberration function $\chi(\mathbf{K})$, and the specific contributions from each term in Table 2.2, must be measured.

Using the methods of Zemlin [72], the changes induced in the final image by the successive tilting of the beam relative to the specimen can be analysed in order to measure the wave-aberrations present. Diffractograms (power spectra) are measured from an amorphous region of material for a number of specified tilt positions, as shown in figure 2.17. Through analysis of the shape of the diffractograms at each tilt, the wave-aberration function may be measured [72], as shown using simulated measurements in figure 2.17.

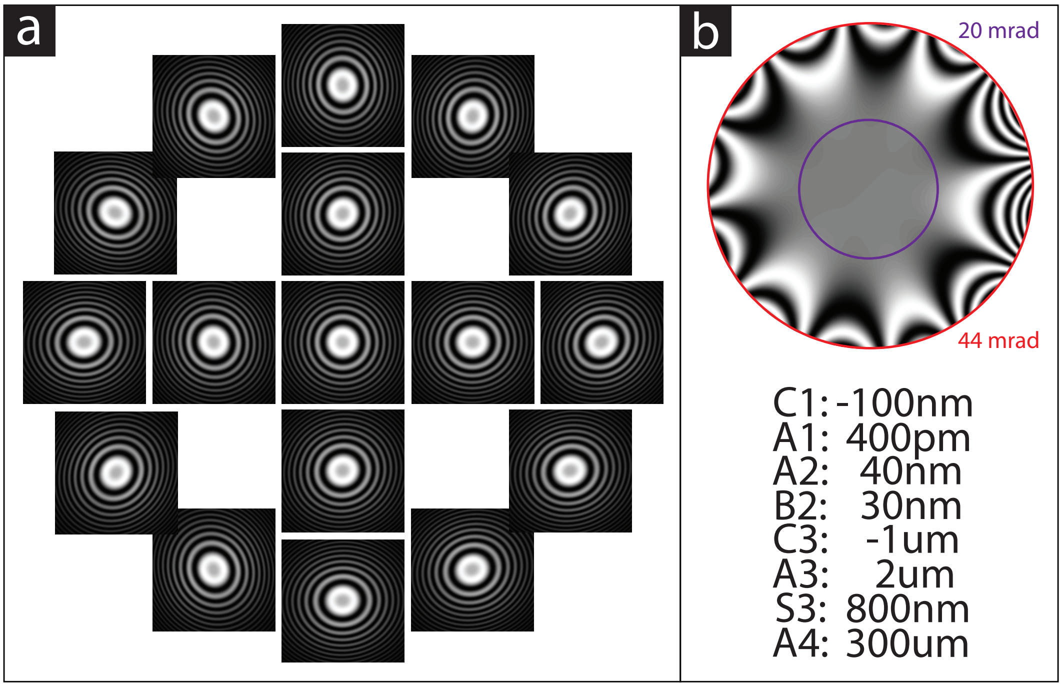

Figure 2.17: Measuring the wave-aberration function using the Zemlin tableau method. a) Multiple diffractograms taken at different beam tilts showing the presence of significant aberrations. b) Measured wave-aberration profile shown in azimuthal projection. Aberration coefficient values used for the simulation are also listed.

With the wave-aberration function measured, along with the specific contributions from different aberration sources, it is possible to apply the necessary beam correction using a series of multipole lenses contained within a corrector-lens stage. Multipole lenses comprise of a number of magnetic poles aligned perpendicular to the optical axis, as shown in figure 2.18. This has the effect of producing a magnetic field predominantly perpendicular to the electron beam, differing to the case for circular magnetic lenses that produce a field predominantly parallel to the electron beam. Multipole lenses allow a desired deflection to be imparted on the electron beam, as shown in figure 2.18.

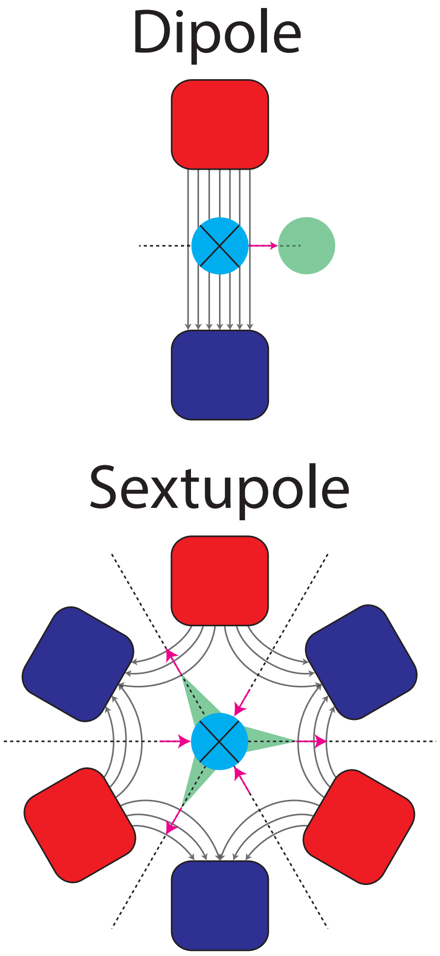

Figure 2.18: Multipole lens schematics formed from different north (red) and south (blue) pole configurations. The electron beam (blue) is directed out of the page, and the magnetic field lines (grey arrows) are perpendicular to the beam. The resulting Lorentz forces on the electron beam are indicated by the pink arrows, producing a change in shape of the electron beam (green).

With the main sources of objective-lens-induced aberration corrected for, the effects of source coherence must be addressed. These additional effects combine to form a partial coherence envelope, which acts to dampen the PCTF at large spatial frequencies (high resolution). The spatial coherence envelope $E_s(\mathbf{K})$ results from the finite size of the electron source, meaning that the specimen receives illumination from a range of directions:

$$E_s(\mathbf{K}) = \exp\Big[\Big(\frac{-\alpha^2}{4\lambda^2}\Big)\Big(\frac{\partial\chi(\mathbf{K})}{\partial\mathbf{K}}\Big)^2\Big] \tag{2.45}$$

where α is the semi-angle subtended by the illuminated source aperture and focused spot on the specimen. The partial temporal coherence envelope $E_t(\mathbf{K})$ originates from fluctuations in the accelerating voltage, objective lens current, and the finite energy spread in the electron source:

$$E_t(\mathbf{K}) = \exp\Big[-\frac{1}{2}(\pi\lambda\Delta)^2\mathbf{K}^4\Big] \tag{2.46}$$

where Δ is the standard deviation of the distribution in Gaussian-distributed foci resulting from the fluctuations in accelerating voltage (ΔV), source energy (ΔE), and objective lens current (ΔI):

$$\Delta = C_c\sqrt{\Big(\frac{\Delta V}{V}\Big) + \Big(\frac{\Delta E}{E}\Big) + 4\Big(\frac{\Delta I}{I}\Big)} \tag{2.47}$$

Together, these coherence envelopes combine to form the overall PCTF:

$$PCTF(\mathbf{K}) = E_s(\mathbf{K})E_t(\mathbf{K})H(\mathbf{K})\sin(\chi(\mathbf{K})) \tag{2.48}$$

As shown in figure 2.19, the combined partial coherence envelope suppresses the PCTF signal at high spatial frequencies, limiting the resolution of the instrument.

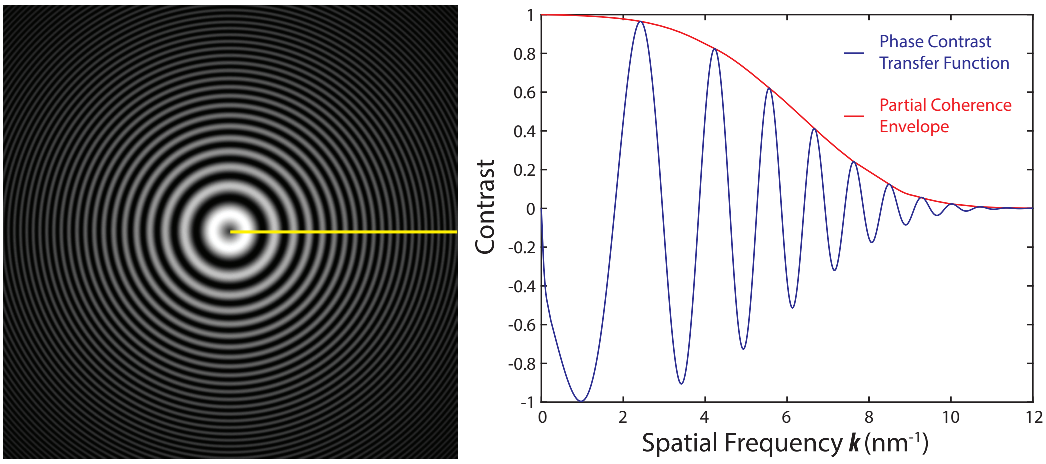

Figure 2.19: Simulated Phase Contrast Transfer Function (PCTF). Line profile (yellow) taken from PCTF image shows the total PCTF (blue) and also the partial coherence envelope function (red) as a function of spatial frequency.

Image Simulation

For phase contrast imaging in TEM, phase shifts induced by objective lens aberrations strongly affect the final image intensity. Difficulties therefore arise in the direct interpretation of images, due to contrast reversals under certain imaging conditions. It is therefore necessary to simulate images for comparison against, in order to aid interpretation.

There are several techniques available for simulating TEM images [65]. One such method is the multislice method, first proposed by Cowley and Moodie in 1957 [73] in order to describe the dynamically diffracted intensities from crystals. Their work was further adapted by Goodman and Moodie in 1974 [74] into a numerical procedure that could yield simulated TEM images and diffraction patterns using an atomic structure model as an input. With the development of the Fast Fourier Transform (FFT) algorithm [75], the method was further developed by Ishizuka and Uyeda in 1977 [76], leading to dramatically reduced computational efforts for multislice calculations. There have been several further refinements since, and the work of this thesis adopted the refinements made by Dr Adam Dyson and Dr Jonathan Peters, who developed the clTEM multislice simulation package [77–79]. Key additions to the basic calculation include graphical-processing unit (GPU) accelerated computations, enabling more complex simulations to be carried out with reduced effort, as well as a more precise modeling of the atomic potentials of specimen atoms.

The basic premise of the multislice method involves the modeling of a specimen using a number of thin slices, described using the specimen transmission function $t(x, y, z)$. Using the Fresnel free-space propagator (Equation 2.32), the wavefunction resulting from propagation through a thin specimen slice of thickness δz can be calculated:

$$\psi(x, y, z + \delta z) = \mathcal{P}_{\delta z}(x, y) \otimes [t(x, y, z)\psi(x, y, z)] + \mathcal{O}(\delta z^2) \tag{2.49}$$

For a specimen that is divided into N slices, this may be applied recursively to yield the final exit-wavefunction emerging from the specimen:

$$\psi_{n+1}(x, y) = \mathcal{P}_{\delta z}(x, y) \otimes [t(x, y, z)\psi_n(x, y)] + \mathcal{O}(\delta z^2) \tag{2.50}$$

where $n = 0, 1, 2, ...N$. The application of the multislice method for simulating the exit-wavefunction is illustrated in figure 2.20. With the exit-wavefunction simulated, it is trivial with the application of Equation 2.41 and simulation of the aperture function $A(\mathbf{K})$ to arrive at a noise-free intensity image. Finally, the effects of the detection device are accommodated for using the following formula [80]:

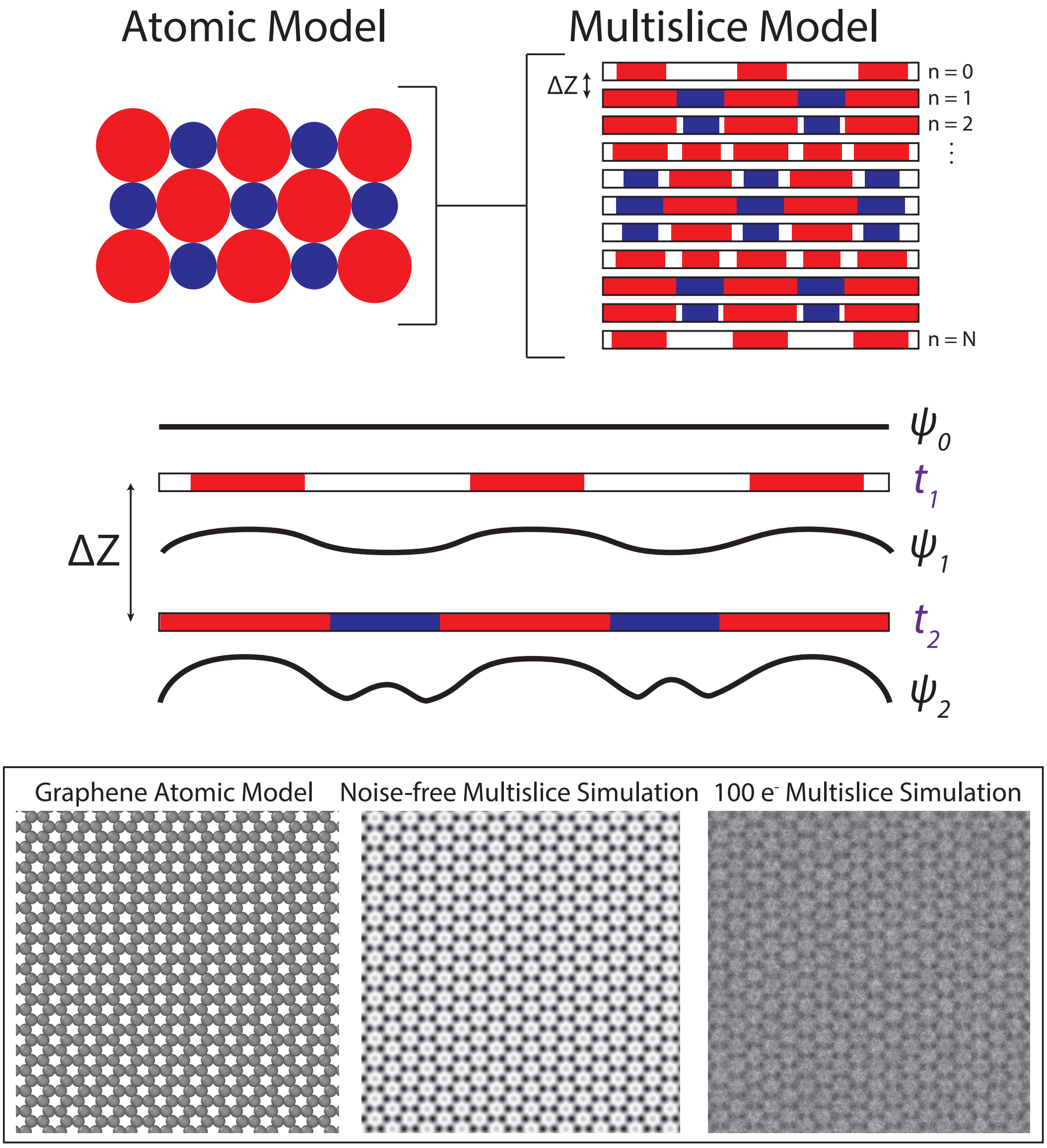

Figure 2.20: Multislice simulation method. (Top) Atomic model is sliced into N thin transmission function elements $t(x, y, z)$ of thickness Δz. The wavefunction $\psi_0(x, y, z)$ is recursively Fresnel propagated between slices and the transmission function of each new slice applied, in order to generate the final exit-wavefunction $\psi_{exit}(x, y, z)$ leaving the specimen. (Bottom) Graphene atomic model and corresponding multislice simulations for noise-free and limited-dose imaging conditions. Additional image artifacts at the centre of each graphene hexagon have been introduced due to approximations made in the programme.

$$I(r) = I_{rn} + I_{dc} + CF \cdot \mathcal{F}^{-1}\Bigg[\mathcal{F}\Bigg[P_{oiss}\Bigg(\phi_e \cdot \mathcal{F}^{-1}\Bigg[I_0(q)\sqrt{DQE(q.N)}\Bigg]\Bigg)\Bigg] \cdot NPS_{out}(q,N)\Bigg] \tag{2.51}$$

where $I(r)$ is the final image with limited electron dose and I_0 is the Fourier transform of the noise-free image arriving at the detector. The other functions included within the equation relate to various properties of the detection device, and are described in greater detail in chapter 4.

In order to simulate an image of a specimen using the multislice method, it is necessary to construct an accurate atomic model of the specimen. Typical multislice image simulation software packages, including clTEM [77], require a .xyz file format input, which consists of a list of atom types and their respective (x, y, z) co-ordinates. The simplicity of this file type enables complex structures to be constructed with relative ease, without the need for direct manipulation of atoms using software such as CrystalMaker®, which necessitates image rendering of the .xyz file during manipulation which can prove to be highly inefficient.

For the work presented in this thesis, a short Java programme was developed to enable complex atomic/molecular structures to be constructed [81]. In addition, the various structures can be rotated, duplicated, displaced, and cropped along defined axes. An example of a molecular crystal constructed using a single molecule of vanadyl-oxide phthalocyanine (VOPc) is shown in figure 2.21, alongside experimental and simulated TEM images. The power spectra of both images show good correspondence between lattice-plane distances.

Electron Diffraction

In addition to direct imaging, electron diffraction is another powerful tool in the transmission electron microscopist's arsenal. As outlined in section 2.2, elastically scattered waves from a real-space crystal lattice **R** will produce a set of diffraction (Bragg) peaks at the locations of the reciprocal-space lattice **G**. For the case of the TEM, an illuminated specimen will produce a set of diffraction peaks within the back focal plane, as shown in figure 2.22. As shown, the intermediate lens strength is varied in comparison to figure 2.14, allowing a diffraction pattern to be formed at the image plane.

Electron diffraction allows large areas (defined by the selected-area aperture) to be sampled in the formation of an image, providing crystal structure information

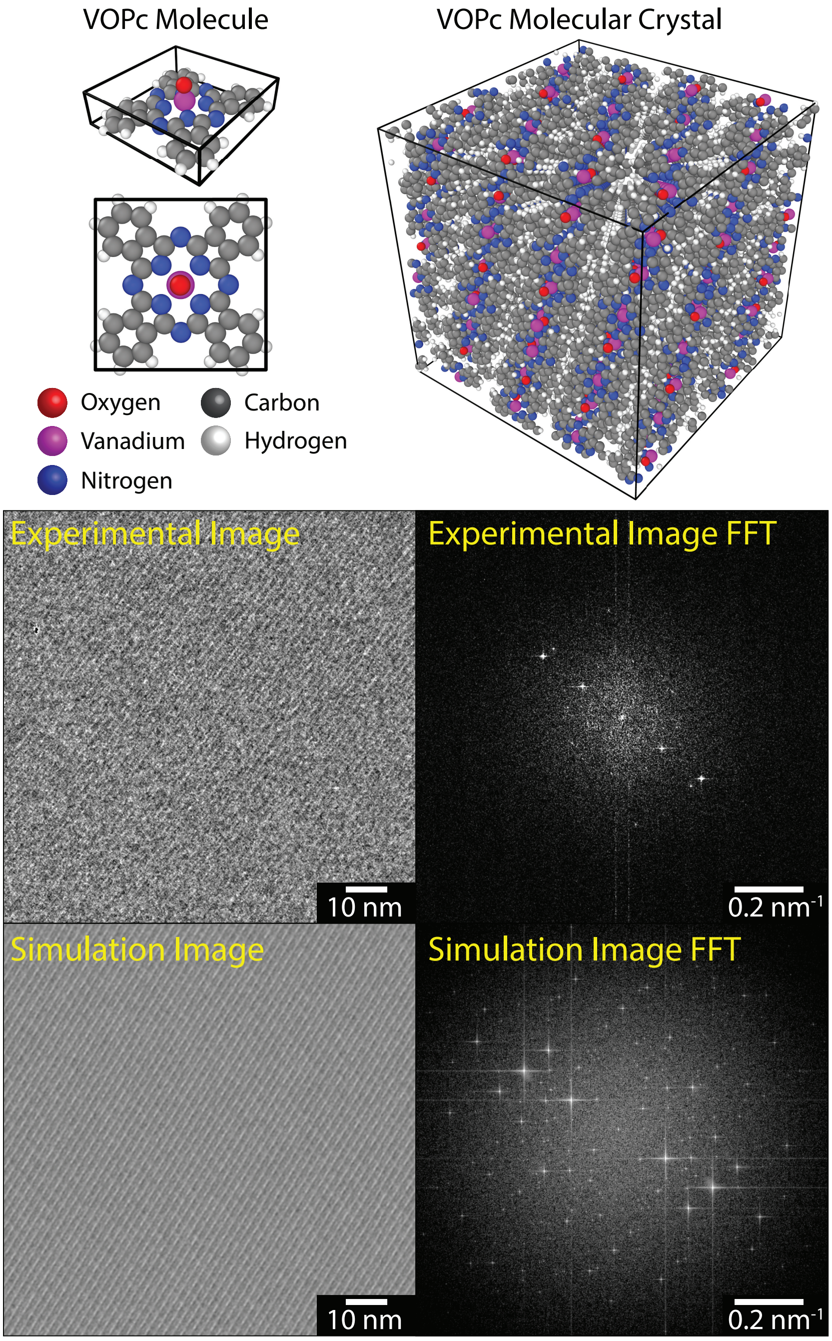

Figure 2.21: VOPc molecular crystal model and multislice simulations. (Top) Molecular model of single VOPc molecule and molecular crystal constructed along the $[1\bar{3}\bar{2}]$ direction with 2° tilt. (Bottom) Experimental and simulated multislice TEM images of VOPc molecular crystal, with good correspondence shown between images and FFTs.

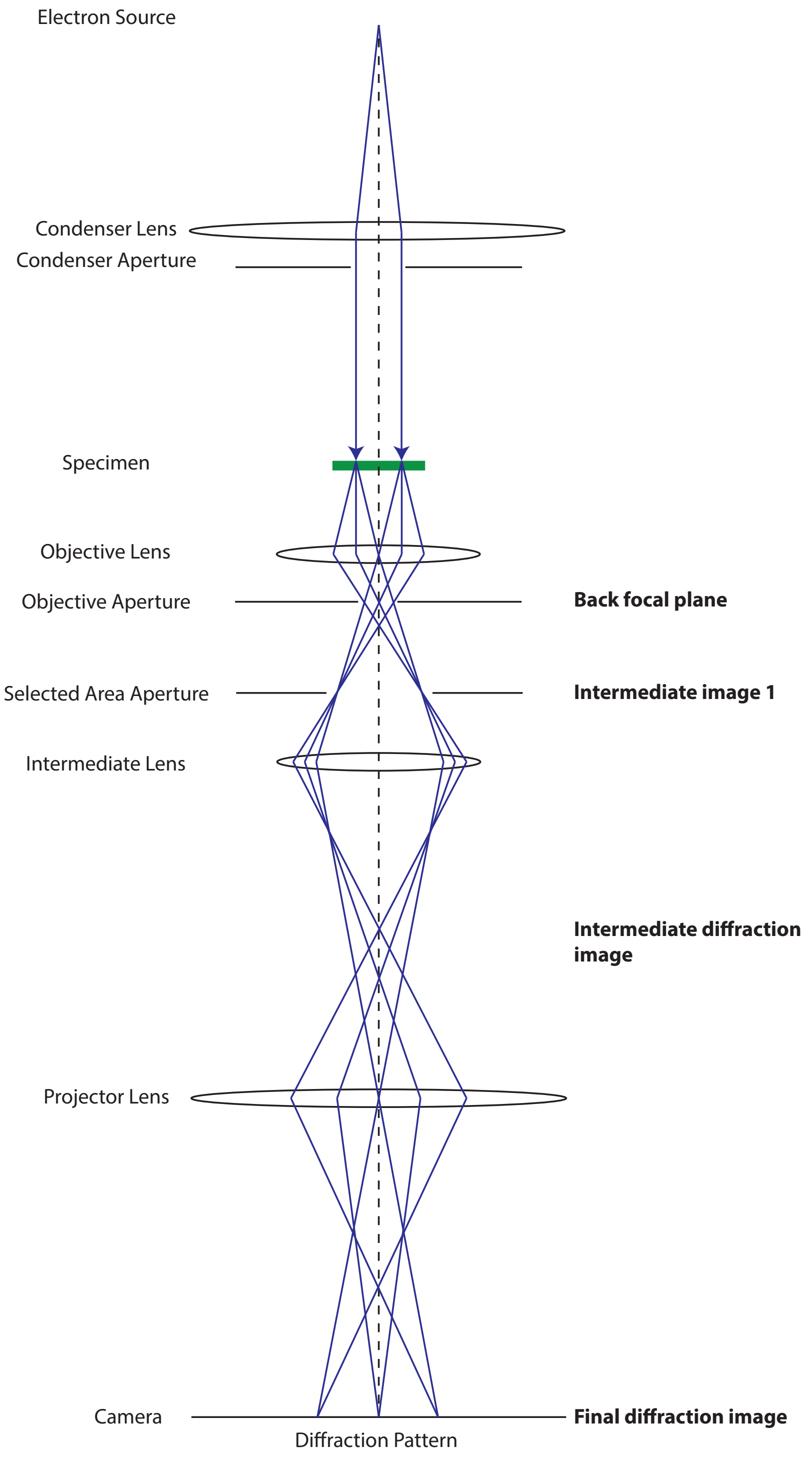

Figure 2.22: TEM ray diagram for electron diffraction mode.

over much larger length scales than direct imaging. In addition, the much larger sampling area exposes the specimen to a much lower local dose of electrons, allowing very beam-sensitive materials to be studied. The concept of low-dose diffraction as a means of studying beam-sensitive materials is investigated in detail in chapter 4.

As outlined in Equations 2.7 and 2.11, the scattered wave in the back focal plane (diffraction pattern) is equivalent to the crystal structure factor (equation 2.6). However, due to the nature of the image detection in TEM, the actual image obtained contains information on the diffraction peak intensities I rather than the diffraction peak amplitudes and phases:

$$I = \mathbf{E}(\mathbf{r}, t)^* \mathbf{E}(\mathbf{r}, t) = |\mathbf{E}(\mathbf{r}, t)|^2 \propto F(hkl)^* F(hkl) = |F(hkl)|^2 \tag{2.52}$$

meaning that the phase information in $F(hkl)$ is lost. This is referred to as the *phase problem* in crystallography, and arises because the lost phase information prevents a direct image of the crystal lattice being obtained from an inverse Fourier transform of the diffraction pattern.

Although a direct image of the crystal lattice cannot be obtained from a diffraction pattern, valuable information can still be gathered. The positions of the diffraction peaks are not affected by the loss of phase information, and so the unit cell dimensions can be obtained to high precision and accuracy. In addition, differences between peak intensities are affected by the relative positions between atoms/molecules within the lattice. It is possible to use the multislice method outlined in section 2.3.1 to simulate diffraction pattern images which can be compared against experimental data. Figure 2.23 shows a simulated diffraction image of graphene alongside an experimental image, as well as an FFT from a real-space atomic-resolution image. As shown, the simulated and experimental diffraction patterns show good correspondence. The experimental diffraction pattern also contains a central bright hue resulting from inelastically scattered electrons that do not contribute to the elastically scattered diffraction peaks.

2.3.2 Scanning Tunneling Microscopy

Scanning tunneling microscopy (STM) is a technique capable of imaging surfaces at the atomic level and was invented by Gerd Binnig and Heinrich Rohrer in 1981, earning them the Nobel Prize in Physics in 1986 [82]. With use of coarse motors and piezoelectric transducers for fine movement, a sharp metallic tip is brought into close proximity with a surface, normally at only a few angstroms separation, allowing the

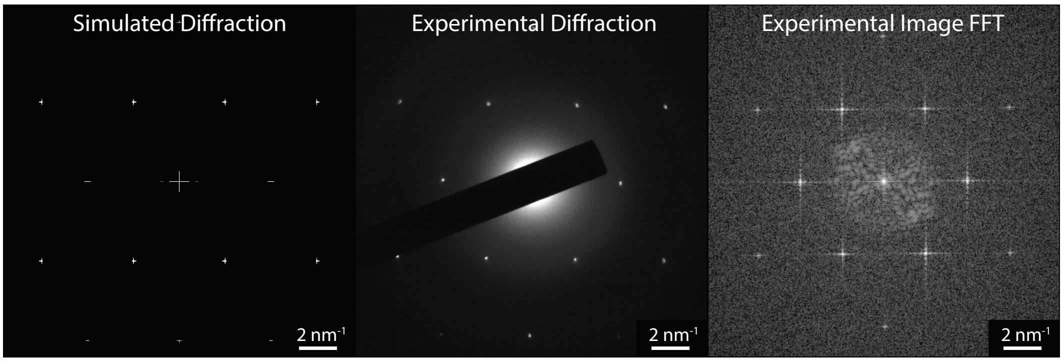

Figure 2.23: Comparison between multislice-simulated diffraction (left), experimental diffraction (centre), and experimental FFT (right) patterns for graphene.

overlap of tip and surface wavefunctions. Applying a voltage bias between the tip and surface results in electrons tunneling through the vacuum barrier between tip and surface, or surface and tip depending on the direction of voltage bias. This tunneling of electrons gives rise to a measurable tunneling current of the order $10^{-12} - 10^{-9}$A (pA - nA), which is used as an input signal for a feedback loop. This feedback loop acts to maintain a constant tunneling current as the tip is scanned across the surface. The feedback loop sends an output signal to the z-piezoelectric transducer, resulting in movement either away from or towards the surface by a certain amount, in order to maintain a constant current (the current set point). This process is repeated continuously as the tip is raster-scanned across the surface (figure 2.24).

The tunneling concepts exploited in STM imaging can be described using elementary theories of electron tunneling through a one-dimensional potential barrier. A particle of mass m, with energy E, experiencing a potential $U(z)$ must satisfy the time-independent Schrödinger equation:

$$-\frac{\hbar^2}{2m}\frac{d^2}{dz^2}\psi(z) + U(z)\psi(z) = E\psi(z) \tag{2.53}$$

at a position z. The STM environment can be simplified to the one-dimensional model shown in figure 2.25, with a sample wavefunction ψ^s, tip wavefunction ψ^t, and with a potential barrier of height $U > E$ modeling the vacuum barrier.

As the square modulus of the wavefunction $|\psi(z)|^2$ represents the probability density of the particle, it must be everywhere finite. The wavefunction $\psi(z)$ must therefore also be everywhere finite, along with E and $U(z)$. In order to satisfy Equation 2.53, $d^2\psi(z)/dz^2$ must also be finite. Therefore, using the condition that both $\psi(z)$ and $d^2\psi(z)/dz^2$ must be everywhere continuous functions of z, regardless

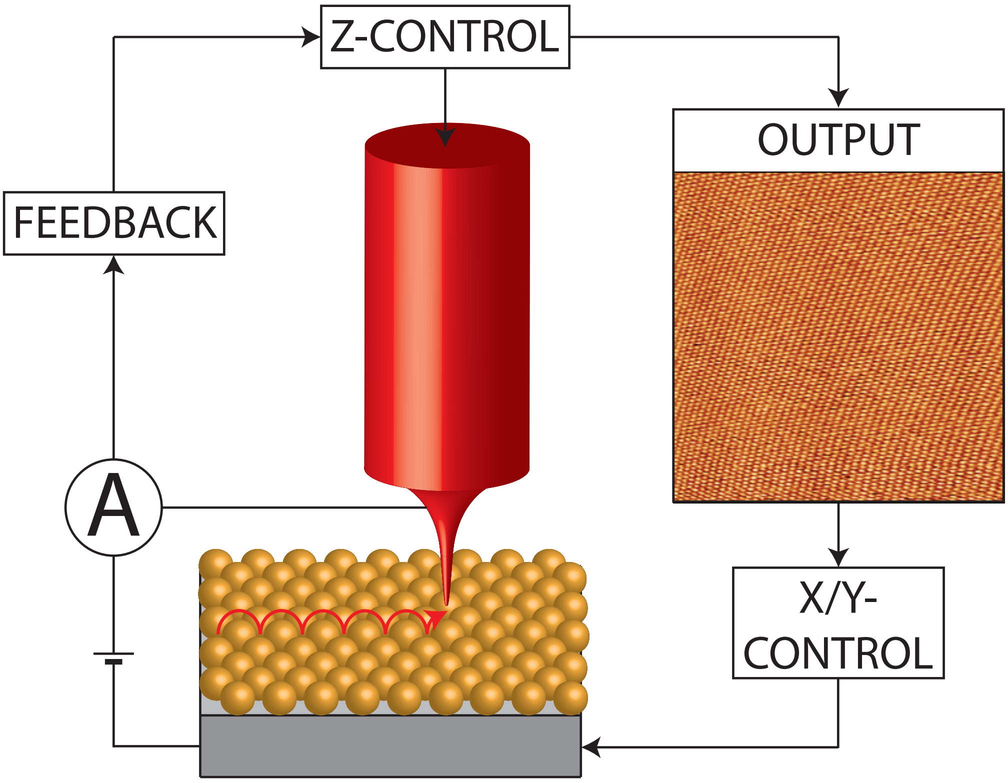

Figure 2.24: Scanning Tunneling Microscope layout. A feedback loop is used to maintain a constant tunneling current between tip and sample. Any change in tunneling current triggers a change in z position as the tip is raster-scanned across the sample surface. The resulting map of z-positions is output to the console.

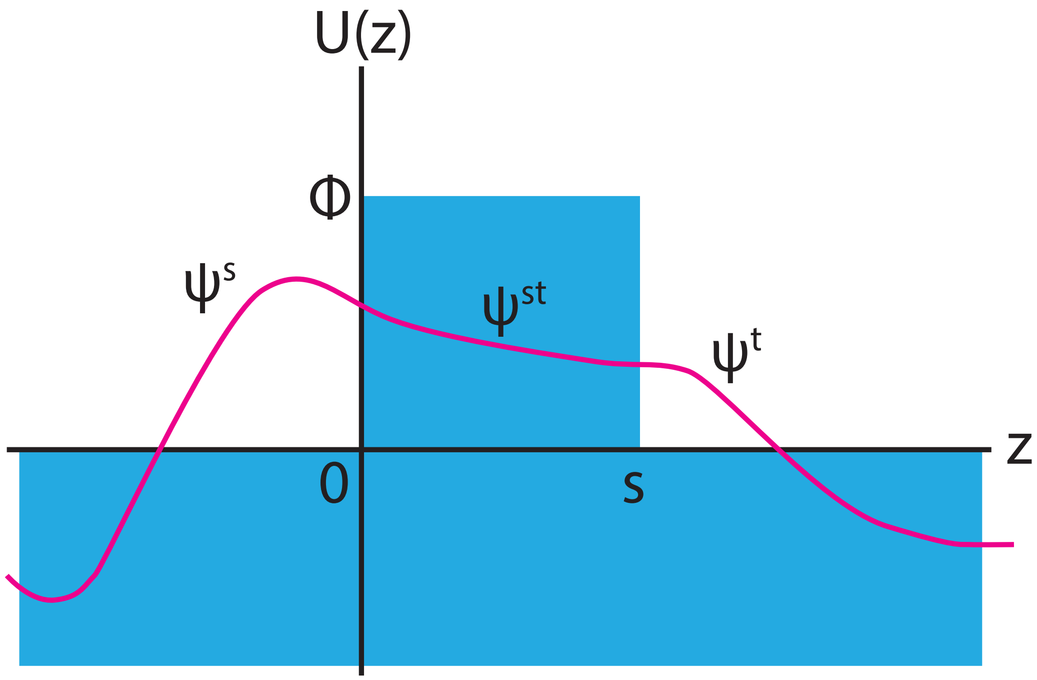

Figure 2.25: One-dimensional tunnel junction. The sample-tip separation is s, and the wavefunctions ψ^s, ψ^{st}, and ψ^t represent the sample, barrier, and tip wavefunctions respectively.

of discontinuities in $U(z)$, Equation 2.53 may be solved:

$$\psi(z) = \begin{cases} e^{ik_1 z} + re^{-ik_1 z}, & z < 0 \\ Ae^{ik_2 z} + Be^{-ik_2 z}, & 0 < z < s \\ te^{ik_1 z}, & z > s \end{cases} \tag{2.54}$$

where $k_1 = \sqrt{\frac{2mE}{\hbar^2}}$ and $k_2 = \sqrt{\frac{2m(E-U(0))}{\hbar^2}}$. Here, r denotes the reflected amplitude of the incident wavefunction and t denotes the amplitude of the transmitted wavefunction. The coefficients r, t, A, and B may be obtained by matching the wavefunctions and their derivatives $d\psi(z)/dz$ at the two interfaces between sample-barrier and barrier-tip due to their continuous nature:

$$t = \frac{2k_1 k_2 e^{-ik_1 s}}{2k_1 k_2 \cos(k_2 s) - i(k_1^2 + k_2^2)\sin(k_2 s)} \tag{2.55}$$

The transmitted wavefunction coefficient t is of interest as this relates directly to the probability of a particle tunneling through the potential barrier. The transmittivity T gives the transmission probability of tunneling through a finite barrier:

$$T = |t|^2 = \frac{1}{1 + \frac{1}{4}\left(\frac{k_1}{\kappa_2} - \frac{\kappa_2}{k_1}\right)^2 \sinh^2(\kappa_2 s)} \tag{2.56}$$

where $k_2 = i\kappa_2$ is pure imaginary. For $\kappa_2 s \gg 1$ (the weak tunneling limit, appropriate for a strongly attenuating barrier), the transmittivity becomes:

$$T \simeq \frac{16k_1^2\kappa_2^2}{(k_1^2 + \kappa_2^2)^2} e^{-2\kappa_2 s} \tag{2.57}$$

Although basic, this simple model provides insights into how the important features of metal-vacuum-metal tunneling can be explained. The decay constant magnitude can be evaluated using the work function Φ (the minimum energy required to remove an electron from bulk to vacuum level) primarily if the tunneling electrons lie close to the Fermi energy of sample and tip. For simplicity, the sample and tip work functions are assumed to be equal ($\Phi_s = \Phi_t = \Phi$), and the potential barrier height U is replaced by the work function Φ. For a gold surface/tip, with a work function of $\phi = 5$ eV, the transmittivity exponent becomes $-0.1821z$ Å^{-1}. Plotting the exponential decay factor for T in figure 2.26, it can be seen that an increase in barrier width of 1 Å results in a reduction in tunneling current by an order of magnitude. This rapid decay of tunneling current with small changes in tip-surface separation is what is responsible for the atomic resolution that may be achieved using STM.

There are several more extensive models in the literature, including the Tersoff-Hamann first-order approximation [83, 84], and the extended versions presented by Baratoff [85], Chen [86], and Green [87]. Importantly, these models show that constant tunneling current contours are in fact contours of constant local density of states (LDOS) at the Fermi level, rather than total charge density, and so $z(x, y)$ does not necessarily provide a faithful representation of the topography of the surface. However, in most cases $z(x, y)$ does provide a very close image of the surface topography at a scale where LDOS variations are small. In addition, the metal tip used in the microscope is assumed to terminate at a single atom, as shown in figure 2.27. It is therefore important to fabricate atomically sharp tips in order to facilitate high-quality STM imaging. For this work, PtIr tips (GoodFellow, product no. PT045120/19, Pt 80% Ir 20%) were mechanically cut to provide immediate atomic resolution (figure 2.27). For the work presented in this thesis, STM images were acquired by Zachary Laker using a Bruker Multimode STM with Nanonis controller.

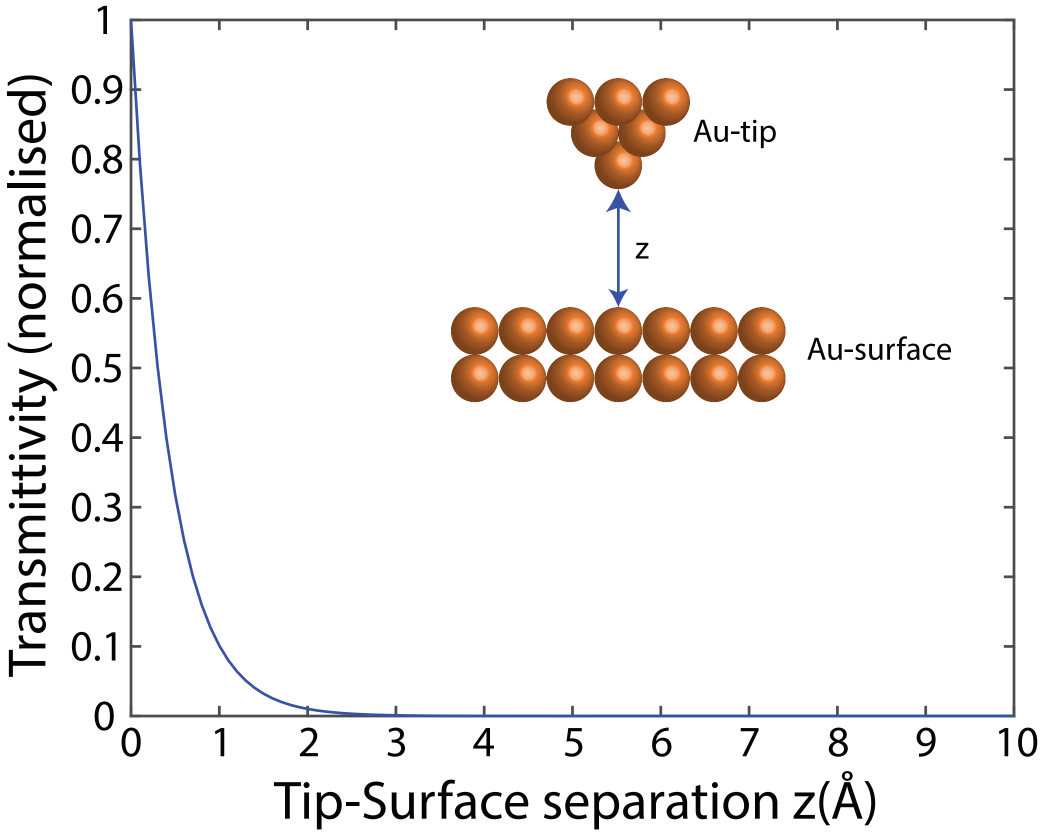

Figure 2.26: Normalised transmittivity T as a function of tip-surface separation z. The transmittivity T decays rapidly with separation, providing a means for atomic-resolution STM imaging.

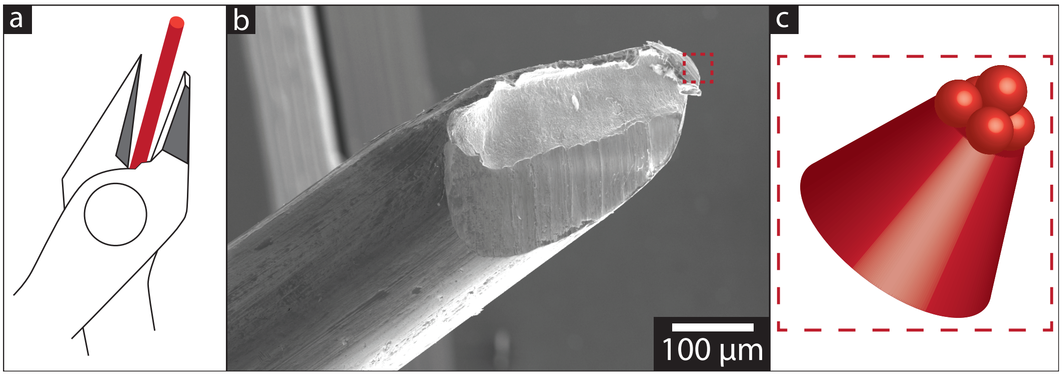

Figure 2.27: Mechanical cutting of PtIr wire (red) to produce sharp STM tips. a) Wire cutters are used to simply cut the wire into a sharp conducting tip. b) SEM image of prepared tip. c) Magnified cartoon of boxed region in a) showing the termination of the tip with a single atom.

Chapter 3

Graphene Membranes for Electron Microscopy

3.1 Introduction

Since the first published report on the isolation of a graphene monolayer in 2005 by Novoselov and Giem [9], there has been widespread fascination in developing novel graphene-based materials and technologies with enhanced properties. Progress is being made in realising graphene's potential in several fields, although some technologies such as graphene DNA sequencers and supercapacitors are still likely at least a decade away from being available commercially [12]. One area of technology that graphene has been applied successfully to is in the fabrication of TEM grid support membranes. Graphene's ultimate thinness, combined with the low atomic number of carbon, results in graphene films having very low contrast when imaged in a TEM [88]. In addition, the unchallenged strength of graphene allows it to lie across a TEM support window several microns in diameter without collapse (although this can be influenced by the presence of grain boundaries and defects in the graphene film, originating from the method of graphene synthesis) [89]. The third major benefit of graphene when used as a TEM support membrane derives from its incredible electrical and thermal conductivity [9].

In TEM, samples must be made conductive in order to prevent the build up of charge, which can influence the trajectories of electrons incident from the beam due to the high electrostatic fields generated (known as 'charging'), and can also degrade samples [65]. Even though graphene is only a monolayer thick, it can readily dissipate charge and heat when exposed to the electron beam. Traditionally, non-conductive samples would need to be coated in a thin layer of amorphous carbon in order to protect them during imaging, although this carbon film reduces image contrast, particularly for high-resolution imaging of low-mass atoms (high-mass atoms provide sufficient contrast to be visible against an amorphous carbon background). Combining graphene with insulating samples allows sample contrast to be preserved whilst still preventing charging effects [88, 90].

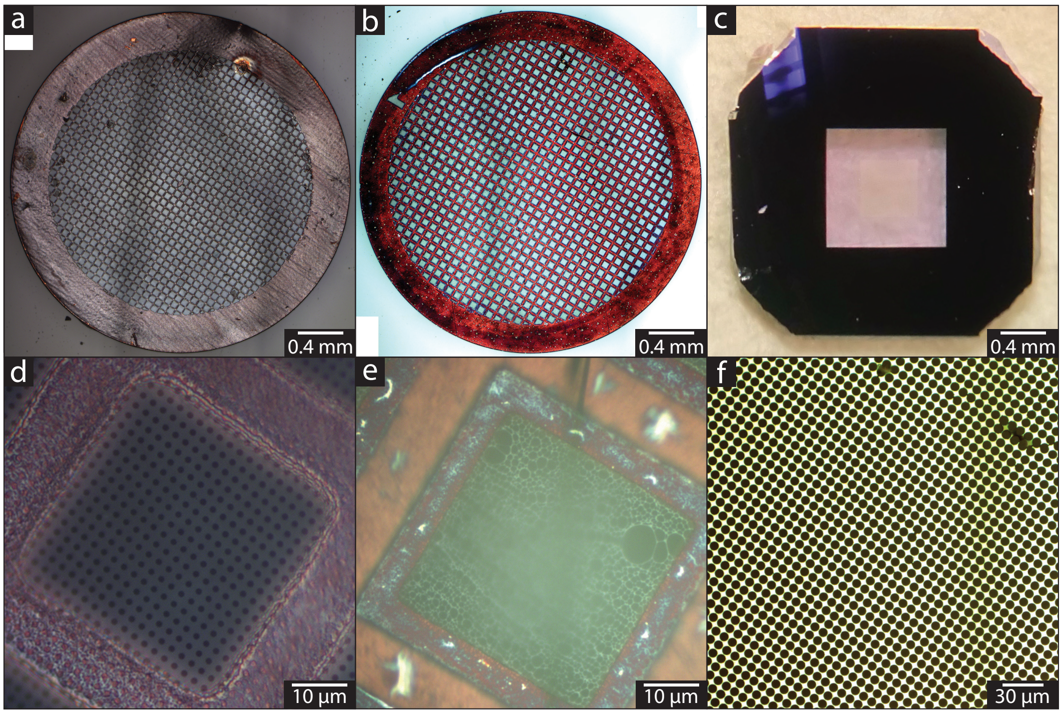

Figure 3.1: Optical images of different TEM grid supports. a,d) Quantifoil ® perforated amorphous carbon membrane. b,e) Holey amorphous carbon membrane. c,f) Silicon-Nitride perforated membrane.

The high conductivity and strength of graphene allows a range of different TEM support grids to be used. These include holey carbon, Quantifoil®, and perforated Si_3N_4 (silicon-nitride) grids, as illustrated in figure 3.1. Holey carbon grids consist of a thin mesh of amorphous carbon spanning a metal support grid, with a range of hole sizes averaging 100 nm - 5 μm in diameter.

The carbon mesh is conductive and can be subject to heating to approximately 400 °C. Quantifoil® grids consist of thin amorphous carbon film containing an array of perforated holes, with diameters 1 - 2 μm and a variable pitch of several μm. The thin perforated carbon film is conductive and can be subject to heating to approximately 400 °C. Finally, silicon-nitride grids consist of a 200 μm thick silicon oxide outer frame, with a 200 nm silicon-nitride membrane lying across the frame. The centre portion of the silicon-nitride membrane contains a perforated array of holes, with diameters 3, 6, and 9 μm, with a variable pitch of several μm. The silicon-nitride grids are not conductive under the electron beam, and can survive heating to over 1000 °C.

Although graphene is a useful support membrane, the process of transferring graphene to a TEM grid in an efficient, high-yield, and clean manner has proven difficult [12]. The problem stems from the fact that the key routes to synthesising graphene (CVD, mechanical and chemical exfoliation, and SiC sublimation) do not lend themselves to the easy transfer of graphene. This has led to widespread interest in the fabrication of graphene-oxide (GO) TEM grids, due to the easy preparation and deposition of GO onto a TEM grid support.

GO gained attention as a method of chemically exfoliating graphene from graphite in a process that could be scaled to industrial sizes [12]. The most widely used technique involves the oxidation of graphite in order to form graphite-oxide, which may then be dispersed into water [91]. In order to separate individual GO layers the dispersed graphite-oxide is exfoliated by stirring or sonicating, producing a colloidal suspension of GO, as shown in figure 3.2. The GO is then reduced in order to return to a graphene-like state, although current methods fail to reproduce a product with a similar pristine structure, conductivity, and strength to that of graphene [92].

However, GO has found widespread use in TEM studies [88, 93, 94]. Its colloidal nature facilitates easy deposition by placing a drop of the GO suspension onto a support grid and allowing it to dry in air, as shown in figure 3.2. This process may be carried out on large scales in an efficient and repeatable manner. The GO grids offer a low-contrast support that is hydrophilic and able to withstand moderate levels of electron dose without degradation [88]. For HRTEM uses, however, graphene is still the ideal substrate of choice due to its much higher conductivity and robustness to the electron beam [95].

In addition, the pristine structure of graphene offers a better understood surface for the deposition of molecular systems [1, 6, 43, 96]. Graphene has been utilised for the deposition and study of molecular self-assemblies [1, 6], individual nanoclusters [2, 7, 97], and individual molecules [96, 98, 99].

CVD has become the most popular method for cheap, high-quality, and large-area graphene production, with the end product being a sheet of monolayer graphene grown on a transition metal foil, commonly either copper or nickel [12, 100, 101]. In order to transfer graphene from the transition metal catalyst on which it was grown, however, it must be coated in a thin layer of polymer before the metal is dissolved using acid. The polymer acts to support the graphene whilst the metal

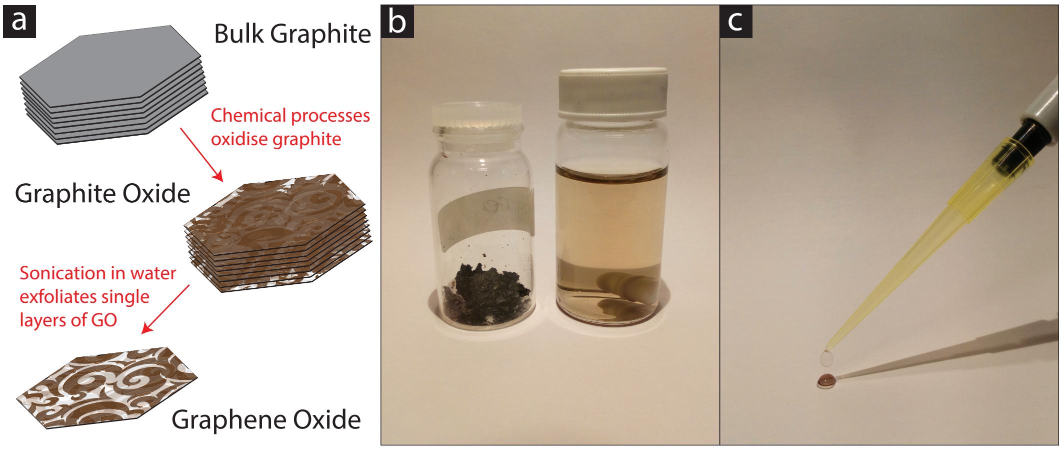

Figure 3.2: Graphene-oxide (GO) TEM grid fabrication. a) GO sheets are isolated in solution through sonicating graphite-oxide in water. b) Graphite-oxide (left) and GO emulsion (right). c) GO TEM grid fabricated by drop-casting GO emulsion droplets onto a TEM support grid.

is removed, to prevent it from breaking, and is removed once the graphene has been transferred to the TEM support.

The act of removing the polymer is itself complex, involving solvent washes, drying using a critical point dryer (CPD), and several heat treatments. This polymer removal process does not lend itself to the production of large batches of grids, and has an associated low yield ($\approx 50\%$). The low yield results from the fact that the polymer coating must be made thin enough to allow its easy removal with solvents and heat treatment, but not so thin as to become too weak to support the graphene. It is common for polymer-coated graphene films to break apart during the initial metal-removal steps as a result of the polymer coating being too thin.

In addition to studying pristine graphene membranes, there is interest in modifying graphene's surface functionality in a controllable manner; graphene's simple and robust structure presents difficulties in the selective adsorption of biomaterials [102, 103], making sensors based on pristine graphene unselective in their response, and leads to compatibility issues for aqueous processing routes. This necessitates chemical modification which should be done in such a way so as to retain the beneficial physical properties of graphene and in as thin a modified layer as possible so as to maximise the contribution of graphene to the hybrid material. Even low-level covalent functionalisation rapidly degrades the electronic properties of graphene [104–106], so non-covalent functionalisation which retains the $-sp^2$ graphene structure is preferred.

In order to measure the effect of a functionalisation method on the mechan-

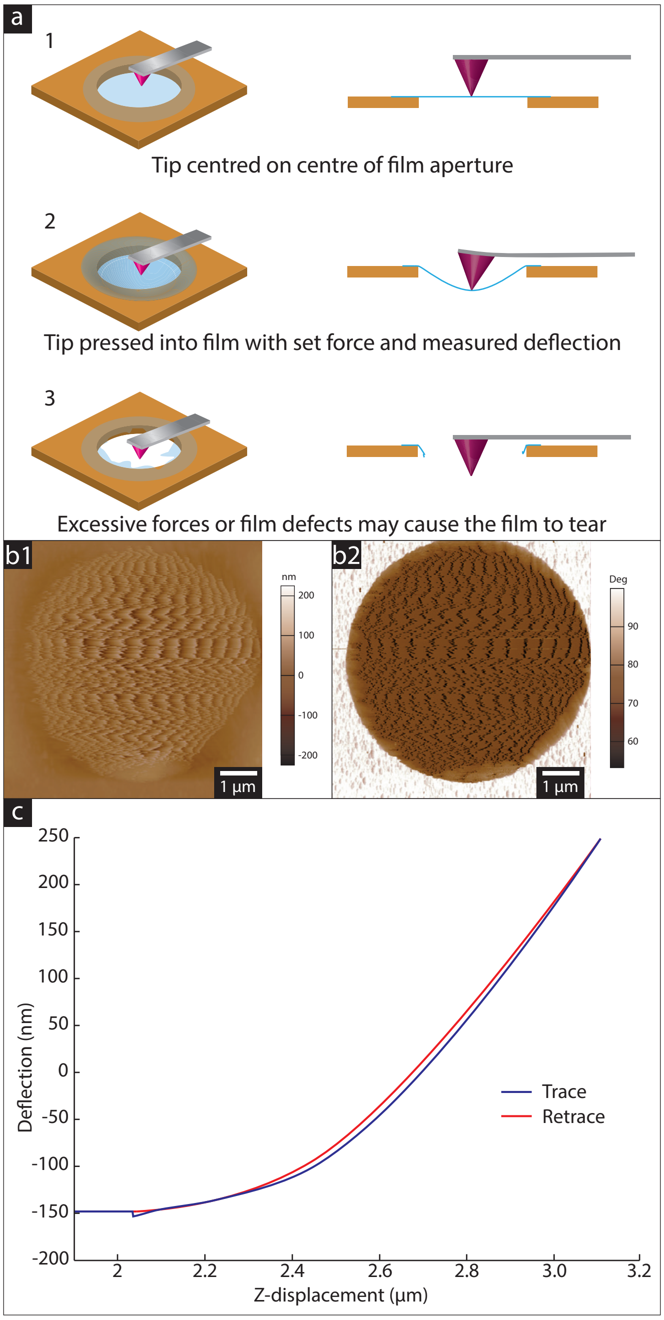

Figure 3.3: AFM Nano-indentation procedures. a) 1. Tip is positioned at centre of film aperture. 2. Tip is depressed into film up to a specified force, with the tip deflection measured. 3. The tip either breaks through the film, or returns to its initial z-position if the film is strong enough to withstand the applied force. b1,b2) Height and phase maps from tapping-mode images of a graphene film suspended over a circular aperture. c) Force response curve for the suspended film imaged in b), with the trace and retrace curves showing elastic response.

ical strength of graphene, AFM nano-indentation can be used. This involves the measurement of the Young's modulus from the deflection of an AFM cantilever as it is extended against a freestanding region of graphene. Specifically, the freestanding region must lie across a circular aperture of diameter a. The force-displacement relation for a suspended 2D film is given by:

$$F = \sigma_0^{2D}\left(\pi a\right)\left(\frac{\delta}{a}\right) + E^{2D}\left(q^3 a\right)\left(\frac{\delta}{a}\right)^3 \tag{3.1}$$

where F is the applied force, δ is the deflection at the centre point, E^{2D} is the 2D Young's modulus of the film, σ_0^{2D} is the pretension in the film, ν is Poisson's ratio (0.165 for graphite in the basal plane), and $q = 1/(1.05 - 0.15\nu - 0.16\nu^2) = 1.02$ is a dimensionless constant [89]. This may be rearranged to give E^{2D}:

$$E^{2D} = \frac{\left(F - \sigma_0^{2D}\left(\pi a\right)\left(\frac{\delta}{a}\right)\right)}{\left(q^3 a\right)\left(\frac{\delta}{a}\right)^3} \tag{3.2}$$

Thus, with knowledge of the aperture diameter a, applied force F, and measurement of the deflection δ at this force, E^{2D} may be calculated. Figure 3.3 illustrates the process of AFM nano-indentation, as well as an example deflection curve for graphene showing elastic behaviour under force loading. In order to compare to bulk materials, the 2D Young's modulus is divided by the interlayer spacing of the material (h =0.335 nm for graphite) [89]:

$$E = \frac{E^{2D}}{h} \tag{3.3}$$

3.2 Chapter Outline

This chapter describes refined graphene TEM grid fabrication processes as well as methods to produce double-layer graphene membranes. In addition, methods to encapsulate samples within two monolayers of graphene are outlined, which are utilised in the following chapter.

A new approach to fabricating monolayer graphene TEM grids is presented, which provides a fabrication route with much higher throughput and yield than the standard method. This involves coating CVD graphene with a perforated polymer film that is used to support the graphene when the metal support is removed. The simple method produces graphene with equivalent cleanliness and pristine areas as the standard method.

Finally, two methods to funtionalise graphene without detrimentally affecting its mechanical properties are introduced. The first method involves gas-phase thermochemical functionalisation, and relies on the functionalisation of pre-existing defects in the graphene film. No further defects are induced in the film, preventing any additional mechanical deterioration, as shown by AFM measurements. A non-covalent functionalisation method is also described, involving the deposition of a self-assembled monolayer of pyrene molecules with associated positive or negative charge. The pyrene molecules make the graphene surface hydrophilic, and induce either a net positive or negative charge to the surface. The charged nature of the surface is exploited through the electrostatic attachment of positively and negatively charged nanoparticles.

3.3 Results and Discussion

3.3.1 High-quality single-layer graphene membranes

In order to study graphene using TEM it is necessary to transfer it from the copper foil growth substrate to an appropriate TEM support. This process is carried out using a number of steps, with a central focus on achieving the highest levels of cleanliness possible (least contamination). A step-by-step schematic of the transfer process is shown in figure 3.4. Firstly, the CVD-grown graphene must be coated by a uniform thin film of polymer. The polymer film prevents the graphene from collapsing or tearing once the copper substrate has been dissolved, and is removed at a later stage. The polymer support is spin-coated (0.1 s ramp, 3000 rpm, 45 s dwell) using a solution of 0.1 mg ml^{-1} poly(bisphenol A carbonate) dissolved in chloroform.

Next, the copper foil is dissolved, using an aqueous solution of 20 mg ml^{-1} ammonium persulfate. The foil is first placed onto an etching solution for 2 hours, before it is removed, rinsed with DI water, and dried. It is then floated onto a fresh solution of etchant and left for 8 hours, allowing the copper foil to completely dissolve. Using an initial partial etch allows the graphene film grown on the underside of the foil to be removed. Using a glass slide, the polymer/graphene film is transferred to a petri dish of DI water and left for 30 minutes. This removes etchant/copper residues from the graphene; the process is repeated 3 more times (for a total of 4 DI water washes).

With the polymer/graphene film floating on the surface of DI water, an appropriate TEM support is used to scoop and lift out the film. This is left to dry for 8 hours, in order to ensure complete adhesion of the graphene to the support without the presence of water pockets.

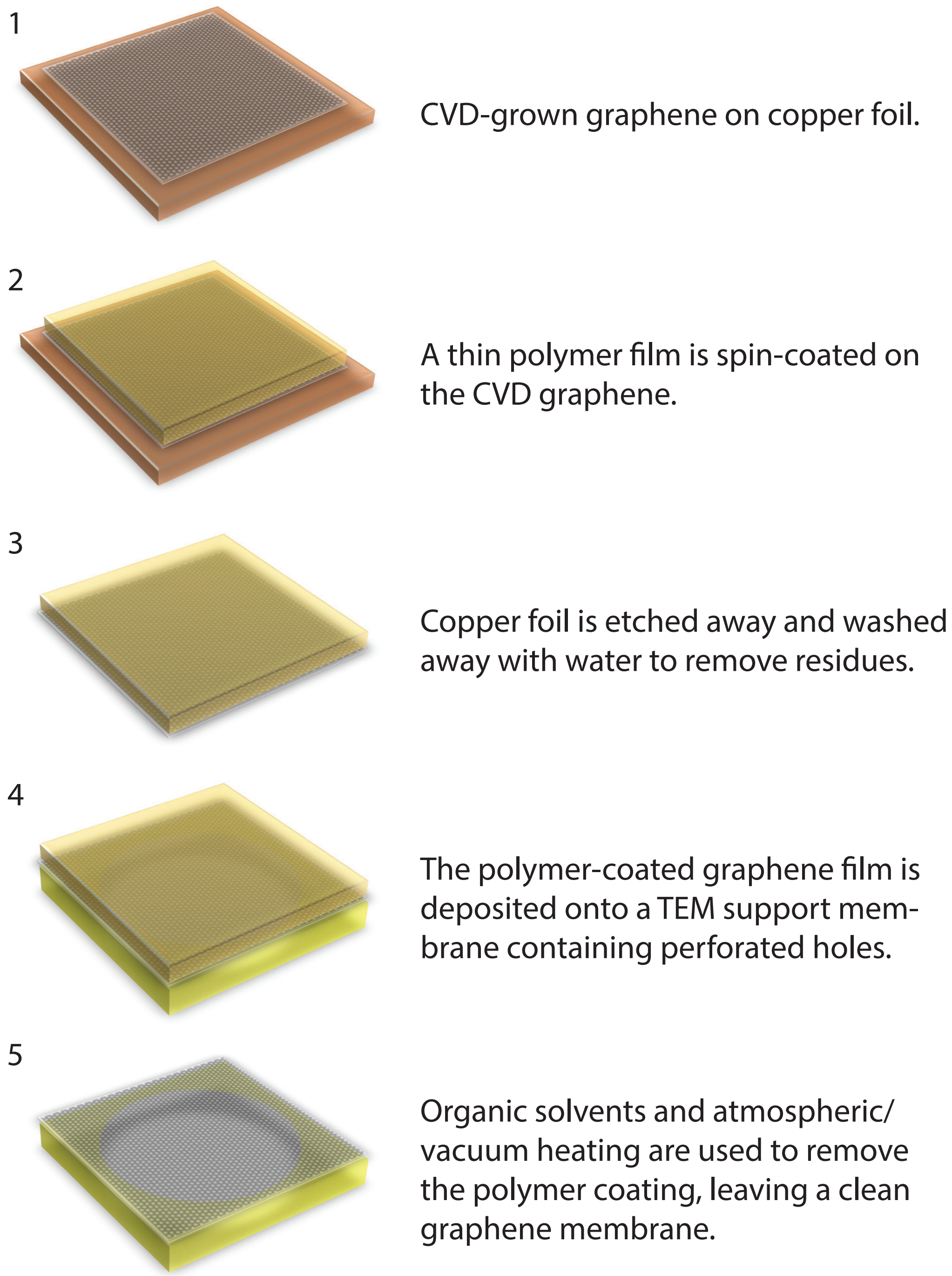

Figure 3.4: Fabrication steps for transferring CVD-grown graphene onto a TEM support grid in a clean manner.

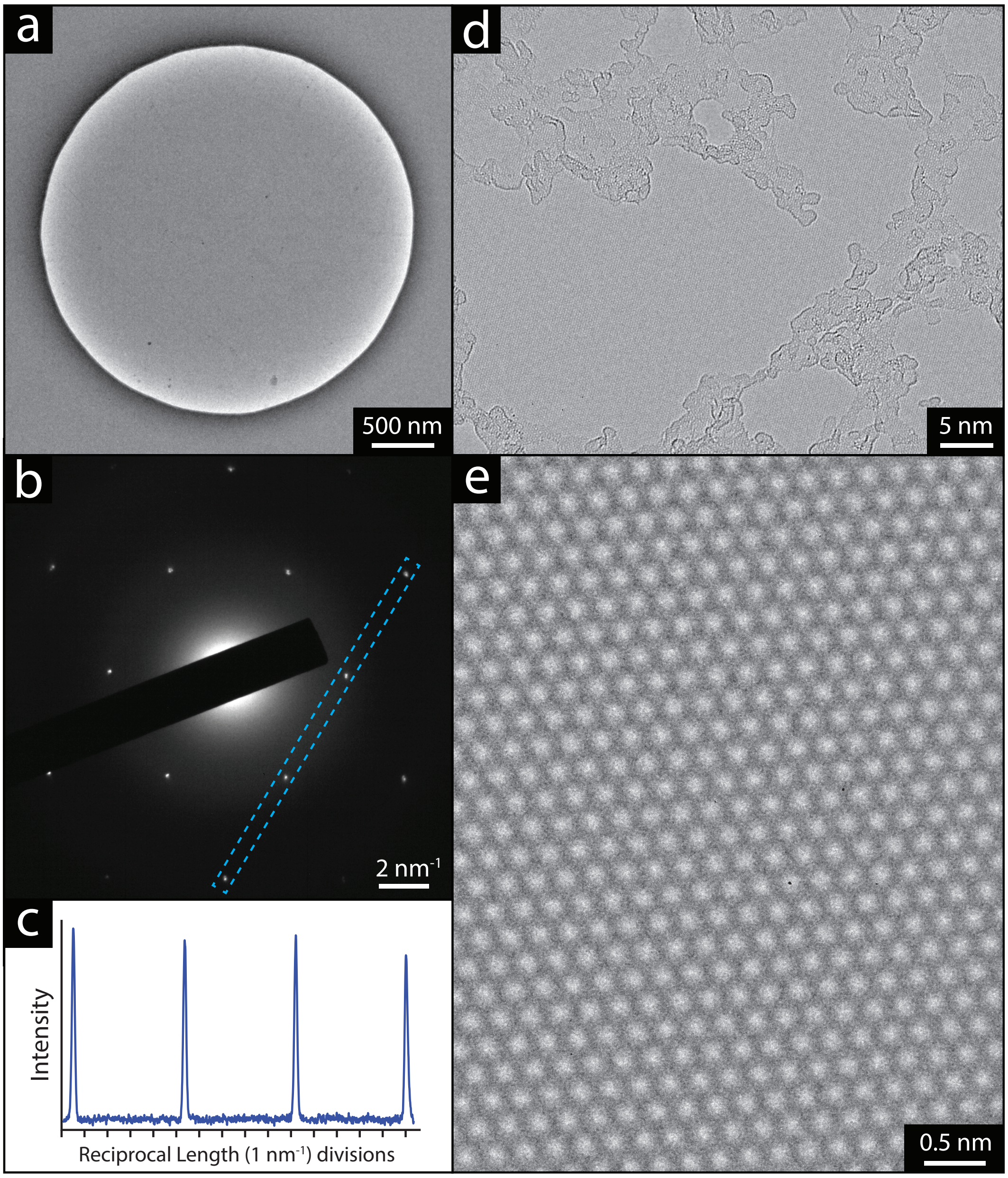

Figure 3.5: Graphene TEM membrane summary. a) TEM image of monolayer graphene suspended over 3 μm diameter hole in silicon-nitride support grid. b) SAED pattern taken from the hole imaged in a), showing a single-crystal graphene lattice. c) Profile taken from the SAED pattern in b), verifying the presence of monolayer graphene due to the relative intensity of inner and outer reflections. d) TEM image showing remaining contamination after thorough cleaning. e) TEM image showing at atomic-resolution the pristine graphene lattice.

With the film now sitting on a TEM support, the polymer coating is no longer necessary to provide structural integrity to the graphene membrane. It is therefore removed using a combination of organic solvents and heating. Three successive 15 minute washes in chloroform are used to dissolve the majority of the polymer. However, due to the rapid evaporation of the solvent, any freestanding regions of graphene will tear/collapse under drying as a result of the surface tension [43]. To circumvent this, a critical point dryer (CPD) is used, whereby drying can occur around the critical point of a solution such that no surface tension is induced on the graphene. Liquid CO_2 is used due to its practically achievable critical point (37 °C and 1072 psi) [107]. With the grid dried, a combination of 2 hour heating at 200 °C on a hot plate, and 4 hours heating at either 800 °C for SiN grids, or 400 °C for other grids, under vacuum (1 bar) with a hydrogen/argon gas mixture flow, removes any major remaining contamination.

These steps allow graphene to be transferred in a clean enough manner to produce pristine regions ≈ 20 nm in width, as shown in figure 3.5, which are sufficient for HRTEM studies. In addition, the average grain size of the graphene film is ≈ 20 μm, which is sufficient to provide single crystal graphene coverage over the majority of the 3 μm diameter apertures present in the TEM support. This is revealed by SAED as shown in figure 3.5. In order to verify that this is indeed monolayer graphene and not multilayer, the relative intensity of outer (10) and inner (01) reflections can be compared, as shown by figure 3.5 c. The ratio (10)/(01) ≈ 1, confirming the presence of monolayer graphene [93].

3.3.2 Double layer graphene membranes

For certain experiments (see chapter 6) it was necessary to create a double layer graphene membrane consisting of two graphene monolayers oriented randomly with respect to each other. In order to achieve this, the above fabrication process was modified. In figure 3.4, steps 1 - 3 are followed normally, but instead of scooping and drying the polymer/graphene film onto a TEM support, a new CVD graphene foil is used. This results in the following film structure: polymer/graphene/graphene/copper foil. The standard fabrication process is then followed from steps 3 - 5 as normal, with the final membrane consisting of two randomly oriented graphene monolayers suspended across the TEM support. Figure 3.6 shows a SAED pattern with two sets of graphene reflections, along with a HRTEM image and corresponding FFT, again demonstrating the presence of two graphene monolayers.

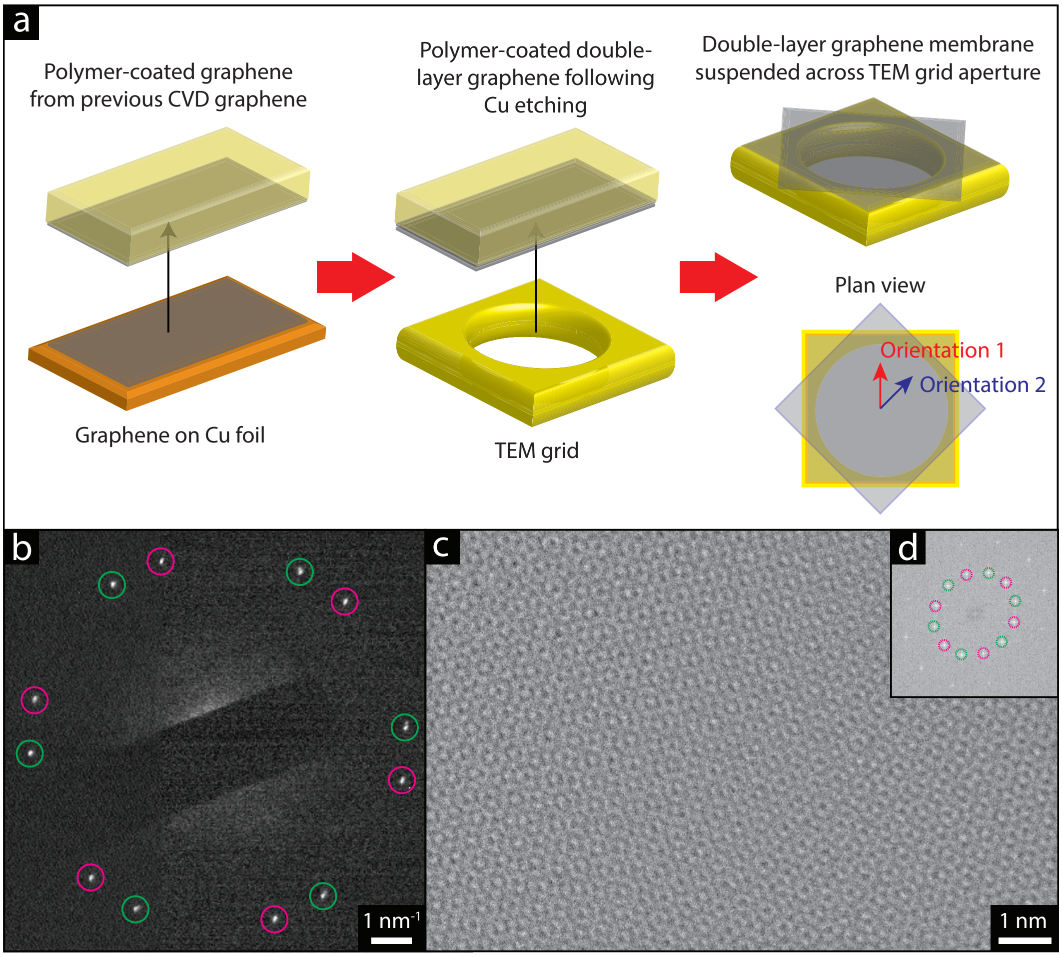

Figure 3.6: Double-layer graphene membranes summary. a) Summary of double-layer membrane fabrication. A pre-made polymer-coated graphene membrane is scooped onto a new CVD foil. The copper foil is dissolved and the polymer-coated double-layer graphene membrane is scooped onto a TEM grid. The polymer is then removed to leave a membrane consisting of two rotationally-mismatched layers of graphene. b) Example SAED pattern of double-layer graphene membrane, revealing two distinct sets of graphene reflections. c) HRTEM image of a double-layer graphene membrane, revealing two superimposed graphene lattices as shown in the FFT. d) The FFT reveals two distinct graphene lattices, as well as the presence of minor image astigmatism.

3.3.3 Graphene-encapsulated films

It is necessary in some instances (see chapter 4) to encapsulate samples such as molecular films and nanoparticles between two monolayers of graphene. This presents some unique challenges in achieving cleanliness due to the organic nature of the samples encapsulated and their response to heating.

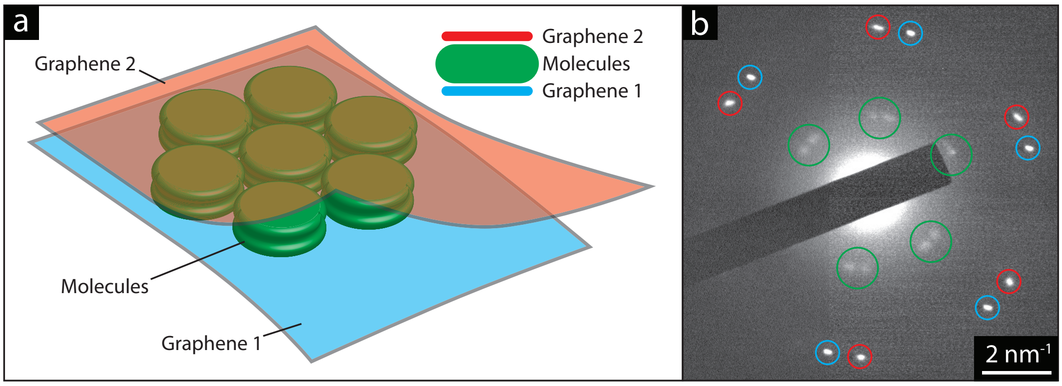

Figure 3.7: Graphene-encapsulated films summary. a) Schematic of the sample created by depositing molecules on graphene and then coating in another layer of graphene. b) Example SAED pattern of graphene-encapsulated pyrene assembly, revealing two distinct sets of graphene reflections as well as the inner molecular reflections.

Standard high quality single-layer graphene TEM grids are initially fabricated using the procedures already outlined. Once sufficiently cleaned, the molecular system of choice is deposited onto the graphene. A fresh CVD graphene sample is prepared up to step 3 in figure 3.4, and instead of being scooped onto a new TEM support, it is scooped onto the pre-prepared molecule/graphene coated membrane. The structure of the film is then: polymer/graphene/molecule/graphene/support grid. The standard cleaning and hot-plate heating procedures are then followed in order to remove the polymer coating, leaving a clean film consisting of two graphene monolayers encapsulating the molecular system of choice. The use of heating to 200°C in air does however limit the types of organic systems that can be encapsulated. An illustration of the final graphene-encapsulated system, along with an example SAED pattern for graphene-encapsulated pyrene, is presented in figure 3.7. Pyrene assemblies and pyrene-functionalised graphene are discussed in more detail in section 3.3.5.

3.3.4 Holey-formvar graphene membranes

Although graphene TEM grids can be successfully fabricated with high levels of cleanliness, as described in section 3.3.1, this requires the use of specialist critical point drying (CPD) equipment, and is a very low-yield process (≈ 25 % success). In addition, the fabrication process does not lend itself to high volume throughput. Here, a new high-yield, high-volume method of creating clean graphene TEM grids is described.

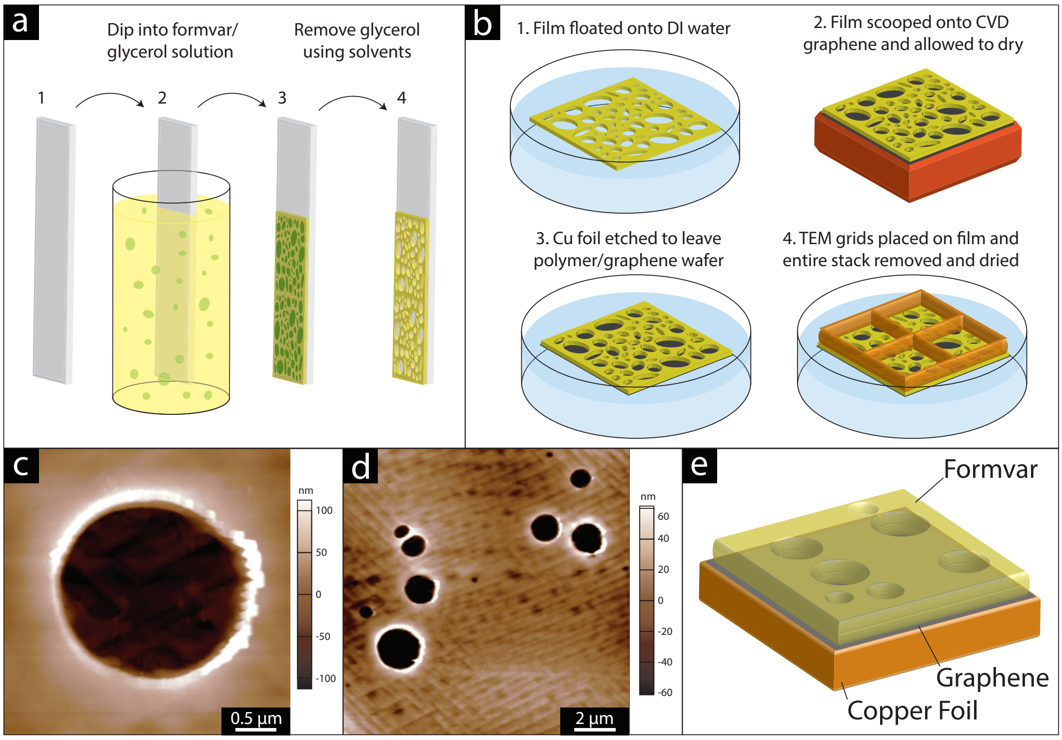

Figure 3.8: Fabrication steps of holey-formvar graphene membranes. a) Steps to produce a holey-formvar film on glass slide. b) Steps to coat CVD graphene in holey-formvar film and transfer to TEM grid support. c), d) Tapping-mode AFM images of CVD graphene once coated in the holey-formvar film showing the individual holes. e) Schematic of the sample imaged in c), d).

To begin with, a glass slide is coated in a thin film consisting of formvar with small glycerol droplets dispersed throughout, as described by Baumeister and Seredynski [108]. The formvar/glycerol film is deposited by dipping the glass slide in a colloidal suspension consisting of formvar solution (100 mL chloroform and 0.35 g formvar powder) and 50 μL glycerol. The dipping process involves a 1 s immersion in the suspension before allowing the film to dry. Once dry, the film is then placed above a steam bath for 20 s, before drying again. The slide is then immersed in acetone for 20 s, and is dried for a final time. The film is removed from the glass slide by scoring the edge of the film and then immersing the slide in distilled water. The entire film may be floated off as a whole, and then ‘scooped’ onto a piece of graphene-coated copper foil. This results in a perforated formvar film of thickness 40 nm coating the CVD graphene, with many small holes of average diameter 1 μm, as shown in figure 3.8.

In order to remove the copper foil, the same etching steps described in 3.3.1

are used. With the holey formvar/graphene film floating on the surface of DI water, standard copper grids may be placed onto the film surface, and the entire film then lifted from the water using a wire mesh and left to dry, as shown in figure 3.8. The grids may be removed with ease from the dried film, producing a large quantity of high-quality graphene TEM grids with low failure rates.

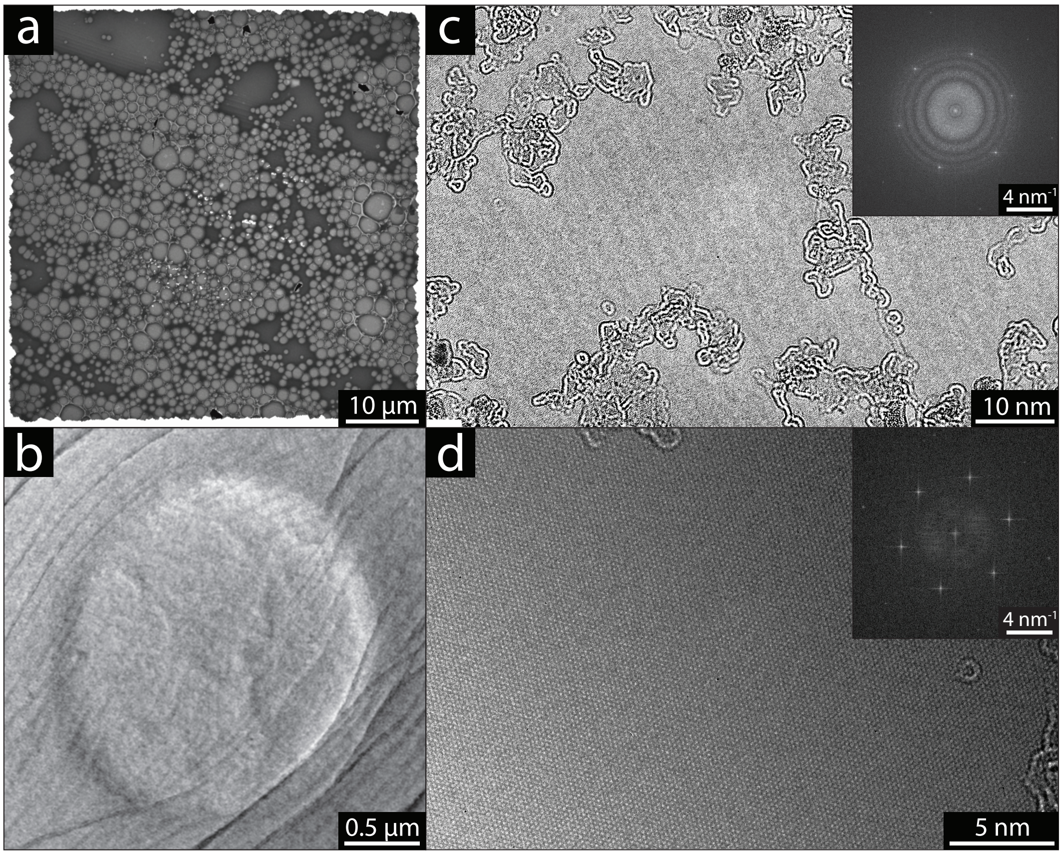

Figure 3.9: Electron Microscopy of holey-formvar graphene membranes. a) SEM image of TEM grid showing distribution of holes. b) TEM image of individual hole. c) HRTEM image of suspended graphene revealing standard contamination residues. d) HRTEM image of suspended graphene revealing pristine lattice regions.

The holey film acts as a supporting exoskeleton to prevent the graphene from collapsing whilst suspended across the TEM grid, and also provides areas of the film where pristine graphene can be found that has not been contaminated at all during the transfer. A summary of electron microscope images of the final grids is presented in figure 3.9. Low-magnification SEM reveals the average size and distribution of the holes, whilst HRTEM shows the freestanding graphene areas to be as clean as that produced via the previously outlined method (Section 3.3.1). These holey areas are therefore ideal for study to the user.

3.3.5 Functionalised graphene membranes

Non-covalent modification: Pyrene coatings

When functionalising graphene, there are two strategies available: covalent and non-covalent functionalisation. Covalent functionalisation of graphene involves covalently bonding specific functional groups to the graphene lattice and can degrade its electronic and mechanical properties [104–106]. Non-covalent functionalisation involves adsorbing specific molecules to the graphene lattice through non-covalent mechanisms such as van der Waals interactions, allowing the graphene to retain its electrical and mechanical properties.

Molecules with planar-delocalised π systems are often chosen for non-covalent functionalisation of graphene [106], as these can interact with the extended electronic system of the graphene surface by van der Waals or electrostatic interactions, commonly referred to as π stacking [109]. To this end, layers of small molecules on graphene, such as perylenebisimides [110–112], phthalocyanines [1, 113] or pyrenes (pyr) [114–117], have been investigated. Pyr derivatives are particularly interesting as their chemical versatility has been widely exploited to create carbon-based hybrid materials through π stacking [98, 118–120], and to assist the exfoliation of graphite to graphene [98, 121]. Hence, they provide an easy and flexible route to modifying the surface properties of graphene.

In a collaboration with Dr Jon Rourke and Dr Concha Bosch-Navarro, whom synthesized the materials, pyrene derivatives were designed that would non-covalently bind to the graphene surface, but would remain non-reactive [2]. Non-coordinating charged moieties were attached via a flexible linker to a pyrene core, as shown in figure 3.10. The pyr-carrying ammonium cation (trimethyl-(2-oxo-2-pyren-1-yl-ethyl)-ammonium bromide; pyr^{+}) and pyr-carrying sulfonate anion (sodium (2-oxo-2-pyren-1-yl-ethyl)-sulfonate; pyr^{-}) were synthesized [2]. During deposition from solution, the hydrophobic π-conjugated pyrene core should bind strongly to the graphene surface by π stacking, whilst electrostatic repulsion between the charged moieties should self-limit the film to monolayer coverage. The charged molecular layer turns the graphene from hydrophobic to hydrophilic and enables controlled macro-molecule adsorption through electrostatic interactions [2].

As shown in figure 3.11a, diffraction analysis of the pyr modified graphene membranes showed the characteristic hexagonal diffraction pattern of graphene, but also an inner hexagon of diffraction spots, aligned to those of graphene, with a cor-

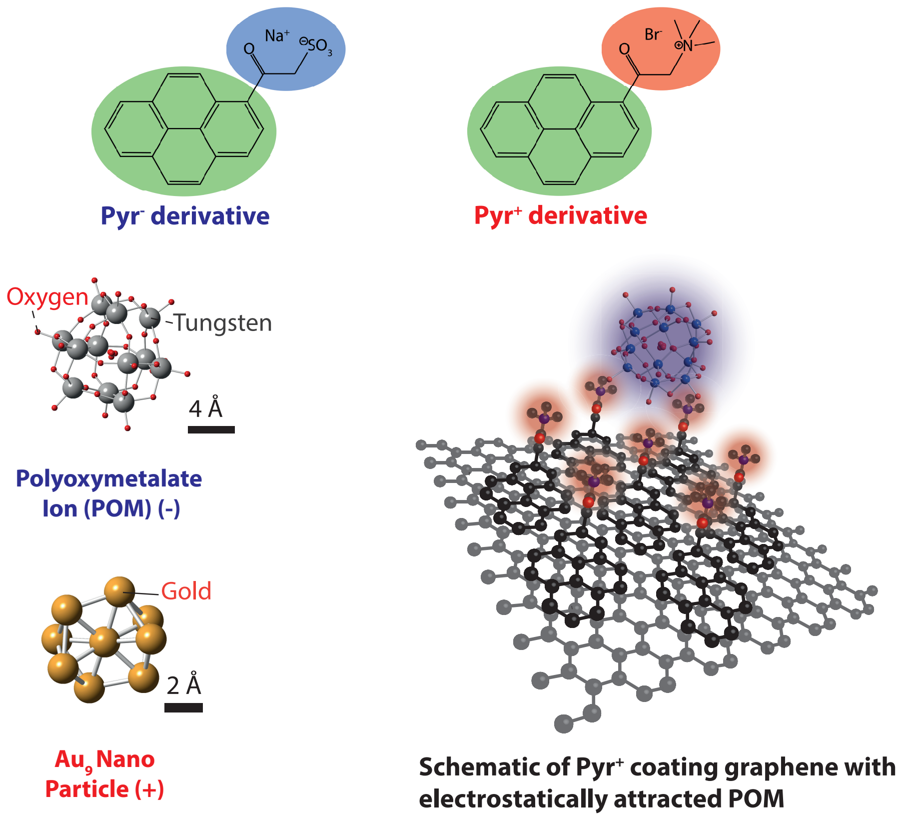

Figure 3.10: Pyrene$^{\pm}$ molecule and charged nanoparticle illustrations

responding lattice parameter of 0.28 ± 0.01 nm, similar to previously reported for a pyrene derivative on graphene [118]. These inner spots decayed rapidly with exposure to the electron beam, figure 3.11b, with a characteristic dose of $10\ \mathrm{e}^{-}\text{Å}^{-2}s^{-1}$, as to be expected for a molecular overlayer with only weak, non-covalent, intermolecular bonds. Further details on the measurement of characteristic dose are outlined in chapter 4. The diffraction thus shows the presence of the pyrene and indicates that it is forming an ordered layer.

Due to the low characteristic dose of the pyrene derivatives, HRTEM imaging of the molecular overlayer is not viable. However, the presence of the pyr overlayer can be inferred from the selective adsorption of anionic clusters on pyr^{+}, and cationic on pyr^{-}, modified graphene, as verified by HRTEM. For the anionic and cationic clusters, two oppositely charged inorganic clusters of defined atomic structure were chosen. Each is readily identified by HRTEM: the anionic polyoxometalate (POM) phosphotungstic acid $[W_{12}O_{40}P]^{3-}$, and the cationic nanocluster $[Au_9(PPh_3)_9]^{+}$

(abbreviated henceforth as Au_9). Both have been studied by TEM before [7, 97], both are of interest in their own right for applications such as catalysis, but most importantly here, both can be positively identified by HRTEM due to their distinctive atomic geometries (see figure 3.10).

Graphene TEM grids were functionalised by immersion overnight in solutions of $pyr^{\pm}$ dissolved in ethanol for pyr^{+} and methanol for pyr^{-}. The $pyr^{\pm}$-graphene TEM grids were incubated for 3 min in a solution containing either the POM (0.1 mg/mL) or Au_9 (1 mg/mL), dried and then analysed by HRTEM. The pyr^{+} modified graphene showed a strong affinity for the negatively charged POM with average coverage measured to be (500 ± 10) molecules μm^{-2} , identified by their signature atomic arrangement (figure 3.11d). By contrast, no POM was observed on pyr^{-} - or un-modified graphene [2]. Consistent with its cationic nature, the pyr^{-} modified graphene showed a strong affinity for the Au_9 with average coverage measured to be (100 ± 10) molecules μm^{-2} (figure 3.11c). Measurements of molecule coverage was carried out by analysing HRTEM images and identifying the number of molecules present in the image area. In addition, the presence of Au and W was identified via energy-dispersive X-ray analysis of the respective samples. By contrast, no Au_9 is observed on pyr^{+} - or unmodified graphene [2]. Coupling together these HRTEM studies as well as additional AFM measurements [2], this clearly demonstrates how control over the electrostatic interactions enables control over the adsorption of a variety of macro-molecules. As a result, these pyr-derivatives are expected to be widely effective for surface modification of graphene based materials.

Covalent modification: Gas-phase thermochemical functionalisation

Although covalent functionalisation of graphene can degrade its electronic and mechanical properties [104–106], it is still possible to maintain its unique qualities using certain covalent functionalisation methods. This can be achieved through the thermal decomposition of pre-existing defect groups to generate surface radicals which are then able to graft several different reagents. Additional damage to the graphene lattice is avoided since only the existing defect sites are activated [122]. Provided the grafting reagent is volatile enough to be introduced by vacuum, the whole process may be carried out in the complete absence of solvents, minimising additional contamination or damage. The gas-phase thermochemical functionalisation (GPTF) method is illustrated in figure 3.12.

Working in collaboration with the group of Professor Milo Shaffer, whom carried out the GPTF experiments, pristine graphene TEM grids were functionalised. The aim of this investigation was to determine the degree of functionalisation and its

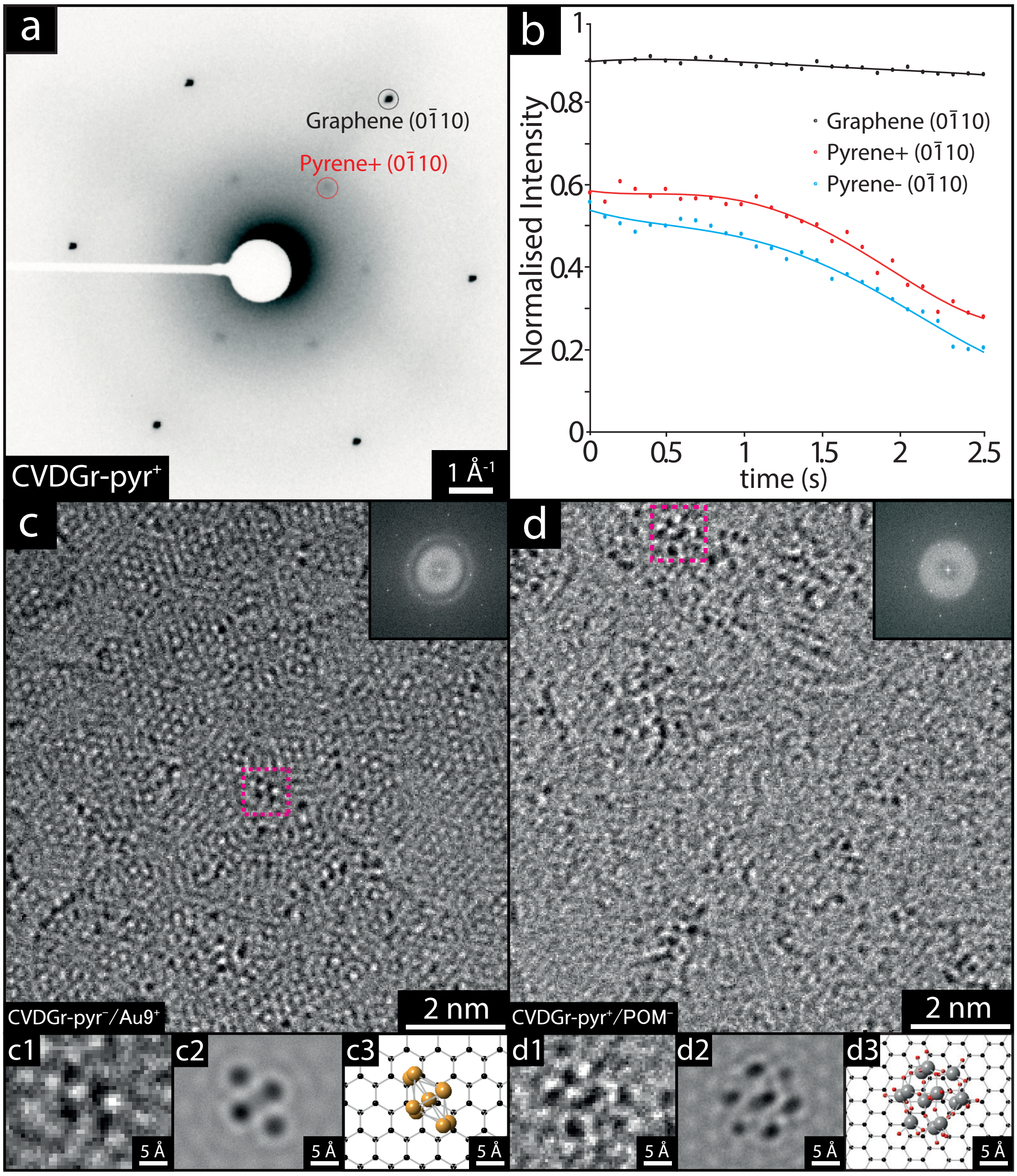

Figure 3.11: Pyrene TEM summary. a) TEM low-dose diffraction of CVDGr-pyr^{+} b) Diffraction spot intensities plotted as a function of time for graphene at a dose rate of 4 $e^{-}\text{Å}^{-2}s^{-1}$ for CVDGr-pyr^{+} and CVDGr-pyr^{-} demonstrating their beam-sensitive nature. c) and d) are HRTEM images showing Au$_9$ clusters attached to CVDGr-pyr^{-} and POM clusters attached to CVDGr-pyr^{+} respectively, with inset FFT showing the characteristic hexagonal pattern of graphene monolayer. A magnified view of the boxed areas, c1 and d1, are shown alongside corresponding multi-slice simulations, c2 and d2, and atomic models, c3 and d3.

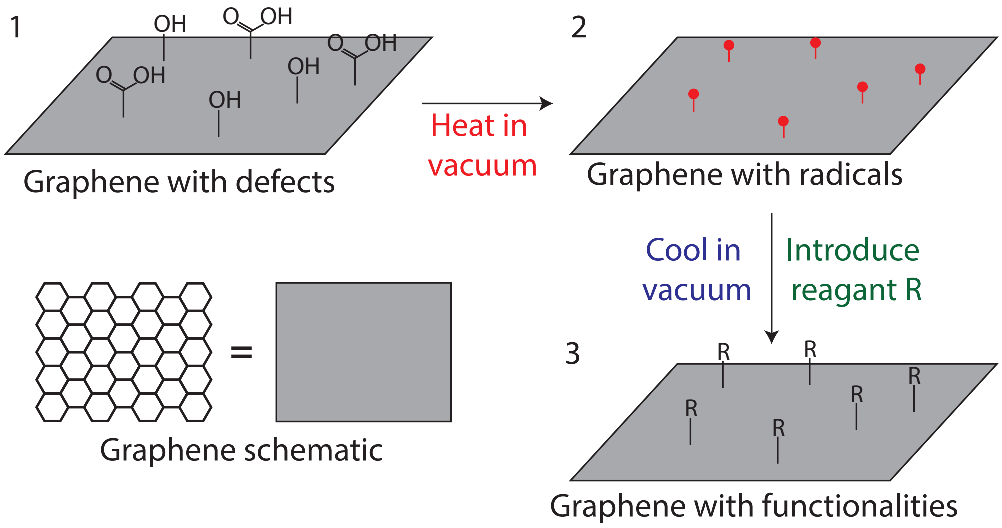

Figure 3.12: Reaction schematic for thermochemical functionalisation of graphene. The graphene is heated under vacuum in order to radicalise pre-existing defects on the graphene surface. The radicalised graphene is cooled whilst maintaining vacuum, and a grafting reagent R is introduced in order to functionalise the radical sites.

influence on the mechanical properties of graphene, as the effects of functionalisation on chemical processing had been previously investigated [122, 123].

Graphene TEM grids were processed by heating under vacuum (≈ 100 mbar) to 850 °C. Thermochemical activation is usually performed at 1000 °C [122–124]. However, a lower temperature was used in order to avoid damaging the graphene and silicon nitride support membrane. The activated membranes were then allowed to cool to room temperature, before exposing them to grafting agents. A small, rigid, volatile species was selected for graphene grafting: 1,1,1−trifluoro−2−iodoethane (TFI). In order to monitor whether heating−induced effects were minimised, a set of control samples were heated under vacuum and allowed to cool without exposure to the grafting reagent, referred to here as thermally-treated control graphene (TTC−G). The TFI−G and TTC−G membranes were then probed using a combination of HRTEM and AFM, to inspect individual functionalities and the mechanical properties of the functionalised graphene.

The HRTEM images of TFI−G show distinctive features, as presented in figure 3.13. These features were seen to remain in a fixed position on the graphene lattice, whilst undergoing a continuous change in contrast attributed to rotation of the functionality about a bond site. Comparison to multislice TEM image simula-

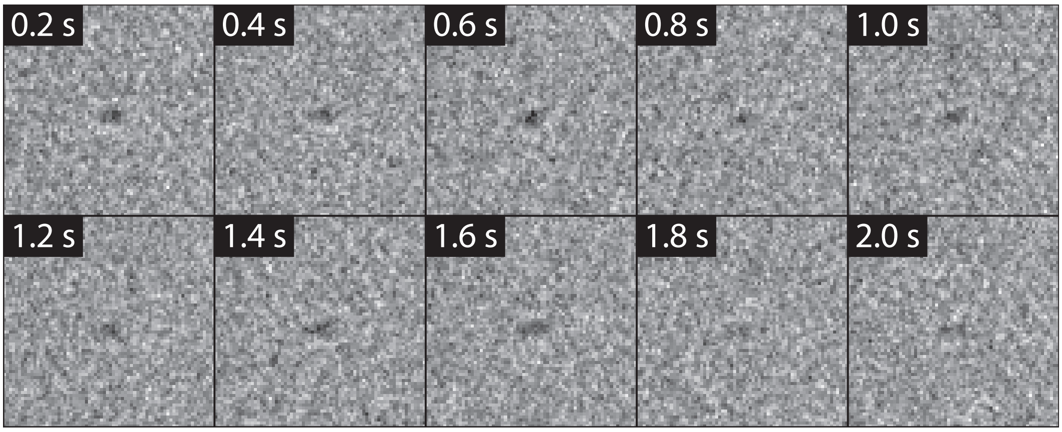

Figure 3.13: HRTEM time series showing presence of functionalities on graphene. The functionality remains in a fixed location with time, indicating a bond with the graphene. The change in contrast with time indicates the functionality is rotating about its bond site.

tions [73] allows these features to be attributed to the grafted TFI molecules (figure 3.14). Interestingly, the imaged functionalities did not degrade or move laterally across the graphene during moderate exposure to the beam. Instead, some motion (likely rotation) about the bonding site was visible. This behavior suggests a covalent bond at a defined site.

The features appeared on the TFI−G surface with an approximate concentration of 1×10^{-3} nm^{-2}, but were not observed on the TTC−G. The equivalent grafting concentration, defined by the graphitic carbon to TFI site ratio (C/R), can be estimated to be 38,000:1, by normalising the grafting site concentration to atomic areal density of graphene (5.246×10^{-2}nm^2 per two carbon atoms). This value is seemingly low, compared to previous results on multi−walled carbon nanotubes (MWCNTs, 1000:1) [122] and carbon black nanoparticles (CB NPs, 250:1) [123]. However, the high quality of the graphene used means that the concentration of initial defect sites available for activation is low. Furthermore, the functional groups could only be clearly identified when present as individual species against clean, perfect regions of the graphene lattice. Thus, the contribution from grafting occurring at larger defects, grain boundaries, or in clusters are not included. The lower activation temperature (850 °C) can also reduce the grafting ratio slightly but is unlikely to be the dominant effect, since the grafting ratio previously reported on CNTs was only halved by this change in temperature [125]. Overall, the low grafting density on the highly perfect graphene surface, and high quality of the structure after grafting is consistent with the proposed defect-initiated mechanism.

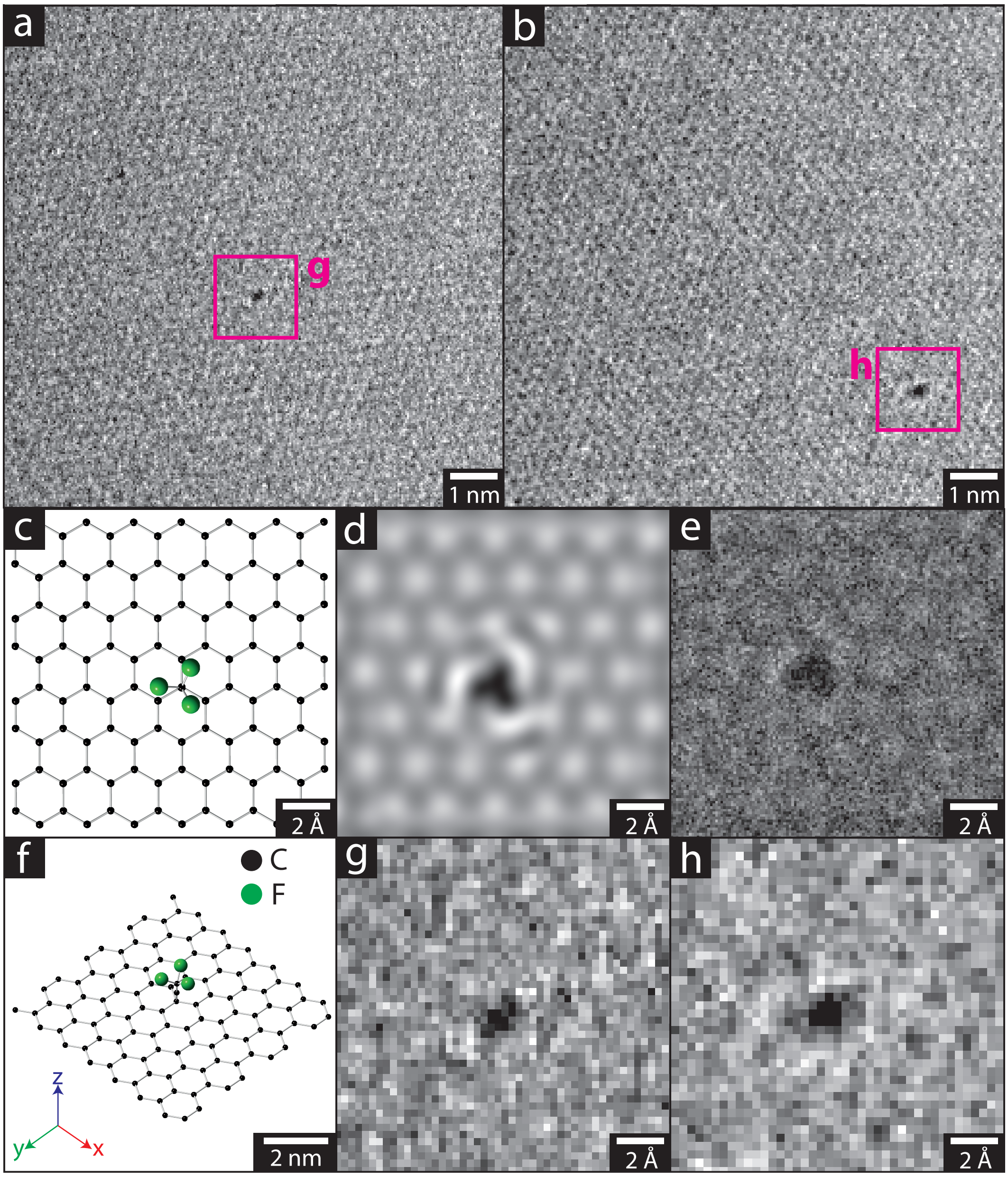

Figure 3.14: HRTEM results showing presence of functionalities on graphene. a), b) HRTEM images show localised high−contrast functionalities on graphene surface. c), f) Model used for multislice simulations in plan and perspective views. d), e) Multislice simulations of TFI functional group modelled using perfect and experimentally measured noise. g), h) Magnified regions of interest from a), b) displaying similar appearance and contrast to the realistic multislice simulation presented in e).

AFM nano−indentation was used to measure the mechanical properties of the functionalised graphene sheet, using the methods of Lee *et.al.* [89]. As shown in Table 3.1, neither the thermochemical treatment (TTC−G) nor the functionalization (TFI−G) changed the Young's modulus measurably in comparison to a pristine as−produced graphene (AP−G) grid. The number of holes used for measurements for each graphene type are presented alongside the Young's modulus in Table 3.1. In addition, the Young's modulus measure for graphene-oxide (GO) [92] is added for comparison, showing the significant degradation in mechanical strength resulting from the strong functionalisation applied to GO.

Table 3.1: A summary of mechanical properties of AP−G, TTC−G, TFI−G, and graphene-oxide (GO) [92].

Sample	Young's Modulus (TPa)	Measurements
AP−G	1.2±0.4	75
TTC−G	1.4±0.1	72
TFI−G	1.3±0.2	76
GO	0.2076±0.0234	-

In addition to successfully applying thermochemical functionalisation to single-layer graphene, these methods were further demonstrated when applied to bulk commercially-available graphene nano-particles (GNPs) [3], illustrating the versatility of the functionalisation. The solvent-free methodology provides an alternative, generic, clean, robust and versatile strategy to functionalise graphene and related materials, providing enough functional groups to change the solubility, complementing the existing liquid-phase and plasma processing approaches.

3.4 Conclusions

Methods for the clean transfer of graphene from as-grown CVD foils to TEM supports have been described, including a new, simpler methodology for high volume, high yield fabrication. In addition, techniques to fabricate double-layered graphene membranes and samples encapsulated with two monolayers of graphene were presented.

A method to alter the surface functionality of graphene using a self-limiting monolayer film of pyr-modified ions was outlined. These enable control over electrostatic interactions in solution to selectively bind charged macro-molecules, and similarly should be effective for other charged species. This approach is expected to be generically applicable to graphene on any surface or indeed free-standing membrane, making it useful in a wide variety of fields including biomedicine, electrochemical sensors or catalysis, as well as for selective adsorption to supported graphene membranes for cryo- and HRTEM imaging

Finally, thermochemical functionalisation was successfully applied to single-layer graphene. Functionalisation of pre-prepared graphene TEM grids allowed direct imaging of the covalently-grafted functional group attached to an otherwise highly crystalline layer, revealing the grafting density of the 1,1,1-trifluoro-2-iodoethane functionality to be 1×10^{-3} nm^{-2}. AFM nano-indentation analysis of the single layer graphene confirmed there is no significant damage to the carbon framework during the thermochemical processing.

Chapter 4

Low-dose molecular microscopy

4.1 Introduction

Since the invention of the transmission electron microscope by Max Knoll and Ernst Ruska in 1931, improvements in electron microscope technology have been relentless. With the correction of spherical aberration that is commonplace in many transmission electron microscopes (TEMs), sub-angstrom resolution imaging is now possible, allowing samples to be routinely imaged at the atomic level [126, 127]. One of the main issues that now encumbers resolution improvements is the radiation damage suffered by the sample during exposure to the electron beam [128]. This is especially problematic when dealing with soft-matter samples, as a result of the weak bonding, poor conductance, and large population of light atoms in such systems [90, 129]. Damage can also occur in inorganic specimens, predominantly through the knock-on displacement of atoms [130].

The process of beam-induced damage in soft-matter specimens occurs through a combination of primary, secondary, and tertiary damage effects [130]. Knock-on displacement and radiolysis are the dominant primary damage effects, whereby chemical and intermolecular bonds are broken through electron-atom and electron-electron scattering, generating ionisation interactions [65]. This form of damage may be reduced by increasing the incident electron energy E_0, resulting in a reduction in the electron scattering cross-section σ [65]. However, at higher accelerating voltages knock-on damage is increased, as the energy transferred during inelastic scattering events exceeds the atomic displacement threshold for the material being studied. In the case of graphene, accelerating voltages less than 80 kV have been shown to prevent knock-on displacement of individual carbon atoms during continuous exposure to the electron beam [131].

In addition to radiolysis, inelastic scattering events produce secondary damage effects through the generation of phonons, secondary electrons, the accumulation of charge, and free radical species, all of which may propagate through the sample, causing heating and further damage [65, 90, 129, 132, 133]. For less-conductive samples, damage can occur more rapidly due to the increased build up of charge and heat from the generation of secondary electrons[90, 129, 132, 133]. For organic specimens in particular, the buildup of gas (generally oxygen and hydrogen) produced from the cross-linking of carbon chains can lead to tertiary damage effects [134]. Individual atoms and molecular fragments, as well as gaseous products of cross-linking such as hydrogen and oxygen, may readily desorb into vacuum with the energy provided by the electron beam, further degrading the local crystallinity [128].

All of these damage effects lead to a loss of crystallinity in atomic/molecular lattices, and hence to a weakening of the diffraction reflection intensities. As larger areas of the sample damage, the diffraction reflections weaken further, until the sample no longer holds any of its initial crystallinity. The overall crystalline order of the sample can be maintained whilst individual molecules still suffer bond breakage and damage, leading to the reduction in higher-order reflection intensity more rapidly than lower-order reflections [130].

There are several methods available for reducing the rate of damage induced by the electron beam for soft matter samples, three of which are investigated here: changing the accelerating voltage of the microscope, changing the temperature of the sample, and encapsulating samples with graphene either side [65, 90]. Each of these acts to reduce the effect of inelastic scattering on the sample through different ways.

Reducing the accelerating voltage reduces the energy of the incident electrons, thereby reducing the potential knock-on damage. However, the reduction in energy, and velocity, of the incident electrons also can have the effect of increasing the scattering cross-section of the sample σ, increasing the interaction between electrons and specimen, thereby increasing the damage rate [65]. This balance between reduction in electron energy and increase in sample interaction governs the overall benefit, or hindrance, of using a reduced accelerating voltage, and varies between molecular systems [65].

Cooling the sample helps compensate for the poor thermal conduction of organic specimens, thereby mitigating phonon induced heating [130]. In addition, cooling the sample reduces the motion of radicals and hence slows the growth of damaged regions [65, 90].

Encapsulating samples within graphene has a number of benefits. Firstly, graphene has exceptionally high thermal and electrical conductivities, providing effective heat sinks either side of the sample which act to reduce phonon-induced heating effects [135–137]. In addition, graphene is atomically impermeable, allowing it to restrict the desorption of free atoms and molecular fragments into vacuum from the encapsulated molecular film [23]. Any damaged molecules are thus limited to attacking neighbouring molecules and degrading into a fully amorphous state, allowing the molecular crystal lattice to be maintained for longer periods.

Despite the development of techniques to minimise radiation damage in the TEM, it remains an ongoing problem [90, 129, 133]. The use of a low-dose of electrons presents several additional technical challenges in capturing images with sufficient resolution and contrast, whilst operating within the dose limits of the specimen. Many studies have been conducted commenting on the mechanisms of damage and new techniques aimed at reducing it, although no study has yet focused on combining such techniques to give the optimal effect in practice.

Considerations must also be made regarding the operating performance of the electron detector used in conjunction with the TEM, especially when using low-dose conditions. There are two distinct classes of electron detectors that are widely available for use in TEM: indirect scintillator-based and direct electron detection devices (DDDs).

Detecting electrons using an indirect device involves four stages. First, the electron is incident on the scintillator part of the detector, producing a number of photons. These photons are channeled through a fibre-optic coupling plate to the CCD detector. The photons incident on the CCD produce an accumulation of charge within each detector pixel. In order to read-out the charge image, a global-shutter principle is implemented whereby all CCD pixels are exposed simultaneously. Once a single exposure is complete, the charge from each pixel is transferred serially along pixel columns once a new row has been completely transferred along the single ADC, as shown in figure 4.1. This readout bottleneck limits the CCDs ultimate frame rate - in the case of a Gatan ORIUS™SC1000 to 14 fps [138]. In addition to the issues relating to readout speed, the use of a scintillator-based detector presents a number of other challenges when operating with a low-dose of electrons and limited exposure time.

When electrons are incident on the scintillator they are scattered, producing photons in a volume leading to a distribution of pixels receiving counts rather than a single pixel. The photons distribution generated by the scintillator is also subject to additional blurring due to scattering through the scintillator and optical coupling, as well as leakage into adjacent fibres in the coupling. In addition, due to the thickness of the detector and support, electrons can scatter back into the active layer, resulting in spurious photon creation. The sensor electronics detecting the photon counts also introduce a source of Poisson noise due to their independent nature. These effects may be quantitatively described by the detector quantum efficiency (DQE):

$$DQE = \frac{SNR_{out}}{SNR_{in}} \tag{4.1}$$

where SNR_{in} is the signal-to-noise ratio of the input signal and SNR_{out} is the signal-to-noise ratio of the output signal. The DQE may be expressed in terms of measurable quantities:

$$DQE(q, N) = N\frac{MTF(q)^2}{NPS(q, N)} \tag{4.2}$$

where $MTF(q)$ is the modulation transfer function, describing the effect of the detector on the input signal, $NPS(q, N)$ is the noise power spectrum, describing the effect of noise sources on the output signal, and N is the dose rate of the incident electron beam. The MTF and NPS may be readily measured using several methods outlined in specific detail in previous literature [139–143]. Here, measurements were made from a series of uniformly illuminated images, as described by de Ruijter and Weiss [143]. Finally, the modulated image is subject to additional noise from dark current and electronic amplification/readout [143]. The combined effects of DQE, dark current, and readout noise combine to produce the final image [80]:

$$\begin{split} I(r) = I_{rn} + I_{dc} + CF \cdot \mathcal{F}^{-1}\Bigg[\mathcal{F}\Bigg[P_{oiss}\Bigg(\\ \phi_e \cdot \mathcal{F}^{-1}\Bigg[I_0(q)\sqrt{DQE(q.N)}\Bigg]\Bigg)\Bigg] \cdot NPS_{out}(q, N)\Bigg] \end{split} \tag{4.3}$$

where I_{rn} is the readout noise image, I_{dc} is the dark current image, CF is a conversion factor, ϕ_e is the electron flux, $P_{oiss}(x)$ returns a random value from a Poisson distribution with expected value x, and I_0 is the Fourier transform of the image arriving at the detector.

The use of DDDs offers the possibility of significantly improving the image quality. The structural makeup of back-thinned direct detectors allows electrons to exit the active layer before significant lateral scattering has occurred, and also prevents the scattering of electrons back into the active layer, leading to a considerable improvement in DQE. Of particular interest for low-dose studies is the counting mode implemented by several commercially available DDDs.

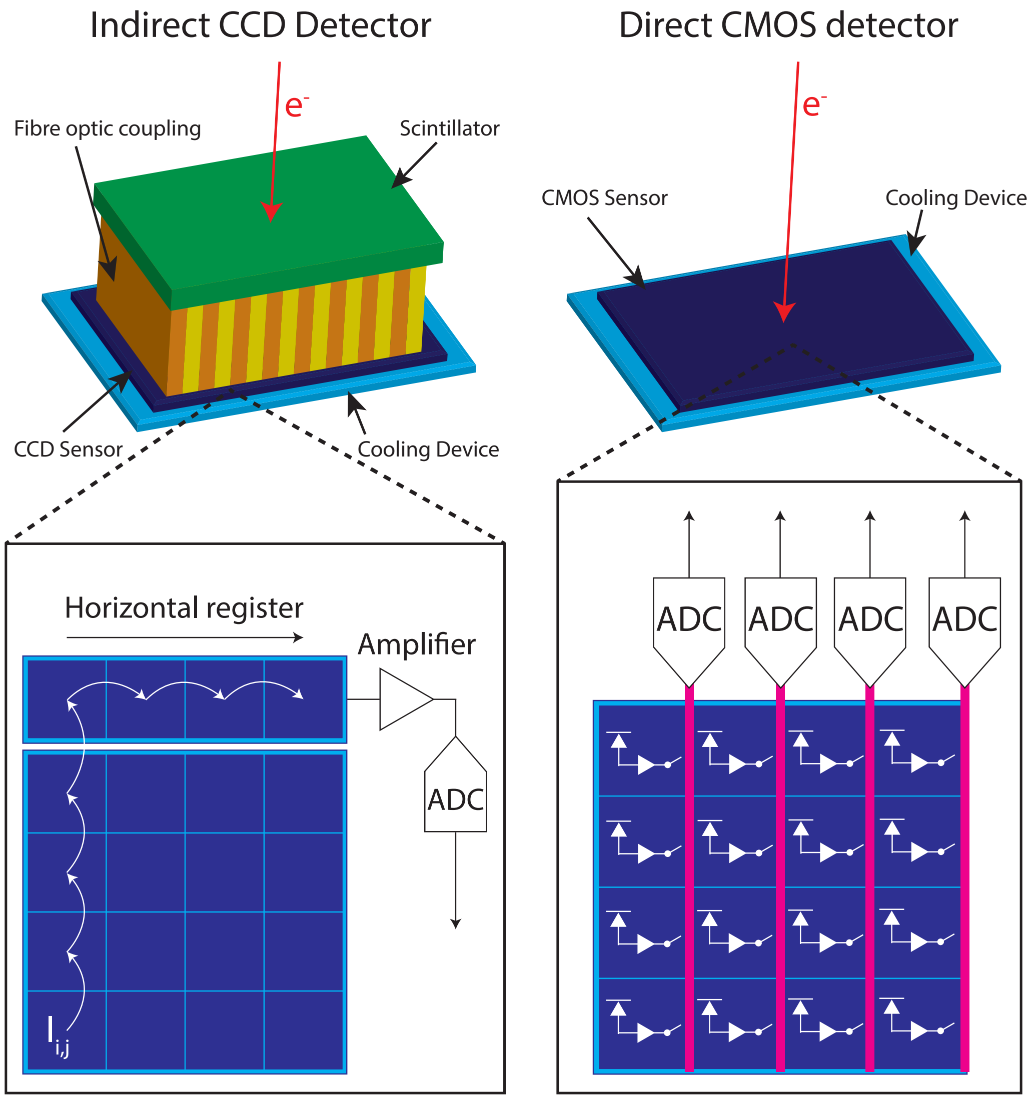

Figure 4.1: Scintillator and Direct detection camera schematics and readout electronics circuitry.

Counting mode operation works through the detection of ionization trails caused by an arriving electron, as illustrated in figure 4.2. The tracking of ionization trails allows the arrival location of the electron to be pinpointed with pixel accuracy, and allows binary registry of the detection event [144]. This method produces a significant increase in DQE and also benefits from negligible sources of dark current and readout noise [144–146]. An additional benefit of the CMOS-based design of DDDs is the highly-parallelised readout electronics circuitry. The readout bottleneck present for CCD-based devices, whereby a global shutter requires all pixels being read through a single amplifier and ADC, is eliminated by using an ADC for every column of pixels. The reduction in readout times allows imaging to be carried out with much faster frame rates, which is important when operating in counting mode due to the large coincidence loss present: when too many counts are received by individual pixels in the detector [145–147]. Finally, high frame rates provide benefits in drift correction, compensating for beam-induced sample movement [145, 146].

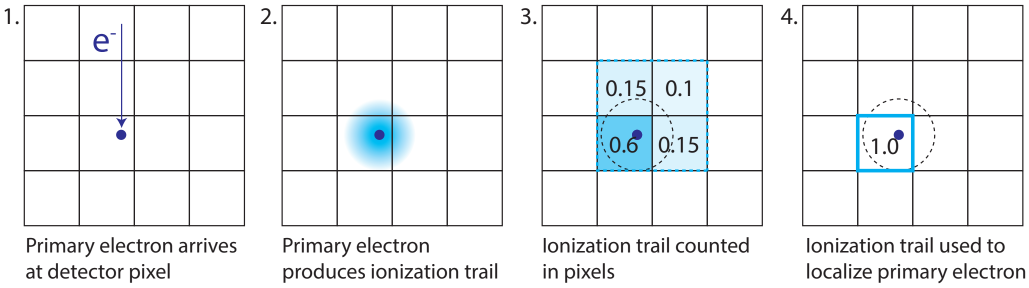

Figure 4.2: DDD counting mode operation principle. Adapted from [144].

4.2 Chapter Outline

This chapter studies the effects of accelerating voltage, cryogenic cooling, and encapsulation within graphene, on the robustness of organic samples to the electron beam. These parameters are studied in combination using low-dose selected-area electron diffraction (LD-SAED), to gain insight into the optimal conditions for systems possessing different intermolecular bonding and structural makeup.

Cryogenic cooling, and encapsulation of samples within graphene, is shown to always increase their lifetime substantially when exposed to the electron beam, although the optimal choice of accelerating voltage varies between systems. The relative increase in sample lifetime when using the optimal conditions also varies between samples.

In addition to investigating the optimal sample protection conditions, the DQEs of a Gatan ORIUS™SC1000 CCD (the current detector mounted on the University of Warwick JEOL ARM 200F) and Gatan K2 Summit counting mode detector (one of the current best performing and most widely used DDD), are studied as a function of dose. Experimental images of monolayer graphene captured using a variable electron dose with a Gatan ORIUS™SC1000, Gatan OneView (the new Gatan scintillator-based detector implementing highly-parallelised readout electronics, mounted on a JEOL ARM 300F), and Medipix3 CMOS DDD (mounted on a JEOL ARM 300F) are also compared. The quality of these images is studied using a contrast metric, which demonstrates the substantial performance gains when using a DDD at low dose levels. Finally, simulated HRTEM images of a monolayer assembly of Ni(II)-octaethylporphyrin (NiOEP) molecules using a dose of electrons below the characteristic dose of the system, in combination with a Gatan K2 summit counting mode detector, are shown to provide sufficient contrast and SNR to resolve the constituent molecules and their atoms.

4.3 Results and Discussion

4.3.1 Dose-dependence of molecular systems

Characteristic Dose Measurement

When dealing with beam-sensitive systems, it is important to accurately and efficiently capture diffraction patterns before significant damage has occurred. For many of the systems investigated throughout this thesis the time frames for capturing images is limited to a few seconds, even when using optimal protection strategies. It is therefore necessary to minimise unnecessary exposure to the electron beam. This is achieved using a step-by-step procedure for capturing diffraction patterns, as outlined in figure 4.3.

With the microscope aligned using a small area of sample and appropriately low dose rate [90, 95], the displacement of the stage $(\Delta x, \Delta y)$ required to move to a new area of sample is measured and input into a computer programme linked to the stage controller. Upon running the programme the beam is deflected into the column using the projector lens, the stage is then moved through the measured displacement and allowed to settle, the CCD begins capturing successive frames in a live recording, and finally the beam is shifted back to its initial alignment. Having the stage moved without exposure to the beam prevents any damage occurring before imaging has occurred, and the use of a live recording allows the first moments of exposure to the beam to be captured. These frames are the most important as they contain information on the system prior to any damage occurring.

The current density of the beam incident on the focus screen may be measured using the standard magnification imaging mode, as shown in figure 4.4. The current density J_{screen} incident on the focus screen is automatically measured through the microscope. The area of the focus screen is provided by the microscope manufacturer, allowing the current incident on the screen to be calculated:

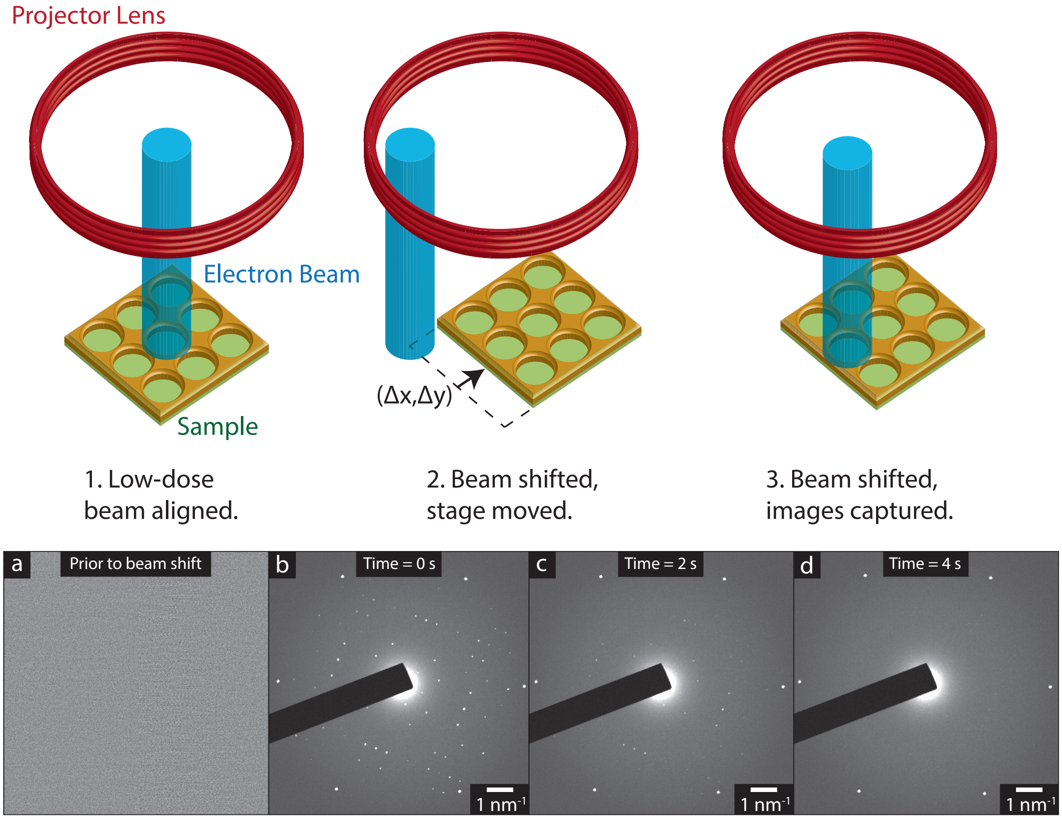

Figure 4.3: Low-dose acquisition protocol. Frames (a) - (d) show example images from a live capture sequence of NiOEP molecules. Frame (a) shows the dark current of the detector at the start of the recording sequence prior to the beam being shifted back onto the sample.

$$I_{screen} = J_{screen}A_{screen} \approx I_{sample} = J_{sample}A_{sample} \tag{4.4}$$

where the current passing through the sample is approximately equivalent to that incident on the screen (with the exception of negligible backscatter and secondary electron events). The area of the inserted aperture can be measured by the CCD in standard magnification imaging mode, as shown in figure 4.4. Using the measured screen current, I_{screen}, and aperture area, A_{sample}, the sample current density can be calculated:

$$J_{sample} = \frac{I_{screen}}{A_{Aperture}} \tag{4.5}$$

When studying beam-sensitive systems using EM, the characteristic dose D_c is introduced in order to quantify the robustness of the system to beam-induced

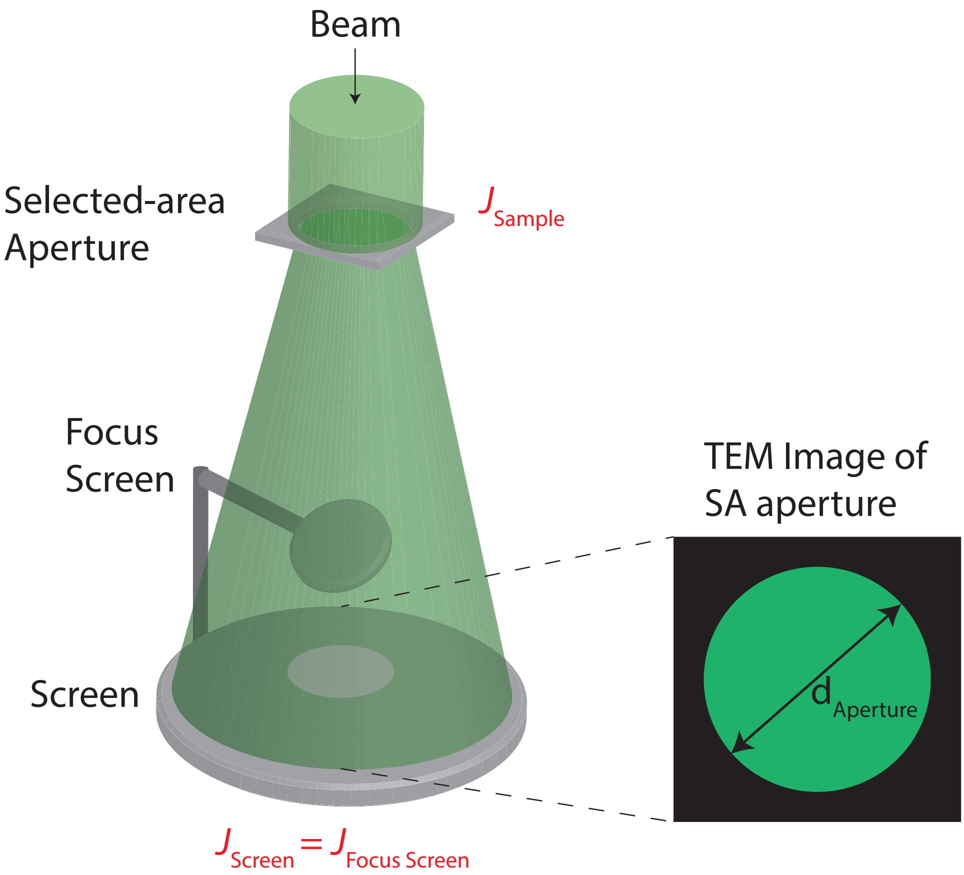

Figure 4.4: Simplified schematic of the TEM showing the quantities measured in order to calculate the sample-plane current-density J_{sample}.

degradation [90]. The characteristic dose is defined as the dose (e^{-} Å^{-2}) received by the system after time T_c (the characteristic time), at which point the intensity of a measured diffraction reflection has reduced by a factor $e \approx 2.71828$. The characteristic time T_c is measured through the fitting of decay curves to the measured intensity changes of molecular diffraction peaks in diffraction movies. It is commonly assumed that such decay process follow an exponential relationship [90, 129]. However, the majority of systems studied here exhibited complex multi-stage decay processes modeled by a cubic polynomial fit, as shown in figure 4.5. For matters of consistency, the same criterion of characteristic time T_c measurement (the time at which the measured signal has reduced by a factor e) was used for both exponential and cubic polynomial fitted curves.

In order to correctly measure the intensity changes of both the molecular and graphene reflections, small windows (for instance, 5×5 pixels) are centred on the diffraction peaks of interest, as well as a neighbouring region of background noise at equal distance from the central beam, as shown in figure 4.5. The uncorrected peak intensity is summed across this pixel window, as well as for the corresponding background region, with the difference between the two giving the background-corrected diffraction peak intensity:

$$I = I_0 - I_B \tag{4.6}$$

where I is the background−corrected intensity, I_0 is the uncorrected intensity, and I_B is the corresponding background intensity, as marked by the blue window in figure 4.5. The background is assumed to be radially symmetric and decays from the centre of the pattern due to inelastic scattering effects. Measurement of the corrected intensity I then allows the characteristic time to be measured. Combined with measurements of the dose rate, the characteristic dose may be calculated using Equation 4.7. A plot of corrected intensity I versus time is shown in figure 4.5, with the characteristic time (after which I has reduced by e) marked.

Using measurements of T_c and J_{sample}, the characteristic dose D_c may be calculated:

$$D_c = J_{sample} T_c \tag{4.7}$$

The rapid loss of crystallinity of an assembly of NiOEP molecules is clearly illustrated in figure 4.5. Initially, the graphene and NiOEP reflections are clearly resolved, before the NiOEP pattern quickly decays. An amorphous halo remains, indicating the complete loss of crystallinity of the molecular system, whereas the graphene diffraction peaks remain constant in intensity with time, due to graphene's exceptionally high conductivity and consequent robustness to the electron beam. The overall crystallinity of the sample can be maintained whilst individual molecules still suffer bond breakage and damage, leading to the reduction in higher-order reflection intensity more rapidly than lower-order reflections. For consistency when comparing between molecular systems, only the characteristic doses relating to first order diffraction peaks are used in the comparative values.

Strategies at maximising molecule lifetimes

Combining the three methods of protection mentioned in the introduction (choice of operating voltage, cryogenic cooling, graphene encapsulation) together in each

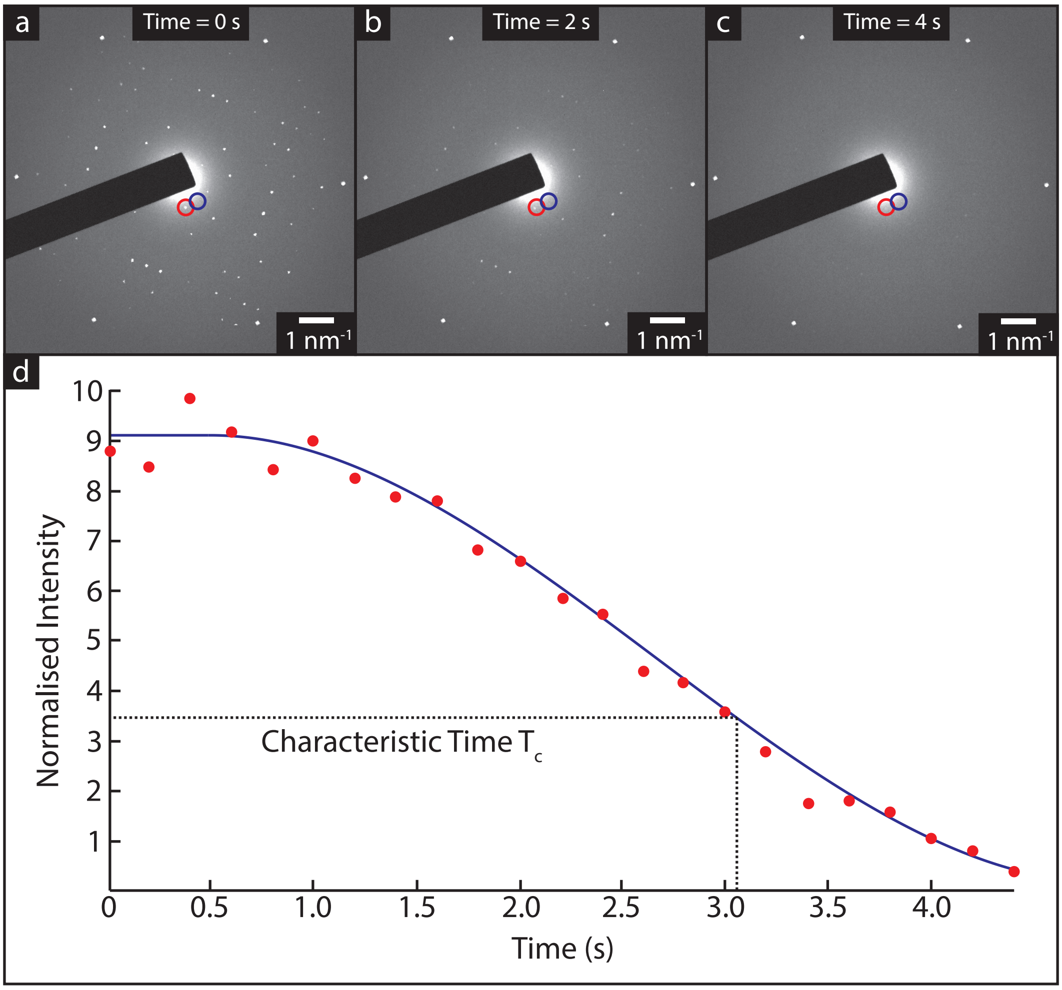

Figure 4.5: Characteristic time T_c measurement of NiOEP. (a), (b), (c) Diffraction pattern frames at time 0 s, 2 s, 4 s from a single exposure movie. Red circles indicate the peak location, and blue circles indicate the local background measurement area. (d) Plot of corrected intensity versus time for the (100) NiOEP reflections.

available permutation, and for different samples, allows the optimal protection conditions to be determined for different organic systems. The combined decay curves measured for all systems are presented in figure 4.6. Here, samples sandwiched between two layers of graphene are listed as Molecule+Gr. As already outlined in the previous chapter, the restrictions placed by the cleaning steps prevented the TMA and NiOEP systems from being sandwiched. A summary of characteristic dose measured for each system from the curves in figure 4.6 is presented in Table 4.1.

As is to be expected, cooling each system increases the characteristic dose

Table 4.1: Characteristic dose D_c values for different systems under different temperature and accelerating voltage conditions.

Molecule	V = 200 kV T = 300 K ($e^{-}\text{Å}^{-2}$)	V = 200 kV T = 100 K ($e^{-}\text{Å}^{-2}$)	V = 80 kV T = 300 K ($e^{-}\text{Å}^{-2}$)	V = 80 kV T = 100 K ($e^{-}\text{Å}^{-2}$)
$\text{Pyr}^{\pm}$	5.0±0.3	25±4	35±6	70±7
$\text{Pyr}^{\pm}$ + Gr	90±7	180±9	30±4	140±12
PLLA	2.0±0.2	4.5±0.5	0.5±0.2	1.9±0.3
PLLA + Gr	1.0±0.1	3.0±0.2	1.0±0.1	11.0±0.3
TMA	15±5	30±7	32±6	96±9
NiOEP	13±3	20±3	30±4	57±6

regardless of the accelerating voltage or whether the sample is coated in graphene [65, 90, 130]. The average increase in characteristic dose when cooling from 300 K to 100 K is a factor of 3.6 across all voltages and systems.

Reducing the accelerating voltage from 200 kV to 80 kV at both 300 K and 100 K increases the characteristic dose for all systems except PLLA and $\text{Pyr}^{\pm}$+Gr, illustrating the complex nature of the electron interactions [65]. In addition, the encapsulation of graphene alters the characteristic dose of each system for each set of temperature/voltage conditions, with some systems having lower doses except for a specific temperature/voltage, as is the case for PLLA. PLLA+Gr has lower characteristic dose values than PLLA, except at 100 K and 80 kV, where the dose is improved by a factor 5.5 compared to 300 K and 200 kV.

As is clear from the table, the conditions for maximum characteristic dose for each system are specific, indicating that the choice of sample and its properties have a significant effect on characteristic dose D_c. In order to maximise the lifetime of a system, the conditions must be tailored specifically.

4.3.2 Low-dose High-Resolution Transmission Electron Microscopy

As has already been shown, there are fundamental limitations on the level of electron dose that molecular systems can be exposed to before significant damage has been caused, even when implementing the most optimal protection schemes as outlined above. The limitations on molecular lifetimes hinder the use of HRTEM as a method of study, predominantly due to the behaviour of common CCD cameras used with the majority of HRTEM systems.

The current HRTEM CCD camera in operation at the University of Warwick is a Gatan ORIUS™SC1000 indirect detector system. As an indirect detector, the

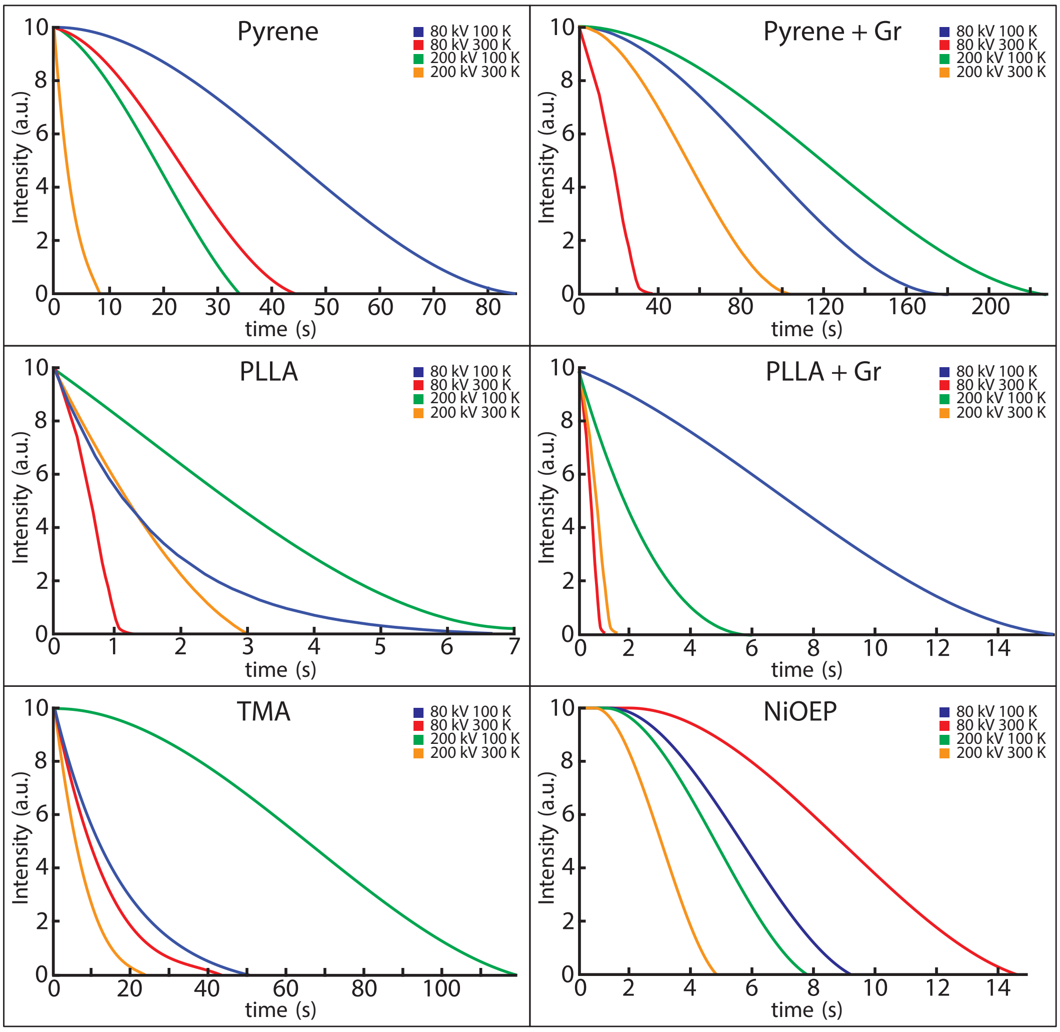

Figure 4.6: Decay curves for each molecular system obtained for the four combinations of accelerating voltage and temperature. Characteristic dose D_c measurements from each of these curves are presented in Table 4.1.

CCD is limited by its readout noise, dark current, and quantum efficiency (QE) when operating with a low dose of electrons, as is evident from the dose-dependent QE maps shown in figure 4.7.

The DQE map for the Gatan ORIUS™SC1000 was calculated using a series of measurements of MTF and NPS obtained using the methods described by de Ruijter and Weiss [143]. The DQE map for the Gatan K2 summit counting mode DDD was calculated using published dose-dependent MTF and NPS [140, 145].

In order to investigate the performance of different detectors types in practice, a series of experimental HRTEM images of graphene taken at different dose

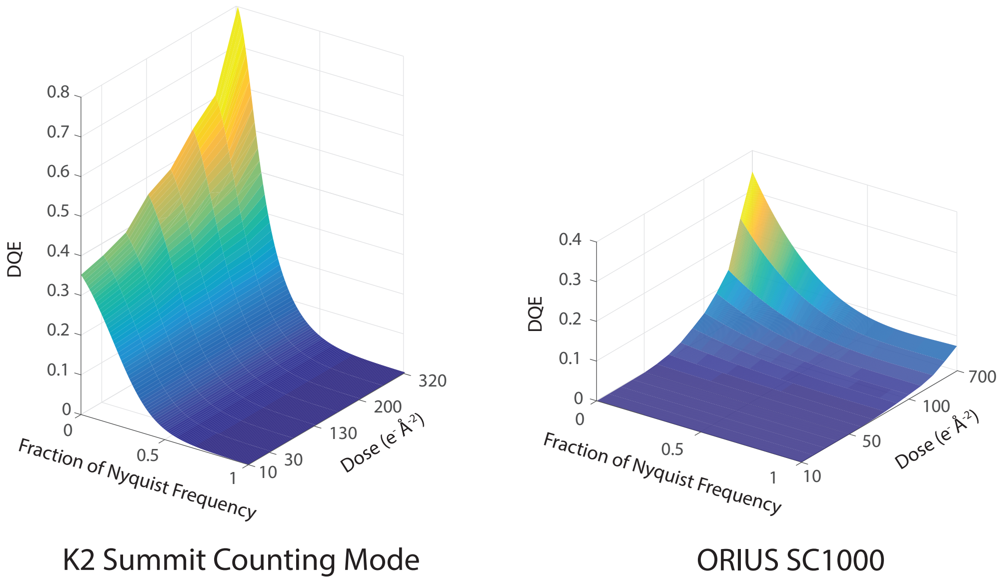

Figure 4.7: Experimentally determined DQE maps as a function of electron dose for Gatan ORIUS™SC1000 and K2 summit counting mode detectors. Below approximately 100 e^{-} Å^{-2} the ORIUS™SC1000 detector performance drops considerably, whereas the K2 summit counting mode DDD maintains high performance at significantly lower dose levels. K2 summit counting mode data used for calculation sourced from [140, 145].

levels using three different detectors were compared (figure 4.8). The detectors used were a Gatan ORIUS™SC1000 (mounted on the JEOL ARM 200f at the University of Warwick), Gatan OneView, and Medipix3 DDD (both mounted on the JEOL ARM 300F at the electron Physical Science Imaging Centre, Diamond Light Source). There is a considerable improvement in image quality when using both the Gatan OneView fast-readout scintillator detector and the Medipix3 DDD, particularly at very low dose levels. Additionally, the Medipix3 device used for these measurements was a prototype 256×256 pixel device with several dead pixels and a non-uniform sensor film. Despite these hindrances, the Medipix3 DDD still provides substantial enhancements in image quality at low dose levels.

In order to better quantify the quality of HRTEM images, a figure-of-merit was defined using the background-corrected intensity of first-order lattice peaks in the HRTEM image power spectrum:

$$metric = \frac{I_0 - I_B}{I_B} \tag{4.8}$$

where I_0 is the average intensity of the first-order lattice peaks and I_B is the average local background intensity to the first-order lattice peaks. The process of peak measurement and background removal is identical to that described for diffraction pattern data, as presented in figure 4.5. The metric can range from $0 - 1$ based on the signal-to-noise ratio in the HRTEM image, with good SNR giving $I_0 \gg I_B$ and poor SNR giving $I_0 \approx I_B$. A plot of the contrast metric as a function of electron dose is presented in figure 4.9. As shown, the metric drops off considerably for the ORIUS detector at doses below approximately 100 e^- Å^{-2}, due to the drop in DQE below this dose level, as shown in the DQE plots in figure 4.7. Comparing to the OneView and Medipix3 metric, the Medipix3 performs substantially better at low dose levels, as is to be expected from the DQE profile shown in figure 4.7 (although not a Medipix3 DQE profile, similar detection principles and engineering are employed on both devices). The Medipix3 metric behaviour at low dose indicates the possibility of achieving high-contrast, low-noise HRTEM images using a very low dose of electrons, within the characteristic dose limits of many molecular systems, when employing a DDD.

As a test example, a model system was constructed using a monolayer assembly of NiOEP molecules deposited on both the top/bottom faces of a freestanding layer of graphene. Using a limited dose of 40 e^- Å^{-2} 80 kV electrons, below the characteristic dose limit of the system under 300 K conditions, the simulated image shown in figure 4.10 was obtained. The limited dose is implemented in clTEM using equation 4.3. The simulation was carried out using C_0 = -10 nm and C_3 = -1 μm. As shown in the simulated HRTEM image, the individual NiOEP constituent atoms within the molecular lattice are well resolved, without requiring a dose level greater than the characteristic dose of the system.

This is truly remarkable, given the limitations to all soft$-$matter specimens when imaging using high-voltage electron microscopy under low$-$dose conditions. Even without further image processing and unit$-$cell averaging the image provides sufficient contrast and low noise to distinguish individual light atoms, suggesting that for even lower dose conditions valuable information will still be available in images following processing routines; there is the possibility of imaging even the most fragile of organic systems using HRTEM techniques, which would lead to a complete paradigm shift in the study of soft-matter systems.

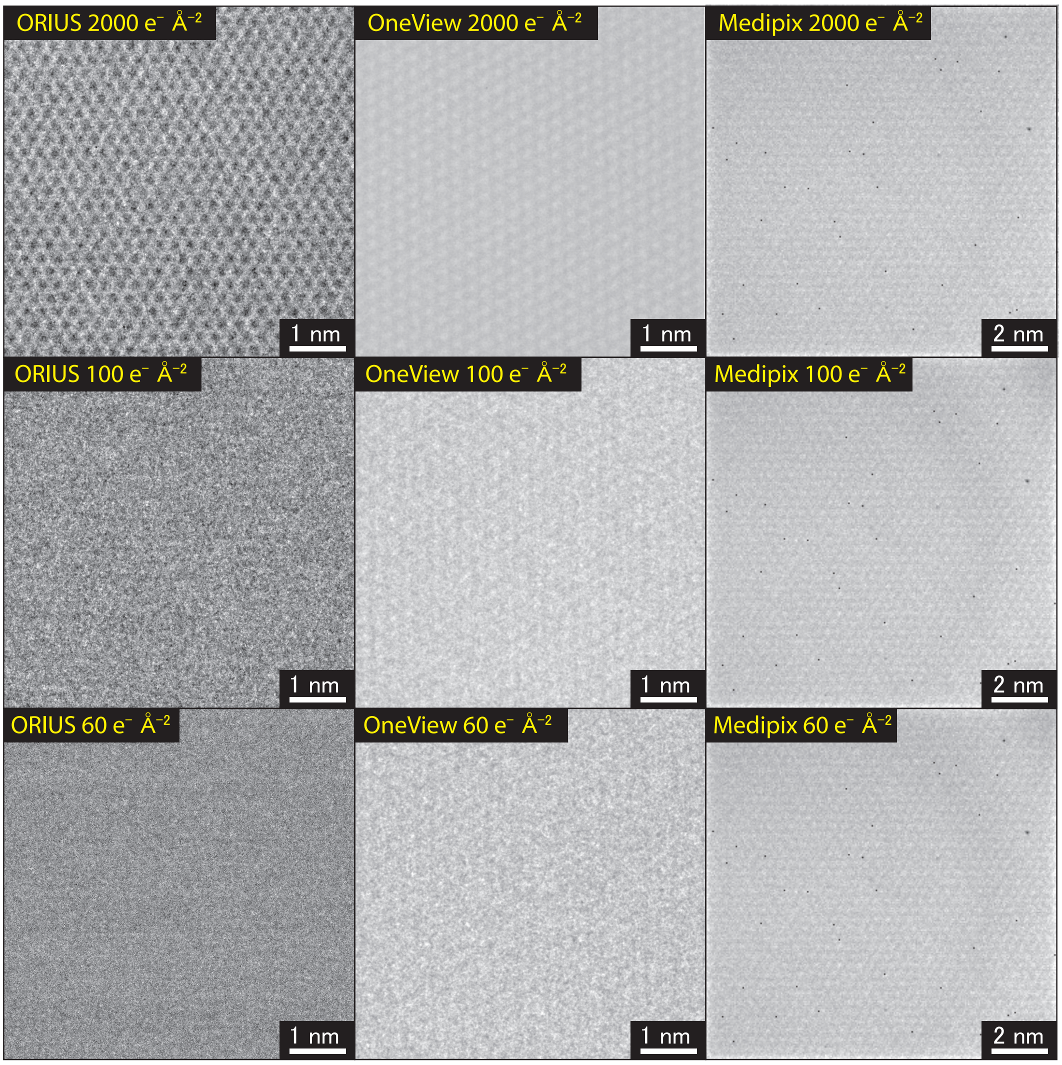

Figure 4.8: Experimental HRTEM images of graphene at different electron dose levels. Column A shows images taken using a Gatan ORIUS™SC1000 camera. Column B shows images taken using a Gatan OneView camera model. Column C shows images taken using a Medipix3 DDD.

4.4 Conclusions

The first part of this chapter investigated the best way to maximise the lifetime of beam-sensitive samples using a combination of 80/200 kV, 300/100 K, and a graphene coating. Several molecular assemblies with different properties were investigated, with results showing that a graphene coating and lower temperature provide optimal protection regardless of accelerating voltage. The change in accelerating voltage between samples for ideal protection implies a complex relationship

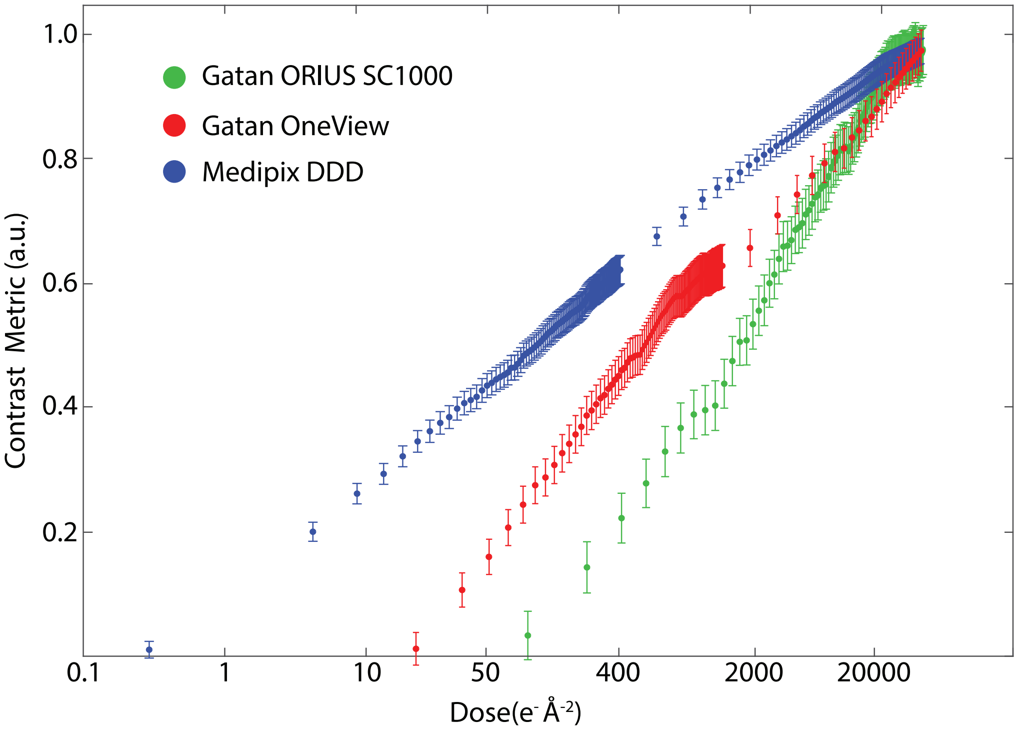

Figure 4.9: Experimental contrast measurements from HRTEM images of graphene taken at different electron dose levels using Gatan ORIUS™SC1000, Gatan OneView, and Medipix3 DDD.

between scattering cross section and energy deposition by knock-on/radiolysis of the beam, as opposed to the common assumption of lower accelerating voltages providing better protection due to the absence of knock-on damage. Although lower voltages indeed reduce the effect of elastic knock-on displacement, this mechanism is not solely what drives the disintegration of molecular crystals and soft-matter systems. The processes involved are clearly very complex, as observed by the widely varying characteristic doses for the varying conditions of accelerating voltage, temperature, and graphene encapsulation. In order to optimise probing conditions, samples must be dealt with on a sample-by-sample basis.

As shown in the second part of this chapter, the use of a DDD provides significant benefits in studying beam-sensitive systems such as supramolecular assemblies. Indeed, without the use of a DDD, the study of such systems via HRTEM would in many instances be impossible, due to the poor performance of scintillator-based detectors at low-dose that are implemented on many HRTEM systems. The development of DDDs and their increase in availability is encouraging, and suggests

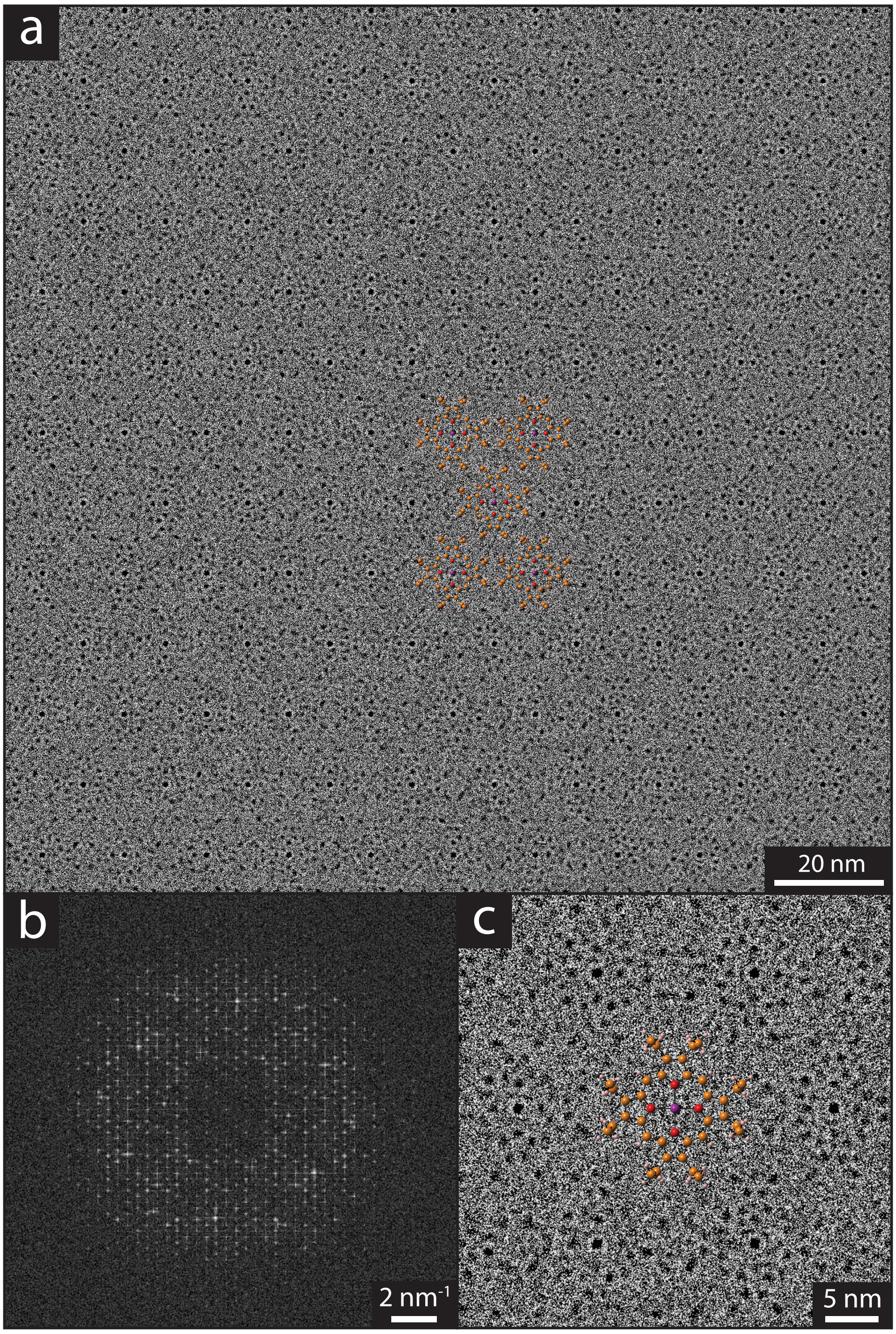

Figure 4.10: Simulated HRTEM image of NiOEP monolayers assembled either side of a layer of graphene using 40 e^{-} Å^{-2} 80 kV electron dose. a) Image with individual NiOEP molecule model overlays. b) FFT of the image in a), showing lattice components present to approximately 7 nm^{-1} resolution. c) Magnified view with overlaid molecular model of a NiOEP unit. Orange atoms indicate carbon, red indicate nitrogen, purple indicate nickel.

that within the near future HRTEM studies of the most beam-sensitive systems will become routine, allowing the true potential of HRTEM to be unlocked in a field that has been lagging behind the studies of inorganic specimens since the inception of aberration corrected TEM.

Chapter 5

Monolayer-to-thin-film transition in supramolecular assemblies: the role of topological protection

5.1 Introduction

Supramolecular assembly is a well-established route for the controlled synthesis of nanomaterials, utilizing non-covalent forces to direct the assembly of complex nanostructures from functional molecular precursors that can be precisely tuned through chemical design. Assembly on surfaces can result in well-ordered 2D molecular crystals, with interactions with the surface stabilizing the molecular overlayer and influencing the nanoscale organization and crystallography [48, 148, 149].

These structures can be further used to direct the assembly of host molecules, acting as templates or traps for the formation of ordered arrays of molecules in subsequent layers [150–153]. Such templated growth shows promise for creating nanostructured films for applications such as organic electronics and optoelectronics,[154] or to control surface reactivity [148, 155, 156].

The structure of the 2D molecular crystal, influenced by its interaction with the surface, usually differs from the preferred 3D molecular crystallography although, with increasing thickness, a molecular film will eventually adopt the 3D crystalline structure. Understanding how this transition occurs, and at what thickness, is essential since most applications of functional organic layers (e.g. in organic electronics, organic photovoltaics, sensors, etc.) rely on films with thicknesses that fall precisely into this transition regime. On the other hand, studying the 2D-3D evolution is particularly challenging because high-resolution analytical techniques that are traditionally used are optimized either for near monolayers (scanning tunneling microscopy, STM) or for thicker films (X-ray diffraction).

Supramolecular self-assembly at surfaces has been extensively investigated on single crystal metal substrates and highly oriented pyrolytic graphite (HOPG) [59, 149], although more recently the study of molecular assembly on crystalline 2D materials, such as graphene [96, 157, 158] and hBN [159], has become increasingly important. For example, non-covalent molecular functionalisation has been widely explored as a means to controllably alter the electronic properties of graphene [106, 160], either for electronic doping [161, 162] or in search of a usable semiconducting band gap [98, 163]. Alternatively, graphene has been proposed as an electrode material in organic electronics [164], with the ability to control molecular assembly to increase the crystallinity and define the orientation of the organic thin film, hence improving its electrical properties [1, 99, 154, 165].

STM has been the method of choice for resolving the 2D structure of the molecular overlayer as it allows direct, non-destructive imaging with sub-molecular resolution [148]. However, it is limited to monolayer (or close-to-monolayer) films and is unable to resolve the crystallographic order in multilayer structures. Early studies used TEM based electron diffraction to probe the structure of self-assembled monolayers and free standing ultrathin molecular films, forming the basis of our understanding of structural transitions from monolayer to multilayer crystalline films [166–168]. These studies were technically challenging: supramolecular assemblies are rapidly damaged by the electron beam, are extremely thin, and are typically carbon-based making it difficult to acquire TEM data with acceptable signal to noise levels. In addition, studying assembly on surfaces required fabrication of electron transparent single crystal TEM supports [166] which was both time consuming and complicated. On the other hand, analysis in the TEM through combined diffraction and imaging experiments has in principle the potential to resolve organic structures with sub-molecular resolution [169, 170].

Recent technical advances in TEM, such as aberration correction for sub-angstrom resolution imaging and single electron detection cameras for low noise acquisition, are opening up new possibilities for studying molecular systems at even higher resolution [171]. For TEM, graphene is a particularly exciting and relevant substrate as it is almost perfectly electron transparent, conductive, crystalline, strong, and stable [172]. When grown on metal substrates, it is often atomically smooth and hence also well-suited for STM imaging, enabling direct comparison between the two techniques.

5.2 Chapter Outline

Here the supramolecular assembly on graphene of benzene-1,4-dicarboxylic acid (terephthalic acid, TPA) and benzene-1,3,5-tricarboxylic acid (trimesic acid, TMA), two molecules with planar phenyl cores that can form intermolecular hydrogen bonds through their carboxylic moieties, is studied; both have been intensively studied as prototypical systems for 2D supramolecular assembly on graphitic substrates [49, 58, 62, 158, 173–175].

*Add brief sentence about TMA/TPA applications *

It is found that both molecules self-assemble on graphene to form well-ordered crystals from a 2D monolayer to thin films of several nanometer thickness. Combining STM, electron diffraction, and HRTEM imaging, a structural transition is identified that occurs as molecular deposition proceeds, and the critical thickness beyond which the film structure is no longer defined by the molecular 2D crystal at the substrate surface is determined. While the structure of TPA thin films varies continuously towards the 3D lattice, TMA retains its planar monolayer structure up to a critical thickness, after which a transition to a polycrystalline film occurs.

These distinctive structural evolutions can be rationalized in terms of the topological differences in the 3D crystallography of the two molecules. The templated 2D structure of TPA can smoothly map to its 3D structure through continuous molecular tilting within the unit cell, whilst the 3D structure of TMA is topologically distinct from its 2D form, so that only an abrupt transition is possible. The concept of topological protection of the 2D structure gives a new tool for the molecular design of nanostructured films and demonstrate how recent advances in TEM make it a powerful tool for studying surface-driven supramolecular self-assembly.

5.3 Results and Discussion

5.3.1 Monolayer structure of TMA and TPA

The packing density (number of molecules per unit area) of TPA is found to be much higher than of TMA. Both were deposited onto CVD-grown graphene-on-copper foils by OMBD and imaged in ambient conditions by STM at the liquid-solid interface under a drop of heptanoic acid. STM images of TMA on Gr-Cu, as in figure 5.1(a), show a hexagonal lattice, consistent with a monolayer of chicken-wire TMA structure (shown in figure 5.1(b)), with lattice parameters $a = b = (1.65 \pm 0.06)$ nm and $\gamma = (60 \pm 1)$ °. These are consistent with the values previously reported for TMA deposited on HOPG [58, 173] and on graphene [158, 176]. While other types of TMA assemblies have been reported on various graphite and graphene substrates [58, 173, 176, 177], only the chicken-wire packing on Gr-Cu was observed, as also described by MacLeod *et al.* [158].

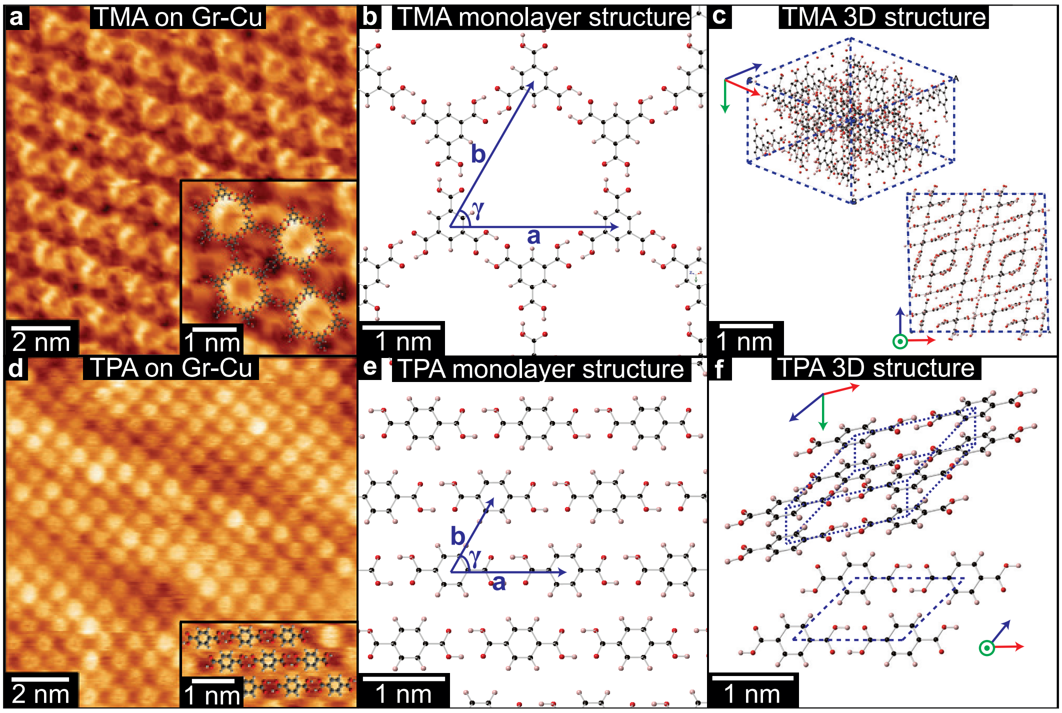

Figure 5.1: STM images of TMA (a) and TPA (d) on Gr-Cu. (Tunneling currents and voltages: (a) I = 50 pA, V = −1.3 V; (d) I = 80 pA, V = −1.5 V.) The insets show enlarged regions with superposed molecular models. Schematics of the 2D chicken-wire structure for TMA (b) and brickwork structure for TPA (e), and of the 3D structures for TMA (c) and TPA (f).

By contrast TPA packs more densely: Figure 5.1(d) shows the characteristic brickwork arrangement of TPA molecules, with lattice parameters $a = (0.95 \pm 0.02)$ nm, $b = (0.75 \pm 0.06)$ nm, and $\gamma = (53 \pm 3)$ °, consistent with previous reports for TPA deposited onto graphene on Pt(111) [175]. For both TPA and TMA, the supramolecular assembly on Gr-Cu is thus similar to that previously found for other graphitic samples.

The difference in the 2D supramolecular packing between TMA and TPA is driven by the difference in their chemical structure. The 3-fold symmetric carboxylic acid moieties of TMA lead to hexagonal assembly, whilst dimeric hydrogen-bonding between the two linearly-aligned carboxylic acid groups in TPA creates strongly bonded molecular rows with a weak interaction between them (figure 5.1 (b) and (e)). The changes in packing are even more profound in their 3D bulk crystalline structures [178, 179], as shown in figure 5.1 (c) and (f). While TMA forms crystals of interweaving planes of TMA molecules that are hydrogen bonded in small units of the chicken-wire structure, for TPA the bulk structure is formed of tilted hydrogen bonded lamellar rows, that resemble quite closely the monolayer structure. Although the molecular packing is denser in the 3D structure, its projected view (figure 5.1(f)) is very similar to the 2D structure shown in figure 5.1(e).

5.3.2 Resolving the structure of TMA thin-films

TEM analysis of TMA deposited on freestanding graphene was used to reveal the structural changes that occur as film thickness increases. TMA and TPA were deposited by OMBD directly onto graphene TEM membranes, and the structures of the resultant films were characterised by TEM imaging and diffraction, as shown in figure 5.2. Simultaneously, the films were deposited on as-grown Gr-Cu for comparative topographic imaging and film thickness measurements by AFM, as shown in figure 5.3.

SAED patterns of TMA on graphene with increasing deposition times are presented in figure 5.2: (a) 15 seconds (measured film thickness of 2.1 ± 0.2 nm, equivalent to ≈ 6 monolayers, ML), (b) 1 minute (5.5 ± 0.2 nm, ≈ 15 ML), (c) 3 minutes (12.3 ± 2.0 nm, equivalent to ≈ 35 ML), (d) 5 minutes (14.7 ± 3.0 nm, equivalent to ≈ 42 ML), (e) 6 minutes (16 ± 2 nm, ≈ 45 ML), (f) 9 minutes (32 ± 4 nm, equivalent to ≈ 95 ML), (g) 12 minutes (36 ± 6 nm, equivalent to ≈ 110 ML), and (h) 18 minutes (60 ± 10 nm, ≈ 170 ML). Figure 5.2(a1 - d1) show low-magnification TEM images for the deposition times: (a) 15 seconds, (b) 1 minute, (c) 6 minutes, (d) 18 minutes. For all deposition times less than 18 minutes, the TEM images show uniform contrast and the only obvious features can be attributed to residue from the transfer process used to make the graphene membranes, suggesting the TMA is deposited as a uniform thin film, as also confirmed by AFM topography images (figure 5.3(a)). For the 18 minute deposition, there are clear variations in TEM contrast, with features of ≈ 100 nm, as also seen by AFM (figure 5.3(a)), suggesting a granular structure and polycrystalline film.

Despite TEM images showing little contrast, SAED reveals the molecular ordering in TMA layers and their orientation relative to the free-standing graphene substrate. For all films except the 18 minute deposition, sharp diffraction spots are seen with spacings and symmetry consistent with the 2D chicken-wire TMA struc-

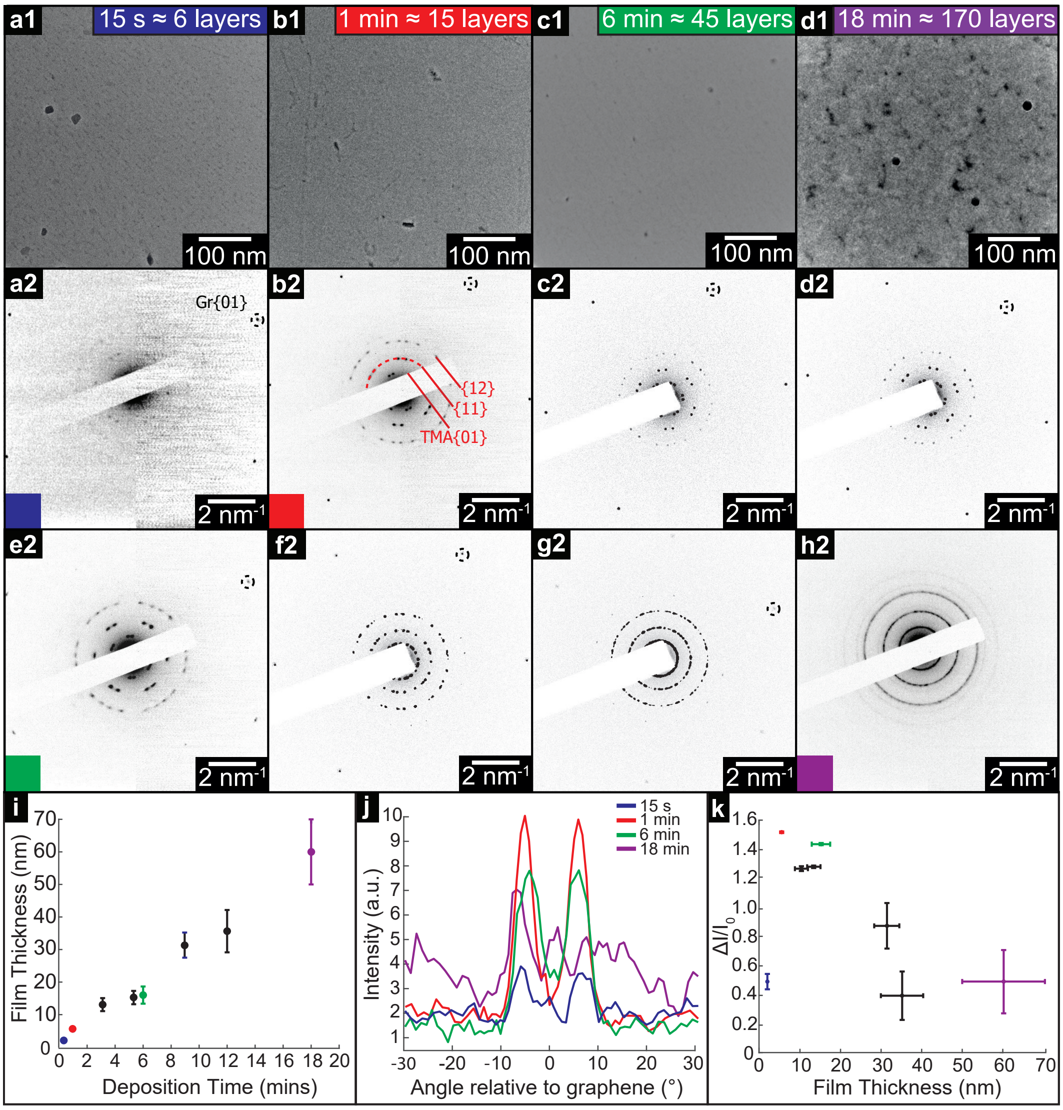

Figure 5.2: TEM analysis of thin films of TMA deposited onto freestanding graphene. (a1) to (d1), brightfield TEM images of TMA thin films of increasing deposition time as marked, with corresponding SAED patterns (a2, b2, e2, h2) on which graphene and TMA diffraction peaks are labeled. SAED of thin films for 15 s to 18 minute depositions are presented in (a2) - (h2). (i) TMA film thickness, as measured by AFM, with deposition time. (j) Radial line profiles of the diffraction intensity through the TMA {11} diffraction peaks, as labeled by the dashed arc on (b2); here 0° is defined by the graphene {01} spots. (k) Modulation of diffraction intensity, $\Delta I/I_0$ along TMA {11} profile, as a function of film thickness.

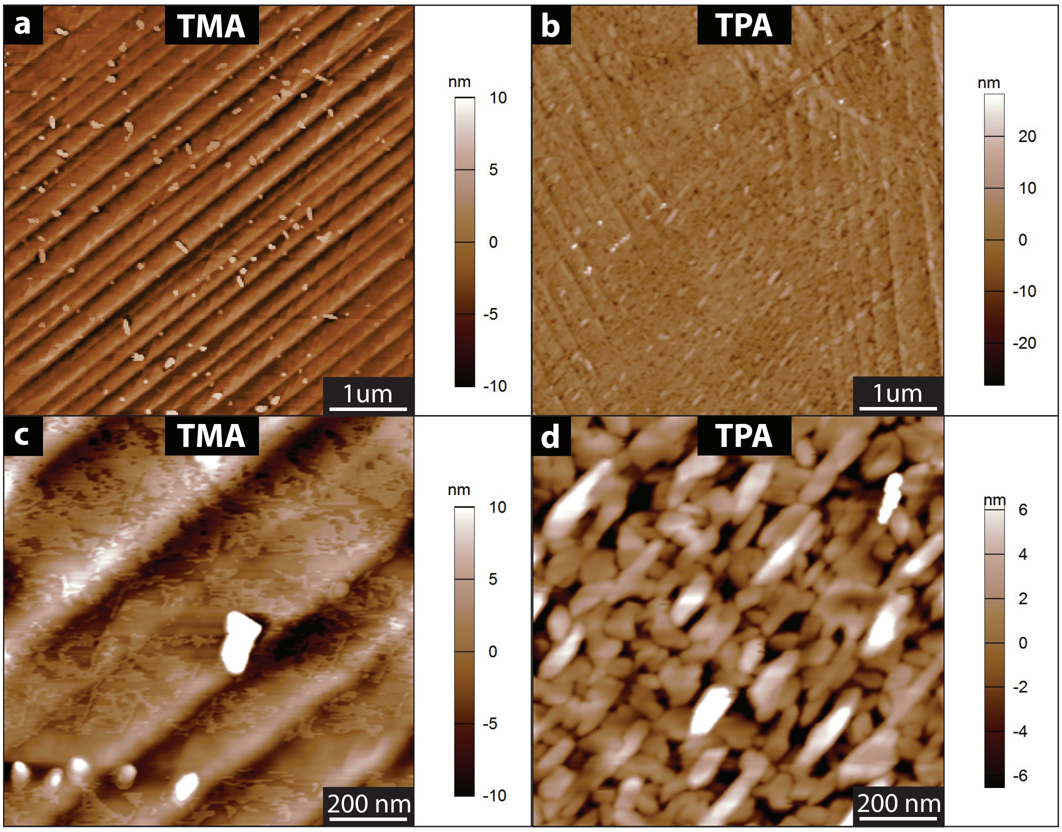

Figure 5.3: Tapping mode AFM images of TMA, (a) and (c), and TPA films, (b) and (d), on graphene on copper for 6 minute depositions.

ture observed by STM. TMA lattice parameters calculated from these diffractions spots are given in Table 5.1: using the graphene diffraction spots to calibrate the diffraction patterns [88] allows the TMA lattice parameters to be easily measured from the electron diffractions spots to a significantly higher accuracy and precision than those obtained from STM images, as shown in Table 5.1.

Two distinct orientations of the chicken wire lattice are observed, equally spaced (6.8 ± 0.1) ° either side of the graphene orientation, indicating an epitaxial relationship between the TMA and graphene lattices. Two orientations of the TMA lattice in STM images of monolayer TMA on Gr-Cu were also observed, as shown in figure 5.4. The STM measured angles of (7 ± 1) ° relative to the graphene lattice are consistent with the electron diffraction results. Macleod *et al.* [158] studied supramolecular assembly of monolayer TMA on graphite and graphene by STM, finding similar lattice parameters to those measured here also by STM, and deduced the following epitaxy matrix relating the TMA lattice vectors, $\mathbf{a}_{TMA}$, to those of graphene, $\mathbf{a}_{Gr}$:

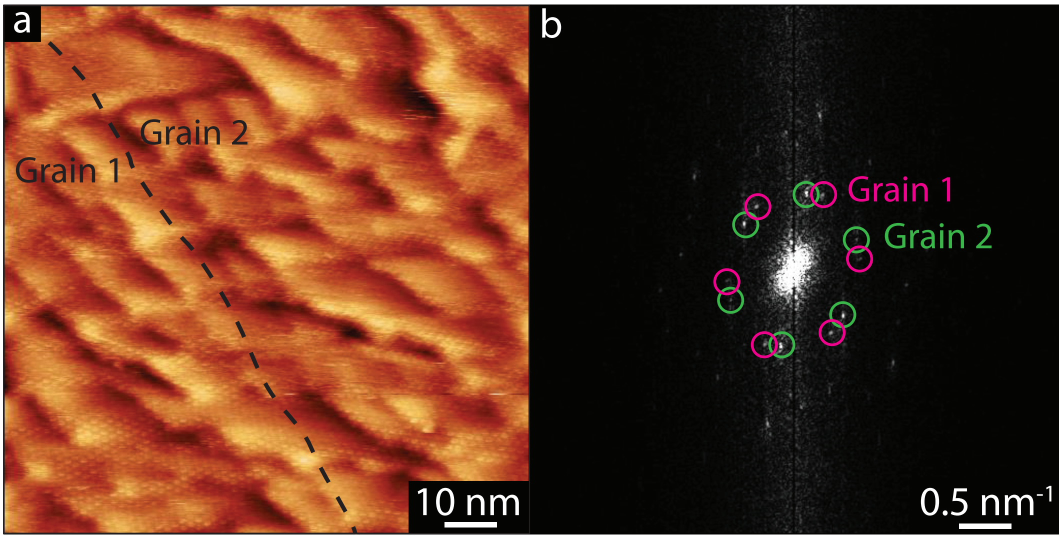

Figure 5.4: STM of TMA on graphene. (a) Large scale STM image (100×100 nm^2) of a TMA monolayer at the interface between heptanoic acid and graphene on copper. Dashed line marks the boundary between two differently oriented TMA grains. Tunneling parameters: V = −1.3 V, I = 50 pA. (b) FFT of the whole image indicating the presence of two distinct orientations of the TMA chicken-wire lattice.

$$\mathbf{a}_{TMA} = \begin{bmatrix} 6 & 1 \\ -1 & 7 \end{bmatrix} \mathbf{a}_{Gr}$$

This relationship predicts the TMA lattice parameter to be $\sqrt{43}$ times the graphene lattice constant, i.e. a=b=0.2461$\sqrt{43}$=1.614 nm, and the angle between the TMA and the graphene lattice to be $\cos^{-1}(13/\sqrt{172}) = 7.589°$. Although the STM results are consistent, within uncertainties, with these values, the higher accuracy and precision of the SAED measurements reveals that, for the films analyzed in figure 5.2, the relationship between TMA and graphene lattices is not exactly described by such an epitaxy matrix.

This typifies van der Waals epitaxy [37]. Due to the weak van der Waals interactions between surface and molecular overlayer, the 2D molecular structure is not constrained to exactly follow the lattice parameters of the surface but is relaxed and almost unstrained, allowing lattice mismatch and differences in symmetry between surface and overlayer. Despite this, the orientation of the 2D molecular layer is defined relative to the graphene {01} spots.

For thick films, this epitaxial relationship no longer holds. Electron diffraction from 9 minute (≈ 95 ML) and 12 minute (≈ 110 ML) films (figure 5.2(f2,g2)) show many distinct TMA orientations, while the 18 minute (≈ 170 ML) TMA depo-

Table 5.1: Film thicknesses (determined by AFM), lattice parameters and characteristic dose calculated for the monolayer and thin films of TMA. For the 18 min deposition, the angle γ is measured from 2D Fourier transforms of HRTEM images (see figure 5.5).

Deposition time	Thickness (nm)	a (nm)	b (nm)	γ (°)	D_c ($e^-\ nm^{-2}$)
Monolayer (STM)	-	1.65±0.06	1.65±0.06	60±1	-
15 seconds	2.1±0.2	1.64±0.02	1.64±0.02	60.0±0.2	-
1 minute	5.5±0.2	1.64±0.02	1.64±0.02	60.0±0.3	13±3
6 minutes	16±2	1.65±0.02	1.65±0.02	60.0±0.2	100±50

sition shows rings rather than spots, as shown in figure 5.2(h2), though with similar spacings, indicating a polycrystalline film with random in-plane orientation relative to the graphene.

The SAED patterns can be analysed to give a more quantitative insight into the degree of order in the thin films [168]. Figure 5.2(j) shows radial line profiles through the {11} TMA diffraction peaks; here 0° is defined by the graphene {01} spots. The two peaks corresponding to the two orientations of TMA are readily apparent for all but the 18 min deposition. Defining I_0 as the average intensity and ΔI as the difference between maximum and average intensity, the intensity modulation $\Delta I/I_0$ along the arcs gives a relative measure of the order within the film and is plotted in figure 5.2(k) as a function of film thickness. The apparent order increases up to a maximum at $\approx$ 15 nm, due to the diffraction peak intensity increasing relative to the local background. Beyond this critical thickness, the intensity modulation (I_0) decays rapidly as more TMA orientations appear, indicating a transition to a rotationally disordered phase with textured but randomly oriented grains.

As expected, the thin films of TMA rapidly degraded upon exposure to the electron beam. For such materials, structural analysis should be performed with low levels of exposure to the electron beam, below the characteristic dose [90]. As described in the previous chapter, the characteristic dose was calculated for each film by measuring the decay in intensity of diffraction spots with exposure time, as shown in Table 5.1. All diffraction results were acquired under low dose conditions with total doses less than this characteristic dose, and so are representative of the film structure after assembly.

Electron diffraction reveals the spatially averaged crystal structure of TMA on suspended graphene, but leaves important questions open. Are the two orientations within the TMA thin films separated into domains (as suggested by STM in the monolayer), or stacked one on the other? If in domains, what is the domain size? Similarly for the thicker, polycrystalline film, what is the grain size and do they persist through the film thickness? Here these questions are addressed by directly imaging the TMA layers with HRTEM. All images were acquired such that the total exposure was less than the characteristic dose, as measured from the diffraction patterns, to ensure that the observed structure was typical of the as-deposited film. An example image from a 1 minute TMA deposition on graphene is shown in figure 5.5(a); although there are no immediately obvious features, a 2D fast Fourier transform (FFT, inset in top right corner) shows clear spots and closely resembles the SAED patterns in figure 5.2. This FFT of the whole image is consistent with the expected 2D TMA structure with two orientations, labeled by red and blue circles in the FFT (henceforth orientation 1 and 2). Selecting smaller areas of the image, FFTs corresponding to only one orientation are found, as shown in figure 5.5 (b1) and (b2) taken from the dashed boxes 1 and 2 in figure 5.5(a). By analyzing the relative intensity of these two orientations in selected area FFTs, a map of the local TMA orientation can be constructed, as shown in figure 5.6. Here, the intensity of red gives the intensity of orientation 1 and, correspondingly, the intensity of blue gives that of orientation 2. This color map (figure 5.5(c)) thus shows that the two orientations are distinct - i.e. they are separated into domains, with stacked layers of the same orientation in each domain - and reveals that the average domain size is ≈ 40 nm in diameter for all film thicknesses, as measured from figure 5.6.

Unlike the diffraction patterns, the Fourier transform operation generates both amplitude and phase information which, when recombined, can be used to reconstruct a real space image. Individual structure factor amplitudes and phases are measured in a Fourier transform (power spectrum) of an image of a unit cell or multiple unit cells (these appear as the lattice spots in the power spectrum). The original unit cell potential $\phi(\mathbf{r})$ is therefore related to the structure factor $F(\boldsymbol{\mu})$ for the unit cell through a scaled inverse Fourier transform [64]:

$$\phi(\mathbf{r}) = F^{-1}[F(\boldsymbol{\mu})] = \frac{h^2}{2\pi m_e V} \sum_{i=1}^{\infty} F(\boldsymbol{\mu}_i) \exp\left(\boldsymbol{\mu}_i \cdot \mathbf{r}\right) \tag{5.1}$$

Truncating this series to some finite order of $\boldsymbol{\mu}$, and removing the scaling factor, gives an approximation to the unit cell potential $\phi(\mathbf{r})$:

$$\phi(\mathbf{r}) \approx \sum_{i=1}^{N} F(\boldsymbol{\mu}_i) \exp\left(\boldsymbol{\mu}_i \cdot \mathbf{r}\right) \tag{5.2}$$

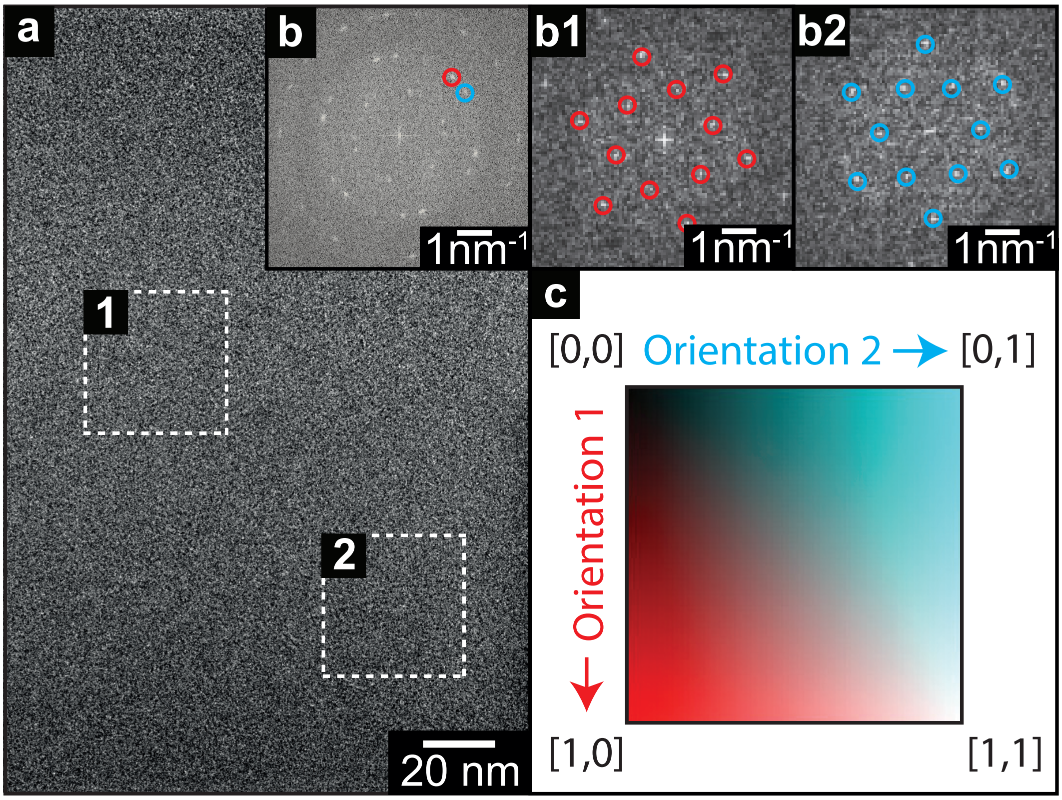

Figure 5.5: HRTEM of TMA (1 minute deposition) on graphene. (a) Brightfield TEM image. (b) Corresponding FFT. (b1) FFT of selected region 1 in (a). (b2) FFT of selected region 2 in (a). FFT spots due to TMA are circled in red/blue showing the two different TMA orientations present. (c) Colour map of TMA orientations, as used in figure 5.6, formed from processing the image in panel (a); the red intensity corresponds to the intensity of orientation 1 and, correspondingly, the blue intensity is due to orientation 2. White regions indicate the presence of both orientations, and dark regions indicate the presence of neither orientation.

This truncation results in a loss of resolution, resulting from the limited resolving power of the microscope and finite number of structure factors present in the image Fourier transform [64]. With knowledge of the lattice structure from SAED, the amplitude and phases from peaks in the FFT of HRTEM images were measured out to 0.7 Å^{-1} resolution. Using Equation 5.2 and a set of real-space co-ordinate positions, reconstructed TEM images of the lattice can be constructed (figure 5.7(a)). This is, in effect, a modified Bragg filter averaging over the entire crystal structure present in the HRTEM image.

The reconstructed image is consistent with a multislice image simulation, figure 5.7(b), assuming an 'AA' stacked molecular structure, as shown in the molec-

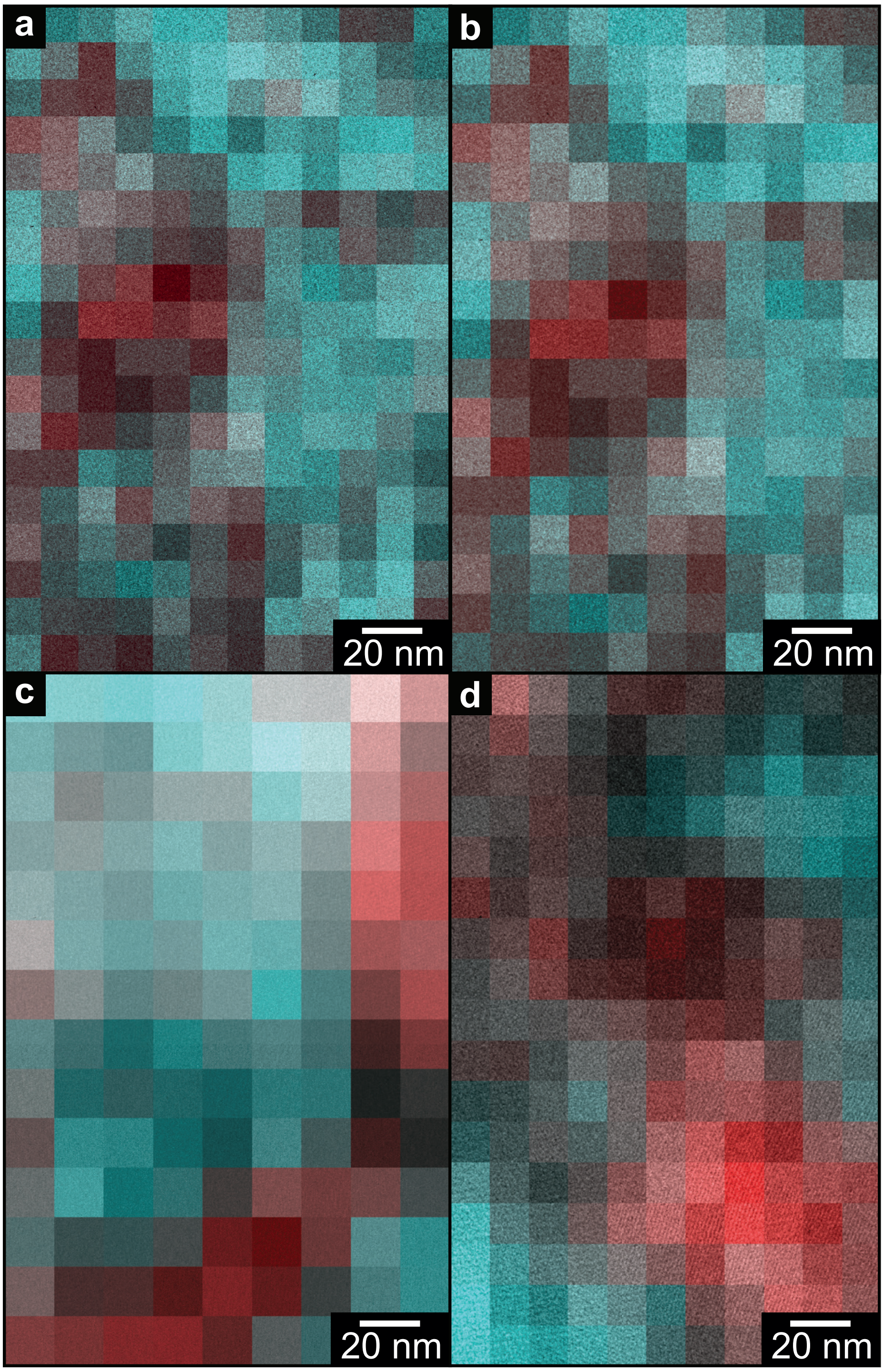

Figure 5.6: HRTEM TMA film structure colour maps, processed using the colour map presented in figure 5.5. (a) 15 s, (b) 1 minute, (c) 6 minutes, (d) 18 minutes.

ular model in figure 5.7 (d), but not with structures that do not assume direct molecular stacking, figure 5.7(c,e). HRTEM imaging thus proves that the TMA molecules are stacked vertically one on another, consistent with density functional theory (DFT) calculations of the most energetically favorable stacking geometry [174], and hence that initially TMA film growth proceeds via a layer-by-layer, or Frank-van der Merwe, growth mode [45]. Significantly, this stacking is expected to create well-ordered arrays of high-aspect ratio nanopores, around 1.5 nm in diameter and up to 15 nm deep, open at the top and reaching the pristine graphene surface at the bottom.

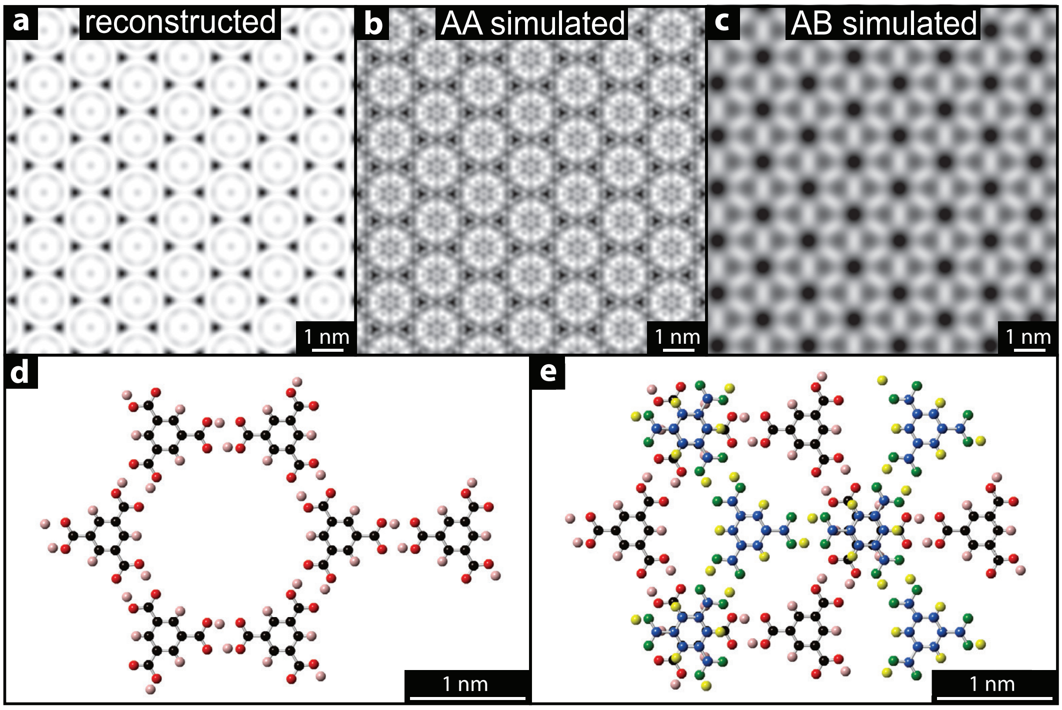

Figure 5.7: High resolution reconstruction of the TMA film structure. (a) Reconstructed high-resolution image of the TMA structure from the HRTEM image data in figure 5(a). (b) Multislice image simulation from the 'AA'−stacked molecular model shown (d). (c) Multislice image simulation from the 'AB'−stacked molecular model shown in (e). Multislice simulations were performed using spherical aberration −1 μm and defocus −40 nm (as measured from HRTEM images).

For films beyond the critical thickness, where SAED shows polycrystalline rings, high-resolution imaging shows a small grain size (< 30 nm) with evidence that the grains do not normally persist through the film (figure 5.6), again indicative of a polycrystalline film.

5.3.3 Structural transition in TPA thin-films

A similar methodology was used to study structural transitions in TPA thin films on graphene. Figure 5.8 (a) to (d) show brightfield TEM images and corresponding SAED patterns of TPA thin films with increasing deposition times as marked. The TEM images show a strikingly different trend to that observed for TMA: fiber-like features $\approx$ 100 nm in length are apparent from 1 minute and persist at longer deposition times, suggesting that TPA forms 3D islands from an early stage. These features are also clearly visible in AFM images (figure 5.3). The presence of an initial wetting monolayer, as suggested by STM (figure 5.1), combined with topographical changes revealed in AFM images (figure 5.3), suggest that TPA on graphene is following either a layer-plus-island (Stranski-Krastanov) growth mode [45], although this is not confirmed. It is possible that the film could be growing via an island (Volmer Weber) mode. In order to investigate this, the presence of the initial wetting monolayer in electron diffraction patterns was investigated, although it wasn't observed. Due to the low SNR of the TPA signal, the lack of observation was unusable as a growth mode probe.

The corresponding SAED patterns also show behavior distinct to that observed for TMA. For the 15 s deposition, clear diffraction spots are apparent which are consistent with the measurements taken for the brickwork 2D lattice observed for the monolayer by STM, with 6 distinct orientations symmetrically arranged relative to the graphene lattice (figure 5.9). This implies a similar brickwork structure growing in a templated fashion in three dimensions. As the deposition time increases, although the graphene diffraction spots are still as clear and well-defined as before, SAED from the TPA thin films gives short arcs rather than sharp spots. Radial line profiles through the TPA {01} arcs are shown in figure 5.8 (f) with the corresponding $\Delta I/I_0$ shown in figure 5.8 (g). The line profiles are roughly symmetric relative to the graphene {01}, indicating that van der Waals epitaxy still plays an important role in defining the growth orientations. Both the width of the TPA {01} diffraction peaks and $\Delta I/I_0$ increase with deposition time. However, careful analysis of the positions of these diffraction arcs shows an important difference compared to TMA: the electron diffraction spacings, and hence the 2D projection of the lattice parameters, change with deposition time. This is also observed in FFTs of high-resolution images (figure 5.10) which show the same lattice parameters as the corresponding diffraction patterns. Interestingly, these FFTs show distinct spots rather than arcs, indicating that the SAED diffraction arcs are due to small changes in orientation between grains rather than molecular tilting within grains [180]. The sharp spots in the FFTs enable accurate measurements of the angle between lattice vectors, as

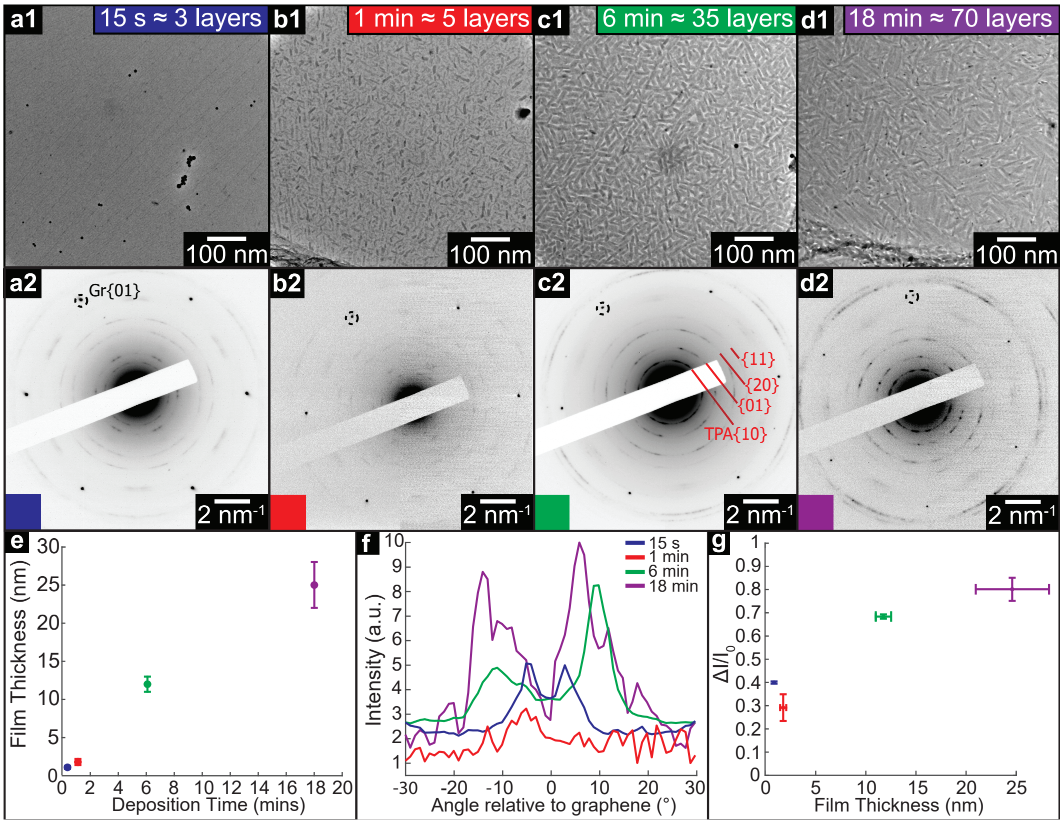

Figure 5.8: TEM analysis of thin films of TPA on graphene. (a1) to (d1), bright-field TEM images of TPA thin films of increasing deposition time (15 s, 1 min, 6 min, and 18 min), with corresponding electron diffraction patterns (a2) to (d2) on which graphene and TPA diffraction peaks are labeled. (e) TPA film thickness, as measured by AFM, as a function of deposition time. (f) Azimuthal line profiles of the diffraction intensity through the TPA {01} diffraction peaks; 0° is defined by the graphene {10} spots. (g) Modulation of diffraction intensity, $\Delta I/I_0$ along TPA {11} azimuths, as a function of film thickness.

Table 5.2: Film thickness, lattice parameters and characteristic dose for TPA on graphene. Also shown are the lattice projections looking down the c-axis of the reported TPA bulk structure [179]. Note that the exact 3D crystallographic orientation of the thicker films here is not known.

Deposition time	Thickness (nm)	a (nm)	b (nm)	γ (°)	Unit Cell area (nm^2)
Monolayer (STM)	-	0.95±0.02	0.75±0.06	53±3	0.57±0.05
15 seconds	1.1±0.4	0.95±0.02	0.74±0.02	50±2	0.54±0.02
1 minute	1.2±0.2	0.90±0.02	0.72±0.02	53±2	0.52±0.02
6 minutes	12±3	0.85±0.02	0.62±0.02	57±2	0.44±0.02
18 minutes	25±1	0.86±0.02	0.60±0.02	56±2	0.43±0.02
Bulk projection	-	0.92±0.01	0.65±0.01	52±1	0.47±0.01

presented in Table 5.2. The high-resolution images also show that the crystalline grain size here is ≈ 20 nm (figure 5.11), consistent with the width of the fibers in the low magnification brightfield images.

The key result from TEM analysis of TPA films on graphene is the change in projected lattice parameters with deposition time, as summarized in Table 5.2. The reduction in both a and b lattice parameters, and the subsequent contraction of the unit cell area, is consistent with the molecules tilting with respect to the graphene surface and hence packing more densely, as in the bulk structure. The gradual change observed here reflects the smooth transition that can occur from the 2D, flat, structure to the 3D, tilted, structure.

The differences between the TMA and TPA film deposition are intriguing. TMA deposition results in layer-by-layer growth, templating the 2D structure upwards and creating open nanopores up to ≈ 20 nm deep and ≈ 1.5 nm wide, until, after a critical thickness of $>$ 20 nm, the film abruptly becomes polycrystalline with random in-plane orientations. By contrast, TPA rapidly forms fiber-like islands after the first 2D molecular overlayer and its lattice parameters gradually reduce from those of the 2D structure, smoothly becoming more consistent with the bulk structure.

The origin of these differences is speculated on through inspection of their 2D structure (stabilized by interactions with their surface) relative to their 3D crystallography (determined only by their intermolecular interactions). The TPA bulk structure is characterized by parallel hydrogen-bonded lamellar rows and its (001) plane displays a structural similarity with the 2D lattice of TPA-on-graphene (the main difference being a contracted lattice parameter in 3D, through tilting of the molecule towards the [223] direction). As the film thickness increases, surface-

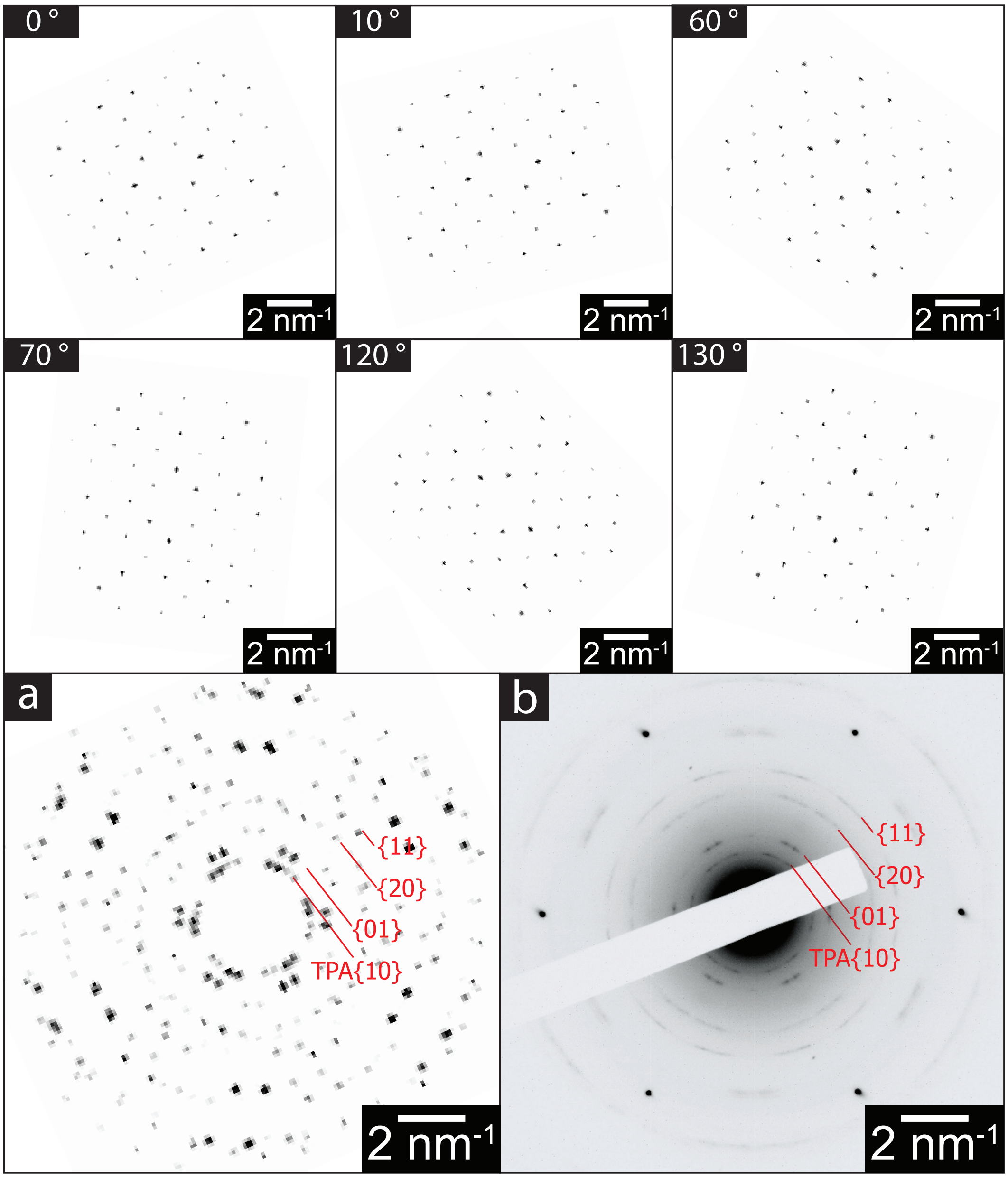

Figure 5.9: Comparison between simulated diffraction patterns and experimental measurements for 15 s TPA deposition. Simulated electron diffraction patterns, assuming the 2D brickwork structure, are shown at six different orientations as labeled. The sum of these simulations is presented in (a) and shows good correspondence with the experimental pattern shown in (b). This indicates the presence of six TPA grains within the selected area used for diffraction

interactions become less significant and the intermolecular interactions are expected to increasingly dominate. This explains the observed behavior of TPA; the 2D struc-

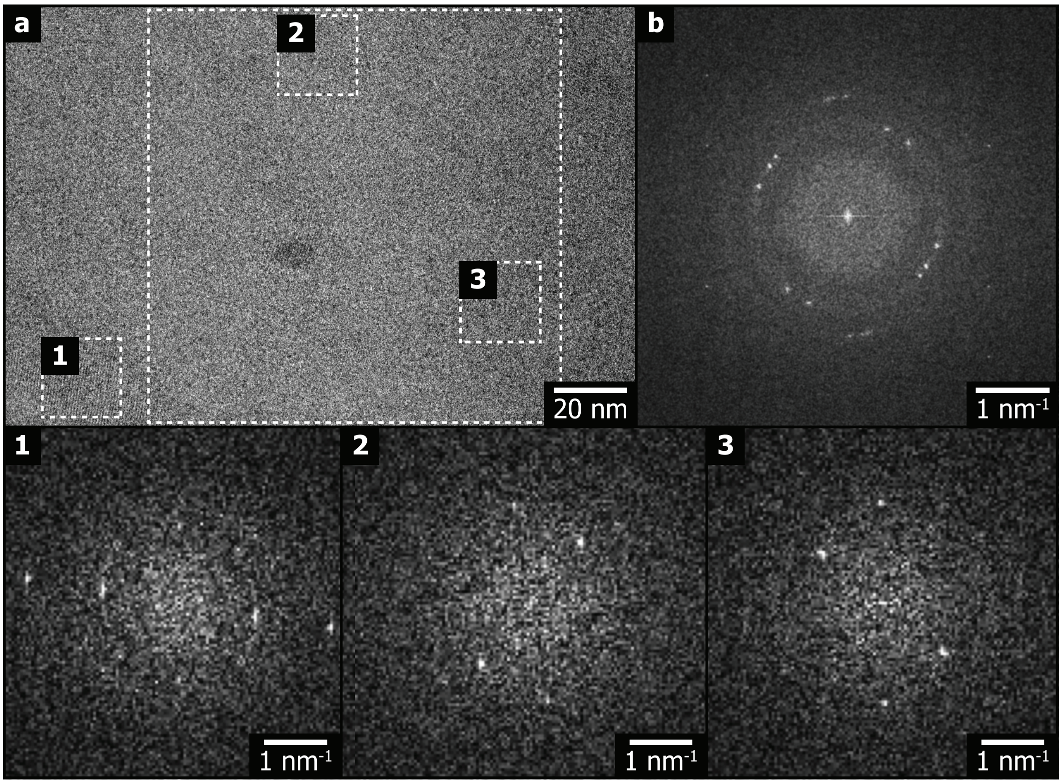

Figure 5.10: HRTEM of the 1 minute-deposition of TPA. Brightfield image, (a), and corresponding FFTs from the large dashed box, (b), and the smaller dashed boxes 1, 2 and 3 as labeled.

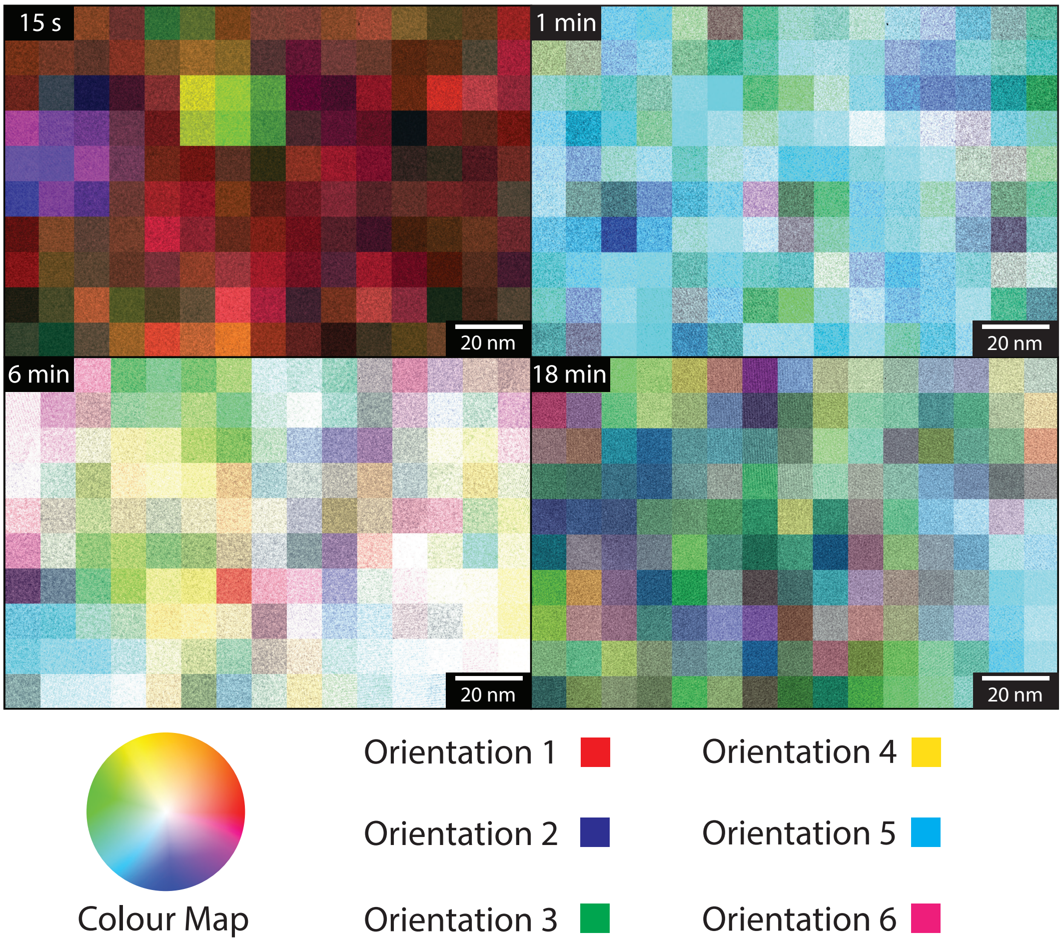

Figure 5.11: HRTEM TPA film structure colour maps. Polycrystalline grains are apparent at all film thicknesses.

ture is a distorted (strained) component of the 3D structure and hence a smooth transition can occur. This also explains the formation of crystallites (here fiber-like) to reduce strain [57].

However, the 3D crystal structure of TMA is composed by interpenetrating non-planar chicken-wire frameworks and is thus very different and, crucially, topologically distinct from the planar 2D molecular lattice of the monolayer. As a result, the 2D layer cannot be thought of as a strained component of the 3D structure, and no smooth transition is possible. Hence, the TMA templates from the initial 2D layer until an abrupt transition to a polycrystalline phase; the 2D structure is topologically protected against transitions to the 3D structure.

5.4 Conclusions

A fundamentally new insight into the growth of supramolecular thin films on surfaces is demonstrated through a detailed study into the structural evolution of layers of prototypical benzenecarboxylic acids. To achieve this, an innovative combination of low-dose HRTEM and STM was used to accurately determine molecular-resolution structural information on films of increasing thickness from monolayer through to tens of nanometers, a precision and range that is difficult to attain by other analytical techniques. For both TMA and TPA, the structure and orientation of the first molecular overlayer are dictated by the comparatively strong hydrogen bonding between molecules and the interactions with the graphene surface that determine a weak van der Waals epitaxial relationship. As the film thickness increases beyond a monolayer, however, TMA and TPA display distinctly different behaviors, despite their chemical similarities. TMA templates from the 2D structure, stacking molecular layers directly on top of each other until, above a certain thickness, the film transitions to a polycrystalline phase with random in-plane orientations. By contrast, TPA forms fiber-like islands and the in-plane lattice parameters change continuously with thickness, smoothly becoming more consistent with the bulk structure. It is proposed that these differences in behavior can be understood through comparison between the 2D and 3D structures of the two molecules: the bulk structure of TMA is topologically distinct from the monolayer structure with no possible smooth transition between the two, whereas, for TPA, tilting of the molecules with respect to the surface gives a continuous transition from 2D to 3D structures. As a result, the 2D TMA structure is topologically protected and templates through the initial film growth. This new insight - topological protection of the 2D structure - will help design functional structural features into molecular building blocks in order to control the growth of organic thin films by supramolecular assembly.

Chapter 6

Remote molecular epitaxy across graphene

6.1 Introduction

The study of macrocyclic compounds such as porphyrins and phthalocyanines is important due to their tendency to form organised self-assembled structures on a wide variety of substrates. These are interesting from both a fundamental and technological viewpoint, as the extended π-electron systems that are formed from the large ordering of planar molecules makes them useful for a variety of organic electronic applications such as photovoltaic cells [181], organic light-emitting diodes [182], gas sensors [183], and molecular wires [184].

Directed assembly of molecules on surfaces occurs due to a combination of molecule-molecule and molecule-substrate interactions, and can be utilized in the formation of molecular thin films for a wide variety of purposes [96, 157, 185]. The factors influencing the resultant assembly are numerous, and can be categorised into three key groups: molecule properties, substrate properties, and environmental factors. These are summarised in figure 6.1.

Molecule properties include its size, shape, and composition. These factors determine the intermolecular bonding that exists, and can result in a host of different intermolecular bonding mechanisms. These include electrostatic, hydrogen, and van der Waals bonding. As shown in chapter 5, the crystal growth behaviour of TMA compared to TPA is completely different, despite the chemical similarity between the molecules [6]. Self-assembly of molecular films can be further influenced by the state of surrounding molecular grains through Ostwald ripening effects. Ostwald ripening, whereby molecules detach from small islands with high chemical potential

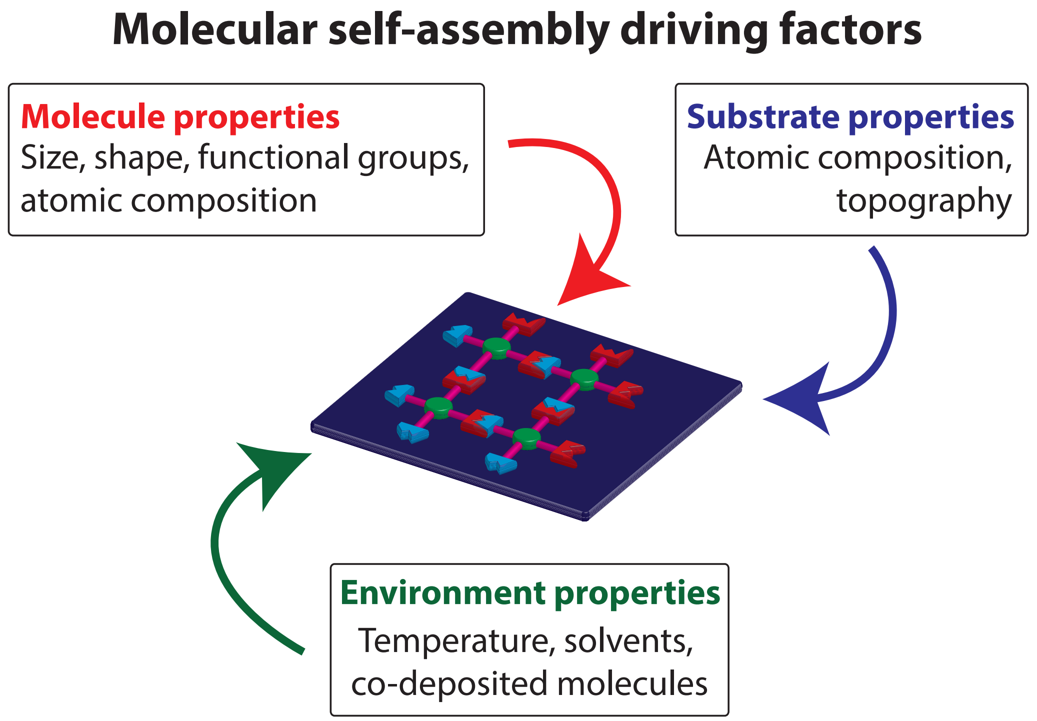

Figure 6.1: Key driving factors determining the resultant molecular self-assembly structure.

as monomers, diffuse on the support, and subsequently attach to larger islands with a lower chemical potential, leads to the growth of larger islands at the expense of smaller islands [186]. An initial monolayer can spontaneously crystallize via homogeneous nucleation in different locations with different network structures, before evolving into a smaller series of much larger grains with a critical radius [187–189]. The deposition of multiple different molecular species can also have a significant effect on the resulting assembly through host-guest architecture interactions and limitations in the available substrate adsorption sites [59, 151, 190–192].

Substrate properties include its atomic structure and topography. These factors can produce adsorption sites that are more favourable to certain molecules, driving an epitaxial relationship in the resultant assembly [59]. The favourable assembly sites can be produced from both topographical height differences as well as electrostatic periodicities, and can result in residual charges being transferred to the adsorbed molecule [59, 182, 193–195]. This can influence the state of the adsorbed molecule, producing dipole moments [194] and chromatic shifts in the fluorescence spectra [159].

Environmental factors can include the temperature at which depositions are carried out and the nature of the solvent used in liquid-phase deposition. Previous studies have shown that very similar porphyrin-based molecules can have different desorption rates at equal temperatures when deposited together [196]. Controlling the temperature of the substrate during molecular film growth has also been used to control the crystallography of the resulting film [197, 198]. Finally, entirely different TMA polymorph structures can be achieved when depositing using a specific alkanoic acid [49].

As well as the substrate influencing the geometry of the self-assembly and the state of individual molecules, the substrate can also be strongly modified by the molecular adsorbate [59]. Previous investigations have revealed an organic layer interacting strongly enough with a substrate such that its surface atoms rearrange: The Au(111) herring-bone reconstruction is strongly modified when a tetrathiafulvalene (TTF) derivative, a strong electron donor molecule, is adsorbed [59]. In addition, the structure of the Cu(100) surface is distorted after the adsorption of the strong electron acceptor tetracyanoquinodimethane TCNQ; coppers atoms involved in bonding with the TCNQ cyano groups are pulled away from the surface and towards the molecules [59].

Recently, the use of 2D materials, such as graphene, as molecular substrates has received increasing attention [96, 177]. 2D materials are characterized by strong in-plane bonding but only weak out-of-plane interactions. These weak interactions can be sufficient for van der Waals epitaxy whereby crystalline molecular films are grown with their orientation specified relative to the 2D substrate, but equally crystalline molecular film growth can proceed without an epitaxial relationship to the 2D layer [1, 152, 165, 199], demonstrating the importance of the weak interactions between molecule and 2D substrate.

Interestingly, at a single atom thick, graphene can be considered as both a 2D substrate and a membrane, with both top and bottom identical crystalline surfaces separated by only a single atom. However, graphene is impermeable to atoms and molecules, not even helium can pass through the lattice [23], which presents the intriguing question: To what extent can interactions extend across the graphene membrane?

As has been shown in previous studies investigating the wetting transparency documented for graphene, it is possible for water molecules to feel an interaction either side of a graphene monolayer in solution that diminishes on the order of 0.9 nm [200, 201]. The existence of a remote van der Waals interaction has been further demonstrated in the homoepitaxial growth of zinc-blende GaAs(001) thin films, whereby GaAs(001) films can be grown with an epitaxial relationship to an underlying GaAs(001) film coated in monolayer graphene [202]. During this study, density functional theory (DFT) computations were performed to probe the transmission of crystallographic information of GaAs through graphene, with significant charge density existing between GaAs slabs. This charge density was shown to diminish when the GaAs-GaAs separation was increased beyond 0.9 nm. Interestingly, this study did not account for the effects of van der Waals interactions between layers, which play a significant role in the formation of epitaxial films and molecules assemblies. Whether such a remote interaction can exist between molecular assemblies remains unanswered.

6.2 Chapter Outline

This chapter investigates the existence of remote van der Waals interaction between molecular assemblies. In this work the first TEM investigations of supramolecular assemblies adsorbed onto both surfaces of a freestanding graphene membrane are reported. Using a combination of LD-SAED and STM, the molecular structures of self-assembled Ni(II) octaethylporphyrin (NiOEP) and 2H-octaethylporphyrin (OEP) on metal-supported and freestanding graphene are studied. Both have been intensively studied as prototypical systems for 2D supramolecular assembly on a range of substrates, including HOPG [203–209].

STM measurements reveal that NiOEP and OEP assume a flat 2D lattice on both copper-supported graphene and on HOPG. LD-SAED measurements of NiOEP deposited on both the top and bottom faces of a suspended graphene membrane reveal the same 2D molecular lattice. There is no epitaxial alignment between the graphene lattice and the molecular layers but, crucially, the two molecular films on either side of the graphene are aligned with each other. By contrast, when the molecular layers are separated by two layers of graphene, they are randomly oriented with respect to each other and with respect to the graphene. The same results - ordered 2D molecular layer on each graphene surface, but aligned only when separated by monolayer graphene - are found for self-assembled octaethylporphyrin (OEP) without a metal centre.

These results demonstrate that graphene is at least partially transparent to molecule-molecule interactions, but these are rendered ineffective once the barrier width is increased to two layers of graphene. This new phenomenon of molecular alignment through 2D films gives a new tool for the study and design of nanostructured films, and demonstrates how molecular interactions can extend across the otherwise impermeable graphene membrane.

6.3 Results and Discussion

6.3.1 Porphyrin test systems

In order to verify the existence of a remote epitaxial interaction, a typical planar porphyrin was selected that has been the subject of extensive studies [203–209]. Octaethylporphyrin (OEP) consists of a porphyrin core with eight ethyl groups attached, four of which are oriented facing up, and four of which are oriented facing down, as shown in figure 6.2. This leads to the molecule having an approximate height of 600 pm, as verified from atomic models [203]. The OEP itself can contain either a single metal atom (MOEP) or two H atoms. For this study, Ni(II)OEP (NiOEP) and OEP assemblies were studied. Both a common metal-centred and non-metal centred porphyrin were chosen in order to establish whether any remote interactions were affected by the presence of a metal centre. Both systems have been extensively studied previously and imaged using STM [204, 208], whereby the molecules were deposited using liquid-phase deposition in a chloroform solvent. Washing with chloroform following deposition was used to remove any additional molecular layers, and the samples were then allowed to dry in a desiccator overnight.

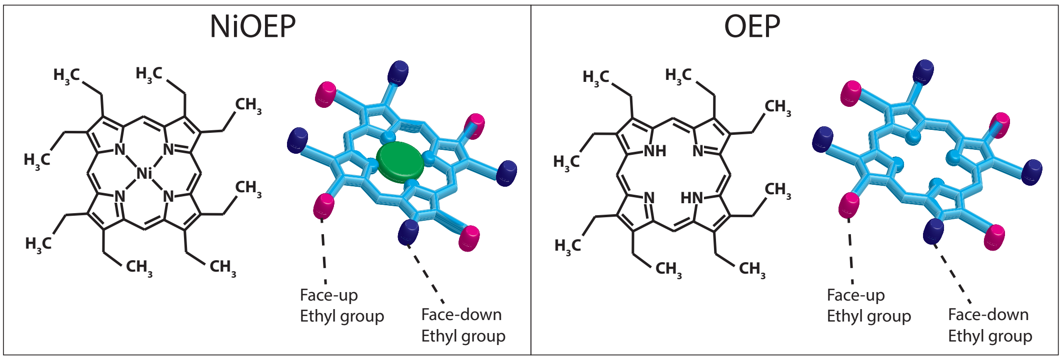

Figure 6.2: NiOEP and OEP molecule schematics with perspective views.

6.3.2 Monolayer structures of NiOEP and OEP

The monolayer ‘brickwork’ structures of NiOEP and OEP are found to be very similar. Both were deposited onto CVD-grown graphene-on-copper foils, as well as freshly-cleaved HOPG wafers, by solution-phase deposition. After drying in a desiccator overnight, the samples were imaged in dry ambient conditions by STM. STM images of NiOEP on Gr-Cu and HOPG, as shown in figure 6.3, reveal a brickwork assembly structure. The images on Gr-Cu reveal the much rougher surface of the underlying copper foil compared to the atomically flat HOPG steps. The lattice parameters of the NiOEP brickwork structure can be accurately determined using half-and-half imaging, whereby an image is taken using two sets of tunneling parameters in the top/bottom halves on an image. The different tunneling parameters enable different electron states to be probed, revealing either the overlying molecular lattice or the underlying graphene atomic lattice (figure 6.3c). The NiOEP is seen to assemble with lattice spacings (2.4 ± 0.1) nm by (1.6 ± 0.1) nm with a lattice angle of (86 ± 5) °, in agreement with previous reports [203, 204]. A very similar lattice structure was measured for OEP, with lattice spacings (2.4 ± 0.1) nm by (1.6 ± 0.1) nm with a lattice angle of (87 ± 5) °.

The STM images featured in figure 6.3 can be further analysed through investigation of the image Fourier transforms, provided below each STM image. The much larger scale image of NiOEP on HOPG provides reciprocal lattice peaks out to ≈ 3 nm^{-1}, and reveals the true brickwork nature of the NiOEP lattice. The poorer quality image on graphene does not reveal the subtle rotational differences between molecules located at centre or corner sites in the lattice, and so information is lost in the FFT in the form of missing reciprocal lattice peaks. The precise structure of the brickwork lattice is further confirmed through SAED measurements in the next section. A prior report on ultra-high vacuum high-resolution STM measurements of NiOEP assemblies on Au(111) showed a very similar structure, with clearly visible rotational differences between centre and corner sites in the brickwork unit cell [204]. Working in collaboration with Dr Tiffany Walsh at Deakin University, preliminary computational molecular dynamics (MD) simulations have revealed a near identical structure, with small rotational differences between centre and corner sites.

Although previous literature specifies that the solution-phase deposition method is sufficient in providing specifically monolayer coverage of molecules, this can be checked explicitly by measuring the thickness of the film using AFM. Using a Gr-Cu foil coated in NiOEP molecules, the film is first imaged in tapping-mode as shown in figure 6.4a. The faceted copper surface is clearly seen in the image, indicating the presence of monolayer graphene [43]. A region is selected to 'dig' a trench, whereby the AFM cantilever makes contact with the surface and repeatedly scratches away any soft material using contact mode imaging. The graphene is not removed in this procedure, enabling a measurement of the step height of the trench. This corresponds to a measurement of the thickness of the film. A rectangle of slightly lower height (darker colour) is visible in the centre of figure 6.4b, and there

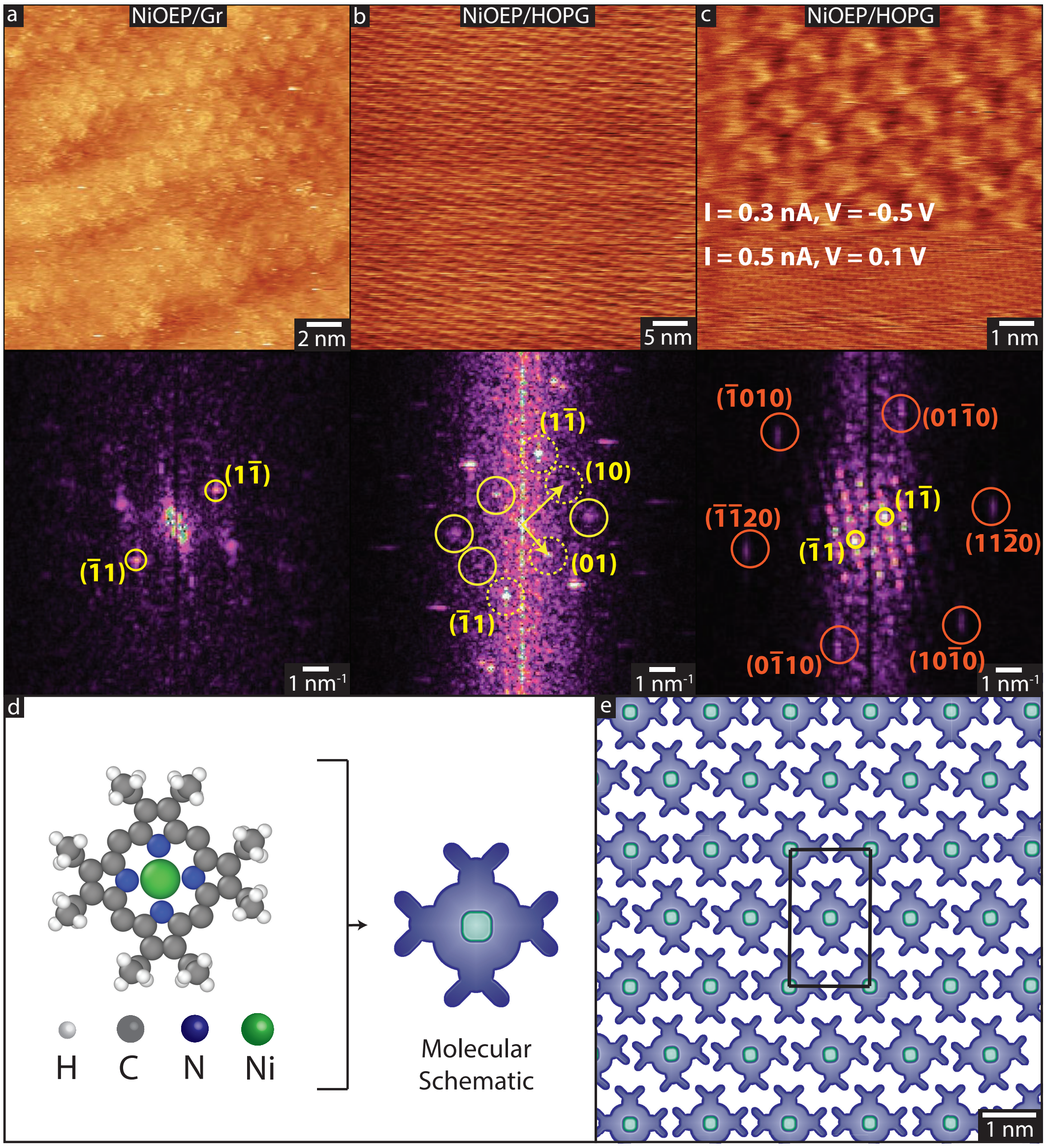

Figure 6.3: Molecular structure of NiOEP monolayer. a) STM image of NiOEP monolayer deposited on CVD graphene. b) STM image of NiOEP monolayer deposited on HOPG. c) STM image using two sets of tunneling parameters in order to resolve both the NiOEP overlayer and the HOPG lattice underneath. Top-half scanning parameters: I = 0.3 nA, V = -0.5 V. Bottom-half scanning parameters: I = 0.5 nA, V = 0.1 V. Each STM image has a corresponding FFT below it. d)Atomic model of NiOEP molecule with schematic representation. e) NiOEP lattice model based on STM unit cell measurements. A unit cell is marked by the black box.

is a clear build up of molecular debris at the top/bottom of the trench (white material). The step height is measured by first averaging a profile taken across the white boxed region in figure 6.4b, as shown in figure 6.4c. The profile has an approximate height of 600 pm, in agreement with a monolayer coverage of molecules.

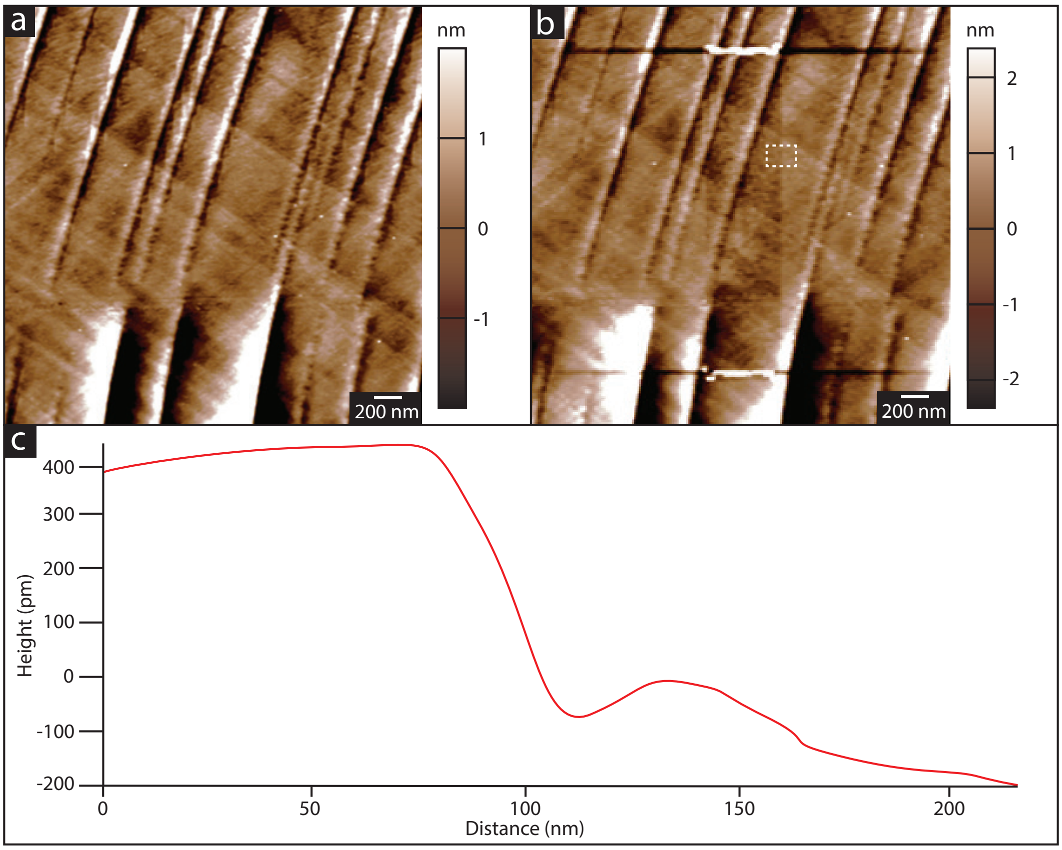

Figure 6.4: Determining the thickness of NiOEP films. a) AFM tapping-mode image of NiOEP film deposited on CVD-graphene. b) AFM tapping-mode image of the region imaged in (a) following contact-mode trench digging in the centre. Build up of molecular material from the trench digging is visible at the top and bottom centres of the image. The small change in contrast indicates a very shallow trench, reflecting the very thin nature of the film. c) Height profile taken from the dashed box in (b). The profile is averaged along the direction perpendicular to the step. As shown, the step has an approximate height of 600 pm, consistent with a monolayer coverage of NiOEP molecules.

6.3.3 Structures of NiOEP and OEP films on freestanding graphene

In order to further investigate the structure of NiOEP and OEP films, graphene TEM grids were fabricated and then coated in NiOEP/OEP molecules using solution-phase deposition. Interestingly, this process exposes molecules to both sides of the 2D graphene film. During deposition onto Gr-Cu or HOPG, only the top surface is exposed to molecules, allowing only one monolayer film to deposit (figure 6.5). When immersing a freestanding graphene membrane in solution, molecules can assemble either side of the graphene, as shown in figure 6.5. This provides a system that cannot be probed using STM, but which TEM is ideally suited to study.

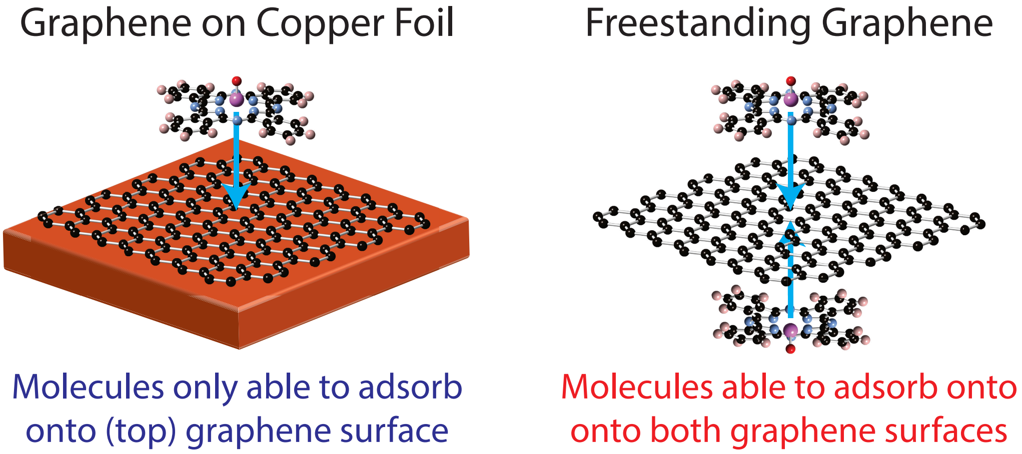

Figure 6.5: Schematic illustration of molecule deposition on substrate-supported and freestanding graphene.

Using low-dose diffraction, as outlined in chapter 4, SAED of NiOEP and OEP-coated graphene were acquired. An example NiOEP SAED pattern is shown in figure 6.6a (with inverted contrast for clarity), revealing a single highly-crystalline molecular lattice alongside a single set of graphene reflections. The SAED pattern was obtained from the area marked by the purple dotted line in figure 6.6b.The molecular reflections may be indexed out to ≈ 4 nm $^{-1}$ resolution, and reveal a brickwork structure very similar to that determined by STM imaging. The large number of reflections allow a more precise measurement of the reciprocal (and corresponding real-space) lattice compared to STM. In addition, the small width (sharpness) of the NiOEP/OEP reflections indicates that there is little deviation of NiOEP/OEP molecules from their individual lattice sites even over the large areas probed [210]. The NiOEP spacings measured are (2.31 ± 0.01) nm by (1.52 ± 0.01) nm with a lattice angle of (89.5 ± 0.1) °, and the OEP spacings measured are (2.37 ± 0.1) nm by (1.53 ± 0.1) nm with a lattice angle of (89.7 ± 0.1) °, both in agreement with the structures measured on HOPG using STM. These lattice measurements are summarised in Table 6.1.

Intriguingly, the diffraction patterns show only a single set of molecular reflections, indicating a single molecular crystal grain. The majority of SAED patterns

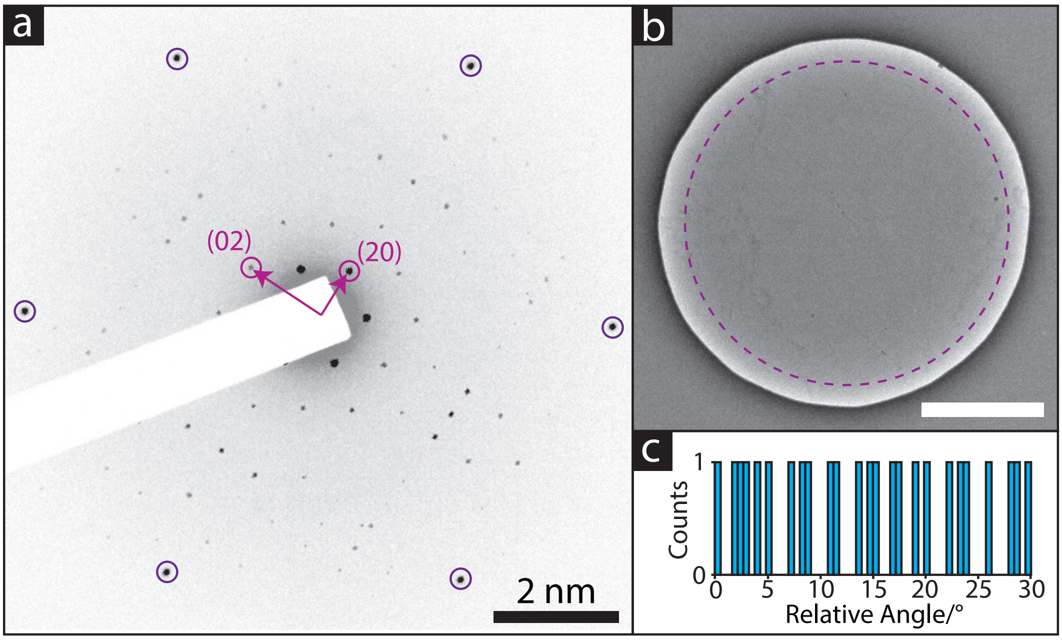

Figure 6.6: TEM SAED of co-deposited NiOEP monolayers. a) SAED pattern from SL graphene with NiOEP monolayers deposited either side, showing a single set of molecular lattice reflections (circled in pink) and graphene reflections (circled in purple). b) TEM image showing a circular hole with freestanding SL graphene stretched across following molecule deposition (scale bar 1 μm). c) Histogram showing orientation of aligned NiOEP lattice relative to SL graphene. No epitaxial relationship is revealed between the graphene and molecular lattices.

measured revealed only a single molecular pattern, indicating a grain size of the molecular film > 3 μm (the diameter of the TEM grid hole); significant ordering of molecules over large distances is indicative of a very dominant source of bonding.

Even more intriguing than the grain size itself, however, is the fact that only a single set of molecular reflections are present. Given that both sides of the graphene membrane are exposed during molecule deposition (figure 6.5), it is clear that molecular material must be present either side of the graphene membrane. If two independent molecular films were present either side of the graphene membrane, this would manifest itself in the form of two independent sets of molecular reflections in the SAED pattern, unless the two films were perfectly aligned. The significant ordering of the molecular films could be driven by an epitaxial relationship with the graphene membrane, which would manifest itself in a specific rotational offset between molecular film and graphene reflections in the diffraction pattern (As seen for TMA and TPA in the previous chapter). In order to test for such a relationship, the rotational offset between molecular film and graphene reflections was measured and plotted as a histogram for a series of different diffraction patterns (figure 6.6c). As can be seen, the histogram is plat, indicating a random distribution of rotational offsets, and therefore no epitaxial relationship between molecular layers and the graphene membrane: something else must be driving the molecular ordering of the two independent films.

Table 6.1: Lattice parameters of NiOEP and OEP self-assemblies measured on HOPG through STM and freestanding graphene through SAED.

Molecule	a (nm)	b (nm)	γ (°)
NiOEP (STM)	2.4±0.1	1.6±0.1	86±5
NiOEP (SAED)	2.31±0.01	1.52±0.01	89.5±0.1
OEP (STM)	2.4±0.1	1.6±0.1	87±5
OEP (SAED)	2.37±0.01	1.53±0.01	89.7±0.1

Given the presence of a single set of molecular reflections, it is clear that there must be two films that are aligned with each other over very large distances. The driving force responsible for this molecular alignment must arise from either an epitaxial relationship with the graphene, or from a remote interaction between the two molecular films. Any epitaxial relationship with the graphene will result in a specific rotational offset between the graphene and molecular lattices [43]. A histogram of relative angle between graphene and NiOEP lattices is shown in figure 6.6c. There is no epitaxial relationship present between the NiOEP and graphene, as indicated by the absence of a dominant peak in relative angle between lattices. In order for the top/bottom molecular films to be aligned over large areas without epitaxial influence from the graphene layer, the molecules must be remotely interacting across the graphene membrane. The observation of a single, well-ordered diffraction pattern across large areas and different graphene grains indicates that the top/bottom NiOEP/OEP layers must experience a remote interaction across the graphene membrane to form a single, highly-organised superstructure.

The 2D lattice structures revealed by STM, AFM and SAED provide enough information to construct a hypothesised model of the remotely-interacting assemblies. The crystal system must contain a monolayer assembly either side of the graphene, both organised into a brickwork structure with lattice parameters equal to those presented in Table 6.1. Both top/bottom molecular layers must also be orientated in the same direction. The remote interaction is likely van der Waals in nature, and it follows that the molecules must sit above/below their mirror image as shown in figure 6.7; DFT studies alongside experiments featured in chapter 5 have shown the energetically favourable and significant π-coupling of TMA molecules when stacked on top of one another [6, 174]. In addition, the π-coupling interaction between TMA molecules was shown to increase with the number of molecules stacked. A similar Van der Waals footprint effect is expected to drive the large-scale assembly of NiOEP/OEP molecules, following an Otswald-ripening behaviour.

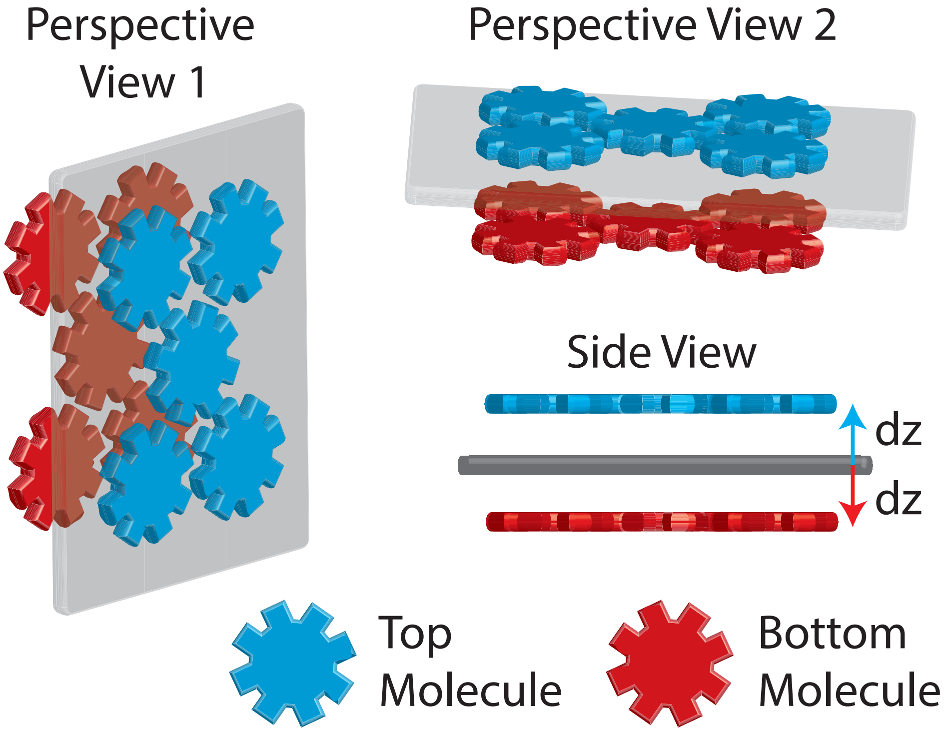

Figure 6.7: Model structure for remotely interacting NiOEP/OEP molecules. The top (blue) and bottom (red) assemblies align with eachother across the single-layer graphene membrane (gray). Both monolayer assemblies adsorb onto the graphene at a distance dz.

6.3.4 Probing the structure of NiOEP and OEP films on freestanding graphene using tilted diffraction

In order to further probe the structure of NiOEP and OEP films deposited on freestanding graphene, and to test the hypothesised structure presented in figure 6.7, diffraction analysis can be carried out with the sample tilted relative to the optical axis of the microscope. Tilting of samples leads to several changes in the resulting diffraction pattern. Firstly, the angle θ_{hk} through which electrons are scattered for the Bragg (hk) reflection is inversely proportional to the projected separation between lattice planes $d_{hk}\cos\alpha$ [64]:

$$\theta_{hk}\left(\alpha\right) = \frac{\lambda_e}{d_{hk}\cos\alpha} \tag{6.1}$$

where λ_e is the electron wavelength, d_{hk} is the separation between lattice planes and α is the tilt angle of the specimen (figure 6.8). Thus, tilting of the sample results in a contraction of the real-space lattice perpendicular to the tilt axis, and a corresponding expansion of the reciprocal-space lattice in diffraction images.

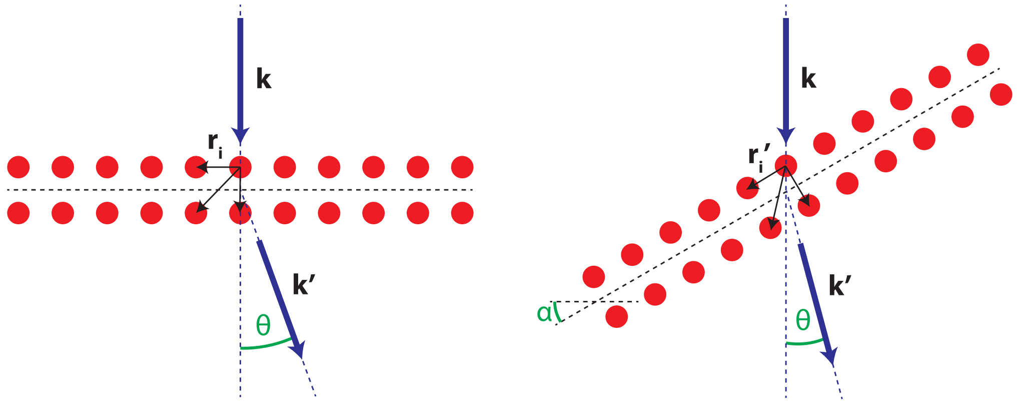

Figure 6.8: Change in scattering angle θ of the emergent wavevector k' following titling of a crystal through an angle θ normal to the optical axis.

The change in projected view of the sample relative to the optical axis also produces a change in interference conditions of the scattered wave. The structure factor, which describes how a material scatters incident radiation, can be expressed as a sum of scattering components from all N atoms in a unit cell: /

$$F_{hkl} = \sum_{i=1}^{N} F_i e^{-i\mathbf{q}\cdot\mathbf{r}_i} \tag{6.2}$$

where F_{hkl} is the structure factor of the (hkl) reflection, which has intensity I:

$$I \propto \left[F_{hkl}\right]^2 \tag{6.3}$$

The structure factor F_{hkl} is composed of a sum of amplitude and phase components for each atom in the unit cell. The amplitude F_i is defined as the atomic scattering factor, which describes the strength of scattering for a given atom [64]. The phase component $e^{-i\mathbf{q}\cdot\mathbf{r}_i}$ describes the modulation of the scattering factor based on its position within the unit cell, and is influenced by the atomic positions $\mathbf{r}_i$

[64]. Upon tilting, there is a shift in atomic positions $\mathbf{r}_i$ to a new set of positions $\mathbf{r}'_i$. This shift in atomic coordinates leads to a change in the value of the phase factor, and consequently to a change in the intensity I of the (hkl) reflection. It follows that as well as the intensity I of the (hkl) reflection depending upon the tilt angle α, it must also depend on the direction of the tilt axis relative to the sample. As illustrated in figure 6.9, applying a 30 ° tilt to a double layer of graphene produces significantly different projected views depending on the orientation of the tilt axis.

For simple crystal systems, the intensity I for a particular (hkl) reflection is trivial to calculate when subject to a certain tilt angle α. However, for a complex system such as the suggested NiOEP/OEP assembly described in figure 6.7, an analytical approach is far more complex. Instead, we use multislice simulations utilising a crystal model of the NiOEP/OEP assembly to carry out a computational calculation; the crystal model can be further refined to achieve a more accurate model. In order to carry out such a refinement, however, experimental data is necessary.

Difficulty arises in measuring the intensity I for a set of $\{hkl\}$ reflections for a full range of tilts with the NiOEP/OEP systems. This is because each measured diffraction pattern must be taken from a new location on the TEM grid, as each diffraction pattern fatally damages the specimen region, and the TEM grid contains a series of different molecular grains, as shown in figure 6.10. It is thus impossible to measure a full range of tilted diffraction patterns for a single molecular grain orientation. However, it is possible to capture diffraction patterns at a single tilt angle across the whole TEM grid, and consequently for a large number of molecular grain orientations.

As described earlier, the orientation of the tilt axis relative to the crystal system, as well as the value of the tilt angle itself, greatly influence the intensity of the measured (hkl) reflection. Therefore, the change in orientation of the molecular assembly relative to the optical axis provides sufficient variation in the intensity of scattered reflections. The intensity I is also dependent on the volume of scattering material present [65], and so it is insufficient to measure only the absolute intensity. Instead, the ratio of two reflections I_1/I_2 are measured for each SAED pattern [93]. This provides a set of data on the ratio of reflection intensities I_1/I_2 as a function of molecular grain orientation relative to the optical axis. Two example SAED patterns are shown in figure 6.10, alongside projected crystal models for each grain orientation as measured in the SAED patterns. The two SAED patterns have been background-corrected for accurate reflection intensity measurements and have been rotated to the same alignment. Both show large differences in reflection intensities

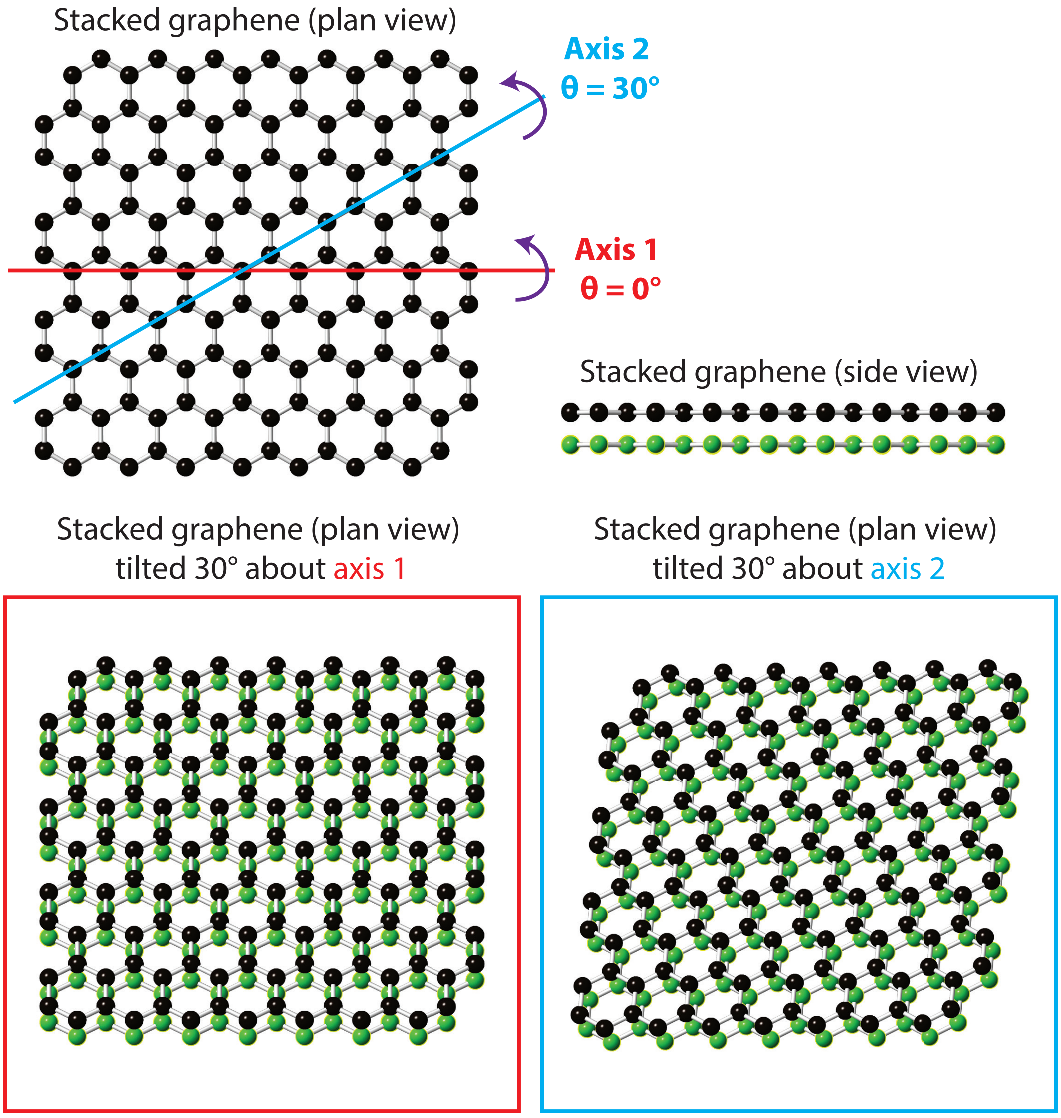
Stacked graphene (plan view)

Stacked graphene (side view)

Stacked graphene (plan view) tilted 30° about axis 1

Stacked graphene (plan view) tilted 30° about axis 2

Figure 6.9: Change in projected view of tilted crystal due to in-plane rotation. The top image shows a plan view of a stacked graphene model. Top atoms (black) sit directly above bottom atoms (green). If the crystal is tilted normal to the red axis by 30°, the projected view reveals the bottom graphene layer. If the crystal is tilted normal to the blue axis by 30°, which is rotated 30° relative to the red axis, the projected view changes. This change in projection due to the orientation of the crystal relative to the tilt axis causes a change in the scattering of electrons through the crystal.

due to the change in structure factors for each.

With a number of SAED patterns obtained for a set 30 ° tilt angle, two reflections (h_1k_1) and (h_2k_2) were selected that showed large changes in intensity

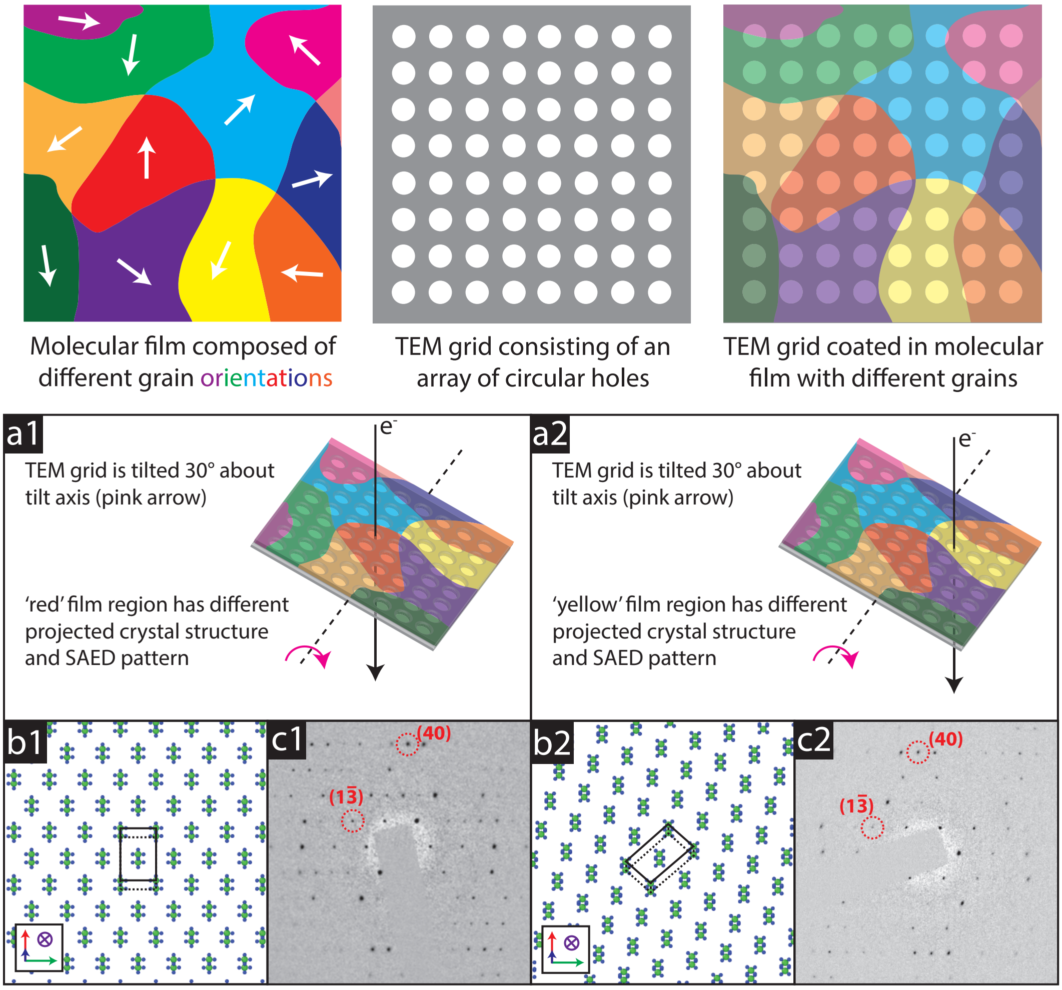

Figure 6.10: Tilted Diffraction applied to molecular film composed of differently-orientated grains. The molecular film has large grains of different orientations laying across multiple TEM grid holes. a1,a2) Schematics showing how shifting the stage provides SAED patterns from two different crystal grains. b1,b2) Projected views of the tilted NiOEP films imaged in c1,c2), showing large differences. c1,c2) Tilted SAED patterns taken from different areas of the grid will produce patterns with different intensities of reflections due to the change in structure factors.

with changing grain orientation, and were also visible in all SAED patterns. The reflections selected were (40) and (1$\bar{3}$), as labeled in figure 6.10 (c1,c2). The ratio $I_{40}/I_{1\bar{3}}$ can be calculated for the experimental data and plotted as a function of polar angle (orientation of grain relative to optical axis), as shown in figure 6.11.

In order to compare to experimental data, simulation models were created for the models featured in figure 6.7 at a range of polar angles θ = [-90:90] ° for a tilt angle α = 30 °. The models were created using a set separation z between

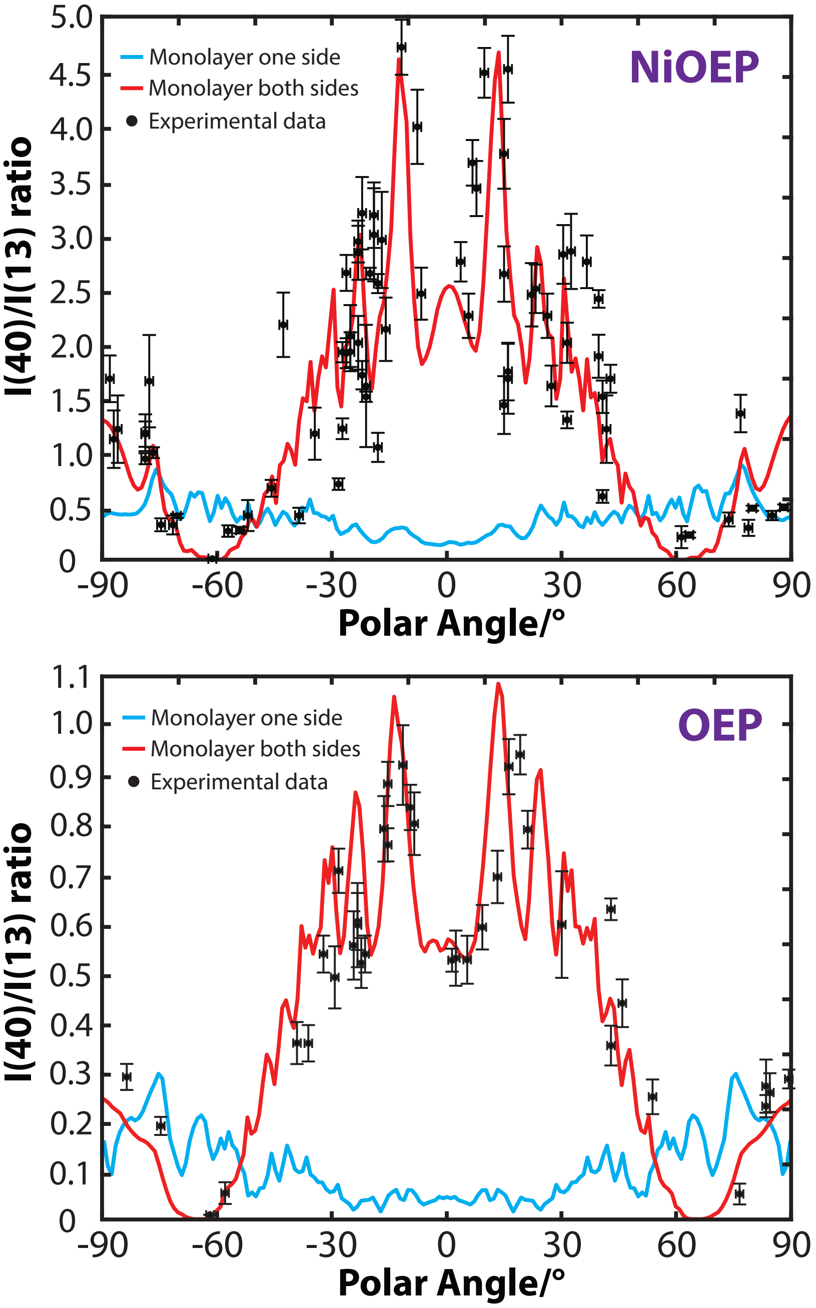

Figure 6.11: Tilted diffraction data for NiOEP (top) and OEP (bottom). Both plots contain experimental data (black), refined simulation data for monolayer films on both sides of a graphene membrane (red), and simulation data for a single monolayer film on one side of a graphene membrane (blue). There is a clear difference between the two simulation curves, with the experimental data matching well with the refined curve for monolayer films on both sides of the graphene.

molecular layer and graphene. The full set of simulated SAED patterns based on simulation models were analysed and the ratio $I_{40}/I_{1\overline{3}}$ calculated and plotted as shown in figure 6.11. In order to refine the separation between molecular layers and graphene, simulation series were produced for a range of separations z, as shown in figure 6.12. To determine the best matching simulation model, the χ^2 value for each series was calculated:

$$\chi^2 = \sum_{i=1}^{N} \left[\frac{y_i - \overline{y}\,(x_i)}{\alpha_i} \right]^2 \tag{6.4}$$

where y_i is the experimental data with uncertainty α_i, and $\overline{y}(x_i)$ is the corresponding simulation value. For both NiOEP and OEP data, a minima in χ^2 is seen at $z = 3.0$ Å. The simulated curves for $z = 3.0$ Å are plotted against the experimental data in figure 6.11, showing good correspondence.

As well as confirming the hypothesised unit cell and refining the intermolecular separation distance, tilted diffraction simulations can be used to further prove the existence of a monolayer assembly either side of the graphene membrane. AFM analysis suggests a monolayer film coating the graphene on copper (figure 6.4), and this is assumed to be true for the freestanding graphene due to the use of identical methods of molecule deposition. However, this can be proved through simulating a full tilt series using molecular models coating only one side of the graphene membrane. Using a separation of $z = 3.0$ Å and tilt angle $\alpha = 30$ °, a full tilt series was simulated for a single layer of NiOEP/OEP molecules and plotted alongside the corresponding top/bottom layer simulations, as shown in figure 6.11. As shown, there is a significant difference between simulation curves for monolayer coverage on one side/both sides of the graphene membrane, further proving the hypothesised model shown in figure 6.7.

6.3.5 Probing the remote interactions of NiOEP and OEP molecules across graphene

With the structure of the NiOEP/OEP molecular assemblies established, it is clear that the molecular layers align through some form of remote interaction. To investigate the properties of this interaction further, samples were fabricated using a double-layer graphene membrane (as described in Chapter 3). The double-layer graphene membrane consists of two independent monolayers of graphene layered on top of each other, producing two randomly oriented graphene films. The solution-phase molecular depositions were repeated, with molecules now assembling at a greater separation either side of the double-layer graphene membrane.

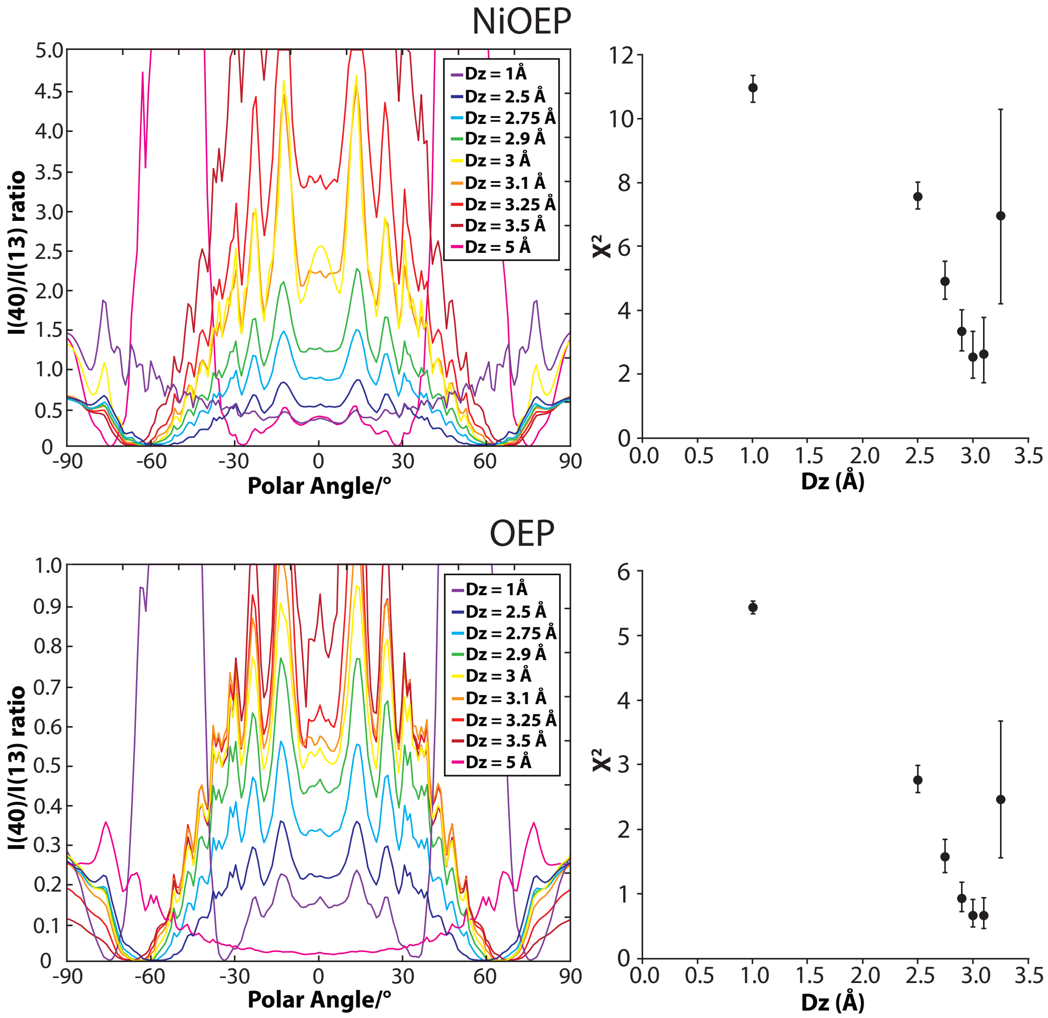

Figure 6.12: Refinement of molecular layer separation through tilted diffraction simulation. NiOEP (top) and OEP (bottom) simulation refinement.χ^2 plots (right) for both NiOEP/OEP show a minima around $z = 3.0$ Å.

With two non-identical surfaces now available, separated by two carbon atoms, SAED reveals a completely different top/bottom molecular film structure compared to the single-layer graphene case, as shown in figure 6.13. There are now two individual sets of molecular reflections, relating to the top/bottom molecular films, in addition to the two individual sets of graphene reflections, relating to the randomly oriented sheets of single-layer graphene comprising the double-layer membrane. Figure 6.13 shows histograms of both the relative angle between sets of molecular reflections and the relative angle between molecular reflections and graphene reflections, again revealing no epitaxial relationship between either of the molecular films and the double-layer graphene membrane. In addition, the absence of a rotational relationship between individual molecular reflections indicates that the films are no longer interacting, as a result of the second layer of graphene present in the double-layer membrane. Combined with the SAED measurements from single-layer membranes, it is clear that the additional separation causes the molecular interaction to cease. The relative height different between bilayer and monolayer graphene has been reported as 0.76 nm [211], which implies a very short-range force potential for the remote interaction between molecules.

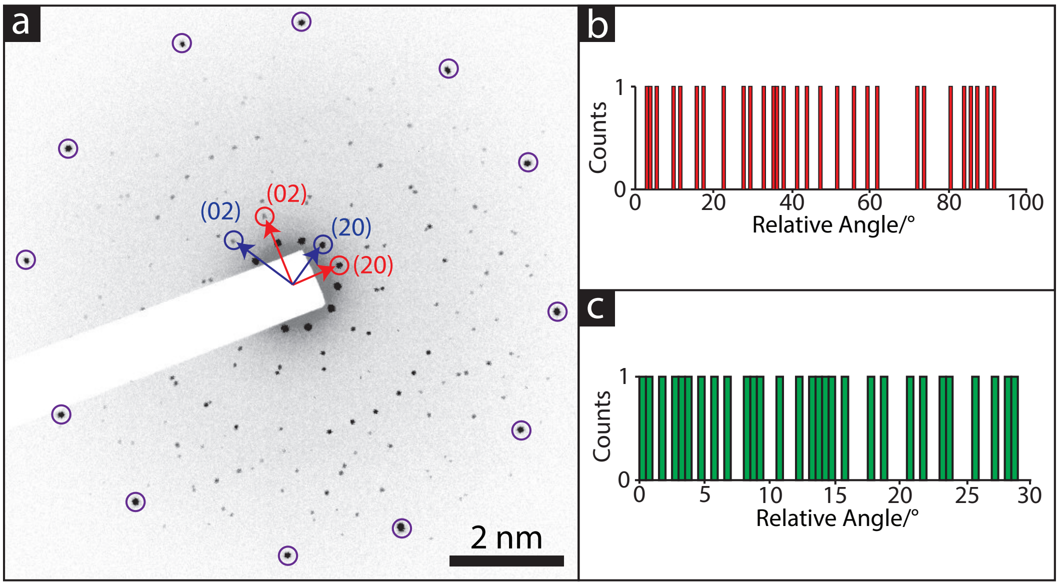

Figure 6.13: TEM SAED of co-deposited NiOEP monolayers. a) SAED pattern from DL graphene with NiOEP monolayers deposited either side, showing two distinct set of molecular lattice reflections (circled in red, blue) and graphene reflections (circled in purple). b) Histogram showing orientation of aligned NiOEP lattice relative to SL graphene. No epitaxial relationship is revealed between the graphene and molecular lattices. c) Histogram showing orientation of aligned NiOEP lattice relative to SL graphene. No epitaxial relationship is revealed between the graphene and molecular lattices.

6.4 Conclusions

All this is correct if Au9 and Ir4 behave as rigid rotators under 80 keV e-beam

Et to Au and Ir from e-beam should be considered and compared to Au-Au and Ir-Ir bond dissociation barrier

This detailed study into the structural coupling of monolayers of NiOEP/OEP across a single layer of freestanding graphene gives new insight into the growth and behavior of supramolecular thin films on surfaces. To achieve this, an innovative combination of low-dose SAED/tilted SAED and STM was used to accurately determine molecular-resolution structural information on films deposited on both bulk and freestanding substrates of different thicknesses, something that is difficult to attain using other analytical techniques.

For free-standing graphene, the structure and orientation of the molecular top/bottom-layers of NiOEP/OEP is dictated by remote van der Waals interactions between molecules and the graphene has no epitaxial influence on the crystallography of the assembly. STM measurements reveal that NiOEP/OEP assume a flat 2D lattice on both copper-supported graphene and on HOPG. SAED measurements reveal that NiOEP/OEP layers on both the top and bottom surfaces of freestanding single-layer graphene align through the graphene, producing a single, larger unit cell. This molecular coupling produces a highly-organised, large-scale superstructure; the two molecular films are oriented in the same direction and positioned on top of one another due to mutual coupling across the graphene layer. The coupling interaction is shown to diminish on a length scale of two carbon layers, with NiOEP/OEP layers deposited on either side of a membrane consisting of two randomly-oriented layers of graphene showing no alignment. Further work is required to understand the nature of this interaction and establish the role of graphene - is it an inert spacer or does it play an active role in enhancing the dipole interactions - and to quantify their strength. As already mentioned, preliminary MD simulations undertaken by our collaborator Dr Tiffany Walsh at Deakin University are fully consistent with these experimental data and suggest that this will be a generic effect. Hence, this new phenomenon of molecular alignment through 2D films gives a new tool for the study and design of nanostructured films, and demonstrates how molecular interactions can extend across the otherwise impermeable graphene membrane.

Chapter 7

Atomically-resolved molecular dynamics on graphene

7.1 Introduction

Materials studied at the nanoscale may be categorised into three main size-dependent regimes: atoms/molecules, metal nanoclusters (M-NCs) and nanoparticles, and larger bulk structures (figure 7.1). Typical bulk metals are good electrical conductors and optical reflectors, whilst metal nanoparticles exhibit intense colours as a result of surface plasmon resonance [212, 213]. Reducing the size of metal nanoparticles to around 2 nm or less (M-NC regime) alters the band structure considerably. Consisting of only a few atoms, the electronic structure becomes discontinuous and consists of a discrete set of energy levels, similar to the electronic structure of molecules [212–216]. As shown in figure 7.1, with a lack of plasmonic behaviour M-NCs bridge the gap between atoms/molecules and nanoparticles [212–222]. M-NCs are of interest due to their attractive electronic, optical, and chemical properties in comparison to their larger nanoparticle counterparts [212, 213, 223, 224].

Due to their unique optical, electrical, and magnetic properties, there is significant interest in the application of M-NCs. The fluorescence properties and biocompatibility of M-NCs, along with their ultrasmall size, makes them ideally suited for fluorescene bio-imaging and cellular labeling [217]. In addition, M-NCs can be used in metal ion and biological entity detection and sensing applications. The precise size controllability and consequent reactivity of M-NCs also provides a way to tune the selectivity in catalytic applications [212–216, 223].

Recent developments in aberration-corrected TEM, low-dose imaging conditions, and low-contrast 1D/2D carbon supports, have enabled atomic-resolution

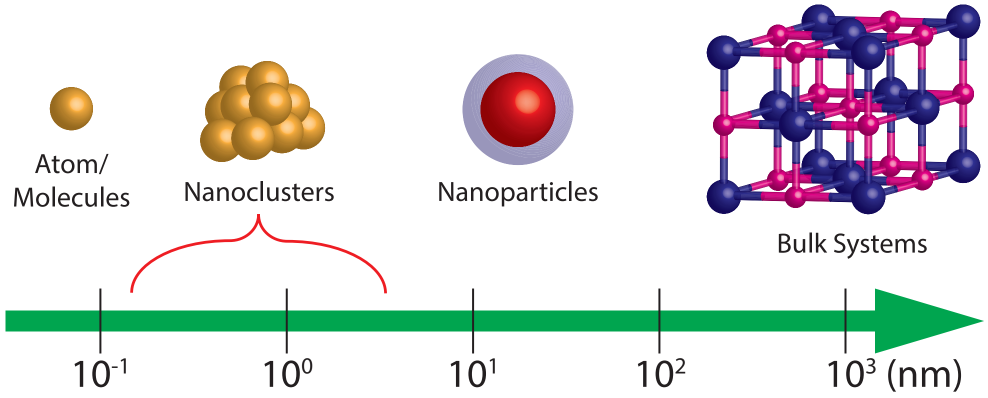

Figure 7.1: Size regime of different materials. Nanoclusters provide a bridge between atoms/molecules and larger nanoparticle/bulk crystal systems.

imaging of single-molecules and M-NCs in real time [7, 69, 97, 225–229]. The use of HRTEM to study single molecules/M-NCs provides a complete revolution in the study of their behaviour; atomic-resolution real-time analysis of particle structures, conformational and rotational changes, and chemical reactions is now possible.

There have been several strategies described in order to directly visualise chemical and self-assembly processes with TEM, including *chemTEM* [69, 229] and SMART-TEM [228]. Both of these methods exploit the use of the electron beam in TEM as both an imaging tool and a source of energy in order to drive chemical processes. As shown by Koshino *et al.*, the major energy source for observed molecular motions in TEM is the electron beam used for imaging, and the sample temperature has only a small effect on the observed conformational changes [226]. For particularly thin specimens, direct interactions of the electron beam with atomic nuclei are the dominant sources of energy exchange, such that the kinetic energy of the electrons is transferred directly to the atoms via ballistic collisions [229]. The maximum energy transferred to a stationary atom during a collision is directly related to the accelerating voltage of the electron beam, and the rate of interactions is proportional to the dose rate of the electron beam [229]. This allows moderation of observed chemical reactions, in order to be properly captured by the TEM detector [69, 229].

Graphene, as a two-dimensional system with outstanding electronic properties and a high surface area [230], offers the ideal platform on which to deposit M-NCs [231]. Due to its atomic thinness, the electron beam may interact elastically with any supported molecules or NCs. Additionally, the low contrast nature of graphene allows supported molecules to be imaged with high resolution, and its highly conductive nature allows it to serve as a sink for both charge and heat [69, 229]. In addition, the diversity of carbon chemistry offers many routes to producing chemically modified graphene (CMG) [230, 232, 233], which also facilitates the stable attachment of M-NCs [234].

When analysing HRTEM images, identification of atomic positions through direct interpretation of image contrast proves difficult, due to the effects of microscope aberrations, particularly defocus [65]. To aid image contrast interpretation, it is necessary to compare between experimental and simulated HRTEM images [65]. This allows matching features of contrast to be linked to the particular atoms responsible in the atomic model used for simulating the image.

When studying M-NCs that undergo rapid rotational changes, each frame in an image series can be identified as the M-NC in a single rotational state. As time progresses, the rotational state changes, and the M-NC is seen to switch between states [7, 97, 225]. Furthermore, it is possible to identify specifically the rotational state of the M-NC for each frame of an image series by matching to a specific simulated image [7, 97, 225]. Constructing a catalogue of possible M-NC images using multiple atomic models and a multislice simulation procedure, it is possible to match each experimental frame to the best corresponding simulation image by eye [7].

This process of matching images may be made more robust using a cross-correlation routine [228], whereby a much larger catalogue of simulated images is constructed, and a correlation metric is calculated for an experimental frame with all entries in the catalogue. Firstly, experimental images are compared to a catalogue of simulated images using a cross-correlation routine [235, 236], as described in Equation 7.1 and figure 7.2. The 2D cross-correlation of an M-by-N matrix, X, and a P-by-Q matrix, H, is a matrix, C, of size $(M + P{-}1)$ by $(N + Q{-}1)$. Its elements are given by:

$$C(k,l) = \sum_{m=0}^{M-1} \sum_{n=0}^{N-1} X(m,n)\bar{H}(m-k, n-l), = \begin{cases} -(P-1) \leq k \leq (M-1), \\ -(Q-1) \leq l \leq (N-1), \end{cases} \tag{7.1}$$

where the bar over H denotes complex conjugation. The output matrix, $C(k,l)$, has negative and positive row and column indices [237]. These negative and positive indices result in directional shifts in the columns/rows of H and are automatically compensated for when using MathWorks® MATLAB's (version R2017a) inbuilt

$xcorr2$ function.

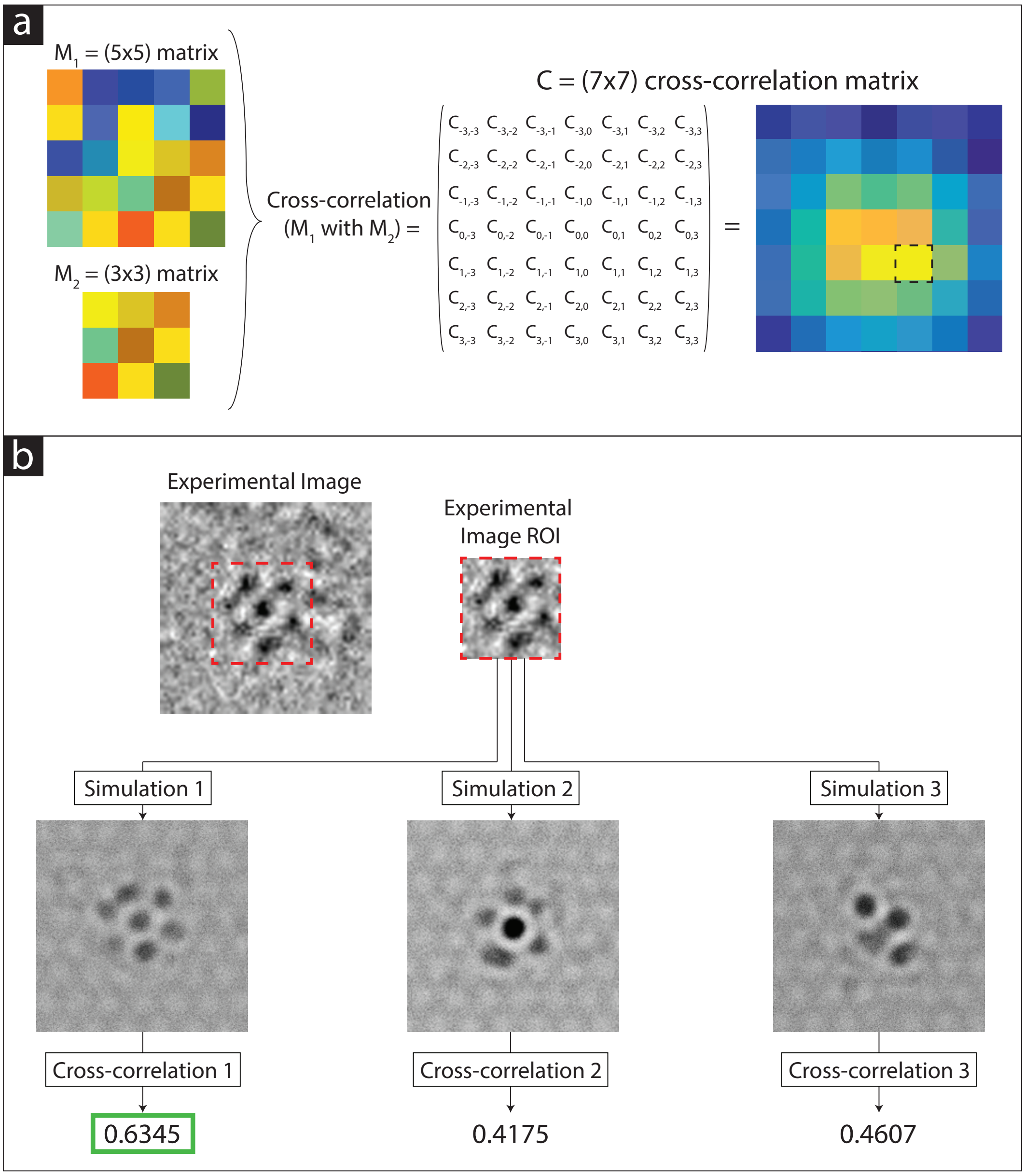

Figure 7.2: Cross-correlation between two images. a) Cross-correlation between two matrices, M_1 and M_2, to produce a matrix of correlation values C. The maximum value of C, C_{max} may be obtained in order to calculate the position and value of greatest correlation between M_1 and M_2. b) Cross-correlation between single experimental Au_9 HRTEM image and 3 differently-orientated Au_9 HRTEM simulation images. The highest cross-correlation value allows the best matching simulation and corresponding model to be selected, with other simulations and models rejected.

Defining X as an experimental image, and H as a specific simulation image, a normalised maximum value of correlation C_{max} may be calculated, providing a value between 1 and 0, with 1 being a perfect match and 0 being no match. A value of C_{max} can be calculated for all simulation images present in the catalogue, with the overall maximum being selected as the best match to the experimental frame. This allows each successive experimental image to be matched to an exact simulated image and corresponding molecular model, providing information on the exact state of the molecule at each moment in time. In figure 7.2 three different simulated images are compared to a single experimental frame, with the simulation with greatest correlation selected as best match. This corresponds to the first simulation, with a cross-correlation value of 0.6345. The two other simulation images are rejected due to their much lower cross-correlation values of 0.4175 and 0.4607.

7.2 Chapter Outline

In this chapter, in collaboration with the Rourke group (University of Warwick, Department of Chemistry), two different M-NCs are studied using HRTEM and 2D graphene-based supports. A gold-based M-NC is attached to a chemically-modified graphene oxide support and simple comparisons are made between experimental and simulated images, to accurately identify the M-NC and its structure. Insights into the rotational behaviour of the M-NC are obtained through analysis of the rate of change in the rotational state of the M-NC.

Further analysis is conducted on HRTEM images of an iridium-based M-NC using cross-correlation methods, enabling a more rapid, extensive, and accurate comparison between experimental and simulated images. Exact information on the rotational state of the M-NC allows the most favourable orientations to be identified.

Both M-NCs are seen to rotate without lateral diffusion, as a result of a covalent interaction between the M-NC and graphene support. The gold-based M-NC is seen to rotate continuously between metastable states on the order of seconds, whereas the iridium-based M-NC is seen to remain in metastable states on the order of seconds before rapidly switching between unstable states.

7.3 Results and Discussion

7.3.1 Au_9 nanoclusters: An initial HRTEM study

Recently, the Rourke group reported an easy method to chemically modify graphene with sulfur functionalities [238]. Chemically modified graphene with sulfur functionalities is synthesized by treatment of graphene oxide (GO) with potassium thioacetate, followed by an aqueous work-up. This route gives a single-layer material with reactive thiol groups that offer anchoring points for further functionalisation, and is referred to as GOSH. In a collaboration with Dr Jon Rourke and Dr Concha Bosch-Navarro, who synthesized the materials, GOSH was utilised, along with the affinity between gold and sulfur, in order to perform stable attachment of $[Au_9(PPh_3)_8](NO_3)$ (abbreviated as Au_9) NCs [239] to CMG [7].

The Au_9 NC has D_{2h} symmetry and is composed of nine gold atoms arranged such that one central gold atom is surrounded by the remaining eight gold atoms, each of which is coordinated by a monodentate phosphine ligand (figure 7.3). The average metal-metal distance is around 0.27 nm, which results in a cluster diameter between 0.45 nm and 0.54 nm [240], far smaller than that typically exhibited by Au NPs (particle size > 3 nm) [241].

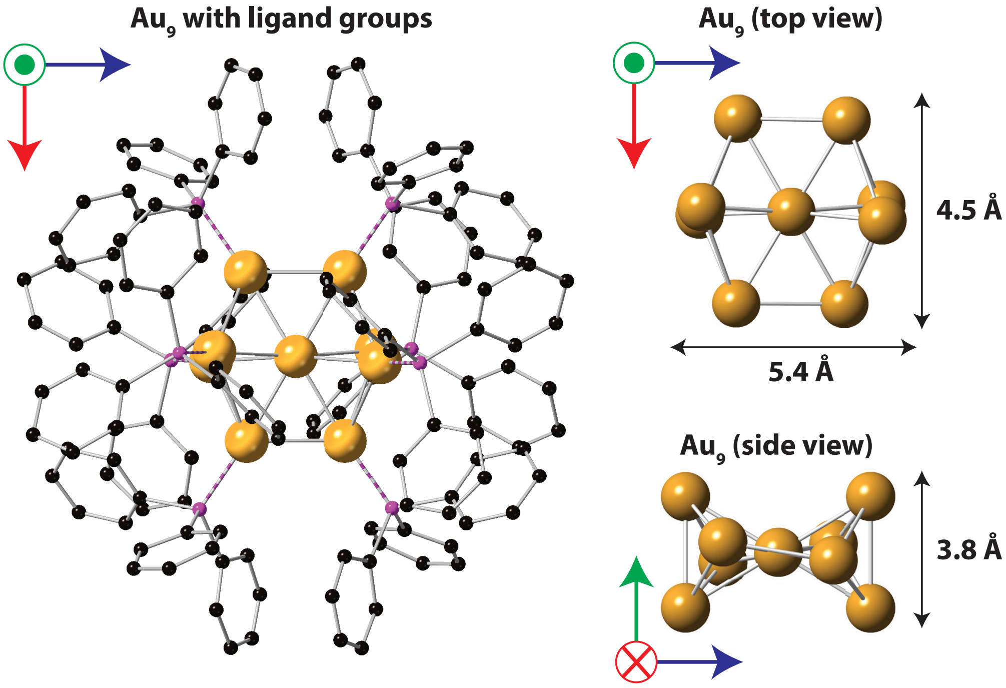

Figure 7.3: Model schematics of Au_9 NC. Left image shows coordinated monodentate phosphine ligands. Right images show top and side views of the central gold cluster only.

The binding between Au_9 and CMG with sulfur functionalities is achieved by simply mixing a dispersion of the two together. A covalent bond is formed between sulfur and gold, which is accompanied by the displacement of a phosphine ligand. As a result, a neutral GOSH-Au_9 hybrid is formed, as shown in figure 7.3.

A HRTEM image of a typical area of GOSH with Au_9 is shown in figure 7.4. Single Au_9 nanoclusters are visible as shown in the boxed area, with clear structure that can be used to unambiguously identify the image features as Au_9 clusters.

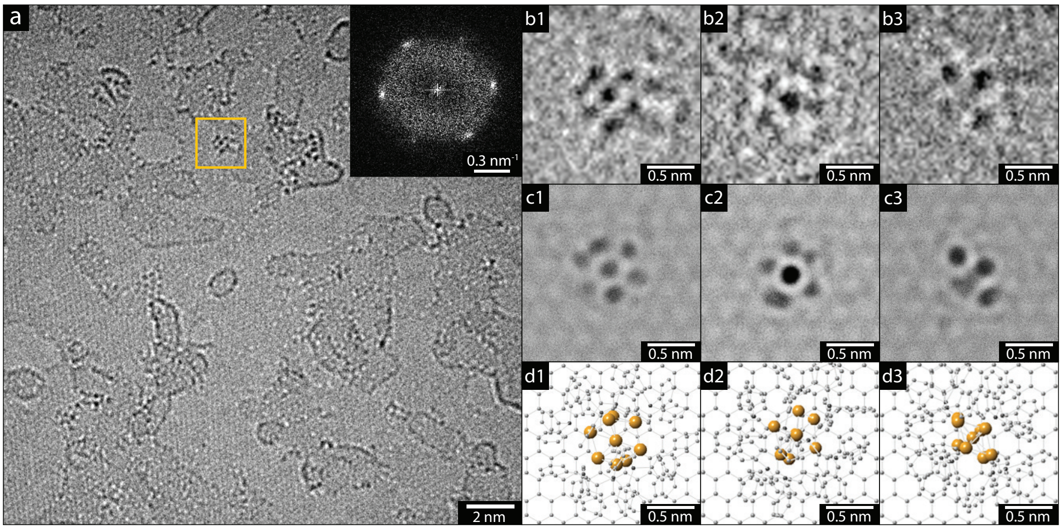

Figure 7.4: HRTEM summary of Au_9 nanoclusters deposited on GOSH. a) HRTEM image of Au_9 nanoclusters. Inset FFT showing the typical hexagonal pattern of a graphene monolayer. b) Three different HRTEM images of single Au_9 nanocluster imaged over GOSH in three different orientations. b1, b2, b3) correspond to the NC highlighted with a square in (a) at different times. c1, c2, c3) HRTEM image simulations produced from the crystal-structure model depicted in d1, d2, d3).

In order to investigate the Au_9 NCs further, a detailed experimental and simulated image comparison is required. Using the known atomic structure of Au_9 [240], a catalogue of multislice image simulations can be constructed by rotating the molecule about two orthogonal symmetry axes (figure 7.5). For M-NCs such as Au_9, TEM image contrast is dominated by the central metal atoms (for Au, $Z = 79$), which scatter the electrons to a greater extent than do the lower mass constituents such as phosphorus ($Z = 15$) or carbon ($Z = 6$). However, for accurate comparison between experimental and simulated images, all atoms are contained in the image simulation, including the coordination sphere of ligands and a section of graphene lattice [97]. Figure 7.4 shows a Au_9 nanocluster with three different orientations, taken from a single location with 0.3 s exposure. A comparison with the simulations (figure 7.4c) allows identification of the orientation of the Au_9 clusters (figure 7.4d).

Comparison between the image simulations and experimental images clearly shows that the clusters are Au_9, with a close match for the contrast arising from the gold atoms and also subtler variations in contrast that are consistent with the

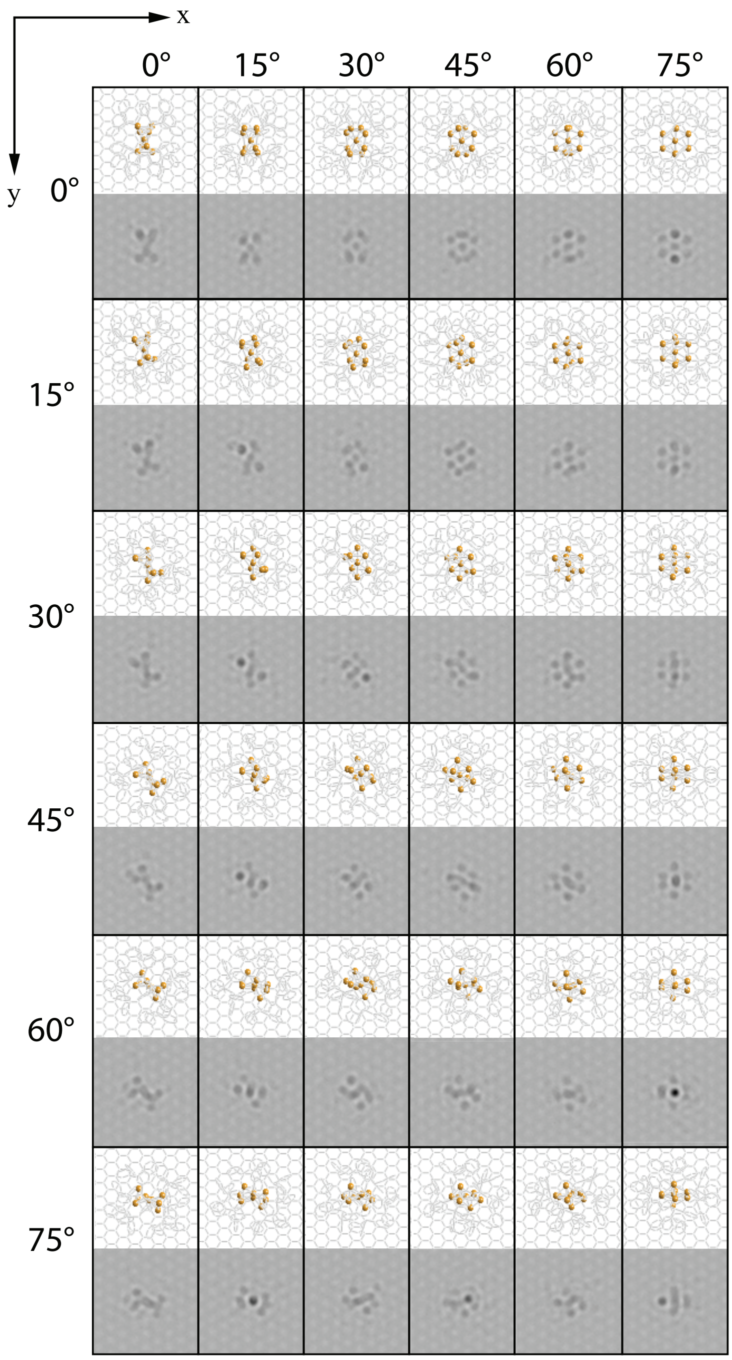

Figure 7.5: Simulated image catalogue for Au_9 NC on graphene showing atomic model and corresponding multislice simulation. The Au_9 is rotated about its two orthogonal symmetry axes in 15 ° steps.

ligands still being present. Further confirmation comes from the measurement of the spacings of the atoms within the clusters, which shows that the Au−Au distances in the experimental images are consistent with those expected for Au$_9$ (figure 7.6). This proves that intact, undamaged, Au$_9$ nanoclusters are present on the GOSH surface.

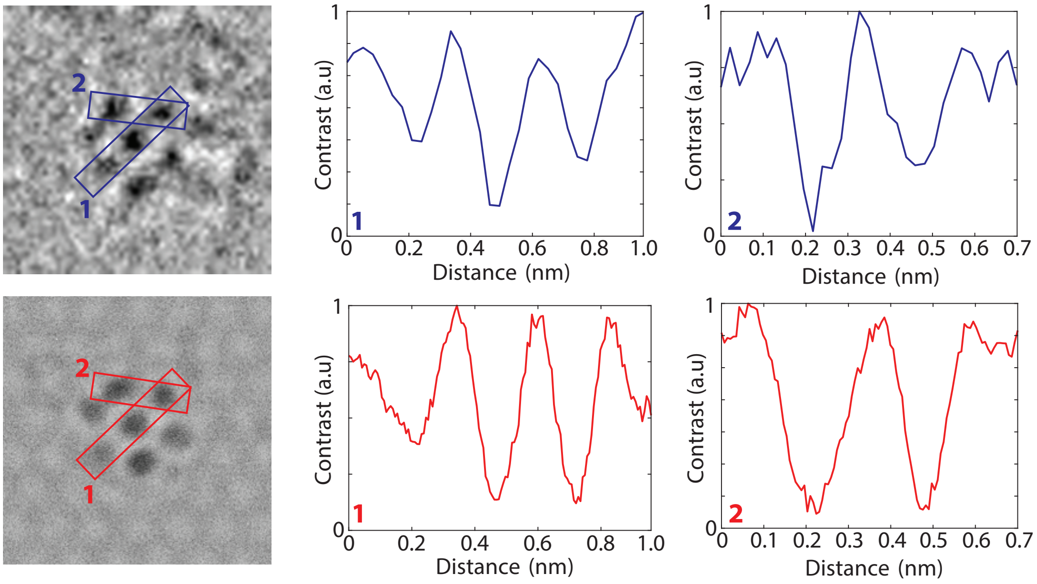

Figure 7.6: Measuring Au$_9$ interatomic spacings using HRTEM image line profiles. Experimental (blue) and simulated (red) line profiles show good correspondence, indicating consistent interactomic spacings between simulation model and the experimental structure.

As well as studying the structure of M-NCs, it is also possible to investigate their dynamics. Matching between experimental and simulated images indicates that the clusters are stationary on the GOSH surface for the period of that exposure. However, inspection of subsequent images shows that the clusters are not permanently fixed and their contrast changes over time. The Au$_9$ clusters remain fixed in place on the GOSH surface whilst undergoing orientational changes, indicating that they are covalently bound to the GOSH and not simply adsorbed to the surface.

Figure 7.7 shows a sequence of HRTEM images of a single Au$_9$ nanocluster on GOSH; images were acquired at 0.3 s intervals over a period of more than 10 s. The images are from the same region and, through comparison with fixed points in the larger image, show no apparent lateral displacement of the cluster relative to the underlying GOSH [7]. The change in contrast is indicative of rotations of the Au$_9$ cluster relative to the GOSH surface, and comparison with the image simulation catalogue (figure 7.5) enables each of the images shown in figure 7.7 to be identified as

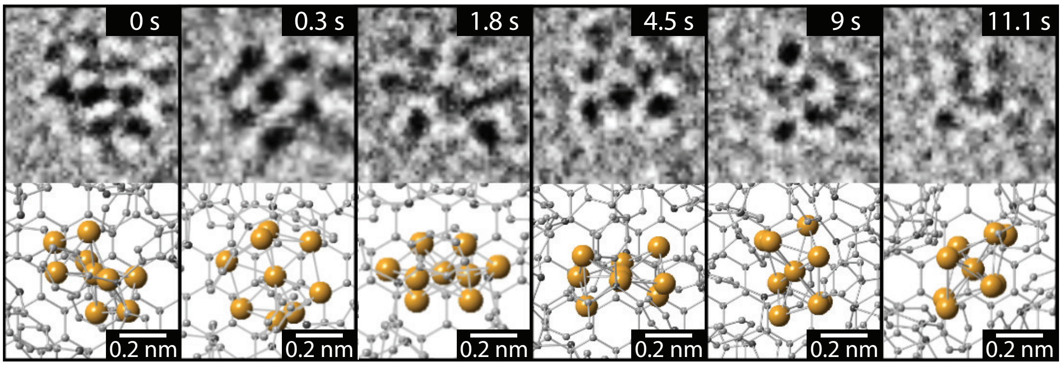

Figure 7.7: Selected HRTEM image frames taken from the dynamics of a single Au_9 nanocluster with their corresponding molecular models.

a specific Au_9 orientation. From this it is apparent that the Au_9 cluster is rotating, but without lateral displacement. This is consistent with covalent attachment of Au_9 to GOSH through the C−S−Au bond.

The inhibited rotation of the Au_9 is induced by the electron beam, and is indicative of a set of metastable orientations. Previous work has observed similar electron beam induced molecular motion on graphene oxide [227, 229], on and inside carbon nanotubes [225, 226], and for molecules attached to carbon nanohorns, where it was shown that lower acceleration voltages in the TEM resulted in a higher frequency of molecular motion as a result of a larger scattering cross-section [97, 228]. For Au_9 imaging, an accelerating voltage of 80 kV was used here in order to minimize damage to the chemically modified graphene by the electron beam. At this acceleration voltage, the clusters are fixed in each orientation for timescales on the order of seconds before switching to another orientation. This indicates that each observed orientation is metastable, and corresponds to a local energy minimum. In addition, the majority of images show well−defined atomic 'spots' rather than blurred streaks, which would be the case if rotational transitions were slow. The metastable orientational states must therefore change with a rapid transition. A more detailed analysis of these molecular dynamics requires an improvement in methodology.

7.3.2 Ir_4 nanoclusters: An extended cross-correlation HRTEM study

The previous section featured a simple by-eye comparison between experimental and simulated images, and allowed much information to be obtained regarding the structure and behaviour of Au_9 NCs. Recently, Nakamrua *et al.* have applied a more robust and quantitative set of methods to the analysis of HRTEM images of a single organic molecule attached to a carbon nanohorn [228]. These methods facilitate greater accuracy and precision in matching between experimental and simulated images by providing a much faster route for comparing images, enabling a much larger catalogue of simulations to be used.

In addition to matching experimental images with specific simulations, the change in state of the M-NC can be further quantified using cross-correlation image analysis between consecutive frames [235, 236]. Differences between successive experimental frames can be compared, which relate directly to changes in the state of the NC, allowing the rate at which significant changes occur to be monitored. The cross-correlation factor between two consecutive frames at times t and t', $\gamma(t, t')$ can be calculated:

$$\gamma(t,t') = \frac{\sum_{ij}^{N} \left[I_t\left(r_{ij}\right) - \bar{I_t}\right] \cdot \left[I_{t'}\left(r_{ij}\right) - \bar{I_{t'}}\right]}{\sqrt{\sum_{ij}^{N} \left[I_t\left(r_{ij}\right) - \bar{I_t}\right]^2} \cdot \sqrt{\sum_{ij}^{N} \left[I_{t'}\left(r_{ij}\right) - \bar{I_{t'}}\right]^2}} \tag{7.2}$$

where $I_t(r_{ij})$ and $I_{t'}(r_{ij})$ are the intensities of pixel (ij) in frames t and t', and $\bar{I_t}$ and $\bar{I_{t'}}$ are the means of $I_t(r_{ij})$ and $I_{t'}(r_{ij})$. This value represents the degree of matching between the two neighboring frames as a number (absolute value) between 1 and 0, 1 being a perfect match and 0 being no match. Thus, any sudden drops of the γ value correspond to a big rotational change followed by small rotational changes [228].

A series of successive HRTEM images of a Au_9 nanocluster are shown in figure 7.8, showing rotational changes occurring between frames. The graph of cross-correlation between successive frames, as calculated using Equation 7.2, shows a significant peak between the 9th and 10th frames, due to their close similarity. This indicates a metastable state for this particular orientation due to its prolonged lifetime. The cross-correlation between other successive frames is much lower due to the large rotational changes occurring between frames.

In order to further investigate the use of cross-correlation methods for M-NC HRTEM studies, an iridium-based test system was used. The tetrairidium dodecacarbonyl NC [$Ir_4(CO)_{12}$], hereafter referred to as Ir_4, consists of 4 iridium atoms (Z = 77) arranged in a tetrahedron, with 3 terminal CO ligands attached to each iridium atom [242]. Molecular models of the Ir_4 nanocluster as well as a perspective view are presented in figure 7.9. Due to their neutral charge, Ir_4 NCs were deposited onto pristine freestanding graphene supports using solution-phase methods. Ir_4 powders purchased from SIGMA-ALDRICH® (98 % purity, CAS Number 11065-24-0, product code 299391) were dissolved in 1,2-dichloroethane. A HRTEM image of a single Ir_4 NC is presented in figure 7.9, along with 3 individual

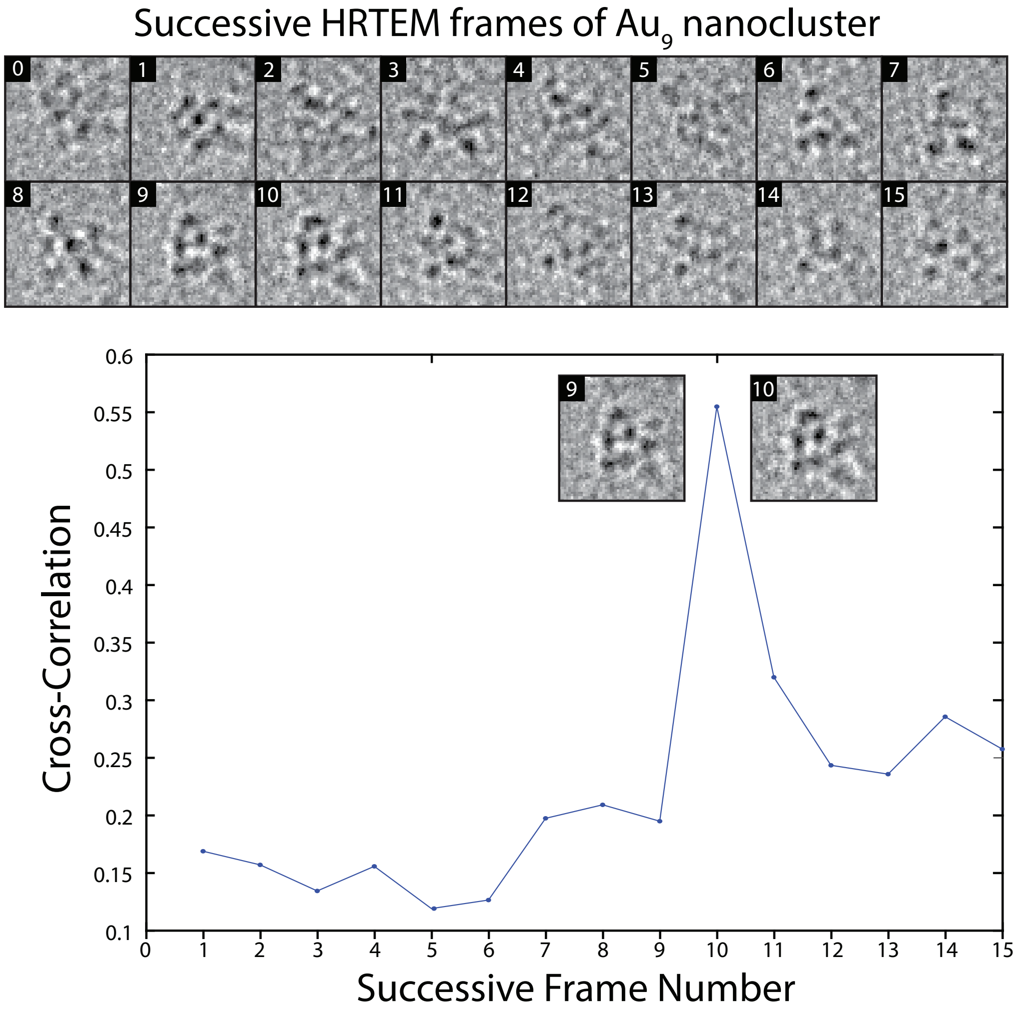

Figure 7.8: Cross-correlation between successive time-series images. Successive HRTEM images of Au_9 nanocluster are cross-correlated with the values plotted as a function of frame number. The significant peak corresponds to a relatively stable orientation that undergoes only small rotational changes between frames 9 and 10. The lower correlation between other frames in the series indicates large rotational changes occurring between frames.

snapshots taken at different times and matched with a corresponding simulation and atomic model. A time series of individual snapshots is presented in figure 7.13 along with corresponding simulations and atomic models. The individual snapshots reveal the cluster rotating rapidly between well-defined states, at a much faster rate than previous Au_9 nanoclusters imaged on GOSH [7].

The underlying assumption made for both the previous Au_9 study and for the present Ir_4 study is that the central metal clusters remain intact and rigid during exposure to the electron beam. In order to verify that the metal-metal bonds within the clusters are not disrupted by the electron beam, the maximum kinetic energy transferred to an atom can be calculated using:

$$E_T(\theta) = \frac{2m_a E(E + 2m_e c^2)}{(m_a + m_e)^2 c^2 + 2m_a E} \tag{7.3}$$

where m_a is the mass of the atom and E is the energy of the electron beam. Calculating for Au and Ir yields $E_T = (0.96 \pm 0.01)$ eV and $E_T = (0.98 \pm 0.01)$ eV respectively. These values may be compared to known bond dissociation energies for Au-Au (2.34 ± 0.05) and Ir-Ir (3.18 ± 0.02) [243]. The maximum kinetic energy deposited in each case is lower than the bond dissociation energy threshold, and so it is appropriate to assume that the metal clusters are stable under the electron beam at 80 kV.

In order to investigate the behaviour of the Ir_4 NC further, a catalogue of simulated TEM images was constructed. Similar to the Au_9 NCs in behaviour, the Ir_4 NCs rotate without lateral diffusion, as a result of a covalent interaction with the graphene support [7]. Therefore, given knowledge of the M-NC structure, a model can be constructed through rotating the M-NC by a specified angle along each rotation axis and placing each new result in a well-defined array, as shown previously for Au_9 (figure 7.5). Implementing a cross-correlation routine for accurate and rapid matching between experimental and simulated images allows a much larger catalogue of simulations to be constructed for Ir_4, as shown in figure 7.10.

Due to the symmetrical nature of some M-NCs, it is unnecessary to rotate through 360 ° about each rotation axis. For the Ir_4 NC with T_d symmetry, it is necessary to rotate only 120 ° about each rotation axis. This is carried out in 10 ° steps, in order to provide sufficient precision for individual simulation matching, whilst providing a simulation catalogue of manageable size (the number of simulations is inversely proportional to the cube of angle step-size when rotating about three independent axes).

There are factors that must be considered in addition to M-NC symmetry and coarseness of angle step when constructing the simulation catalogue. There is a limitation placed by the multislice simulation software on output image size (4096×4096 maximum pixels). This in turn places restrictions on the number of individual M-NCs that can be contained in a single image, in order to maintain a certain resolution for the simulated image. Individual M-NCs cannot be placed in too close proximity with each other, to allow for independent simulations. Therefore,

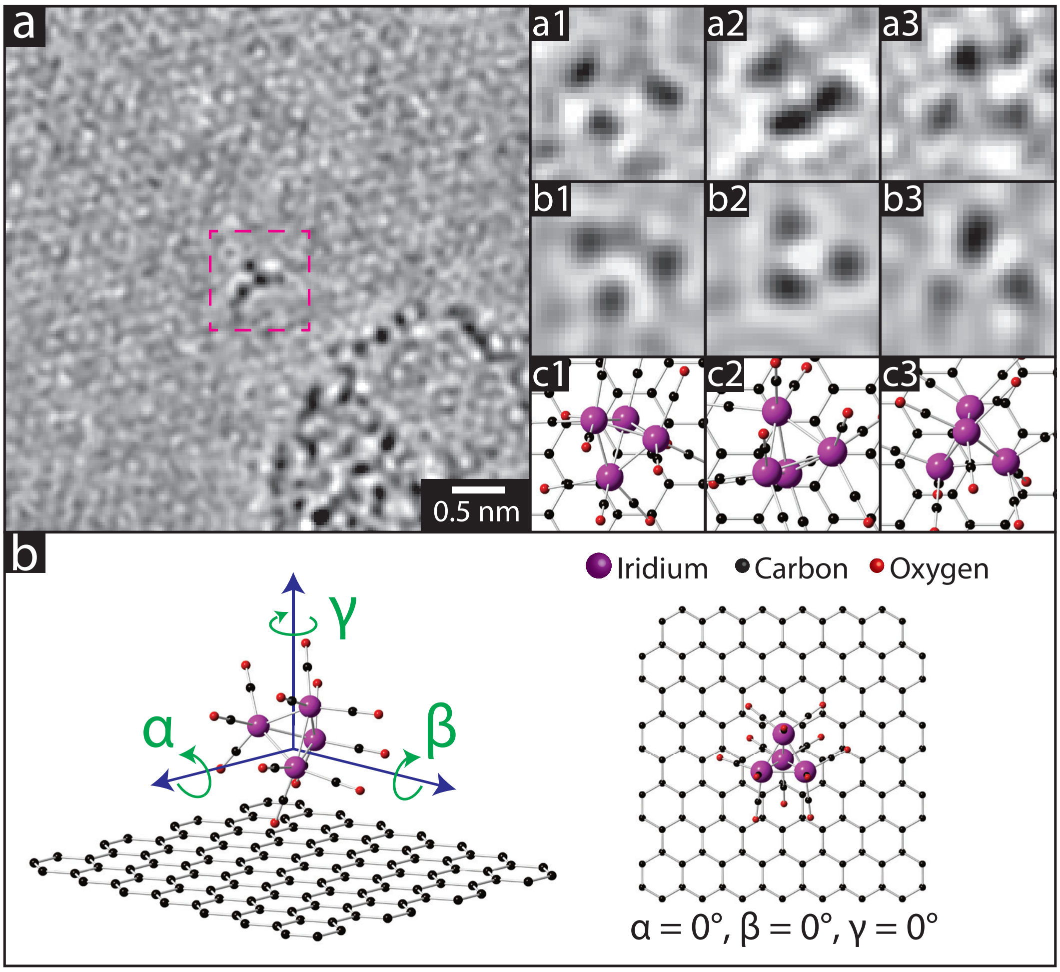

Figure 7.9: HRTEM images of Ir_4 NC on graphene. a) Single HRTEM frame with the boxed region showing a single Ir_4 NC. To the right of the image are 16 different magnified frames showing the same individual M-NC at different times, taken from the boxed region in the main HRTEM image. Clear rotational changes are visible as indicated by the change in image contrast. b) Molecular models showing the Ir_4 NC from different perspectives.

the simulation catalogue is broken down into a series of model frames, each containing a 10×10 array of equally-spaced M-NCs. With the M-NC models constructed, a catalogue of possible TEM images can be simulated using experimentally-measured imaging conditions (accelerating voltage, defocus, astigmatism), as shown in figure 7.10.

With the simulation catalogue established, the methods outlined by Equations 7.1 and 7.2 may be applied to the experimental image sequence. In order to check the validity of the methods, however, a test sequence was first applied to the

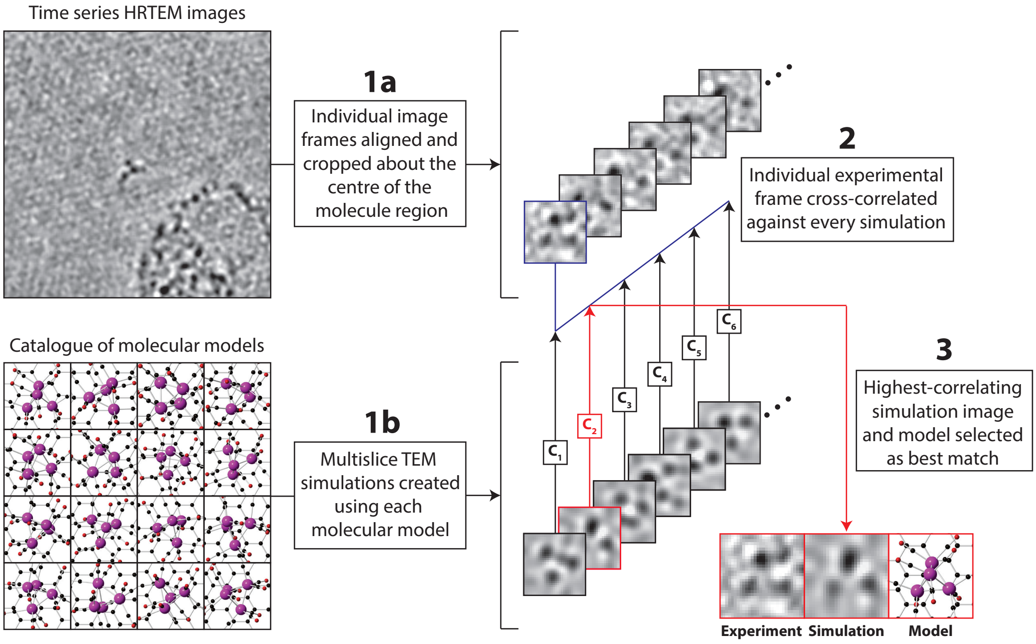

Figure 7.10: TEM image cross-correlation procedure. 1a) TEM image stack is aligned and cropped around the molecule of interest. 1b) Catalogue of TEM simulations is generated based on a set of atomic models. 2) Each experimental frame is cross-correlated with the entire simulation catalogue. 3) The best-matching simulation entry in the catalogue is selected and compared to the experimental frame.

simulation catalogue. The test sequence was constructed by compiling each individual image contained in the simulation into a single image sequence, as shown in figure 7.11. Applying Equation 7.1 to the test sequence, a score can be given to each test sequence frame based on whether it is successfully matched to its duplicate image in the simulation catalogue. A score of 1 is given if frames are successfully matched, and 0 if they are not. The total score then gives a measure of the total number of frames that have been successfully matched, and this can also be quoted as a percentage of the total number of frames in the stack.

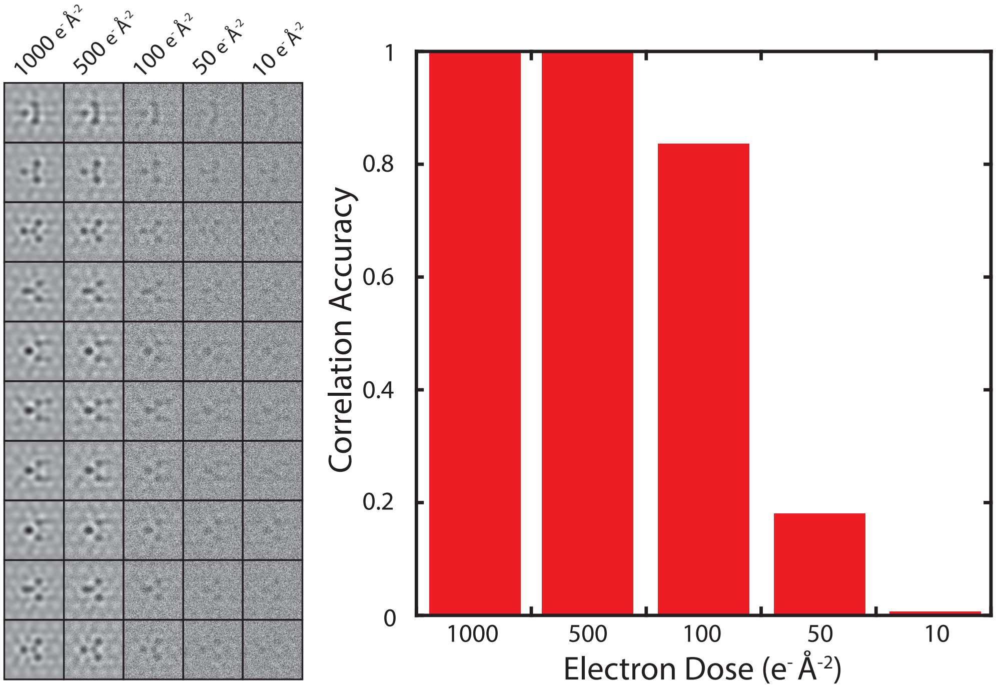

Figure 7.11: Testing the tolerance of cross-correlation matching. Example test image sequences (left) are constructed using the simulation catalogue, generated with a specific dose of electrons. The test sequences are comprised of a full simulation catalogue, with only 10 frames for each shown here for simplicity. The test sequences are matched using cross-correlation to the original simulation catalogue, with the accuracy of the matching plotted as a function of electron dose (right). The cross-correlation techniques operate successfully above 100 e^- Å^{-2} electron dose.

The test sequence itself can be constructed using variable electron doses in the simulation, providing a representation of experimental data obtained with sub-optimal SNR. Test sequences examples with variable electron doses are shown in figure 7.11. Applying the scoring method to the different series shown in figure 7.11, it is clear that the correlation methods fail to work for electron doses less than 100 e^- Å^{-2} (when using a Gatan ORIUS™SC1000 detector). The experimental images obtained in figure 7.9 were captured with an electron dose of 500 e^{-} Å^{-2}, and so the correlation methods of Equations 7.1 and 7.2 are expected to behave accurately. It is noted that the Gatan ORIUS™SC1000 detector has a limited capture rate of 14 fps [138], and so any dynamic behaviour occurring at a faster rate than this will not be sampled accurately; the use of DDDs with much greater frame rate capacity and substantially higher DQE offer the potential to study dynamic M-NC systems in much greater detail [144, 147].

With the tolerance levels of Equation 7.1 established, the experimental image sequence summarised in figure 7.9 can be processed. A graph of correlation score C_{max} for every simulated image for a particular experimental frame is shown in figure 7.12a. The range of correlation scores varies significantly between simulations, allowing accurate discernment of the best-matching simulation. In order to quantify the confidence at which a particular simulation can be selected as the best match, a metric m is defined:

$$m = \frac{C_{max} - \bar{C}}{C_{max}} \tag{7.4}$$

where C_{max} is the maximum correlation for all simulations, and $\bar{C}$ is the average correlation for all simulations. The metric m then has a range between 0 and 1, with 1 indicating a very well-defined maximum correlation. A graph of m for the experimental sequence is plotted in figure 7.12b, indicating the accurate selection of matched simulation image for the majority of experimental frames.

The correlation value between best-matching simulation image and experimental frame is plotted in figure 7.12c. The correlations are well-defined for the majority of frames, with average value ≈ 0.55. Frames are visible with significantly greater correlation, indicating a rotational state that is stable enough to exist for the duration of a 0.1 s exposure. Frames are also visible with a significant drop in correlation, which upon inspection indicate a blurred transition between rotational states (and hence a poor correlation with all well-defined simulations). Finally, the graph in figure 7.12d provides the correlation calculated between successive experimental frames. Interestingly, the graph features several significant peaks, indicating an orientation of relative stability that exists between experimental frames with only small rotational changes. In addition, the graph features significant drops in correlation between frames, indicating a large rotational change occurring between experimental frames. It is clear from the combination of correlation metrics that the Ir_4 is behaving differently to the Au_9 NC studied previously. The Ir_4 exists in several relatively-stable and long-lived states, but also undergoes rapid transitions

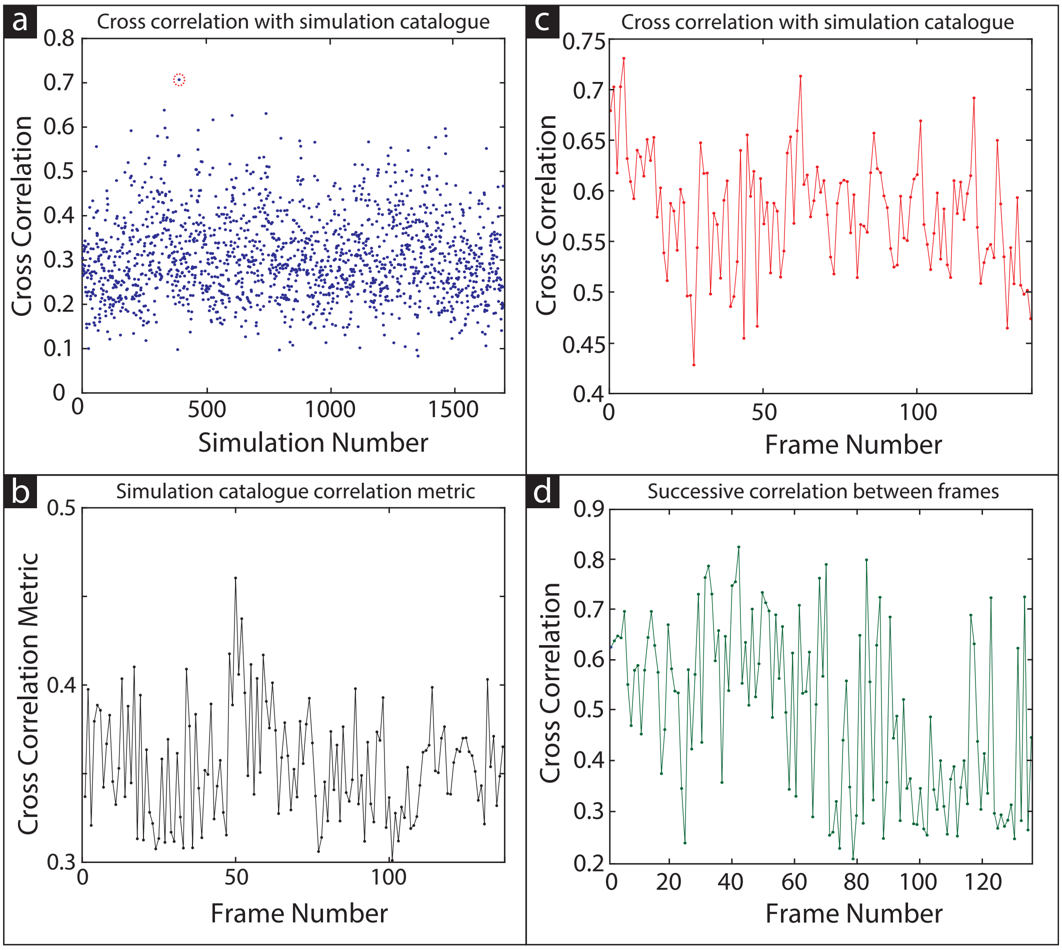

Figure 7.12: Ir_4 cross-correlation summary graphs. a) Cross-correlation results of single experimental frame matched against the full simulation catalogue. The best-matching simulation image is circled in red. b) Correlation metric m calculated using 7.4 for each experimental frame. c) Cross-correlation result of the best-matching simulation image for each experimental frame. d) Cross-correlation result between successive experimental frames. The large correlations are due to similar successive frames, indicating only small rotational changes occurring. Large drops in correlation indicate significant changes in images, due to substantial rotational changes occurring.

between much less-stable rotational states. This behaviour can be visualised directly by analysing the experimental frames and their simulation matches/models.

A sequence of experimental frames, their best matching simulation image, and the corresponding molecular model, are presented in figure 7.13. The experimental images correspond to the same M-NC imaged with 0.1 s successive exposures. The image simulations match well with each experimental frame, with the Ir atoms

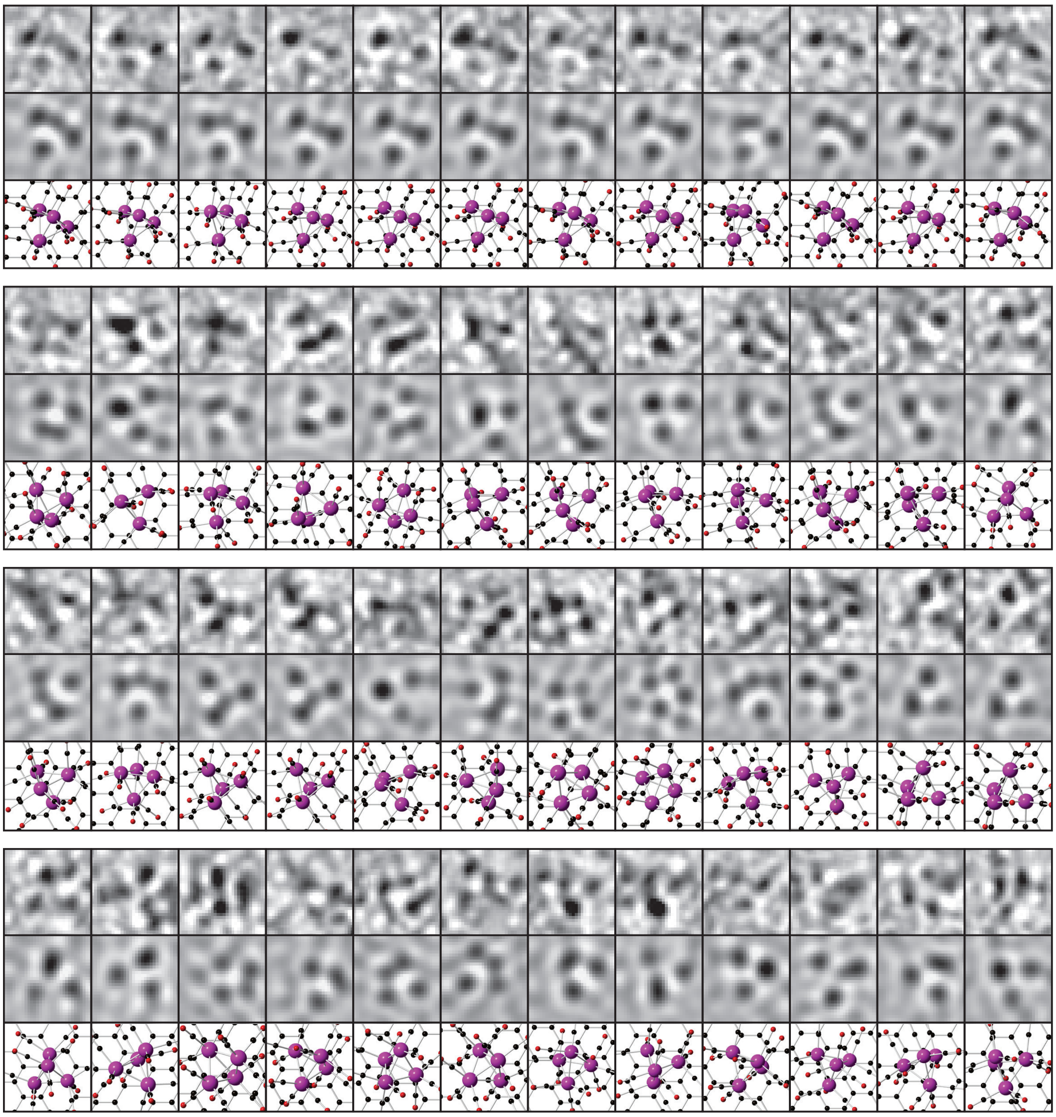

Figure 7.13: Ir_4 experimental TEM images, simulated TEM images, and molecular models, as determined by cross-correlation. Experimental images are taken from a single NC and separated by 0.1 s.

clearly identifiable. Several particular M-NC orientations appear more often than others, indicating rotational states with greater stability. In order to analyse the preferred rotational states, histogram maps can be generated for each pair of orthogonal rotation axes using the full set of experimental data, as shown in figure 7.14. From these histograms, the most stable states of the Ir$_4$ NC can be revealed as having orientations ($\alpha = 60$ °, $\beta = 60$ °, $\gamma = 100$ °) and ($\alpha = 0$ °, $\beta = 0$ °, $\gamma = 100$ °). Molecular models for these two states are illustrated in figure 7.14.

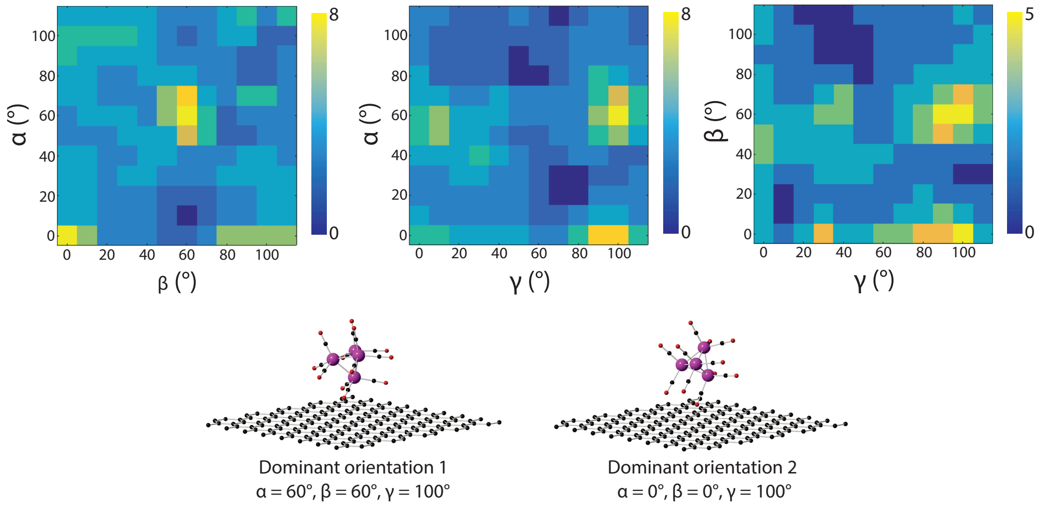

Figure 7.14: Summary of most stable rotational states of Ir$_4$, as determined by cross-correlation. (Top) Orientation maps for each pair of orthogonal rotation axes, showing peaks at the most frequent (stable) rotational states. (Bottom) Molecular model images showin the most stable rotational states.

Comparing the Ir$_4$ and Au$_9$ NCs, both appear to be covalently bonded to the graphene surface and undergo rotational changes between metastable orientations. The transitions between orientations are rapid, and the Ir$_4$ cluster appears to have two preferential orientations. With this work, the limitations of the detection device have also become apparent. The Gatan ORIUS™SC1000 detector is limited to ≈ 0.1 s acquisition rate [138], which prevents any higher time-resolved information on the M-NC rotations being gathered. The simple use of a higher frame-rate device such as the Gatan OneView with an acquisition rate of 0.005 s in (1024×1024) pixel imaging mode [244] would allow far better time-resolved data to be obtained with a much better DQE. Although successful in the study of small, rigid M-NCs, the cross correlation methods applied here could be further extended with better modeling of the specimen. For larger objects and nanoparticles, with more flexible structures, a basic simulation catalogue could be obtained through molecular dynamics simulations, and this could then be further refined based on experimental image matching [228].

As already mentioned, the electron beam acts as the dominant source of energy driving these molecular motions, and so further work investigating the effect of dose rate on the rate of rotational changes would be interesting. As well as studying the rate at which rotational changes occur, the dose rate may also restrict the specific orientations that can be accessed due to energy barriers.

Finally, for both the Ir_4 and Au_9 systems, the effects of beam-induced chemistry were not considered, except in driving the formation of a covalent bond with the graphene surface. For the Au_9 system in particular, with its shell of ligands, it is reasonable to expect some chemical reactions or structural transformations to occur. Due to the significantly stronger contrast provided by the central metal atoms, it is hard to determine to what extent such processes are occurring, and is something that must be considered for adapting the cross-correlation analysis procedure to other molecular systems. Again, with the aid of molecular dynamics simulations in order to provide a simulation catalogue and further refinement against experimental images, it could be envisioned that the cross-correlation methods described here could be applied to the study of structural changes and more exotic chemical processes driven by the electron beam.

7.4 Conclusions

In conclusion, the time evolution and conformational changes of two types of M-NC, Au_9 and Ir_4, have been observed by HRTEM imaging. As analysed by cross-correlation analysis of consecutive images, as well as comparison to a catalogue of simulated images, the motions of both M-NC were found to suggest covalent bonding between the cluster and graphene surface. Both M-NCs were observed to rotate between metastable states on a relatively short time scale, on the order of seconds for Au_9 and tenths of seconds for Ir_4. For Ir_4, two particularly stable orientations were identified using cross-correlation matching to simulated images. The use of cross-correlation techniques applied to time-resolved HRTEM data provides the means for visualising chemical reactions and structural changes in real time at the atomic scale, and will be further enhanced in capability through the use of new-generation electron detectors with significantly improved DQE and acquisition frame rates.

Chapter 8

Conclusions and Future Work

This thesis aimed to address some questions on the mechanisms controlling self-ordering phenomena involving graphene. Specifically, it explored how graphene interacts with a range of atoms and molecules. This included: the role graphene plays in reducing beam-induced sample degradation, how hydrogen-bonded networks interact with graphene, and how this interaction affects the transition from 2D surface driven assembly to 3D films, the use of graphene as an impermeable 2D membrane across which molecular assemblies can interact, and finally the use of graphene as a low contrast support on which to observe atomically-resolved chemical reactions occurring in real time.

In chapter 3, methods were outlined for the clean transfer of graphene from as-grown CVD foils to TEM supports, including a new, simpler methodology for high volume, high yield fabrication. In addition, techniques to fabricate double-layered graphene membranes and samples encapsulated between two monolayers of graphene were presented.

A method to alter the surface functionality of graphene using a self-limiting monolayer film of pyr-modified ions was outlined. These enable control over electrostatic interactions in solution to selectively bind charged macro-molecules, and should be similarly effective for other charged species. This approach is expected to be generically applicable to graphene on any surface or indeed as a free-standing membrane, making it useful in a wide variety of fields including biomedicine, electrochemical sensors or catalysis, as well as for selective adsorption to supported graphene membranes for cryo- and HRTEM imaging.

In chapter 4, the best way to maximise the lifetime of beam-sensitive samples was investigated, studying the role of acceleration voltage, sample temperature, and support substrate. Several types of molecular assemblies were investigated, with results showing that a graphene coating and lower temperature provide optimal protection regardless of accelerating voltage. The role of accelerating voltage was less consistent, demonstrating a complex relationship between scattering cross section and energy deposited by radiolysis of the beam. This contradicts the common assumption that lower accelerating voltages causes less beam-damage. Although lower voltages indeed reduce the effect of elastic knock-on displacement, this mechanism is not the main drive for the disintegration of molecular crystals and soft-matter systems. In order to optimise probing conditions, samples must be dealt with on a sample-by-sample basis.

The use of a high-speed camera and DDD was shown to provide significant benefits in studying beam-sensitive systems such as supramolecular assemblies. Indeed, without the use of a DDD, the study of such systems via HRTEM would in many instances be impossible, due to the poor performance at low-dose of the scintillator-based detectors that are implemented on many HRTEM systems. The development of DDDs and their increase in availability is encouraging, and suggests that within the near future HRTEM studies of the most beam-sensitive systems will become routine, allowing the true potential of HRTEM to be unlocked in a field that has been lagging behind the studies of inorganic specimens since the inception of aberration corrected TEM.

In chapter 5, a fundamentally new insight into the growth of supramolecular thin-films on surfaces was demonstrated through a detailed study into the structural evolution of layers of prototypical benzenecarboxylic acids. For both TMA and TPA, the structure and orientation of the first molecular overlayer are dictated by the comparatively strong hydrogen bonding between molecules and the interactions with the graphene surface that determine a weak van der Waals epitaxial relationship. As the film thickness increases beyond a monolayer, however, TMA and TPA display distinctly different behaviors, despite their chemical similarities. TMA templates from the 2D structure, stacking molecular layers directly on top of each other until, above a certain thickness, the film transitions to a polycrystalline phase with random in-plane orientations. By contrast, TPA forms fiber-like islands and the in-plane lattice parameters change continuously with thickness, smoothly becoming more consistent with the bulk structure. It is proposed that these differences in behavior can be understood through comparison between the 2D and 3D structures of the two molecules: the bulk structure of TMA is topologically distinct from the monolayer structure with no possible smooth transition between the two, whereas, for TPA, tilting of the molecules with respect to the surface gives a continuous transition from 2D to 3D structures. As a result, the 2D TMA structure is topologically protected and templates through the initial film growth. This new insight - topological protection of the 2D structure - will help design functional structural features into molecular building blocks in order to control the growth of organic thin films by supramolecular assembly.

In chapter 6, the structural coupling of monolayers of NiOEP/OEP across a single layer of freestanding graphene gave new insight into the growth and behavior of supramolecular thin-films on surfaces. The graphene has no epitaxial influence on the crystallography of the molecular assembly. Despite this, on freestanding graphene the orientation of the molecular layer on top is always identical to the orientation of the layer below, dictated by remote van der Waals interactions between the molecular layers. STM measurements reveal that NiOEP/OEP assume a flat 2D lattice on both copper-supported graphene and on HOPG. SAED measurements prove that NiOEP/OEP layers on both the top and bottom surfaces of freestanding single-layer graphene align through the graphene, producing a single, larger unit cell. This molecular coupling produces a highly-organised, large-scale superstructure; the two molecular films are oriented in the same direction and positioned on top of one another due to mutual coupling across the graphene layer. The coupling interaction is shown to diminish on a length scale of two graphene layers, with NiOEP/OEP layers deposited on either side of a twisted bilayer graphene membrane showing no alignment. Further work is required to understand the nature of this interaction and establish the role of graphene - is it an inert spacer or does it play an active role in enhancing the dipole interactions - and to quantify their strength. As already mentioned, preliminary MD simulations undertaken by our collaborator Dr Tiffany Walsh at Deakin University are fully consistent with these experimental data and suggest that this will be a generic effect. Hence, this new phenomenon of molecular alignment through 2D films gives a new tool for the study and design of nanostructured films, and demonstrates how molecular interactions can extend across the otherwise impermeable graphene membrane.

Finally, in chapter 7 the time evolution and conformational changes of two types of M-NC, Au_9 and Ir_4, were observed by HRTEM imaging. As analysed by cross-correlation analysis of consecutive images, as well as comparison to a catalogue of simulated images, both M-NC were fixed in position on the graphene, suggesting covalent bonding between the cluster and graphene surface. Both M-NCs were observed to rotate between metastable states on a relatively short time scale, on the order of seconds for Au_9 and tenths of seconds for Ir_4. For Ir_4, two particularly stable orientations were identified using cross-correlation matching to simulated images. The use of cross-correlation techniques applied to time-resolved HRTEM data provides the means for visualising chemical reactions and structural changes in real time at the atomic scale, and will be further enhanced in capability through the use of new-generation electron detectors with significantly improved DQE and acquisition frame rates.

The key challenge involved with all of the work featured within this thesis has been the dose limitations of the organic specimens probed. As has been shown, there is significant promise with the advent of fast acquisition and direct detection devices, which will pave the way for a revolution in the study of molecular materials. No longer relying on low-dose diffraction as the main source of information, direct imaging of molecular systems at atomic resolution with high contrast and SNR is expected to be routine within a number of years. The vast body of research focusing on molecular materials, molecular dynamics modeling, and their applications will undoubtedly benefit from this significant microscopy tool, building on the techniques featured here that are already emerging from their infancy.

Bibliography

1. Marsden, A. J. *et al.* *"Growth of Large Crystalline Grains of Vanadyl Phthalocyanine without Epitaxy on Graphene."* Advanced Functional Materials **26,** 1188–1196 (2016).
2. Bosch-Navarro, C., Laker, Z. P., Marsden, A. J., Wilson, N. R. & Rourke, J. P. *"Non-covalent functionalization of graphene with a hydrophilic self-limiting monolayer for macro molecule immobilization."* FlatChem **1,** 52–56 (2017).
3. Hu, S. *et al.* *"Thermochemical functionalisation of graphenes with minimal framework damage."* Chemical Science, 6149–6154 (2017).
4. Inam, M. *et al.* *"1D vs. 2D shape selectivity in the crystallization-driven self-assembly of polylactide block copolymers."* Chem. Sci. **8,** 4223–4230 (2017).
5. Arno, M. C. *et al.* *"Precision Epitaxy for Aqueous 1D and 2D Poly(ϵ-caprolactone) Assemblies."* Journal of the American Chemical Society **139,** 16980–16985 (2017).
6. Laker, Z. P. *et al.* *"Monolayer-to-thin-film transition in supramolecular assemblies: the role of topological protection."* Nanoscale, 11959–11968 (2017).
7. Bosch-Navarro, C. *et al.* *"Covalently Binding Atomically Designed Au_9 Clusters to Chemically Modified Graphene."* Angewandte Chemie - International Edition **54,** 9560–9563 (2015).
8. Novoselov, K. S. *et al.* *"Electric Field Effect in Atomically Thin Carbon Films."* Science **306,** 666–670 (2004).
9. Novoselov, K. S. *et al.* *"Two dimensional gas of massless Dirac fermions in graphene."* Nature **438,** 197–200 (2005).
10. Geim, A. K. & Grigorieva, I. V. *"Van der Waals heterostructures."* Nature **499,** 419–425 (2013).
11. Novoselov, K. S. *et al.* *"A roadmap for graphene."* Nature **490,** 192–200 (2012).
12. Ferrari, A. C. *et al.* *"Science and technology roadmap for graphene, related two dimensional crystals, and hybrid systems."* Nanoscale **7,** 4598–4810 (2015).
13. Zhang, S. *"Fabrication of novel biomaterials through molecular self-assembly."* Nature Biotechnology **21,** 1171–1178 (2003).
14. Stankovich, S. *et al.* *"Graphene-based composite materials."* Nature **442,** 282–286 (2006).

15. Burroughes, J. H. *et al.* *"Light-emitting diodes based on conjugated polymers."* Nature **347,** 539–541 (1990).
16. Barth, J. V., Costantini, G. & Kern, K. *"Engineering atomic and molecular nanostructures at surfaces."* Nature **437,** 671–679 (2005).
17. Warner, J. H., Schaffel, F., Bachmatiuk, A. & Rummeli, M. H. *"Graphene Fundamentals and emergent applicaitons."* (Elsevier, 2013).
18. Neto, C. A. H., Guinea, F., Peres, N. M. R., Novoselov, K. S. & Geim, A. K. *"The electronic properties of graphene."* Review of Modern Physics **81** (2007).
19. Balandin, A. A. *et al.* *"Superior Thermal Conductivity of Single-Layer Graphene."* Nano Letters **8,** 902–907 (2008).
20. Lee, G.-H. *et al.* *"High Strength Chemical Vapor Deposited Graphene and Grain Boundaries."* Science **340,** 1073–1076 (2013).
21. Bunch, S. J. *et al.* *"Electromechanical Resonators from Graphene Sheets."* Science **315,** 490–493 (2007).
22. Nair, R. R. *et al.* *"Fine structure constant defines visual transparency of graphene."* Science **320,** 1308 (2008).
23. Berry, V. *"Impermeability of graphene and its applications."* Carbon **62,** 1–10 (2013).
24. Miao, M., Nardelli, M. B., Wang, Q. & Liu, Y. *"First principles study of the permeability of graphene to hydrogen atoms."* Physical Chemistry Chemical Physics **15** (2013).
25. Pumera, M. *"Graphene-based nanomaterials for energy storage."* Energy & Environmental Science **4,** 668–674 (2011).
26. Shao, Y. *et al.* *"Graphene-based electrochemical sensors and biosensors: A review."* Electroanalysis **22,** 1027–1036 (2010).
27. Varghese, S. S., Lonkar, S., Singh, K. K., Swaminathan, S. & Abdala, A. *"Recent advances in graphene-based gas sensors."* Sensors and Actuators, B: Chemical **218,** 160–183 (2015).
28. Schedin, F. *et al.* *"Detection of individual gas molecules adsorbed on graphene."* Nature Materials **6,** 652–655 (2007).
29. Wu, Y. *et al.* *"State-of-the-art graphene high-frequency electronics."* Nano Letters **12,** 3062–3067 (2012).
30. Lin, Y. M. *et al.* *"100-GHz transistors from wafer-scale epitaxial graphene."* Science **327,** 662 (2010).
31. Arco, L. G. D. *et al.* *"Continuous, Highly Flexible, and Transparent Graphene Films by Chemical Vapor Deposition for Organic Photovoltaics."* ACS Nano **4,** 2865–2873 (2010).
32. Bae, S. *et al.* *"30 inch Roll-Based Production of High-Quality Graphene Films for Flexible Transparent Electrodes."* Nature Nanotechnology **5,** 1–5 (2009).

33. Kobayashi, T. *et al.* *"Production of a 100-m-long high-quality graphene transparent conductive film by roll-to-roll chemical vapor deposition and transfer process."* Applied Physics Letters **102,** 1–5 (2013).
34. Pimpinelli, A. & Villain, J. *"Physics of Crystal Growth."* (Cambridge University Press, 1998).
35. Venables, J. A. *"Introduction to Surface and Thin Film Processes."* (Cambridge University Press, 2000).
36. Koma, A. *"Van der Waals epitaxy for highly lattice-mismatched systems."* Journal of Crystal Growth **201,** 236–241 (1999).
37. Utama, M. I. B. *et al.* *"Recent developments and future directions in the growth of nanostructures by van der Waals epitaxy."* Nanoscale **5,** 3570–88 (2013).
38. Schlom, D. G. *et al.* *"Strain Tuning of Ferroelectric Thin Films."* Annual Review of Materials Research **37,** 589–626 (2007).
39. Pohl, U. W. *"Epitaxy of Semiconductors - Introduction to Physical Principles."* (Springer, 2012).
40. Schreiber, F. *"Organic molecular beam deposition: Growth studies beyond the first monolayer."* Physica Status Solidi (A) Applied Research **201,** 1037–1054 (2004).
41. Forrest, S. R. *"Ultrathin organic films grown by organic molecular beam deposition and related techniques."* Chemical Reviews **97,** 1793–1896 (1997).
42. Wood, G. E. *et al.* *"van der Waals epitaxy of monolayer hexagonal boron nitride on copper foil: growth, crystallography and electronic band structure."* 2D Materials **2,** 025003 (2015).
43. Marsden, A. *"van der Waals epitaxy in graphene heterostructures."* PhD Thesis, University of Warwick (2015).
44. Wilson, N. R. *et al.* *"Weak mismatch epitaxy and structural Feedback in graphene growth on copper foil."* Nano Research **6,** 99–112 (2013).
45. Ratsch, C. & Venables, J. A. *"Nucleation Theory and the Early Stages of Thin Film Growth."* Journal of Vacuum Science & Technology A **21,** S96–S109 (2003).
46. Oura, K., Lifshits, V. G., Saranin, A., Zotov, A. V. & Katayama, M. *"Surface Science - An Introduction."* (Springer, 2003).
47. Kowarik, S., Gerlach, A. & Schreiber, F. *"Organic molecular beam deposition: Fundamentals, growth dynamics, and in-situ studies."* Journal of Physics Condensed Matter **20** (2008).
48. Slater, A. G., Beton, P. H. & Champness, N. R. *"Two dimensional supramolecular chemistry on surfaces."* Chemical Science **2,** 1440–1448 (2011).

49. Lackinger, M., Griessl, S., Heckl, W. M., Hietschold, M. & Flynn, G. W. *"Self-assembly of trimesic acid at the liquid-solid interface: A study of solvent-induced polymorphism."* Langmuir **21,** 4984–4988 (2005).

50. Yoshikawa, G. *et al.* *"Spontaneous aggregation of pentacene molecules and its influence on field-effect mobility."* Applied Physics Letters **90,** 88–91 (2007).

51. Beernink, G., Strunskus, T., Witte, G. & Wöll, C. *"Importance of dewetting in organic molecular-beam deposition: Pentacene on gold."* Applied Physics Letters **85,** 398–400 (2004).

52. Krause, B., Dürr, A. C., Schreiber, F., Dosch, H. & Seeck, O. H. *"Late growth stages and post-growth diffusion in organic epitaxy: PTCDA on Ag(111)."* Surface Science **572,** 385–395 (2004).

53. Jackson, K. A. *"Kinetic Processes: Crystal Growth, Diffusion, and Phase Transformations in Materials."* (Wiley, 2006).

54. Jackson, K. A. *"The interface kinetics of crystal growth processes."* Interface Science **10,** 159–169 (2002).

55. Lin, K. Y. *et al.* *"Rubrene polycrystalline films growth from vacuum deposition at various substrate temperatures."* Journal of Crystal Growth **439,** 54–59 (2016).

56. Kowarik, S. *et al.* *"Anomalous roughness evolution of rubrene thin films observed in real time during growth."* Physical Chemistry Chemical Physics **8,** 1834 (2006).

57. Käfer, D., Ruppel, L. & Witte, G. *"Growth of pentacene on clean and modified gold surfaces."* Physical Review B **75,** 085309 (2007).

58. Griessl, S., Lackinger, M., Edelwirth, M., Hietschold, M. & Heckl, W. M. *"Self-Assembled Two-Dimensional Molecular Host-Guest Architectures From Trimesic Acid."* Single Molecules **3,** 25–31 (2002).

59. Otero, R., Gallego, J. M., De Parga, A. L. V., Martín, N. & Miranda, R. *"Molecular self-assembly at solid surfaces."* Advanced Materials **23,** 5148–5176 (2011).

60. Li, X. *et al.* *"Large-Area Synthesis of High-Quality and Uniform Graphene Films on Copper Foils."* Science **324,** 1312–1314 (2009).

61. Hiura, H., Miyazaki, H. & Tsukagoshi, K. *"Determination of the number of graphene layers: Discrete distribution of the secondary electron intensity stemming from individual graphene layers."* Applied Physics Express **3,** 2–5 (2010).

62. Zhang, B. *et al.* *"Low temperature chemical vapor deposition growth of graphene from toluene on electropolished copper foils."* ACS Nano **6,** 2471–2476 (2012).

63. Drake, B., Sonnenfeld, R., Schneir, J. & Hansma, P. K. *"Scanning Tunneling Microscopy. Perspectives in Condensed Matter Physics."* (Springer, 1986).

64. Zou, X., Hovmoller, S. & Oleynikov, P. *"Electron Crystallography: Electron Microscopy and Electron Diffraction."* (Oxford University Press, 2011).

65. Williams, D. B. & Carter, B. C. *"Transmission Electron Microscopy."* (Springer, 2004).
66. Iijima, S. & Iijima, S. *"High-Resolution Electron Microscopy of Crystal Lattice of Titanium-Niobium Oxide High-Resolution Electron Microscopy of Crystal Lattice of Titanium-Niobium Oxide."* Journal of Applied Physics **42,** 5891–5893 (1971).
67. Shmueli, U. *"International Tables for Crystallography Volume B: Reciprocal Space."* (International Union of Crystallography, 2010).
68. Prince, E. *"International Tables for Crystallography Volume C: Mathematical, physical and chemical tables."* (International Union of Crystallography, 2006).
69. Skowron, S. T. *et al.* *"Chemical Reactions of Molecules Promoted and Simultaneously Imaged by the Electron Beam in Transmission Electron Microscopy."* Accounts of Chemical Research **50,** 1797–1807 (2017).
70. Goodman, J. W. *"Introduction to Fourier Optics."* (McGraw-Hill, 1996).
71. Kirkland, E. J. *"Advanced Computing in Electron Microscopy."* (Springer, 2010).
72. Zemlin, F., Weiss, K., Schiske, P., Kunath, W. & Herrmann, K. H. *"Coma-free alignment of high resolution electron microscopes with the aid of optical diffractograms."* Ultramicroscopy **3,** 49–60 (1978).
73. Cowley, J. M. & Moodie, a. F. *"The scattering of electrons by atoms and crystals. I. A new theoretical approach."* Acta Crystallographica **10,** 609–619 (1957).
74. Goodman, P. & Moodie, A. F. *"Numerical evaluations of N-beam wave functions in electron scattering by the multi-slice method."* Acta Crystallographica A, 280–290 (1974).
75. Cooley, J. & Tukey, J. W. *"An algorithm for the machine calculation of complex Fourier series."* American Mathematical Society: Mathematics of Computation, 297–301 (1965).
76. Ishizuka, K. & Uyeda, N. *"A New Theoretical and Practical Approach to the Multislice Method."* Acta Crystallographica Section A **33,** 740–749 (1977).
77. Dyson, A. M. & Peters, J. J. P. *"clTEM."* GitHub (2014).
78. Dyson, A. M. *"Advances in computational methods for transmission electron microscopy simulation and image processing."* PhD Thesis, University of Warwick (2014).
79. Peters, J. J. P. *"Structure and ferroelectricity at the atomic level in perovskite oxides."* PhD Thesis, University of Warwick (2017).
80. Vulovic, M. *et al.* *"Image formation modeling in cryo-electron microscopy."* Journal of Structural Biology **183,** 19–32 (2013).
81. Laker, Z. P. L. *"Molecular Cell Generator."* GitHub Gist (2018).

82. Binnig, G. & Rohrer, H. *"Scanning tunneling microscopy."* Surface Science **126,** 236–244 (1983).

83. Tersoff, J. & Hamann, D. *"Theory and application for the scanning tunneling microscope."* Physical review letters **50,** 1998 (1983).

84. Tersoff, J. & Hamann, D. R. *"Theory of the scanning tunneling microscope."* Physical Review B **31,** 805–813 (1985).

85. Baratoff, A. *"Theory of scanning tunneling microscopy - methods and approximations."* Physica B+C **127,** 143–150 (1984).

86. Chen, C. J. *"Effects of m≠0 tip states in scanning tunneling microscopy: The explanations of corrugation reversal."* Physical Review Letters **69,** 1656–1659 (1992).

87. Chen, C. J. *"Introduction to Scanning Tunneling Microscopy: Second Edition."* (Oxford University Press, 2007).

88. Wilson, N. R. *et al.* *"Graphene Oxide: Structural Analysis and Application as a Highly Transparent Support for Electron Microscopy."* ACS Nano **3,** 2547–2556 (2009).

89. Lee, C., Wei, X., Kysar, J. W. & Hone, J. *"Measurement of the elastic properties and intrinsic strength of Monolayer Graphene."* Science **321,** 385–388 (2008).

90. Egerton, R. F. *"Control of radiation damage in the TEM."* Ultramicroscopy **127,** 100–108 (2013).

91. Li, D., Müller, M. B., Gilje, S., Kaner, R. B. & Wallace, G. G. *"Processable aqueous dispersions of graphene nanosheets."* Nature Nanotechnology **3,** 101–105 (2008).

92. Suk, J. W., Piner, R. D., An, J. & Ruoff, R. S. *"Mechanical Properties of Monolayer Graphene Oxide."* ACS Nano **4,** 6557–6564 (2010).

93. Wilson, N. R. *et al.* *"On the structure and topography of free standing chemically modified graphene."* New Journal of Physics **12,** 125010 (2010).

94. Patterson, J. P. *et al.* *"A simple approach to characterizing block copolymer assemblies: graphene oxide supports for high contrast multi-technique imaging."* Soft Matter **8,** 3322 (2012).

95. Wang, C., Qiao, Q., Shokuhfar, T. & Klie, R. F. *"High resolution electron microscopy and spectroscopy of ferritin in biocompatible graphene liquid cells and graphene sandwiches."* Advanced Materials **26,** 3410–3414 (2014).

96. Macleod, J. M. & Rosei, F. *"Molecular self-assembly on graphene."* Small **10,** 1038–1049 (2014).

97. Sloan, J. *et al.* *"Imaging the structure, symmetry, and surface inhibited rotation of polyoxometalate ions on graphene oxide."* Nano Letters **10,** 4600–4606 (2010).

98. Dong, X. *et al.* *"Symmetry breaking of graphene monolayers by molecular decoration."* Physical Review Letters **102,** 135501 (2009).

99. Lee, W. H. *et al.* *"Surface-Directed Molecular Assembly of Pentacene on Monolayer Graphene for High Performance Organic Transistors."* Journal of the American Chemical Society **133,** 4447–4454 (2011).

100. Kim, K. S. *et al.* *"Large-scale pattern growth of graphene films for stretchable transparent electrodes."* Nature **457,** 706–710 (2009).

101. Murdock, A. T. *et al.* *"Controlling the Orientation, Edge Geometry, and Thickness of Chemical Vapor Deposition Graphene."* 1351–1359 (2013).

102. Leenaerts, O., Partoens, B. & Peeters, F. M. *"Water on graphene: Hydrophobicity and dipole-moment using density functional theory."* Physical Review B - Condensed Matter and Materials Physics **79,** 1–5 (2009).

103. Wang, S., Zhang, Y., Abidi, N. & Cabrales, L. *"Wettability and surface free-energy of graphene films."* Langmuir **25,** 11078–11081 (2009).

104. Marsden, A. J. *et al.* *"Effect of oxygen and nitrogen functionalization on the physical and electronic structure of graphene."* Nano Research **8,** 2620–2635 (2015).

105. Georgakilas, V. *et al.* *"Noncovalent Functionalization of Graphene and Graphene Oxide for Energy Materials, Biosensing, Catalytic, and Biomedical Applications."* Chemical Reviews **116,** 5464–5519 (2016).

106. Georgakilas, V. *et al.* *"Functionalization of graphene: Covalent and non-covalent approaches, derivatives and applications."* Chemical reviews **112,** 6156–214 (2012).

107. Marsh, K. N. *"Recommended Reference Materials for the Realization of Physicochemical Properties."* (Blackwell Science Publishing, 1987).

108. Baumeister, W. & Seredynski, J. *"Preparation of performed films with predeterminable hole size distributions."* Micron (1969) **7,** 49–54 (1976).

109. Martinez, C. R. & Iverson, B. L. *"Rethinking the term "pi-stacking"."* Chemical Science **3,** 2191 (2012).

110. Berner, N. C. *et al.* *"Understanding and optimising the packing density of perylene bisimide layers on CVD grown graphene."* Nanoscale **7,** 16337–16342 (2015).

111. Winters, S. *et al.* *"On-surface derivatisation of aromatic molecules on graphene: The importance of packing density."* Chemical Communications **51,** 16778–16781 (2015).

112. Hirsch, A., Englert, J. M. & Hauke, F. *"Wet chemical functionalization of graphene."* Accounts of Chemical Research **46,** 87–96 (2013).

113. Katsukis, G. *et al.* *"Toward combining graphene and QDs: Assembling CdTe QDs to exfoliated graphite and nanographene in water."* ACS Nano **6,** 1915–1924 (2012).

114. Malig, J., Romero-Nieto, C., Jux, N. & Guldi, D. M. *"Integrating water soluble graphene into porphyrin nanohybrids."* Advanced Materials **24,** 800–805 (2012).

115. Ehli, C. *et al.* *"Interactions in single-wall carbon nanotubes/pyrene/porphyrin nanohybrids."* Journal of the American Chemical Society **128,** 11222–11231 (2006).

116. Chung, C.-L., Gautier, C., Campidelli, S. & Filoramo, A. *"Hierarchical functionalisation of single-wall carbon nanotubes with DNA through positively charged pyrene."* Chemical communications (Cambridge, England) **46,** 6539–6541 (2010).

117. Bosch-Navarro, C. *et al.* *"Charge transfer interactions in self assembled single-walled carbon nanotubes/Dawson Wells polyoxometalate hybrids."* Chemical Science **5,** 4346–4354 (2014).

118. Schlierf, A. *et al.* *"Nanoscale insight into the exfoliation mechanism of graphene with organic dyes effect of charge, dipole and molecular structure."* Nanoscale **5,** 4205 (2013).

119. Xu, Y., Bai, H., Lu, G., Li, C. & Shi, G. *"Flexible graphene films via the filtration of water-soluble noncovalent functionalized graphene sheets."* Journal of the American Chemical Society **130,** 5856–5857 (2008).

120. An, X. *et al.* *"Stable acqeous dispersions of noncovalently functionalized graphene from graphite and their multifunctional high performance applications."* Nano Letters **10,** 4295–4301 (2010).

121. Das, A. *et al.* *"Monitoring dopants by Raman scattering in an electrochemically top gated graphene transistor."* Nature Nanotechnology **3,** 210–215 (2008).

122. Chen, S. *et al.* *"Aqueous cationic, anionic and non-ionic multi walled carbon nanotubes, functionalised with minimal framework damage, for biomedical application."* Biomaterials **35,** 4729–4738 (2014).

123. Hu, S. *et al.* *"Aqueous dispersions of oligomer grafted carbon nanomaterials with controlled surface charge and minimal framework damage."* Faraday Discussions **173,** 273–285 (2014).

124. Menzel, R. *et al.* *"A versatile, solvent-free methodology for the functionalisation of carbon nanotubes."* Chemical Science **1,** 603 (2010).

125. Chen, S. *"FePt magnetic nanoparticles: syntheses, functionalisation and characterisation for biomedical applications."* PhD Thesis, University of St Andrews (2015).

126. Haider, M., Rose, H., Uhlemann, S., Kabius, B. & Urban, K. *"Towards 0.1 nm resolution with the first spherically corrected transmission electron microscope."* Journal of Electron Microscopy **47,** 395–405 (1998).

127. Haider, M. *et al.* *"A spherical aberration corrected 200kV transmission electron microscope."* Ultramicroscopy **75,** 53–60 (1998).

128. Stenn, K. & Bahr, G. F. *“Specimen damage caused by the beam of the transmission electron microscope, a correlative reconsideration.”* Journal of Ultrasructure Research **31,** 526–550 (1970).

129. Egerton, R. F. *“Mechanisms of radiation damage in beam-sensitive specimens, for TEM accelerating voltages between 10 and 300 kV.”* Microscopy Research and Technique **75,** 1550–1556 (2012).

130. Carlson, D. B. & Evans, J. E. *“The Transmission Electron Microscope: Low-Dose Imaging Techniques for Transmission Electron Microscopy.”* (InTech, 2004).

131. Tan, Y. W. *et al.* *“Graphene at the Edge.”* Science **666,** 1705–1708 (2009).

132. Egerton, R. F., Li, P. & Malac, M. *“Radiation damage in the TEM and SEM.”* Micron **35,** 399–409 (2004).

133. Egerton, R. F. *“Choice of operating voltage for a transmission electron microscope.”* Ultramicroscopy **145,** 85–93 (2014).

134. Meents, A., Gutmann, S., Wagner, A. & Schulze-Briese, C. *“Origin and temperature dependence of radiation damage in biological samples at cryogenic temperatures.”* Proceedings of the National Academy of Sciences **107,** 1094–1099 (2010).

135. Balandin, A. A. *“Thermal properties of graphene and nanostructured carbon materials.”* Nature Materials **10,** 569–581 (2011).

136. Chen, S. *et al.* *“Thermal conductivity of isotopically modified graphene.”* Nature Materials **11,** 203–207 (2012).

137. Chen, S. *et al.* *“Raman measurements of thermal transport in suspended monolayer graphene of variable sizes in vacuum and gaseous environments.”* ACS Nano **5,** 321–328 (2011).

138. Gatan, I. *ORIUS SC 1000 CCD Camera User’s Guide* (2006).

139. Meyer, R. & Kirkland, A. *“Characterisation of the Signal and Noise Transfer of CCD Cameras for Electron Detection.”* Microscopy Research and Technique **49,** 269–280 (2000).

140. Ruskin, R. S., Yu, Z. & Grigorieff, N. *“Quantitative characterization of electron detectors for transmission electron microscopy.”* Journal of Structural Biology **184,** 385–393 (2013).

141. Vulovic, M. & Rieger, B. *“A toolkit for the characterization of CCD cameras for transmission electron microscopy.”* Acta Crystallographica D: Biological Crystallography **D66,** 97–109 (2010).

142. Zwet, E. J. V. & Zandbergen, H. W. *“Measurement of the modulation transfer function of a slow-scan CCD camera on a TEM using a thin amorphous film as test signal.”* Ultramicroscopy **64,** 49–55 (1996).

143. Ruijter, W. J. D. & Weiss, J. K. *“Methods to measure properties of slow scan CCD cameras for electron detection.”* Review of Scientific Instruments **4314** (1992).

144. Booth, C. & Mooney, P. *"Applications of electron-counting direct-detection cameras in high-resolution cryo-electron microscopy."* Microscopy and Analysis **27,** 13–21 (2013).

145. Li, X., Zheng, S. Q., Egami, K., Agard, D. A. & Cheng, Y. *"Influence of electron dose rate on electron counting images recorded with the K2 camera."* Journal of Structural Biology **184,** 251–260 (2013).

146. Li, X. *et al.* *"Electron counting and beam-induced motion correction enable near-atomic-resolution single-particle cryo-EM."* Nature Methods **10** (2013).

147. Clough, R. N., Moldovan, G. & Kirkland, A. I. *"Direct Detectors for Electron Microscopy."* Journal of Physics: Conference Series **522** (2014).

148. Elemans, J. A. A. W., Lei, S. & De Feyter, S. *"Molecular and Supramolecular Networks on Surfaces: From Two-Dimensional Crystal Engineering to Reactivity."* Angewandte Chemie - International Edition **48,** 7298–7332 (2009).

149. Barth, J. V. *"Molecular Architectonic on Metal Surfaces."* Annual Review of Physical Chemistry **58,** 375–407 (2007).

150. Theobald, J. A., Oxtoby, N. S., Phillips, M. A., Champness, N. R. & Beton, P. H. *"Controlling molecular deposition and layer structure with supramolecular surface assemblies."* Nature **424,** 1029–1031 (2003).

151. Stepanow, S. *et al.* *"Steering molecular organization and host-guest interactions using two-dimensional nanoporous coordination systems."* Nature Materials **3,** 229–233 (2004).

152. Liang, H. *et al.* *"Two-dimensional molecular porous networks constructed by surface assembling."* Coordination Chemistry Reviews **253,** 2959–2979 (2009).

153. Kudernac, T., Lei, S., Elemans, J. A. A. W. & De Feyter, S. *"Two-dimensional supramolecular self-assembly: nanoporous networks on surfaces."* Chemical Society Reviews **38,** 402–421 (2009).

154. Yang, J., Yan, D. & Jones, T. S. *"Molecular Template Growth and Its Applications in Organic Electronics and Optoelectronics."* Chemical Reviews **115,** 5570–5603 (2015).

155. Grumelli, D., Wurster, B., Stepanow, S. & Kern, K. *"Bio-inspired nanocatalysts for the oxygen reduction reaction."* Nature communications **4,** 2904 (2013).

156. Copéret, C., Chabanas, M., Petroff Saint-Arroman, R. & Basset, J. *"Homogeneous and heterogeneous catalysis: bridging the gap through surface organometallic chemistry."* Angewandte Chemie - International Edition **42,** 156–181 (2003).

157. Pollard, A. J. *et al.* *"Supramolecular assemblies formed on an epitaxial graphene superstructure."* Angewandte Chemie - International Edition **49,** 1794–1799 (2010).

158. MacLeod, J. M., Lipton-Duffin, J. A., Cui, D., De Feyter, S. & Rosei, F. *"Substrate Effects in the Supramolecular-Assembly of 1,3,5-Benzene-Tricarboxylic Acid on Graphite and Graphene."* Langmuir **31,** 7016–7024 (2015).

159. Korolkov, V. V. *et al.* *"van der Waals-Induced Chromatic Shifts in Hydrogen-Bonded Two-Dimensional Porphyrin Arrays on Boron Nitride."* ACS Nano **9,** 10347–10355 (2015).

160. Zhang, Z. X., Huang, H. L., Yang, X. M. & Zang, L. *"Tailoring Electronic Properties of Graphene by pi-pi Stacking with Aromatic Molecules."* Journal of Physical Chemistry Letters **2,** 2897–2905 (2011).

161. Chen, W., Chen, S., Qi, D. C., Gao, X. Y. & Wee, A. T. S. *"Surface Transfer p-Type Doping of Epitaxial Graphene."* Journal of the American Chemical Society **129,** 10418–10422 (2007).

162. Coletti, C. *et al.* *"Charge neutrality and band gap tuning of epitaxial graphene on SiC by molecular doping."* Physical Review B **81,** 235401 (2010).

163. Kozlov, S. M., Viñes, F. & Görling, A. *"Bandgap engineering of graphene by physisorbed adsorbates."* Advanced Materials **23,** 2638–43 (2011).

164. Jo, G. *et al.* *"The application of graphene as electrodes in electrical and optical devices."* Nanotechnology **23,** 112001 (2012).

165. Huang, H. *et al.* *"Van Der Waals Heterostructures between Small Organic Molecules and Layered Substrates."* Crystals **6,** 113 (2016).

166. Strong, L. & Whitesides, G. M. *"Structures of self-assembled monolayer films of organosulfur compounds adsorbed on gold single crystals: electron diffraction studies."* Langmuir **4,** 546–558 (1988).

167. Bonnerot, A., Chollet, P., Frisby, H. & Hoclet, M. *"Infrared and electron diffraction studies of transient stages in very thin Langmuir Blodgett films."* Chemical Physics **97,** 365–377 (1985).

168. Cheng, M., Ho, J. T., Hui, S. W. & Pindak, R. *"Electron-diffraction study of free-standing liquid-crystal films."* Physical Review Letters **59,** 1112–1115 (1987).

169. Pope, C. R. & Unger, V. M. *"Electron crystallography - the waking beauty of structural biology."* Current Opinion in Structural Biology **22,** 514–519 (2012).

170. Ubarretxena Belandia, I. & Stokes, D. L. *"Membrane protein structure determination by electron crystallography."* Current Opinion in Structural Biology **22,** 520–528 (2012).

171. Nogales, E. *"The development of cryo EM into a mainstream structural biology technique."* Nature Methods **13,** 24–27 (2015).

172. Pantelic, R. S., Meyer, J. C., Kaiser, U. & Stahlberg, H. *"The application of graphene as a sample support in transmission electron microscopy."* Solid State Communications **152,** 1375–1382 (2012).

173. Korolkov, V. V., Allen, S., Roberts, C. J. & Tendler, S. J. B. *"Green Chemistry Approach to Surface Decoration: Trimesic Acid Self-Assembly on HOPG."* The Journal of Physical Chemistry C **116,** 11519–11525 (2012).

174. Shayeganfar, F. *"Columnar organization of stack-assembled trimesic acid on graphene."* Journal of Physics: Condensed Matter **26,** 435305 (2014).

175. Addou, R. & Batzill, M. *"Defects and Domain Boundaries in Self-Assembled Terephthalic Acid (TPA) Monolayers on CVD Grown Graphene on Pt(111)."* Langmuir **29,** 6354–6360 (2013).

176. Banerjee, K. *et al.* *"Flexible Self-Assembled Molecular Templates on Graphene."* Journal of Physical Chemistry C **120,** 8772–8780 (2016).

177. Zhou, Q. *et al.* *"Switchable supramolecular assemblies on graphene."* Nanoscale **6,** 8387 (2014).

178. Duchamp, D. J. & Marsh, R. E. *"The crystal structure of trimesic acid (benzene 1,3,5 tricarboxylic acid)."* Acta Crystallographica Section B Structural Crystallography and Crystal Chemistry **25,** 5–19 (1969).

179. Bailey, M. & Brown, C. J. *"The crystal structure of terephthalic acid."* Acta Crystallographica **22,** 387–391 (1967).

180. Hui, S.-w. *"Electron diffraction and diffraction contrast imaging of thin organic films."* Journal of Electron Microscopy Technique **11,** 286–297 (1989).

181. Marée, C. H. M. *et al.* *"Photovoltaic effects in porphyrin polymer films and heterojunctions."* Journal of Applied Physics **80,** 3381–3389 (1996).

182. Hill, I. G., Rajagopal, A., Kahn, A. & Hu, Y. *"Molecular level alignment at organic semiconductor metal interfaces."* Applied Physics Letters **73,** 662–664 (1998).

183. Malinski, T. & Taha, Z. *"Nitric oxide release from a single cell measured in situ by a porphyrinic-based microsensor."* Nature **355,** 717–719 (1992).

184. Wada, Y. *"Proposal of atom/molecule switching devices."* Journal of Vacuum Science & Technology A: Vacuum, Surfaces, and Films **17,** 1399–1405 (1999).

185. *"Molecular Self-Assembly in a Poorly Screened Environment: F4 TCNQ on Graphene BN."* ACS Nano **9,** 12168–12173 (2015).

186. Ouyang, R., Liu, J. X. & Li, W. X. *"Atomistic theory of ostwald ripening and disintegration of supported metal particles under reaction conditions."* Journal of the American Chemical Society **135,** 1760–1771 (2013).

187. Poirier, G. E. & Tarlov, M. J. *"Molecular ordering and gold migration observed in butanethiol self-assembled monolayers using scanning tunneling microscopy."* Journal of Physical Chemistry **99,** 10966–10970 (1995).

188. Pacholski, C., Kornowski, A. & Weller, H. *"Self-assembly of ZnO: From nanodots to nanorods."* Angewandte Chemie - International Edition **41,** 1188–1191 (2002).

189. Chun Zeng, H. *"Ostwald Ripening: A Synthetic Approach for Hollow Nanomaterials."* Current Nanoscience **3,** 177–181 (2007).

190. Zhang, H. *et al.* *"Host-guest superstructures on graphene-based Kagome lattice."* Journal of Physical Chemistry C **116,** 11091–11095 (2012).

191. Piot, L. *et al.* *"Long-range alignments of single fullerenes by site-selective inclusion into a double-cavity 2D open network."* Journal of the American Chemical Society **131,** 12864–12865 (2009).

192. Blunt, M. O. *et al.* *"Guest-induced growth of a surface-based supramolecular bilayer."* Nature Chemistry **3,** 74–78 (2011).

193. Wintterlin, J. & Bocquet, M. L. *"Graphene on metal surfaces."* Surface Science **603,** 1841–1852 (2009).

194. Garnica, M. *et al.* *"Long-range magnetic order in a purely organic 2D layer adsorbed on epitaxial graphene."* Nature Physics **9,** 368–374 (2013).

195. Lu, J., Gomes, L. C., Nunes, R. W., Castro Neto, A. H. & Loh, K. P. *"Lattice relaxation at the interface of two-dimensional crystals: Graphene and hexagonal boron-nitride."* Nano Letters **14,** 5133–5139 (2014).

196. Bhattarai, A., Mazur, U. & Hipps, K. W. *"Desorption kinetics and activation energy for cobalt octaethylporphyrin from graphite at the phenyloctane solution-graphite interface: An STM study."* Journal of Physical Chemistry C **119,** 9386–9394 (2015).

197. Forrest, S. R. & Burrows, P. E. *"Direct observation of an organic superlattice structure."* Physical Review Letters **72,** 2308 (1994).

198. Yoshida, Y. *et al.* *"Control of growth mechanism and optical properties of p-sexiphenyl thin films on ionic crystal substrates."* Journal of Crystal Growth **198-199,** 923–928 (1999).

199. Koma, A. *"Van der Waals epitaxy - a new epitaxial growth method for a highly lattice mismatched system."* Thin Solid Films **216,** 72–76 (1992).

200. Driskill, J., Vanzo, D., Bratko, D. & Luzar, A. *"Wetting transparency of graphene in water."* Journal of Chemical Physics **141** (2014).

201. Shih, C., Strano, M. S. & Blankschtein, D. *"Wetting translucency of graphene."* Nature Materials **12,** 866–869 (2013).

202. Kim, Y. *et al.* *"Remote epitaxy through graphene enables two-dimensional material-based layer transfer."* Nature **544,** 340–343 (2017).

203. Ogunrinde, A., Hipps, K. W. & Scudiero, L. *"A scanning tunneling microscopy study of self assembled nickel(II) octaethylporphyrin deposited from solutions on HOPG."* Langmuir **22,** 5697–5701 (2006).

204. Scudiero, L., Barlow, D. E. & Hipps, K. W. *"Scanning tunneling microscopy, orbital-mediated tunneling spectroscopy, and ultraviolet photoelectron spectroscopy of nickel(II) octaethylporphyrin deposited from vapor."* Journal of Physical Chemistry B **106,** 996–1003 (2002).

205. Scudiero, L. & Hipps, K. W. *"Controlled manipulation of self-organized Ni(II)-octaethylporphyrin molecules deposited from solution on HOPG with a scanning tunneling microscope."* Journal of Physical Chemistry C **111,** 17516–17520 (2007).

206. Teugels, L. G., Avila-Bront, L. G. & Sibener, S. J. *"Chiral domains achieved by surface adsorption of achiral nickel tetraphenyl- or octaethylporphyrin on smooth and locally kinked Au(111)."* Journal of Physical Chemistry C **115,** 2826–2834 (2011).

207. Gruden-Pavlović, M., Grubišić, S., Zlatar, M. & Niketić, S. R. *"Molecular mechanics study of nickel(II) octaethylporphyrin adsorbed on graphite(0001)."* International Journal of Molecular Sciences **8,** 810–829 (2007).

208. Bai, Y. *et al.* *"Adsorption of cobalt(II) octaethylporphyrin and 2H-octaethylporphyrin on Ag(111): New insight into the surface coordinative bond."* New Journal of Physics **11,** 125004–125019 (2009).

209. Borghetti, P. *et al.* *"Adsorption geometry, conformation, and electronic structure of 2H-octaethylporphyrin on Ag (111) and Fe metalation in ultra high vacuum."* The Journal of Chemical Physics, 144702–144709 (2013).

210. Lubensky, T. C., Socolar, J. E. S., Steinhardt, P. J., Bancel, P. A. & Heiney, P. A. *"Distortion and Peak Broadening in Quasicrystal Diffraction Patterns."* Physical Review Letters **57,** 1440–1443 (1986).

211. Lin, Z. *et al.* *"Precise control of the number of layers of graphene by picosecond laser thinning."* Scientific Reports **5,** 1–7 (2015).

212. Díez, I. & Ras, R. H. A. *"Fluorescent silver nanoclusters."* Nanoscale **3,** 1963 (2011).

213. Zheng, J., Nicovich, P. R. & Dickson, R. M. *"Highly Fluorescent Noble-Metal Quantum Dots."* Annual Review of Physical Chemistry **58,** 409–431 (2007).

214. Wilcoxon, J. P. & Abrams, B. L. *"Synthesis, structure and properties of metal nanoclusters."* Chemical Society Reviews **35,** 1162 (2006).

215. Shang, L., Dong, S. & Nienhaus, G. U. *"Ultra-small fluorescent metal nanoclusters: Synthesis and biological applications."* Nano Today **6,** 401–418 (2011).

216. Ashenfelter, B. A., Desireddy, A., Yau, S. H., Goodson, T. & Bigioni, T. P. *"Fluorescence from Molecular Silver Nanoparticles."* The Journal of Physical Chemistry C **119,** 20728–20734 (2015).

217. Purusottam Jena A. Castleman, J. *"Nanocluster: A bridge across disciplines."* (Elsevier, 2010).

218. Chakraborty, I. *et al.* *"The superstable 25 kDa monolayer protected silver nanoparticle: Measurements and interpretation as an icosahedral* $Ag_{152}(SCH_2CH_2Ph)_{60}$ *cluster."* Nano Letters **12,** 5861–5866 (2012).

219. Petty, J. T., Story, S. P., Hsiang, J. C. & Dickson, R. M. *"DNA-templated molecular silver fluorophores."* Journal of Physical Chemistry Letters **4,** 1148–1155 (2013).

220. Xu, H. & Suslick, K. S. *"Sonochemical Synthesis of Highly Fluorescent Ag Nanoclusters."* ACS Nano **4,** 3209–3214 (2010).

221. González, B. S., Blanco, M. C. & López-Quintela, M. A. *"Single step electrochemical synthesis of hydrophilic/hydrophobic Ag5 and Ag6 blue luminescent clusters."* Nanoscale **4,** 7632 (2012).

222. Qu, F., Li, N. B. & Luo, H. Q. *"Transition from nanoparticles to nanoclusters: Microscopic and spectroscopic investigation of size-dependent physicochemical properties of polyamine-functionalized silver nanoclusters."* Journal of Physical Chemistry C **117,** 3548–3555 (2013).

223. Kunwar, P., Hassinen, J., Bautista, G., Ras, R. H. A. & Toivonen, J. *"Direct laser writing of photostable fluorescent silver nanoclusters in polymer films."* ACS Nano **8,** 11165–11171 (2014).

224. Kunwar, P., Hassinen, J., Bautista, G., Ras, R. H. A. & Toivonen, J. *"Sub-micron scale patterning of fluorescent silver nanoclusters using low-power laser."* Scientific Reports **6,** 6–11 (2016).

225. Sloan, J. *et al.* *"Direct imaging of the structure, relaxation, and sterically constrained motion of encapsulated tungsten polyoxometalate lindqvist ions within carbon nanotubes."* ACS Nano **2,** 966–976 (2008).

226. Koshino, M., Solin, N., Tanaka, T., Isobe, H. & Nakamura, E. *"Imaging the passage of a single hydrocarbon chain through a nanopore."* Nature Nanotechnology **3,** 595–597 (2008).

227. Nakamura, E. *et al.* *"Imaging of conformational changes of biotinylated triamide molecules covalently bonded to a carbon nanotube surface."* Journal of the American Chemical Society **130,** 7808–7809 (2008).

228. Nakamura, E. *"Electron Microscopic Observation of Selective Excitation of Conformational Change of a Single Organic Molecule."* 3–6 (2015).

229. Chamberlain, T. W. *et al.* *"Stop Frame Filming and Discovery of Reactions at the Single-Molecule Level by Transmission Electron Microscopy."* ACS Nano, acsnano.6b08228 (2017).

230. Zhu, Y. *et al.* *"Graphene and graphene oxide: Synthesis, properties, and applications."* Advanced Materials **22,** 3906–3924 (2010).

231. Upadhyay, S., Bagheri, S. & Abd Hamid, S. B. *"Enhanced photoelectrochemical response of reduced-graphene oxide/$Zn_{1-x}Ag_xO$ nanocomposite in visible-light region."* International Journal of Hydrogen Energy **39,** 11027–11034 (2014).

232. Gao, W. *"The chemistry of graphene oxide."* Graphene Oxide: Reduction Recipes, Spectroscopy, and Applications, 61–95 (2015).

233. Park, S. & Ruoff, R. S. *"Chemical methods for the production of graphenes."* Nature Nanotechnology **4,** 217–224 (2009).

234. Huang, X., Qi, X., Boey, F. & Zhang, H. *"Graphene-based composites."* Chemical Society Reviews **41,** 666–686 (2012).

235. Stobbs, W. M. *"Quantitative high resolution transmission electron microscopy: the need for energy filtering and the advantages of energy-loss imaging."* Ultramicroscopy **151,** 171–184 (1988).

236. Chapman, R. L. & Staehelin, L. A. *"4D Imaging of Transient Structures and Morphologies in Ultrafast Electron Microscopy."* Science **322,** 1227–1232 (1986).

237. Noda, I. & Ozaki, Y. *"Two-Dimensional Correlation Spectroscopy - Applications in Vibrational and Optical Spectroscopy."* (Wiley, 2005).

238. Thomas, H. R., Marsden, A. J., Walker, M., Wilson, N. R. & Rourke, J. P. *"Sulfur-functionalized graphene oxide by epoxide ring-opening."* Angewandte Chemie - International Edition **53,** 7613–7618 (2014).

239. Cariati, F. & Naldini, L. *"Preparation and properties of gold atom cluster compounds: octakis-(triarylphosphine)enneagold trianion."* Journal of the Chemical Society, Dalton Transactions, 2286–2287 (1972).

240. Wen, F., Englert, U., Gutrath, B. & Simon, U. *"Crystal Structure, Electrochemical and Optical Properties of* $[Au9(PPh_3)_8](NO_3)_3$*."* European Journal of Inorganic Chemistry **2008,** 106–111 (2008).

241. Kim, B. H., Hackett, M. J., Park, J. & Hyeon, T. *"Synthesis, characterization, and application of ultrasmall nanoparticles."* Chemistry of Materials **26,** 59–71 (2014).

242. Churchill, M. R. & Hutchinson, J. P. *"Crystal Structure of Tetrairidium Dodecacarbonyl, Ir4(CO)12. An Unpleasant Case of Disorder."* Inorganic Chemistry **17,** 3528–3535 (1978).

243. NIST. *"JANAF Thermochemical Tables, Third Edition."* Journal of Phyiscal Chemistry Reference Data (1985).

244. Gatan, I. *"OneView Camera Model 1095 User's Guide."* (2015).